



---

Università del Salento

Facoltà di Scienze Matematiche, Fisiche e Naturali

Dipartimento di Matematica e Fisica "Ennio De Giorgi"

---

**A beyond the Standard Model journey via Renormalization  
Group methods**

*Supervisor*

Prof. Claudio Corianò

*Candidate*

Carlo Marzo

Tesi di Dottorato di Ricerca in Fisica – XXVIII ciclo



# Contents

<b>List of publications</b>	<b>iii</b>
<b>Preface and Outline</b>	<b>v</b>
<b>Acknowledgements</b>	<b>ix</b>
<b>Introduction</b>	<b>xi</b>
<b>1 Renormalization Group methods and the Effective Potential</b>	<b>1</b>
1.1 Introduction . . . . .	1
1.2 True vacuum of a quantum field theory . . . . .	2
1.3 The Jackiw's method and the scalar QED vacuum . . . . .	3
1.3.1 The Jackiw's Effective Potential . . . . .	3
1.3.2 Massive fields in massless Abelian Higgs model . . . . .	5
1.3.3 Exploding Logs part I: Renormalization Group improvement . . . . .	8
1.4 The Effective Potential in mass independent renormalization schemes . . . . .	10
1.4.1 Exploding Logs part II: Decoupling and Thresholds . . . . .	11
<b>2 The three roads: Stability, Instability and Metastability.</b>	<b>15</b>
2.1 Introduction . . . . .	15
2.2 Tunnelling . . . . .	16
2.2.1 Quantum Fluctuations . . . . .	17
2.2.2 Thermal Fluctuations . . . . .	20
2.3 The Matching Conditions in the SM . . . . .	24
2.4 Finite temperature Effective Potential of SM beyond leading order . . . . .	27
2.5 Bounce solution and thermal tunneling . . . . .	28
2.6 The phase diagram of the Standard Model at finite temperature . . . . .	30
2.6.1 Instability bound at finite temperature . . . . .	31
2.6.2 Instability bound and dependence from cosmology . . . . .	33
2.7 Comments and conclusions . . . . .	37

<b>3</b>	<b>Vacuum stability in low-scale seesaw models</b>	<b>39</b>
3.1	Introduction . . . . .	39
3.2	The inverse seesaw model . . . . .	40
3.2.1	Bounds from low-energy neutrino data . . . . .	42
3.2.2	Relevant parameter space and setup for the numerical analysis . . . . .	43
3.3	Stability of the electroweak vacuum and low-scale seesaw . . . . .	48
3.3.1	The Higgs effective quartic coupling . . . . .	48
3.3.2	The Matching Conditions in the SM plus low-scale seesaw . . . . .	50
3.3.3	The renormalization group equations . . . . .	51
3.4	Comments and conclusions . . . . .	52
<b>4</b>	<b>Non-anomalous <math>U(1)'</math> models, from LHC to GUT scale.</b>	<b>57</b>
4.1	Introduction . . . . .	57
4.2	The model . . . . .	58
4.2.1	Charge assignment in minimal Abelian extension . . . . .	58
4.2.2	Kinetic Mixing . . . . .	60
4.2.3	Scalar sector and spontaneous symmetry breaking . . . . .	62
4.3	Constraints from EWPTs and LHC searches . . . . .	64
4.4	The RG analysis . . . . .	66
4.4.1	RG equations and the Abelian mixing . . . . .	66
4.4.2	The Matching Conditions in the $SM \times U(1)'$ . . . . .	68
4.4.3	The stability analysis . . . . .	70
4.5	LHC Phenomenology . . . . .	76
4.5.1	$Z'$ production and decay . . . . .	76
4.5.2	Higgs production and decay . . . . .	80
4.6	Comments and conclusions . . . . .	89
<b>5</b>	<b>Final remarks</b>	<b>91</b>
<b>A</b>	<b>Linear and double seesaw</b>	<b>93</b>
A.1	Linear seesaw: results . . . . .	95
A.2	Double seesaw: results . . . . .	95
<b>B</b>	<b>One-loop <math>\beta</math> functions for non-anomalous <math>U(1)'</math> model with generic charge assignment</b>	<b>99</b>
<b>C</b>	<b>Two-loop <math>\beta</math> functions for non-anomalous <math>U(1)'</math> model</b>	<b>101</b>

# List of publications

This thesis work is mainly based on the following publications:

- Claudio Corianò, Luigi Delle Rose, Carlo Marzo,  
*"Vacuum Stability in  $U(1)$ -Prime Extensions of the Standard Model with TeV Scale Right Handed Neutrinos"*  
Published in Phys. Lett. B **738**, 13 (2014), [arXiv:1407.8539]
- Luigi Delle Rose, Carlo Marzo, Alfredo Urbano,  
*"On the stability of the electroweak vacuum in the presence of low-scale seesaw models"*  
Published in JHEP **1512**, 050 (2015), [arXiv:1506.03360]
- Luigi Delle Rose, Carlo Marzo, Alfredo Urbano,  
*"On the fate of the Standard Model at finite temperature"*  
Published in JHEP **1605**, 050 (2016), [arXiv:1507.06912]
- Claudio Corianò, Luigi Delle Rose, Carlo Marzo,  
*"Constraints on abelian extensions of the Standard Model from two-loop vacuum stability and  $U(1)_{B-L}$ "*  
Published in JHEP **1602**, 135 (2016), [arXiv:1510.02379]
- Elena Accomando, Claudio Coriano, Luigi Delle Rose, Juri Fiaschi, Carlo Marzo, Stefano Moretti  
*" $Z'$ , Higgses and heavy neutrinos in  $U(1)'$  models: from the LHC to the GUT scale"*  
Published in JHEP **1607**, 086 (2016), [arXiv:1605.02910]

## Publications not discussed

The following completes the list of papers published during my PhD years:

- Claudio Corianò, Luigi Delle Rose, Carlo Marzo, Mirko Serino,  
*"Higher Order Dilaton Interactions in the Nearly Conformal Limit of the Standard Model"*  
Published in Phys. Lett. B **717**, 182 (2012), [arXiv:1207.2930]

- Claudio Corianò, Luigi Delle Rose, Carlo Marzo, Mirko Serino,  
”*Conformal Trace Relations from the Dilaton Wess-Zumino Action*”  
Published in Phys. Lett. B **726**, no. 4-5, 896 (2013), [arXiv:1306.4248]
- Claudio Corianò, Luigi Delle Rose, Carlo Marzo, Mirko Serino,  
”*The dilaton Wess-Zumino action in six dimensions from Weyl gauging: local anomalies and trace relations*”  
Published in Class. Quant. Grav. **31**, 105009 (2014), [arXiv:1311.1804]
- Johar Ashfaque, Luigi Delle Rose, Alon Faraggi, Carlo Marzo,  
”*The LHC di-photon excess and Gauge Coupling Unification in Extra  $Z'$  Heterotic-String Derived Models*”, [arXiv:1606.01052]

## Proceedings

- Luigi Delle Rose, Carlo Marzo, Mirko Serino,  
”*Conformal anomaly actions for dilaton interactions*”  
Published in EPJ Web Conf. **80**, 00015 (2014), [arXiv:1409.4184]
- Claudio Corianò, Luigi Delle Rose, Carlo Marzo,  
”*Stability constraints of the scalar potential in extensions of the Standard Model with TeV scale right handed neutrinos*”  
Published in Nucl. Part. Phys. Proc. **265-266**, 311 (2015), [arXiv:1411.7168]

# Preface and Outline

In this thesis I have tried to emphasize the unique path that crosses the excursions beyond the Standard Model undertaken during my PhD experience. In a way, I have been helped in this by the phenomenological scenario which has emerged at LHC. The absence of new signatures has, in fact, strengthened the importance of the methods evoked and applied in this thesis. The applications of the Renormalization Group have become one of the few supports used to explore a given model along a large energy span. In this regard it completes the equipment at the theorist's disposal, together with the similar roles shared by cosmological analyses and the exploitation of radiative corrections to flavour observables. The Effective Potential is the focus of this kind of studies, absorbing the extrapolation of the model via Renormalization Group and acting as a marker of its phenomenological coherence. I have developed this thesis trying to stress the bound between the Effective Potential, the Renormalization Group and the delicate quantum field methods used to create an efficient interplay in a perturbative framework. In particular I have tried to point out the underestimated role of the matching, both in the Renormalization evolution as in linking different regimes. This has formed the necessary background to move to the part of the thesis devoted to the theoretical and phenomenological test of minimal extensions of the Standard Model.

More precisely the structure of this work is the following:

## **Chapter 1**

This introducing chapter starts outlining a formal and operative definition of the vacuum in quantum field theory. The link between the *true* vacuum and the Effective Potential is formulated and the functional method of Jackiw, for the computation of the latter, is exploited. Some explicit examples are illustrated so to cover all the scalar, fermion and vector cases, needed along this work. In particular the original arena of the Coleman and Weinberg massless scalar electrodynamics is confronted in a functional language. The Renormalization Group is then introduced by a direct application on the improvement of the perturbative computation. The change of the classical expectation, induced by radiative corrections, is firstly met showing explicitly the case of the radiative breaking of symmetry. The control of the perturbative expansion is also highlighted in the context of a massless renormalization scheme, as used in this thesis. The importance of the artificial decoupling of heavy degrees of freedom and the resulting use of an efficient matching procedure is then illustrated.

## **Chapter 2**

The quantum field definition of tunnelling is introduced, in particular the reduction of such computation to the research of the bounce solution. The parametrization of finite temperature fluctuations in the Effective Potential is also illustrated together with the role of quantum and thermal corrections in af-

fecting the transition from a false to a true vacuum. The fate of a theory, which is candidate to describe nature all along a given energy span, is linked to the fate of the vacuum in such range. The three possible phases, unstable, stable and metastable are presented. The use of the Effective Potential, together with the Renormalization Group, is then exploited for an up-to-date investigation of the fate of the Standard Model. The coherent inclusion of thermal corrections is strongly dependent on the cosmological history of the Universe. The precise interplay among the tunnelling (thermal) amplitude and the cosmological assumptions are deeply discussed.

### Chapter 3

In this chapter is presented a first departure from the Standard Model as dictated by pressing evidences of New Physics from neutrino data. The analysis relates the studies of the model's phases to the peculiar signatures of its spectrum. In this way it connects the machinery introduced in the previous chapters to the research of Physics beyond the Standard Model. In particular an implementation of the Inverse Seesaw mechanism is deeply inspected. The parameters of the mechanism are tuned in respect of the experimental bounds and of naturalness. A procedure to randomly generate such parameters and the corresponding link to the Yukawa coupling, expressed by the Casas-Ibarra formula, is presented. In this way is challenged the ability of the model to account for the limits on lepton flavour violating decay and on neutrinoless double beta decay. To compute the phases of the model as affected by the new Yukawa coupling of the Inverse Seesaw, an extension of the matching to coherently include two-loop  $\beta$  functions is shown. With the insights from the successive Renormalization Group analysis, the unstable character of a subgroup of points in the new parameter space is found, leading to a further theoretical bound in our investigation of the model.

### Chapter 4

In the last chapter of this work, a further step is made in the exploration of minimal and testable extensions of the Standard Model, by exploiting the introduction of an extra Abelian gauge factor. The theoretical framework is deeply illustrated. In particular is largely analyzed the peculiar appearance of the kinetic mixing among the two Abelian groups, which furnishes new elements to be taken into account for a proper phenomenological survey. The model is studied with a general view on the possible charge assignments, applying stepwise the impact of the kinetic mixing in their parametrization as well as the constraints from anomaly freedom. The interconnection between the gauge, the scalar and the fermion sector is highlighted. The new parameter space is put on the verge of present LHC probe of new gauge and scalar bosons. The bounds coming from LEP2 data are included and extended to the LHC investigations at 8 TeV, both on the scalar sector as in the gauge one. The gauge sector is constrained by a signal-to-background analysis on the di-lepton channel which represents a strong improvement in respect to the bounds connected to the electroweak tests. On the parameter space shaped by such bounds, a stability analysis is developed starting from the necessary matching conditions. These are illustrated with large detail so to clarify the role of the contribution of new Physics. From the stability analysis a comparison with the Standard Model case is presented, with emphasis on the impact of the new degrees of freedom in worsening or ameliorating its metastable scenario. On this ground some benchmark points, which are shown to be promising to forthcoming test at LHC, are highlighted and characterized with computation of corresponding branchings and cross sections.

## Appendix

Appendix A forms an extension of chapter 3. The methods are the same of those applied to the Inverse Seesaw mechanism, but the arena concerns now the Linear and the Double seesaw case. In both cases the requirement of metastability has produced strong constraints for the new Yukawa sector, affecting the interpretation that would follow a possible discovery in the research for New Physics processes as lepton flavour violating muon decay ( $\mu \rightarrow e\gamma$ ) and the neutrinoless double beta decay ( $0\nu 2\beta$ ).

In Appendix B and C are shown the complete set of one-loop and two-loop  $\beta$  functions used for the analysis of chapter 4. At one-loop the two parameters  $z_Q$ ,  $U(1)'$  charge of the quark doublet, and  $z_u$ ,  $U(1)'$  charge of the right-handed quark up, are given explicitly to account for the residual freedom to assign charges in respect to anomaly cancellation. Such freedom can also be elaborated by choosing directly a  $B - L$  charge assignment and a non-zero mixing. With this observation the following two-loop  $\beta$  functions, where  $z_Q$  and  $z_u$  are chosen to give  $B - L$ , are completely generic for our model.



# Acknowledgements

My greatest gratitude goes to my advisor, Prof. Claudio Corianò, who has always supported and encouraged my efforts, in the good as in the more difficult times, during all my academic education. Without his perseverance I would not have been able to pursue my doctorate degree. My gratitude also extends to my parents, who have been indispensable to successfully conclude this journey started many years ago. Even if I am still not sure I have been able to explain them what a doctorate degree is. It has been a pleasure to meet and work with Profs Elena Accomando, Alon Faraggi and Stefano Moretti and try to assimilate their passion for research. Their insights have always been precious and never trivial, and I will always be grateful for the continuous support they provide. My gratitude also extends to Profs Emidio Gabrielli and Martti Raidal, for the time and the attention they have always shown to me. Luigi is clever enough to know already that much of this work originates from his tireless attitude, tenacity and ability. So I will thank him for his time as an unexpected friend, for all those dinners, the quake fights, and those crazy treasure hunts that have enriched exponentially the last three years. I have also to thank Luigi's partner, Annalisa, for providing her delicious arancini<sup>1</sup>, which fueled most of this work. I want to thank Antonio and Priyo who have been a sweet and fun company but also a competent and original support in our more serious discussions. Working with Alfredo has been a fun and learning experience. His original ideas and style have changed my approach to the subject. Many deductions and computations in this thesis are deeply indebted to his initiative. I thank Prof. Luca Girlanda for his valuable and kind suggestions about this work, which I have done my best to follow.

At last, I'd like to dedicate this work to the more interesting bound states of quarks and leptons I know. To my little niece, Beatrice, who I adore having no idea what she is talking about.

To my brothers, Alberto and Federico, whose academic records testify how we succeeded against the family tradition that, apparently, wanted us to become nuns.

To Perla, who has been standing my jokes for too long and has been pushing and supporting me, all this time, with that irrationality that can only be found in the love bonds.

---

<sup>1</sup><https://en.wikipedia.org/wiki/Arancini>



# Introduction

The hopes to witness a clear evidence of New Physics (NP) at LHC have been shattered by the most recent inspections of data, now that also the promising diphoton resonance has been reduced to the status of a statistical fluctuation. Of all the new proposals developed in the last four decades, it is still a restricted collection of papers published in the sixties, that can perfectly account for the collider outcomes in 2016. The Standard Model (SM) has triumphed as an extraordinarily efficient effective field theory along the energies probed. Yet, its arbitrary formal structure, and, more importantly, the amount of data collected from cosmological measurements and neutrino facilities, are a clear indication that something new and unknown is hiding not so far from our phenomenological reach.

The approach of the model building industry in respect to this clues of NP is twofold. It is possible to have a guess for a simpler and more fundamental theory addressing energy scales many order of magnitudes larger than the one reached at current colliders. Then, hopefully, a procedure can be given to integrate the heavy degrees of freedom and reach a low-energy effective field theory able to include the SM, but explaining also Dark Matter, neutrino masses, baryogenesis...

This is, for instance, the usual path followed by GUT or String-derived proposals.

At the opposite, the other way adopts a more pragmatic approach, searching the minimal adjustments to the SM that are sufficient to give a coherent description for, at least, the more pressing requests from the experiments. In a way, this is the strategy used in this thesis. Still, if we weren't able to draw some hints about the above fundamental structure, our pursuit would be reduced to a pure bookkeeping. The Renormalization Group (RG) may intervene giving us exactly the right instrument to clue the known low, with the unknown high-energy sector, where new structures are expected to replace the SM. This is for example the role that the RG plays when inspecting the prospect that the complicate and varied behaviour at Electroweak scale may be just the manifestation of a unique gauge internal symmetry. Along this implementation has emerged how the RG could also shed light in the same direction, by its contribution in the analysis of the quantum vacuum structure. As we will illustrate in detail along this work, the knowledge that we can build around the true vacuum of a model is essentially of perturbative nature. As an effect of the inclusion of disparate scales in our quantum-field computation, logarithms of their ratios signal that we have not properly isolated the relevant degrees of freedom, spoiling the perturbative reliability. An efficient technique must be invoked and the RG, supported by an effective field theory approach, turned out, as we will illustrate in the first chapters, to be suited for this cause. These ideas go back to the seminal paper of [4] where a leading order analysis of the vacuum and of the perturbative regime resulted in bounds on the mass of top and the Higgs, unknown parameters at the

time. With many intermediate steps and a considerable gain in the computational precision, since its first application, the same technology has been developed for the SM post Higgs discovery [25]. In this case the scenario concerned a model (the SM) with all the relevant parameters experimentally measured, and the survey of the quantum vacuum has served a plethora of theoretical informations: from its phase portrait to its cosmological fate, to the critical and suspect role played by the top and Higgs mass.

We will present in this thesis our personal route enjoying both the approaches of [4], when we have to investigate an unknown sector, and [25], when we will extend their analysis to the inclusion of thermal fluctuations.

It is this latter survey that inaugurates our original work, in our attempt to organize this thesis in order of increasing complexity, from the *pure* SM to the minimal extensions tackled. The conservative approach, SM and nothing else, also in the light of the evidences of NP presented above, is anything but unrealistic. It is an interesting possibility that the SM could represent one of the two oasis, the other being a theory accounting for general relativity, in an energy-desert up to the Planck scale. This is what we expect in case the NP can be accounted by a mild and decoupled modification of the SM, irrelevant in the RG extrapolation. Within this scenario we investigated the impact of the most relevant thermal corrections updating the previous literature [14, 15, 16, 20]. The effects of finite temperature corrections are strongly dependent from the cosmological history of our Universe. As we will investigate across different cosmological assumptions, thermal effects will strengthen or dangerously worsen the instability region in the SM phase portrait, assaulting also values in less than  $1\text{-}\sigma$  from the central top mass. Such possibility would cry even louder for the inclusion of NP to accommodate for the stability of our (until now) stable 246 GeV vacuum.

In presence of a relevant extension of the SM, the vacuum stability analysis has instead to follow more closely the attitude of [4]. In this case we don't have a complete knowledge of the parameter space and the RG extrapolation is explored to draw bounds and constraints over an, otherwise phenomenologically allowed, new sector. We have taken the discovery of non-zero neutrino masses as the more urgent demand to model building. The minimal adjustment to account for massive neutrinos is easily provided by the SM itself, which can envisage the neutrino as a Dirac particle whose mass is due to spontaneous symmetry breaking of the Higgs, by a new Yukawa interaction with three, promptly introduced, right-handed neutrinos. The inclusion of such mechanism, efficient as it can be, is completely invisible in a RG analysis and can be absorbed by our inspection of the high-energy behaviour of the SM. Also, the extraordinarily small value of the Yukawa needed would add a further source of unnaturalness in the already plagued hierarchy of the flavour sector. We instead have focused our effort in the direction of testable and RG-relevant extensions. More natural mechanisms are invoked and the introduction of extra singlet fermions, in addition to the right-handed neutrinos, lead to a class of seesaw models [47, 48, 49, 50, 51, 52] with a rich and influential fabric. Such models provide sources of lepton number and flavour violation, the first a clear hint of a Majorana nature of the neutrino mass eigenstate. Features like these are currently under the lens of the MEG collaboration [87] and, for the neutrinoless double beta decay, by GERDA [88], EXO-200 [89, 90], and KamLAND-ZEN [91]. It is in this arena, putting the class of models studied close to the forthcoming experimental quest, that the stability analysis has shown its extreme effectiveness, by picturing the possible phases and by selecting the testable points linked to an unstable fate.

The last part of this work takes our search a step forward by inspecting the consequences and the LHC discovery potential of a new, massive, neutral vector boson, dubbed Z-prime ( $Z'$ ). This addition to the SM spectrum must be coherently supplemented by an extra Abelian gauge factor. Which in turn asks for new fermionic degrees of freedom, to cancel the induced gauge and gravitational anomalies, and an extra singlet scalar, to give  $Z'$  a mass. The analysis will have a moderate ambition for generality, spanning among all the class of non-anomalous extra  $U(1)$  charge assignment. Also, an extra Abelian factor is a common presence in many breaking chains for GUTs of rank greater than four, as in the promising  $SO(10)$ . Our survey may therefore account for many different unification patterns in the universality class of our  $Z'$  model.

Although representing *the* minimal gauge extension, the model reveals a rich collection of collider signatures that can leave distinctive footprints at LHC. The two-loop stability analysis developed around the (potentially) visible parameter space, will not just furnish a link with the different phases of the model. That is, in answering, in case of discovery, to what energy extent a *given* parameter point would supply an effective description of nature or when, instead, the instability would ask for an urgent UV completion. The richness of this minimal  $Z'$  class allows also to tackle, by studying the vacuum, a larger class of physical aspects, that go beyond their application to this model and are of general theoretical interest. We refer, over all, to the role of new scalar degrees of freedom in mitigating the critical dependence of the SM's fate from its relevant parameters. Or, also, to the peculiar presence of the kinetic mixing and the importance of its RG evolution. That its changing form along the energy scales can enlighten the structure of the UV completion, which breaks also into  $U(1)_Y \times U(1)'$ , is an information that can be read off only via the RG extrapolation of its low-energy value.

A feature that reaffirms the necessity to sustain the phenomenological quest with the insights of the RG methods.



# Chapter 1

## Renormalization Group methods and the Effective Potential

### 1.1 Introduction

The inclusion of the implicit dependence of the renormalization scale in the set of parameters of a quantum field theory has led Gell-Mann and Low, back in 1954 [1], to successfully recover the energy-scaling of the Coulomb potential at high-energy (or small distances, as stated in the paper's title). This was probably not the first, but surely one of the most renowned applications of the renormalization group (RG) used to gain insight towards energy scales far from the one where measurements are realized. The key of the process Gell-Mann and Low carried was to avoid the extrapolation of the electron scattering amplitude at high energies still using a coupling defined (and renormalized) at large distance. Instead a running coupling, renormalized at the scale at which the amplitude is computed, was introduced exploiting the invariance of the complete (and measurable) result from that particular scale.

That this golden rule could also shed light to the real vacuum structure of a quantum field theory was a concept later developed by Coleman and Weinberg in their seminal paper [2], based on previous work on the effective potential by Jona Lasinio [3]. Such new perspective in the quantum computation armory opened a new kind of analysis to draw constraints and investigate the model's properties. Among countless examples, the archetype of these application, at least for our investigation area, is represented by the use of RG methods and the study of the effective potential in constraining the (yet unknown) top and Higgs mass for an  $SU(5)$ -unified theory in [4].

In this chapter we review the main tools developed along the lines of these past investigations and that represent the core of our Beyond the Standard Model search.

## 1.2 True vacuum of a quantum field theory

Our world is quantum but our knowledge of its behavior is mostly confined to perturbative approximations that start from the definition of a classical Lagrangian. As an exciting outcome of this, trivial statements that can hold for the classical description may completely be replaced by new and unexpected ones. The source of this change is encoded in the radiative corrections that the quantum model produces. One of the more dramatic twists brought by radiative corrections was exposed by Coleman and Weinberg's study of the quantum version of scalar massless electrodynamics (scalar QED from now on) [2] which, stated in the words of the authors, does not remain massless nor electrodynamics.

Their study brought to the main audience of quantum field theorists, and adapted, tools already developed for superconductivity researches (as already done by also [3]), which allowed to efficiently control the role of the quantum corrections.

The *effective potential* is the cornerstone of such analysis and, as the *effective* attribute subtly reveals, replaces and improve the classical potential which appears in the starting classical Lagrangian.

To illustrate the main ingredients used for the next chapter's investigation let's start from the classical ground. The classical potential  $V$  of a field theory is, by definition, the derivative-independent part of the Lagrangian. Even when dealing with a quantization of the system described by such classical Lagrangian, the potential is employed as the first (and usually the only) route to shape the vacuum structure. This is, for instance, the usual path envisaged for studying the spontaneous symmetry breaking realized by negative mass terms in the paradigmatic potential:

$$V = -\frac{m^2}{2}\phi^2 + \frac{\lambda}{4!}\phi^4. \quad (1.1)$$

Starting from (1.1) the procedure has no detours from the classical process which defines the vacuum solving for

$$\frac{dV}{d\phi} = 0 \quad \text{and} \quad \frac{d^2V}{d\phi^2} > 0. \quad (1.2)$$

As for every classical statements there is no guarantee that radiative corrections would not spoil such conclusions. In particular, translated in the quantum language: the vacuum expectation value of the (quantum) field  $\hat{\phi}$  may not be represented by the classical solution of (1.2).

The effective potential  $V_E$  enters in the scene as a tool to efficiently inherit the classical procedure (1.2) to define the vacuum but accounting for radiative corrections.

Using functional methods to describe our system it is well known that the vacuum expectation value of the quantum field  $\hat{\phi}$  can be obtained differentiating the generator  $\mathcal{W}$  of the connected diagrams in respect to an external source:

$$\frac{\delta}{\delta\mathcal{J}(x)} \mathcal{W}[\mathcal{J}] = \langle \hat{\phi}(x) \rangle_{\mathcal{J}}, \quad (1.3)$$

defining a field-related function called the *classical field*  $\phi_c$

$$\phi_c = \langle \hat{\phi} \rangle_{\mathcal{J}}. \quad (1.4)$$

The effective potential is built as the *function* of the subclass of constant vacuum expectation values of  $\hat{\phi}$  that, mimicking (1.2), has an extremum for the real (quantum corrected) vacuum

$$\frac{dV_E}{d\phi_c} = 0. \quad (1.5)$$

A functional proof of existence is obtained taking the Legendre transform of the generator  $\mathcal{W}$

$$\Gamma[\phi_c] \equiv \mathcal{W}[\mathcal{J}] - \int d^d y \mathcal{J}(y) \phi_c(y), \quad (1.6)$$

which defines a new functional generator dubbed *effective action*. It is easy to show (see for example [5] for a simple and well readable diagrammatic demonstration) that  $\Gamma[\phi_c]$  realizes the further step in the family of generator functionals providing the one-particle irreducible diagrams. More important for our task is that by its definition follows the functional relation:

$$\frac{\delta}{\delta\phi_c(x)} \Gamma[\phi_c] = -\mathcal{J}(x), \quad (1.7)$$

which closely resembles (1.2). The formula (1.7) must be interpreted as a reverse form of the source-field relation of (1.4), giving the source able to reproduce a given classical field. To further get a function out of a functional, only the class of constant classical fields is considered, so to factorize an overall volume element in the effective action:

$$\Gamma[\phi_c] = - \int d^d x V_E(\phi_c) = V_E(\phi_c) \left( \int d^d x \right). \quad (1.8)$$

The resulting effective potential  $V_E(\phi_c)$ , in virtue of (1.7), is the quantum-derived ordinary function of the variable  $\phi_c$  which returns the true vacuum value as an extremum. In particular the *non-zero* solutions of (1.5) will be the hallmark of the spontaneous breaking of the symmetry.

## 1.3 The Jackiw's method and the scalar QED vacuum

The previous analysis has illustrated the link between the effective potential  $V_E(\phi_c)$  and the functional generator of connected diagrams  $\mathcal{W}[\mathcal{J}]$ . Such relation is the basis of the main methods used to arrive, given a model, to an explicit form of its effective potential. In [2] a diagrammatic approach was employed which resummed the infinite class of one-particle irreducible diagrams with zero-momentum in the external legs. A different and elegant approach was later developed by Jackiw [6] which is more deeply rooted to the functional definition of the Legendre transform (1.6). We sketch his derivation to later move to an explicit application to scalar QED case.

### 1.3.1 The Jackiw's Effective Potential

The starting point<sup>1</sup> is the *bare* action  $\mathcal{S}_0(\phi)$  of the system extended by a linear coupling to an external classical source  $\mathcal{J}_0(x)$ . The bare parameters are then expressed in terms of the renormalized ones,

<sup>1</sup>For illustrative purposes we limit ourselves in the simpler case of a scalar field. Generalization from this are straightforward.

producing the usual splitting in a renormalized action and counterterms

$$\mathcal{S}_0 = \mathcal{S}_R + \delta \mathcal{S}_{Ct} \quad \text{and} \quad \mathcal{J}_0 = \mathcal{J}_R + \delta \mathcal{J}_{Ct}. \quad (1.9)$$

Jackiw's idea was to use the linear counterterm generated by the redefinition of the external source to fulfill a non trivial request on the one-point Green function. To understand this step we make a change of variable in the path integration expanding the action around  $\phi = \phi_c + \eta(x)$ :

$$\begin{aligned} \mathcal{S}_R(\phi) + \int d^d x \mathcal{J}_R \phi(x) = & \\ & \left[ \mathcal{S}_R(\phi_c) + \int d^d x \mathcal{J}_R \phi_c \right]_0 + \left[ \int d^d x_1 \left( \frac{\delta}{\delta \phi(x_1)} \mathcal{S}_R + \mathcal{J}_R \right) \eta(x_1) \right]_1 + \\ & \left[ \frac{1}{2} \int d^d x_1 d^d x_2 \left( \frac{\delta^2}{\delta \phi(x_1) \delta \phi(x_2)} \mathcal{S}_R \right) \eta(x_1) \eta(x_2) \right]_2 + \\ & \left[ \frac{1}{3!} \int d^d x_1 d^d x_2 d^d x_3 \left( \frac{\delta^3}{\delta \phi(x_1) \delta \phi(x_2) \delta \phi(x_3)} \mathcal{S}_R \right) \eta(x_1) \eta(x_2) \eta(x_3) \right]_3 + \dots \end{aligned} \quad (1.10)$$

where the functional derivatives have been evaluated at the classical configuration  $\phi_c$  and the square bracket symbol refers to the (interaction) order in the quantum field  $\eta$ . From the  $[\dots]_1$  term in (1.10) it is clear that such tadpole term can be removed fixing, order by order in perturbation theory, the linear counterterm properly. Stated differently, we ask for  $\delta \mathcal{J}_{Ct}$  to renormalize the one-point function so that

$$\langle \hat{\phi} \rangle_{\mathcal{J}_R} = \phi_c \Leftrightarrow \langle \hat{\eta} \rangle_{\mathcal{J}_R} = 0. \quad (1.11)$$

From basic formulas of quantum field theory the evaluation of the connected diagrams generator  $\mathcal{W}$  can be recovered by

$$\begin{aligned} \mathcal{W} = & -i \log \int \mathcal{D}\eta \exp \left[ i \left( \mathcal{S}_0[\phi_c + \eta] + \int d^d x \mathcal{J}_0(\phi_c + \eta) \right) \right] \\ = & \mathcal{S}_R(\phi_c) + \int d^d x \mathcal{J}_R \phi_c + \delta \mathcal{S}_{Ct}(\phi_c) - i \log \int \mathcal{D}\eta \exp [i ([\dots]_2 + [\dots]_3 + \dots)]. \end{aligned} \quad (1.12)$$

The remaining logarithm of the path integral in (1.12) is performed averaging over a polynomial action of the quantum field  $\eta$  with quadratic, cubic and quartic terms obtained by derivatives of  $\mathcal{S}(\phi_c + \eta)$ . The diagrammatic result is given by connected (due to logarithm's action) bubbles with  $\eta$ 's propagator given by the (inverse of the) quadratic part in (1.10). Similarly the vertices are extracted by cubic and quartic terms of the starting action in the  $\phi_c$  background. This observation allow to identify the leading order correction to the classical action  $\mathcal{S}(\phi_c)$  in (1.10) by the evaluation of the free quadratic term of the path integral. This Gaussian integration can be computed in closed form resulting in the functional definition of an operator determinant

$$\begin{aligned} & \int \mathcal{D}\eta \exp \left[ \frac{i}{2} \int d^d x_1 d^d x_2 \eta(x_1) \left( \frac{\delta^2}{\delta \phi(x_1) \delta \phi(x_2)} \mathcal{S}_R \right) \eta(x_2) \right] \\ & = \left( \text{Det} \left[ - \left( \frac{\delta^2}{\delta \phi(x_1) \delta \phi(x_2)} \mathcal{S}_R \right) \right] \right)^{-1/2}, \end{aligned} \quad (1.13)$$

with the cubic and quartic terms producing high order (at least two-loop) contributions.

With the help of such considerations it is possible to perform the Legendre transformation of  $\mathcal{W}$  as in (1.6). From (1.12) and (1.13) the leading order expression of the effective action  $\Gamma[\phi_c]$  from the Jackiw's method is achieved

$$\Gamma[\phi_c] = \mathcal{S}_R(\phi_c) + \delta\mathcal{S}_{Ct}(\phi_c) + \frac{i}{2} \log \text{Det} \left[ - \left( \frac{\delta^2}{\delta\phi(x_1)\delta\phi(x_2)} \mathcal{S}_R \right) \right] + \dots \quad (1.14)$$

where the ellipsis stand for multiloop corrections.

Focusing on constant field configurations we finally arrive to the form of the effective potential:

$$V_E(\phi_c) = V(\phi_c) + \delta V_{Ct}(\phi_c) - (\text{Volume})^{-1} \frac{i}{2} \log \text{Det} \left[ - \left( \frac{\delta^2}{\delta\phi(x_1)\delta\phi(x_2)} \mathcal{S}_R \right) \right] + \dots \quad (1.15)$$

### 1.3.2 Massive fields in massless Abelian Higgs model

The formalism developed has provided a new quantum-grounded tool to investigate the most fundamental features of a quantum field system. With no surprise the effective potential has become a standard technology with countless applications from exotic models to more efficient renormalization schemes for the Standard Model and the MSSM.

To give a hint of the level of insight that the effective potential may help to reach, we now consider one of the extreme case scenario regarding the transition from a classical to a quantum description. The model is the renowned scalar QED theory analyzed by Coleman and Weinberg [2], a (tree-level) massless Abelian Higgs model:

$$\mathcal{L} = \frac{1}{4} F_{\mu\nu} F^{\mu\nu} + (D_\mu \phi)^\dagger (D^\mu \phi) - \frac{\lambda}{6} (\phi^\dagger \phi)^2, \quad (1.16)$$

where the covariant derivative has the form  $D_\mu \phi = \partial_\mu \phi + i e A_\mu \phi$ . In the following, with the benefit of hindsight, we neglect ghosts contribution other than the ‘‘side-effect’’ of a gauge fixing term that, wisely chosen in the  $R_\xi$  class, can help to avoid annoying scalar-vector mixing terms. Moreover we exploit the Abelian symmetry of (1.16) considering only real values for the classical field  $\langle \hat{\phi} \rangle_{\mathcal{J}}$ .

With these precautions we follow Jackiw's procedure expanding the gauge fixed version of (1.16) over the real components:

$$\phi = \frac{1}{\sqrt{2}} (\phi_c + \phi_1 + i \phi_2), \quad (1.17)$$

so to arrive at

$$\begin{aligned} \mathcal{L} &= \frac{1}{4} F_{\mu\nu} F^{\mu\nu} - \frac{1}{2\xi} (\partial \cdot A)^2 + \frac{1}{2} \left( (\partial\phi_1)^2 + (\partial\phi_2)^2 \right) + e A_\mu (\phi_1 \partial^\mu \phi_2 - \phi_2 \partial^\mu \phi_1) \\ &+ \frac{e^2}{2} A^2 (\phi_c^2 + 2\phi_c \phi_1 + \phi_1^2 + \phi_2^2) - \frac{\lambda}{4!} (\phi_c^2 + 2\phi_c \phi_1 + \phi_1^2 + \phi_2^2)^2. \end{aligned} \quad (1.18)$$

From such expansion the quadratic operators of (1.15) can be extracted directly to define the first quantum correction to the tree-level potential.

In the simpler case of the scalar components the operator in configuration space has the form

$$-\frac{\delta^2 \mathcal{S}}{\delta \phi_i(x) \delta \phi_j(y)} = \delta^4(x-y) \begin{pmatrix} \partial^2 + \frac{1}{2} \phi_c^2 \lambda & 0 \\ 0 & \partial^2 + \frac{1}{6} \phi_c^2 \lambda \end{pmatrix}. \quad (1.19)$$

To take the functional and the matrix determinant of this expression we switch to the momentum representation

$$-\frac{\delta^2 \mathcal{S}}{\delta \phi_i(k) \delta \phi_j(p)} = \delta^4(k-p) \begin{pmatrix} -k^2 + \frac{1}{2} \phi_c^2 \lambda & 0 \\ 0 & -k^2 + \frac{1}{6} \phi_c^2 \lambda \end{pmatrix}. \quad (1.20)$$

Envisioning the continuous variables  $k$  and  $p$  as infinite-dimensional indices allows us to exploit the formula  $\log \text{Det}(F) = \text{Tr} \log(F)$ , adjusted and extended for our mathematical arena. The logarithm of the diagonal matrix (in discrete and continuous indices) (1.20) can be taken respect to the diagonal elements as in usual matrix algebra. To trace we take the diagonal terms  $k = p$  and sum over them obtaining

$$\begin{aligned} \log \text{Det} \left[ -\frac{\delta^2 \mathcal{S}}{\delta \phi_i(k) \delta \phi_j(p)} \right] &= \text{Tr} \log \left[ -\frac{\delta^2 \mathcal{S}}{\delta \phi_i(k) \delta \phi_j(p)} \right] = \\ (2\pi)^4 \delta^4(0) &\left( \int \frac{d^4 k}{(2\pi)^4} \log \left( -k^2 + \frac{1}{2} \phi_c^2 \lambda \right) + \int \frac{d^4 k}{(2\pi)^4} \log \left( -k^2 + \frac{1}{6} \phi_c^2 \lambda \right) \right). \end{aligned} \quad (1.21)$$

The factor  $(2\pi)^4$  has been strategically placed to recover the infinite volume parametrization:

$$\int d^4 x e^{ixk} = (2\pi)^4 \delta(k) \implies \text{Volume} = \int d^4 x = (2\pi)^4 \delta(0). \quad (1.22)$$

Before evaluating the formidably divergent integrals of (1.21) we repeat the same analysis for the vector field  $A_\mu$ .

In general gauge, the quadratic operator that we must analyze is given by

$$-\frac{\delta^2 \mathcal{S}}{\delta A_\mu(k) \delta A_\nu(p)} = \delta^4(k-p) \left( k^2 - (e\phi_c)^2 \right) g^{\mu\nu} - \left( 1 - \frac{1}{\xi} \right) k^\mu k^\nu. \quad (1.23)$$

To better highlight the corresponding momentum/components symmetric matrix we redundantly rewrite the explicit space-time components of (1.23)

$$\begin{pmatrix} k^2 - (e\phi_c)^2 - \left(1 - \frac{1}{\xi}\right) k^0{}^2, & -\left(1 - \frac{1}{\xi}\right) k^0 k^1, & -\left(1 - \frac{1}{\xi}\right) k^0 k^2, & -\left(1 - \frac{1}{\xi}\right) k^0 k^3 \\ -\left(1 - \frac{1}{\xi}\right) k^0 k^1, & -k^2 + (e\phi_c)^2 - \left(1 - \frac{1}{\xi}\right) k^{12}, & -\left(1 - \frac{1}{\xi}\right) k^1 k^2, & -\left(1 - \frac{1}{\xi}\right) k^1 k^3 \\ \dots & \dots & -k^2 + (e\phi_c)^2 - \left(1 - \frac{1}{\xi}\right) k^{22}, & -\left(1 - \frac{1}{\xi}\right) k^2 k^3 \\ \dots & \dots & \dots & -k^2 + (e\phi_c)^2 - \left(1 - \frac{1}{\xi}\right) k^{32} \end{pmatrix} \quad (1.24)$$

With the same recipe of the scalar case, we can get to a functional form of the logarithm after an explicit diagonalization of (1.24). Up to a field-independent term, the chained application of trace and logarithms over our momentum/components space results in the sum:

$$\begin{aligned} \log \text{Det} \left[ -\frac{\delta^2 \mathcal{S}}{\delta A_\mu(k) \delta A_\nu(p)} \right] &= \\ (2\pi)^4 \delta^4(0) &\left( 3 \int \frac{d^4 k}{(2\pi)^4} \log \left( -k^2 + (e\phi_c)^2 \right) + \int \frac{d^4 k}{(2\pi)^4} \log \left( -k^2 + \xi (e\phi_c)^2 \right) \right). \end{aligned} \quad (1.25)$$

To arrive at the desired evaluation of the radiative correction the infinite integrals of (1.21) and (1.25) must be dealt with. As customary we turn to dimensional regularization in  $d = 4 - \epsilon$  to obtain a manipulable expression. After a coherent rephrasing in  $d$ -dimension of all the previous formulas (in particular the 3 in (1.25) should be replaced by  $d - 1$ ) all our divergences can be accounted by the form [7]

$$\int \frac{d^4 k}{(2\pi)^4} (-k^2 + m^2) \rightarrow -i \frac{\Gamma(-\frac{d}{2})}{(4\pi)^{\frac{d}{2}}} (m^2)^{\frac{d}{2}}. \quad (1.26)$$

We update to our field content expression (1.15)

$$\begin{aligned} V_E(\phi_c) &= V(\phi_c) + \delta V_{Ct}(\phi_c) - (Volume)^{-1} \frac{i}{2} \log Det \left[ - \left( \frac{\delta^2}{\delta\phi_i(x_1)\delta\phi_j(x_2)} \mathcal{S}_R \right) \right] + \\ &- (Volume)^{-1} \frac{i}{2} \log Det \left[ - \left( \frac{\delta^2}{\delta A_\mu(x_1)\delta A_\nu(x_2)} \mathcal{S}_R \right) \right] + \dots \end{aligned} \quad (1.27)$$

that, within our scenario and considering the Landau gauge limit of (1.25), becomes

$$V_E(\phi_c) = \frac{\lambda}{4!} \phi_c^4 + \frac{\delta\lambda}{4!} \phi_c^4 - \frac{\Gamma[-d/2]}{(4\pi)^{\frac{d}{2}}} \left( \frac{1}{2} \left( \frac{\lambda}{2} \phi_c^2 \right)^{\frac{d}{2}} + \frac{1}{2} \left( \frac{\lambda}{6} \phi_c^2 \right)^{\frac{d}{2}} + \frac{d-1}{2} (e^2 \phi_c^2)^{\frac{d}{2}} \right), \quad (1.28)$$

always not including field independent terms. To renormalize our effective potential we impose a subtraction condition asking for  $\delta\lambda$  to allow for

$$\frac{\partial^4 V_E(\phi_c)}{\partial \phi_c^4} \Big|_{\phi_c=\mu} = \lambda \quad (1.29)$$

at an *arbitrary* field value  $\mu$ . Expanding (1.28) around  $d = 4 - \epsilon$  with the solution of (1.29) we obtain, after a bit of algebra, the finite expression for the effective potential

$$V_E(\phi_c) = \frac{\lambda}{4!} \phi_c^4 + \frac{\phi_c^4}{(4\pi)^2} \left( \left( \frac{3}{4} e^4 + \frac{5}{72} \lambda^2 \right) \log \left( \frac{\phi_c^2}{\mu^2} \right) - \frac{25}{8} e^4 - \frac{125}{432} \lambda^2 \right). \quad (1.30)$$

That this expression can develop a minimum other than the trivial one can be established, relying on Coleman and Weinberg's acumen, considering the region in the parameter space with  $\lambda \sim e^4$ . Rearranging properly the potential in (1.30) with this new assumption we arrive at the leading order expression

$$V_E(\phi_c) = \phi_c^4 \left( \frac{\lambda}{4!} + \frac{3e^4}{(8\pi)^2} \left( \log \left( \frac{\phi_c^2}{\mu^2} \right) - \frac{25}{6} \right) \right), \quad (1.31)$$

which clearly shows a minimum for the classical field value:

$$\phi_{min}^2 = \mu^2 \exp \left( \frac{33e^4 - 8\pi^2 \lambda}{9e^4} \right). \quad (1.32)$$

To close our long and draining computational route we get rid of the explicit subtraction scale  $\mu$  with the help of (1.32), trading it for the parameter  $\phi_{min}$ .

The jewel of Coleman and Weinberg is now before our eyes

$$V_E(\phi_c) = \frac{3e^4}{(8\pi)^2} \phi_c^4 \left( \log \left( \frac{\phi_c^2}{\phi_{min}^2} \right) - \frac{1}{2} \right), \quad (1.33)$$

radiative corrections have therefore dramatically changed the classical character of the theory (1.16). The unavoidable scale dependence, brought to the arena by renormalization, has broken the Abelian symmetry shaping the form of the quantum corrected potential so to recover the typical spontaneous symmetry breaking pattern fig. (1.1). In this case the role of the tachyonic mass in Higgs-like potential, necessary to ignite the tree-level symmetry breaking, is successfully played by radiative corrections. Our

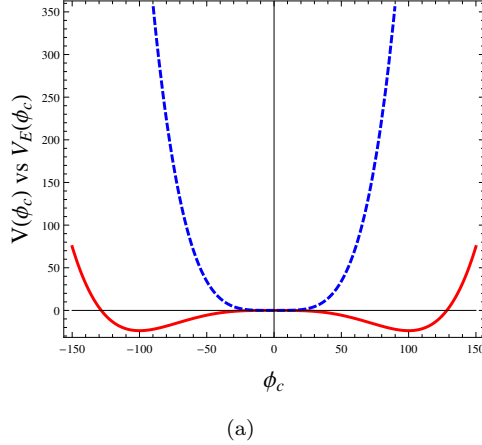


Figure 1.1: Comparison of classical (dashed blue line) vs effective (red line) potential for the massless Abelian Higgs model with  $e \sim 1/100$  and  $\lambda = (33/8\pi^2) e^4$ .

final expression (1.33) also reveals a peculiar and most interesting aspect of radiative symmetry breaking, once the disappearance of the starting dimensionless parameter  $\lambda$  is noticed. This phenomenon, called *dimensional transmutation* by Coleman and Weinberg, concerns the trade of a dimensionless with a dimensionful parameter, as  $\phi_{min}$  in our case. Its origin can be rooted to the fact that, to keep the theory *fixed*, the change in the subtraction point  $\mu$ , and consequently in  $\phi_{min}$ , must be accompanied by a change in the values of the dimensionless couplings.

### 1.3.3 Exploding Logs part I: Renormalization Group improvement

As every perturbative computation the effective potential has been built with awareness of its bounds of pertinence. The loop/coupling expansion, exploited in the use of the background field method of Jackiw, has opened a window to closely look to the model's true vacuum.

*But how far can we trust it?*

If we stick with our scalar QED example (1.31, 1.33), the potential approximation found seems to involve not just powers of the expansion coupling but also, as a leftover of quantum loops, of the logarithm of  $\phi_c/\mu$ . This is a bad news which seems to add a further limit to the perturbative expansion, given that the smallness of the coupling is not enough to produce our trust. The presence of the logarithms forces us to refuse formula (1.31) outside the very narrowed area in which the classic field is of the same order of the subtraction scale (1.29). No warranty is given that, in the regime  $\phi_c \gg \mu$ , the potential will not develop new minima or that the found one is the stable ground state.

This would have been a discouraging start for the effective potential role in quantum field theory if the

cure would not have been presented already in Coleman and Weinberg's work. To understand the process that allow to rescue the effective potential from exploding logarithms, we notice that the renormalization point  $\mu$  has been chosen in complete arbitrariness. As a consequence, *for a given  $\phi_c$  value* such that  $\phi_c \gg \mu$ , the logarithm can be taken completely under control if we redefine the infinite subtraction (1.29) at the new scale  $\mu' \sim \phi_c$ . Of course this is an efficient procedure if we are able to link the parameters, renormalized at two arbitrary scales  $\mu$  and  $\mu'$ , so to maintain the theory fixed. The matching of the parameters that assures this requirement for a continuous change of the subtraction scale is given by the *renormalization group*.

Adopted to our survey, the invariance<sup>2</sup> of the effective potential (1.30) in respect of different renormalization scales is translated in an implicit dependence of the parameters, so to compensate the explicit dependence on it. Therefore the dimensionless functions  $\beta_\lambda$ ,  $\beta_e$  and  $\gamma_{\phi_c}$  must exist so to realize the total  $\mu$  invariance

$$\mathcal{D} V_E(\phi_c, \lambda, e, \mu) = \left( \mu \frac{\partial}{\partial \mu} + \beta_\lambda \frac{\partial}{\partial \lambda} + \beta_e \frac{\partial}{\partial e} - \phi_c \gamma_{\phi_c} \frac{\partial}{\partial \phi_c} \right) V_E(\phi_c, \lambda, e, \mu). \quad (1.34)$$

The beta and gamma functions account for the parameter change with  $\mu$

$$\beta_\lambda = \mu \frac{d\lambda}{d\mu}, \quad \beta_e = \mu \frac{de}{d\mu}, \quad \gamma_{\phi_c} = -\frac{\mu}{\phi_c} \frac{d\phi_c}{d\mu} \quad (1.35)$$

and (for this scale-free model) can only be function of dimensionless couplings. Because of this, the equation for  $\phi_c$  can be immediately solved by separation, the evolution results in a rescaling by a factor  $\xi(\mu')$

$$\phi_c(\mu') = \xi(\mu') \phi_c(\mu) \quad \text{with} \quad \xi(\mu') = \exp\left(-\int_\mu^{\mu'} d\tau \gamma_{\phi_c}(\lambda(\tau), e(\tau))\right). \quad (1.36)$$

If, as customary, we introduce the renormalization time  $t = \log\left(\frac{\mu'}{\mu}\right)$ , a solution of (1.34) can be envisioned by the method of characteristics over the (fixed-theory) trajectory

$$\left\{ \frac{d\mu}{dt} = \mu, \quad \frac{d\lambda}{dt} = \beta_\lambda, \quad \frac{de}{dt} = \beta_e, \quad \frac{d\phi_c}{dt} = -\phi_c \gamma_{\phi_c} \right\}, \quad (1.37)$$

replacing the fixed with the  $t$ -running parameters in the effective potential form

$$V_E = V_E(\phi_c, \lambda, e, 0) = V_E(\phi_c(t), \lambda(t), e(t), t). \quad (1.38)$$

At this stage it seems that no progress have been made to gain some knowledge of the true vacuum. An explicit renormalization time has been introduced and, moreover, its role seems to be completely redundant because precisely of the renormalization invariance. We can turn this in our advantage noticing that the invariance in (1.38) is valid for parameters fixed at a given scale,  $\phi_c$  *included*. The shape of the potential for varying  $\phi_c$  (at a given scale, not along the renormalization evolution) is our real target.

<sup>2</sup>To avoid confusion we do not delve into the interesting subtleties of the renormalization invariance of the effective potential. We prefer to stress instead the established way to perform stability analyses. The role of the cosmological constant for the RG invariance can be found in [8].

With this observation the freedom in (1.38) is of major help given that, for every choice of  $\phi_c$ , we can continuously find a corresponding  $t = t(\phi_c)$  able to improve the perturbation convergence. In particular a smart choice of  $t = t(\phi_c)$  must be exploited to kill the dangerous logarithms, a procedure formally acknowledged as *leading logarithms resummation*. It is with this care that the RG furnishes the best perturbative approximation to the effective potential by:

$$V_E^{RGI}(\phi_c) = V_E(\phi_c \xi(t(\phi_c)), \lambda(t(\phi_c)), e(t(\phi_c)), t(\phi_c)). \quad (1.39)$$

## 1.4 The Effective Potential in mass independent renormalization schemes

Renormalizability and Lorentz invariance are requirements strong enough to spare us the effort of computing the effective potential, from the ground, most of the times. For renormalizable models the effective potential can in fact be put in a simple and concise form (at least at one-loop order). This is realized at the price of confining our computations to mass-independent renormalization schemes, as the  $\overline{MS}$ .

From the previous survey of the scalar QED model, the contribution from loops with scalar and vector fields have been computed resulting in the peculiar functional determinants. To complete our bookkeeping the case of fermion degrees of freedom must be inspected. Obviously most of the Jackiw's procedure that we undertaken in (1.3) would be unchanged by the introduction of fermions, so we jump to the main differences. The crucial point will be the path integration of the quadratic term in the  $\phi_c$  background, which will now concern the anti-commuting fields  $\psi$  and  $\bar{\psi}$ . From well known properties of Grassmann integration we take care of the one-loop fermionic contribution with

$$\begin{aligned} & \int \mathcal{D}\psi \mathcal{D}\bar{\psi} \exp \left[ \frac{i}{2} \int d^d x_1 d^d x_2 \bar{\psi}(x_1) \left( \frac{\delta^2}{\delta \bar{\psi}(x_1) \delta \psi(x_2)} \mathcal{S}_R \right) \psi(x_2) \right] \\ & = Det \left[ - \left( \frac{\delta^2}{\delta \bar{\psi}(x_1) \delta \psi(x_2)} \mathcal{S}_R \right) \right], \end{aligned} \quad (1.40)$$

which provides the last missing block in our formula (1.27)

$$\begin{aligned} V_E(\phi_c) & = V(\phi_c) + \delta V_{Ct}(\phi_c) - (Volume)^{-1} \frac{i}{2} \log Det \left[ - \left( \frac{\delta^2}{\delta \phi_i(x_1) \delta \phi_j(x_2)} \mathcal{S}_R \right) \right] + \\ & - (Volume)^{-1} \frac{i}{2} \log Det \left[ - \left( \frac{\delta^2}{\delta A_\mu(x_1) \delta A_\nu(x_2)} \mathcal{S}_R \right) \right] + \\ & + (Volume)^{-1} i \log Det \left[ - \left( \frac{\delta^2}{\delta \bar{\psi}(x_1) \delta \psi(x_2)} \mathcal{S}_R \right) \right] + \dots \end{aligned} \quad (1.41)$$

Following the same routine as for the vector boson case, we can reach the explicit form of (1.40) diagonalizing the fermion matrix

$$\begin{aligned}
-\frac{\delta^2 \mathcal{S}}{\delta \bar{\psi}_i(k) \delta \psi_j(p)} &= \delta^4(k-p) \left( -(\gamma \cdot k) + m_{1/2}(\phi_c) \right)_{ij} \\
&= \begin{pmatrix} m_{1/2}(\phi_c) & 0 & -p_0 - p_3 & -p_1 + ip_2 \\ 0 & m_{1/2}(\phi_c) & -p_1 - ip_2 & -p_0 + p_3 \\ -p_0 + p_3 & p_1 - ip_2 & m_{1/2}(\phi_c) & 0 \\ p_1 + ip_2 & -p_0 - p_3 & 0 & m_{1/2}(\phi_c) \end{pmatrix}
\end{aligned} \tag{1.42}$$

where  $m_{1/2}(\phi_c)$  is the fermion mass in the  $\phi_c$  background. With what should be now a straightforward sequence of computations we arrive at

$$Tr \log \left[ -\frac{\delta^2 \mathcal{S}}{\delta \bar{\psi}_i(k) \delta \psi_j(p)} \right] = (2\pi)^4 \delta^4(0) \left( 2 \times \int \frac{d^4 k}{(2\pi)^4} \log(-k^2 + m_{1/2}^2(\phi_c)) \right), \tag{1.43}$$

which clarify the multiplicity factor (2) related to the fermion field loop. Luckily also such result ended over the same family of divergent integrals that we know how to regularize. If we limit our survey to the (computationally) simple mass-independent  $\overline{MS}$  renormalization scheme, the step to the relevant finite component of (1.26) is immediate.

Therefore we have now all the instruments to generalize the form of the effective potential to general renormalizable actions by an educate extrapolation of the previous formulas, covering the particle content of spin 0, 1/2 and 1. In Landau gauge and considering up to one-loop corrections in  $\overline{MS}$ , we may write the sum

$$V_E(\phi_c) = V(\phi_c) + \frac{1}{(4\pi)^2} \left( V_E^0 + V_E^{1/2} + V_E^1 \right) + \dots \tag{1.44}$$

where the contribution from the  $i$ -th field of spin  $s$  is expressed in terms of its tree-level mass  $m_{i,s}^2(\phi_c)$ :

$$\begin{aligned}
V_E^0 &= \frac{1}{4} \sum_i m_{i,0}^4(\phi_c) \left( \log \frac{m_{i,0}^2(\phi_c)}{\mu^2} - \frac{3}{2} \right), \\
V_E^{1/2} &= -\frac{1}{2} \sum_i m_{i,1/2}^4(\phi_c) \left( \log \frac{m_{i,1/2}^2(\phi_c)}{\mu^2} - \frac{3}{2} \right), \\
V_E^1 &= \frac{3}{4} \sum_i m_{i,1}^4(\phi_c) \left( \log \frac{m_{i,1}^2(\phi_c)}{\mu^2} - \frac{5}{6} \right).
\end{aligned} \tag{1.45}$$

### 1.4.1 Exploding Logs part II: Decoupling and Thresholds

Consider now the following toy model with two chiral fermions  $\psi_L$  and  $\psi_R$ , interacting with a scalar field  $\phi$  through the potential:

$$V(\psi_L, \psi_R, \phi) = \Lambda - \frac{1}{2} m_\phi^2 \phi^2 + \frac{1}{4!} \lambda \phi^4 + \frac{1}{\sqrt{2}} (Y_L \phi \bar{\psi}_R \psi_L + \text{h.c.}) + \frac{1}{2} m_R \bar{\psi}_R \psi_R^c. \tag{1.46}$$

Over the field vacuum configurations  $\phi_c = \langle \phi \rangle$  their contribution on the theory's effective potential can be easily read off our generic formula (1.45) once the mass eigenvalues are determinate. In the left-handed basis  $\xi = (\psi_L, \psi_R^c)$  the Dirac and Majorana bilinears of (1.46) can be recast in the Majorana form  $(1/2)\bar{\xi}^c M_J \xi$  with mass terms

$$M_J = \begin{pmatrix} 0 & m_D(\phi) \\ m_D(\phi) & m_R \end{pmatrix} \text{ and } m_D(\phi) = \frac{1}{\sqrt{2}} Y_L \phi, \quad (1.47)$$

providing two mass eigenstate of values

$$\left\{ \frac{1}{2} \left( m_R - \sqrt{m_R^2 + 4m_D^2(\phi)} \right), \frac{1}{2} \left( m_R + \sqrt{m_R^2 + 4m_D^2(\phi)} \right) \right\}. \quad (1.48)$$

Their contribution to the one-loop corrections of the potential can therefore be split in two terms, one for eigenstate, resulting in

$$\begin{aligned} V_E^{1/2}(\phi_c) = & -\frac{1}{2} \left( \frac{m_R}{2} - \frac{1}{2} \sqrt{m_R^2 + 4m_D^2(\phi_c)} \right)^4 \left( \log \frac{\left( \frac{m_R}{2} - \frac{1}{2} \sqrt{m_R^2 + 4m_D^2(\phi_c)} \right)^2}{\mu^2} - \frac{3}{2} \right) \\ & -\frac{1}{2} \left( \frac{m_R}{2} + \frac{1}{2} \sqrt{m_R^2 + 4m_D^2(\phi_c)} \right)^4 \left( \log \frac{\left( \frac{m_R}{2} + \frac{1}{2} \sqrt{m_R^2 + 4m_D^2(\phi_c)} \right)^2}{\mu^2} - \frac{3}{2} \right). \end{aligned} \quad (1.49)$$

Then the freedom to choose the renormalization scale  $\mu$  must be exploited to avoid the perturbativity break-out by tracking the field-dependent masses with  $\mu \sim \phi_c$  and replacing the parameters with the running ones. For  $\phi_c \geq m_R$  this procedure has no drawbacks other, of course, than the possible presence of Landau poles in the RG evolution. The logarithms are resummed efficiently and the perturbative expansion is reliable. Let's focus instead on the regime  $\phi_c \ll m_R$  assuming the two masses at very different energy scales. In our "improved" scenario this corresponds to the low-energy sector and it's easy to recognize that we have a new troubling contribution coming from term  $\sim \log(m_R^2/\phi_c^2)$ . Anyway this should not be cause of discomfort. It is instead the usual message coming from perturbative computations which alerts us of the inclusion of degrees of freedom which live far away from the scale under our probe. Something is spoiling the decoupling of the high-energy sector and, as a consequence, our access to the knowledge of the true vacuum. The cause can be rooted to our choice of the renormalization scheme which compensate its simplicity with a complete incompetence to include the Appelquist-Carazzone decoupling theorem [9]. In particular, the absence of any explicit scale other than  $\mu$ , in mass-independent renormalization schemes, provide a framework of calculation with all the fields treated as massless and, therefore, all sources of relevant radiative corrections at any scale.

Of course the decoupling doesn't cease to be true just because we chose a different way of doing calculations. It should be possible to absorb into redefinitions of parameters the effect of large logarithms in the same way as the infinite energy cutoff can be concealed from physical observables<sup>3</sup>.

To see how this scenario can be realized let's sharply split the effective potential computation, for our toy model, in the two sectors of high ( $\mu > m_R$ ) and low ( $\mu < m_R$ ) energy. In the first case all the fields

<sup>3</sup>See [10] for illuminating connections among the RG, effective field theory and renormalizability.

enter in the quantum loops shaping a correction to the classical potential correctly represented by (1.49). In the low-energy sector instead, let's explore how far can we pretend to be in the dark of the heavier eigenstate  $\psi_{heavy}$  with mass  $\sim m_R$  (1.48) and still get the right physics. In this forced blindness we would describe our vacuum using only light degrees of freedom, in the tree-level

$$\tilde{V}(\phi_c) = -\frac{1}{2}\tilde{m}_\phi^2\phi_c^2 + \frac{1}{4!}\tilde{\lambda}\phi_c^4 \quad (1.50)$$

as in the (spin 1/2) loop correction

$$\tilde{V}_E^{1/2}(\phi_c) = -\frac{m_D^4(\phi_c)}{2} \left( \log \frac{m_D^2(\phi_c)}{\mu^2} - \frac{3}{2} \right). \quad (1.51)$$

Where a tilde has been used to discriminate parameters belonging, in principle, to different theories. In particular in our low-energy description we deal with a light Majorana fermion of mass  $m_D(\phi)$ . If we now expand the heavy field contribution *in the full theory* (1.49) in powers of  $\phi_c/m_R$  we can reduce the logarithmic structure in polynomial interactions:

$$\begin{aligned} & \left( \frac{3 - 2m_R^4 \log\left(\frac{m_R^2}{\mu^2}\right)}{64\pi^2} \right) - \left( \frac{m_R^2 Y_L^2 \left(2 \log\left(\frac{m_R^2}{\mu^2}\right) + 1\right)}{16\pi^2} \right) \frac{\phi_c^2}{2} + \\ & \left( -\frac{3Y_L^4 \left(2 \log\left(\frac{m_R^2}{\mu^2}\right) + 5\right)}{16\pi^2} \right) \frac{\phi_c^4}{4!} + \dots \end{aligned} \quad (1.52)$$

which can be completely accounted, up to subleading non-renormalizable terms, by the parameters and the degrees of freedom of our low-energy description (1.50). More precisely, the expansion (1.52) establishes the matching among the low and high-energy parameters to be fulfilled in order to have the same theory and the same effective potential along the different scales [11]. Expliciting the thresholds, asking for  $\mu = m_R$  in (1.52), we arrive at:

$$\Lambda \rightarrow \Lambda + \frac{3}{64\pi^2}, \quad m^2 \rightarrow m^2 + \frac{m_R^2 Y_L^2}{16\pi^2}, \quad \lambda \rightarrow \lambda - \frac{15Y_L^4}{16\pi^2} \quad (1.53)$$

which gives the thresholds *below* the decoupling scale  $m_R$ . In bottom-up RG analysis as ours, the reversed version of (1.53) will assure the correct matching notably improving the precision and reliability of our perturbative computations.



## Chapter 2

# The three roads: Stability, Instability and Metastability.

### 2.1 Introduction

We have learnt how the RG, together with an effective field theory approach in the guise of thresholds, has allowed to build a coherent and reliable picture of the quantum potential. The use of such technology has been, since its first applications in quantum field theory, mostly halved in two areas. Simplifying we could recognize different uses depending on the assumptions on the parameter space. In case of partial ignorance of new couplings, for instance, their free variation can strongly affect the potential, leading to unrealistic scenarios and thus to theoretical bounds on their span. Starting with an assumed perfect knowledge of the parameters involved we may, instead, face different conclusions. The cosmological history of the model can be read and a survey of the effective potential can illustrate different phases of its evolution. Similarly, the RG and the effective field approach will also intervene to declare the model inherent cutoff scale, above which new physics has to be invoked to avoid an unobserved phase transition or perturbative break-out.

But what are the possible scenarios?

In the more basic way, just two: stable or unstable. Stable when the deformation induced by the quantum corrections on the classical potential is not able to create a new minimum with less energy density. Unstable when a new minimum appears at (usually) higher energies and the initial vacuum turns out to be a false one. A starting point before a quantum induced transition with energy emission. Still, an orthodox adherence to phenomenology would allow for a third option: a metastable potential. Our model will (most likely) supply a description of our universe, which has a finite age, at least from the time quantum field theory is applicable. So we should be bothered by the presence of new more energy-convenient minima, only if their destabilizing effect would happen within our cosmic age.

In this chapter we will illustrate the computational schemes developed since the first tunnelling analysis of Coleman and Callan [12, 13] and their extension to the finite temperature case by [14] and [15]. We will consider the Standard Model (SM) post Higgs discovery [22, 23] and perform an up-to-date computation

of the related effective potential with particular emphasis on its phase diagram at zero [25, 26] and finite temperature [36].

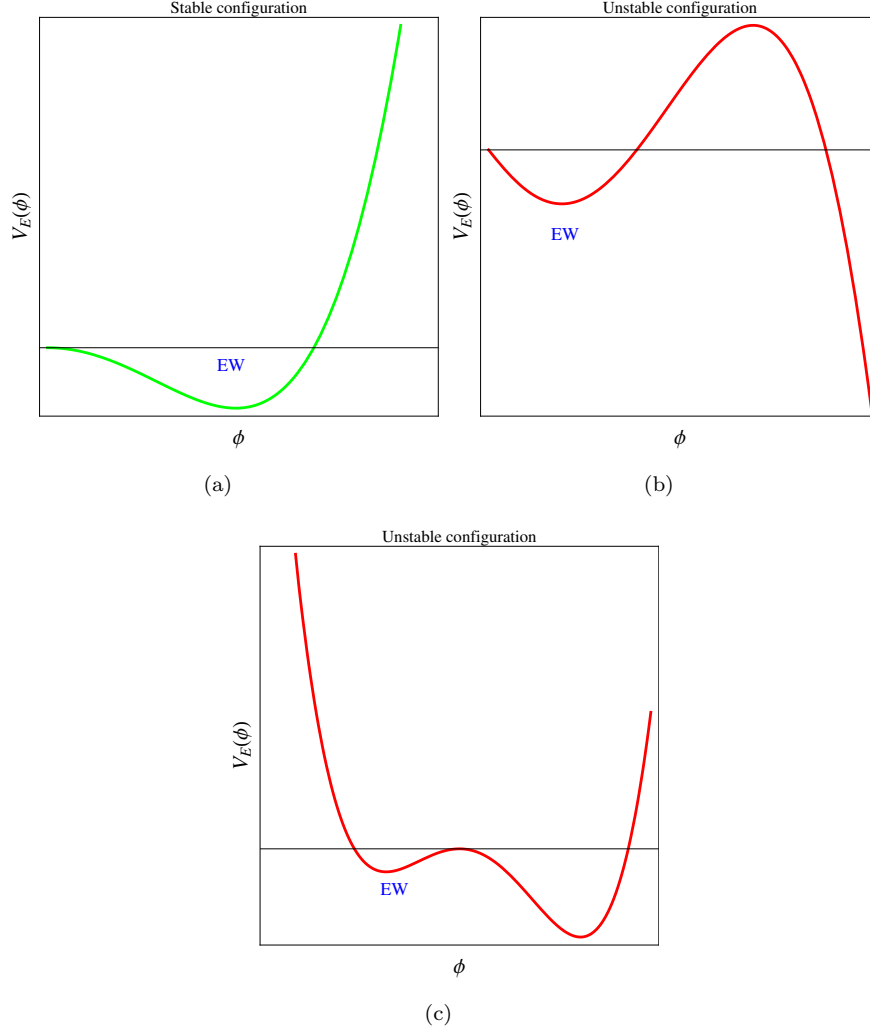


Figure 2.1: Possible stable (a) and unstable (b-c) patterns for the effective potential. EW is the electroweak vacuum. Depending on the barrier's features and on external cosmological inputs, both the unstable patterns could comply for the metastable scenario.

## 2.2 Tunnelling

From a classical point of view all the patterns in fig. (2.1) are stable, for a system placed in the first minimum. No matter how convenient the transition could be, without external pushes the future evolution of a system at rest will be to remain there. Quantum behaviour instead will inherently deal with the unsettled character of the quantum vacuum. Therefore a realistic analysis will lead to, small as it can be, a non-zero amplitude for the barrier crossing in fig. (2.1): *the tunnel effect*. Such amplitude

represents a main target to be computed in quantum field theory both providing an accurate description of the effective potential (and the model's phase diagram) and more precise hints about the validity of the effective theory extrapolation to high-energy.

### 2.2.1 Quantum Fluctuations

The recipe to define the tunnel probability in presence of new minima has originally been illustrated by Coleman and Callan [12, 13], borrowing the language and the formalism of thermodynamic phase transitions. The picture can be assimilated to the one concerning transition from liquid, in a superheated state, to vapor. *Bubbles* of vapor start to be generated and suddenly collapse when the loss in surface energy is not paid back by the gain in volume energy. When a bubble with enough energy is formed, the vapor phase starts to expand eventually covering the entire system. Abstracting to our quantum case, the vapor bubble represents the final state of true vacuum which is intended to dominate the false (classical) unstable vacuum, analogue to the superheated liquid phase.

The field configuration responsible for this transition is a solution of the classical euclidean equation of motion which interpolates between the false vacuum at infinite time and distance, and the true vacuum at the origin<sup>1</sup>. It has been dubbed as *bounce* solution by Coleman [12] and is defined mathematically as the  $\phi_B$  minimizing the euclidean action  $S_E(\phi)$

$$\frac{d^2 \phi}{dr^2} + \frac{3}{r} \frac{d\phi}{dr} - \frac{dV(\phi)}{d\phi} = 0, \quad (2.1)$$

with the radius  $r^2 \equiv x_0^2 + \vec{x}^2$  and the boundary conditions:

$$\phi_B(\infty) = v_{EW} \sim 0, \quad \left. \frac{d\phi}{dr} \right|_{r=0} = 0. \quad (2.2)$$

Then the tunnelling probability (for unit of four-dimensional volume)  $p$  can be computed considering the formula

$$p = \frac{e^{-S_E(\phi_B)}}{\text{Volume}} \quad (2.3)$$

so to explore the dangerous case when, integrated for the universe size  $\sim \tau_U^4$  ( $\tau_U$  the universe time =  $4.35 \times 10^{17}$  sec), results in greater than one values. The quantum character of the computation plays its role in two different steps, of which only the dominant one will be taken into account, modifying the potential. We have already seen (1.45) how the quantum corrections affect the form of the classical potential with new log-type terms and an explicit scale dependence. Giving that our concern on stability issues addresses energy regions far from the EW one, such radiatively corrected potential can safely neglect the contribution from field-quadratic terms. In the case of the SM, for instance, we can always use the form

$$V(\phi) \sim \frac{\lambda_{eff}(\mu)}{4} \phi^4, \quad (2.4)$$

---

<sup>1</sup>Translational invariance allow us to choose this point at the origin.

where  $\lambda_{eff}(\mu)$  is an effective quartic parameter and the scale dependence is driven by the RG evolution. The second kind of, subdominant, quantum effect is due to the use of a semiclassical approximation in the computation of the decay amplitude. A complete quantum derivation [13, 37] would lead to a tunnelling probability (2.3) of the form:

$$p = \frac{e^{-S_E^Q(\phi_B)}}{\text{Volume}} = \frac{e^{-S_E(\phi_B) - \Delta_{Loop}}}{\text{Volume}}, \quad (2.5)$$

where now  $S_E^Q$  represents the complete (euclidean) quantum action,  $S_E$  the tree-level action with a RG-improved potential, and  $\Delta_{Loop}$  is the contribution from functional determinants coming from the path integral computation. In general  $\Delta_{Loop}$  is a small quantity and will be neglected from now on.

The bounce  $\phi_B$  can be numerically computed, via shooting method as illustrated already in [12], and indeed we will mainly rely on such algorithm for more complicate scenarios. The approximation used in (2.4) can, although unrealistically missing necessary negative mass terms, be supplied by an analytic solution which can serve to illustrate very efficiently the main features of the process. The absence of *explicit* scale dependence results in a one-parameter family of solutions fig. (2.2)-a), the Fubini instantons

$$\phi_B(r) = \sqrt{\frac{8}{|\lambda_{eff}|}} \frac{R}{r^2 + R^2}, \quad (2.6)$$

with  $R$  a free positive number which can be easily linked to the value of the bounce at the origin

$$R = \sqrt{\frac{8}{|\lambda_{eff}|}} \frac{1}{\phi_B(0)}, \quad (2.7)$$

and provides the size of the bounce. We see now how the approximation used, which successfully served an analytic description, fails to select the appropriate bounce out of the Fubini family (2.6) because of scale invariance. All the solutions considered will in fact result in the same action

$$S_E(\phi_B) = \frac{8\pi^2}{3|\lambda_{eff}|}, \quad (2.8)$$

independently of their size. To pick the appropriate value for  $R$  we must break scale invariance, a well accepted consequence of the simplest inclusion of quantum corrections. In our case the *implicit* renormalization scale dependence of  $\lambda$  will be enough to pick, by a numerical evaluation by shooting method of (2.1), the correct value of the scale  $R$  which determines the form of the Fubini instanton responsible of the most likely tunnelling transition. Choosing the SM with its tree-level potential improved by one-loop RGE, a numerical evaluation of (2.2) with the appropriate boundary condition results in a bounce of size (or inverse scale)  $R = 434.33/M_P$  (fig. (2.2)). The corresponding tunnelling probability can be read off inserting the related action value on the instanton  $S_E(\phi_B) = 1768.8$  in formula (2.3) and integrating on the four volume of our universe ( $\sim \tau_U^4$ ). For our purposes is even more interesting to translate such limit in a lower bound for the effective quartic coupling spanning, by an identification  $R \sim 1/\mu$ , all the possible bounce configurations and not just the one saturating the path integral. Inserting the bounce action (2.8) back in formula (2.3) and integrating, our *surviving* condition will lead to

$$|\lambda_{eff}(\mu)| > \frac{8\pi^2}{3} \frac{1}{\log(\tau_U \mu)}. \quad (2.9)$$

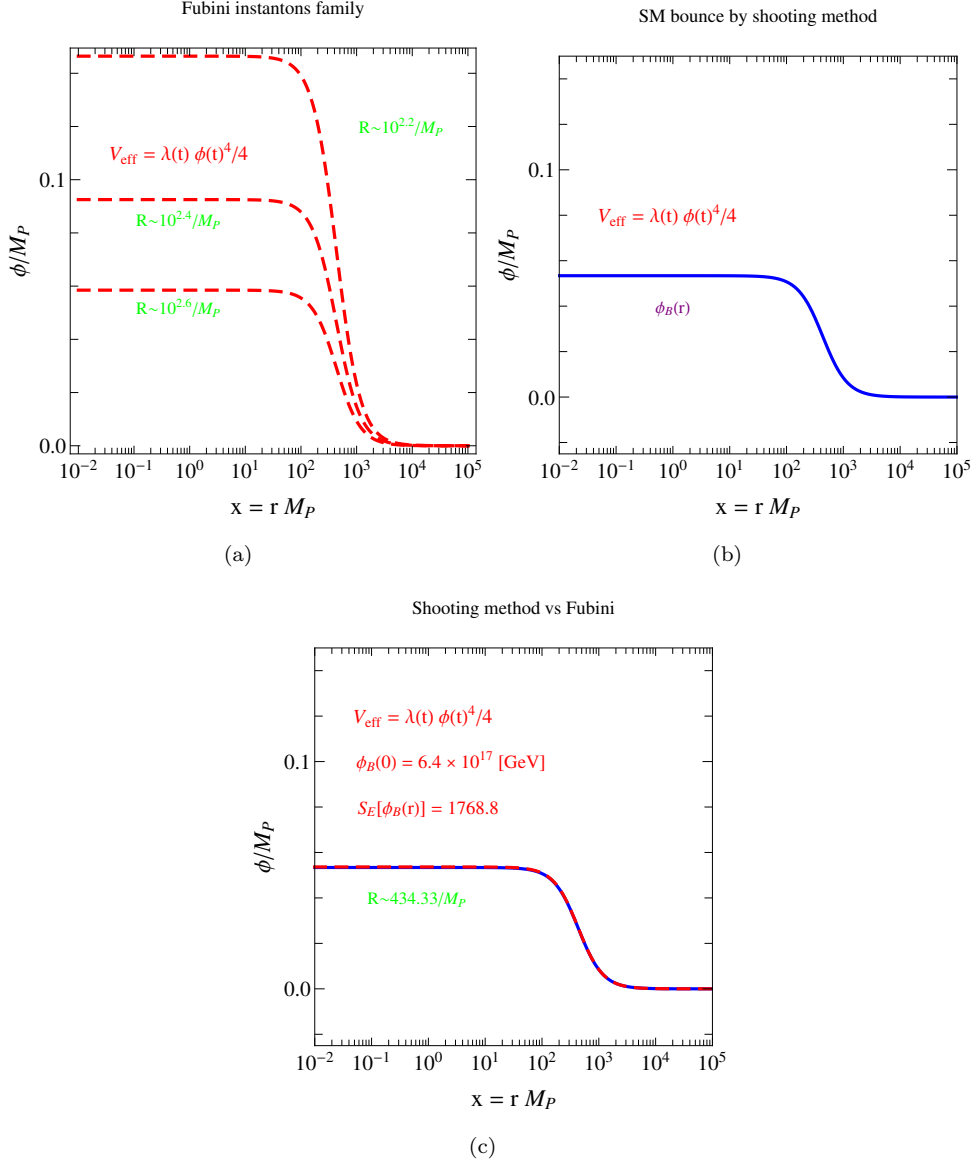


Figure 2.2: For an improved tree-level potential of the SM and for  $M_{top} = 173.34 \text{ GeV}$ ,  $M_h = 125.09 \text{ GeV}$  and  $\alpha_S = 0.1184$  different Fubini bounces a), the bounce solution by shooting method b), and a comparison between the numerical solution and the corresponding analytic one c).

The lower bound (2.9) supplies our analysis with the appropriate tool to investigate in detail the SM phase diagram and in particular the role of different points in the SM parameter space in shaping its fate. For illustrative purposes in fig. (2.3) we span different top Yukawa couplings providing a clear pattern of instability and metastability for the quartic effective (one-loop improved) SM coupling.

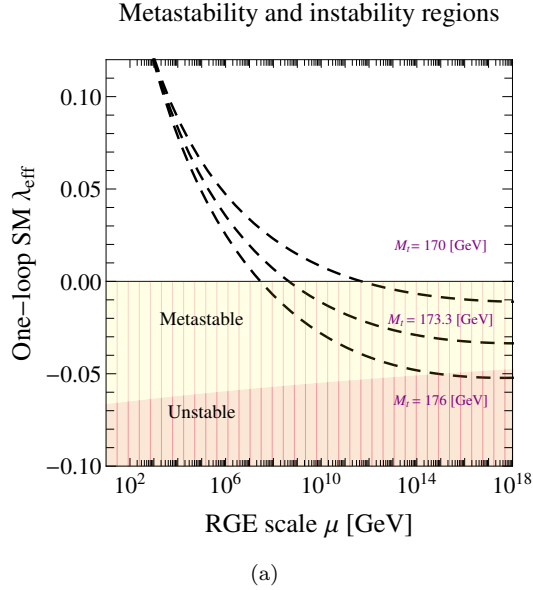


Figure 2.3: Evolution of the quartic effective (one-loop improved) SM coupling for the point  $M_h = 125.09 \text{ GeV}$  and  $\alpha_S = 0.1184$  with three different assignments of  $M_{top}$ . We can recognize the role of the top Yukawa in driving the SM to an unstable fate.

## 2.2.2 Thermal Fluctuations

Quantum corrections are the main source of vacuum instability in respect to a classical stable model. However, a theory which is supposed to account for physics under (at most) Planck energy has to deal with non-zero temperature effect. This is a result of the period in the universe evolution where a high density of particles would ask for a quantum description based on a statistical ensemble. Finite temperature effects have been intensively discussed in the past ([14, 16]) and their role in encouraging possible true-vacuum tunnelling has been highlighted. Intuitively the thermal kinetic energy, borrowed from the heat bath, may supply a sizable push to overcome the energy barrier and facilitating the transition.

The recipe to deal with finite temperature effects in the framework of vacuum stability can be (almost) easily modeled upon the rules that allowed us to account for quantum fluctuations. Without having to delve in the formalism of thermal quantum field theory we can rely on the main results which only ask for a modification of the effective potential by a new term  $\Delta_E V(\phi, T)$ , and a modified bounce equation that, in respect of (2.1), must be solved in a three dimensional euclidean space.

Starting from the modification of the effective potential we will, for now, limit ourselves to the main contributions at one-loop order, as usual we will explore the SM case to settle our computations. The quantum effects have been already computed in a mass-independent renormalization scheme as  $\overline{MS}$  (1.44-1.45). For completeness we explicitly show the  $T = 0$  terms at one-loop for the SM. In Landau gauge we recognize the following terms

$$V_0(\phi) = -\frac{1}{4}m^2(t)\phi^2(t) + \frac{1}{4}\lambda(t)\phi^4(t) \approx \frac{1}{4}\lambda(t)\phi^4(t) \quad (2.10)$$

$$V_{1\text{-loop}}(\phi) = \sum_{i=W,Z,t,\chi,h} \frac{n_i}{64\pi^2} m_i(t)^4 \left[ \ln \frac{m_i^2(t)}{\mu^2(t)} - C_i \right], \quad (2.11)$$

with coefficients  $n_i, C_i$  given by

$$\begin{aligned} n_W &= 6, \quad n_Z = 3, \quad n_t = -12, \quad n_\chi = 3, \quad n_h = 1, \\ C_W &= C_Z = 5/6, \quad C_t = C_\chi = C_h = 3/2, \end{aligned} \quad (2.12)$$

and mass parameters

$$m_W^2(t) = \frac{1}{4} g_2^2(t) \phi^2(t), \quad (2.13)$$

$$m_Z^2(t) = \frac{1}{4} [g_2^2(t) + g^2(t)] \phi^2(t), \quad (2.14)$$

$$m_t^2(t) = \frac{1}{2} y_t^2(t) \phi^2(t), \quad (2.15)$$

$$m_\chi^2(t) = -\frac{m^2(t)}{2} + \lambda(t) \phi^2(t) \approx \lambda(t) \phi^2(t), \quad (2.16)$$

$$m_h^2(t) = -\frac{m^2(t)}{2} + 3\lambda(t) \phi^2(t) \approx 3\lambda(t) \phi^2(t). \quad (2.17)$$

As illustrated in the opening chapters, the SM parameters must run with the RGE to efficiently resum the dangerous logarithms. We stress, mostly for future and more precise applications, that an effective potential at L-loop order, supplied by parameters running with an RGE at L+1-loop order, will resum the leading, next-to-leading, and L-th-to-leading logarithmic terms [40, 41].

The first thermal modifications are included considering the thermal diagrams [17, 18]

$$V_{1\text{-loop}}(\phi, T) = \sum_{i=W,Z,\chi,h} \frac{n_i T^4}{2\pi^2} J_B \left( \frac{m_i^2(t)}{T^2} \right) + \frac{n_t T^4}{2\pi^2} J_F \left( \frac{m_t^2(t)}{T^2} \right), \quad (2.18)$$

with boson and fermion thermal integrals given by

$$J_B(y) = \int_0^\infty dx x^2 \ln \left[ 1 - e^{-\sqrt{x^2+y}} \right], \quad (2.19)$$

$$J_F(y) = \int_0^\infty dx x^2 \ln \left[ 1 + e^{-\sqrt{x^2+y}} \right]. \quad (2.20)$$

The plasma effects must also be included in a thermal leading order analysis, and can be described by one-loop ring resummation of daisy diagrams [19]

$$V_{\text{ring}}(\phi, T) = \sum_{i=W_L, Z_L, \gamma_L, \chi, h} \frac{n_i T^4}{12\pi} \left\{ \left[ \frac{m_i^2(t)}{T^2} \right]^{3/2} - \left[ \frac{\mathcal{M}_i^2(\phi)}{T^2} \right]^{3/2} \right\}, \quad (2.21)$$

in which only the bosonic degrees of freedom are taken into account, in particular, only the longitudinal component of the vector fields defining the degeneracy coefficients

$$n_{W_L} = 2, \quad n_{Z_L} = 1, \quad n_{\gamma_L} = 1. \quad (2.22)$$

The Debye masses are  $\mathcal{M}_i^2(\phi) = m_i^2(t) + \Pi_i(\phi, T)$ , with the following temperature-dependent self-energies

$$\begin{aligned} \Pi_h(\phi, T) &= \left( \frac{3g_2^2 + g^2}{16} + \frac{\lambda}{2} + \frac{y_t^2}{4} \right) T^2 = \Pi_\chi(\phi, T), \\ \Pi_{W_L}(\phi, T) &= \frac{11}{6} g_2^2 T^2, \\ \Pi_{W_T}(\phi, T) &= \Pi_{Z_T}(\phi, T) = \Pi_{\gamma_T}(\phi, T) = 0, \end{aligned} \quad (2.23)$$

where we omitted the RG-induced  $t$ -dependence due to improvement. Finally, mapping  $(W_3, B)$  into  $(Z, \gamma)$ , we find

$$\begin{aligned}\mathcal{M}_{Z_L}^2(\phi) &= \frac{1}{2} \left[ m_Z^2(t) + \frac{11}{6} \frac{g_2^2}{\cos^2 \theta_W} T^2 + \Delta(\phi, T) \right], \\ \mathcal{M}_{\gamma_L}^2(\phi) &= \frac{1}{2} \left[ m_Z^2(t) + \frac{11}{6} \frac{g_2^2}{\cos^2 \theta_W} T^2 - \Delta(\phi, T) \right],\end{aligned}\tag{2.24}$$

with

$$\begin{aligned}\Delta^2(\phi, T) &= m_Z^4(t) + \frac{11}{3} \frac{g_2^2 \cos^2 2\theta_W}{\cos^2 \theta_W} \times \\ &\quad \left[ m_Z^2(t) + \frac{11}{12} \frac{g_2^2}{\cos^2 \theta_W} T^2 \right] T^2.\end{aligned}\tag{2.25}$$

We can have a quantitative idea about the impact of the thermal corrections introduced, by a straightforward comparison as in fig. 2.4 where the three forms of the potential, met until now, are exposed. We

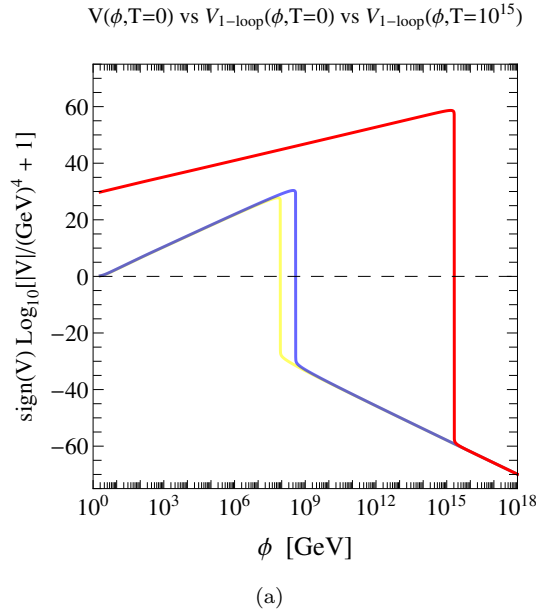


Figure 2.4: *One-loop improved tree-level (yellow line), complete one-loop (blue line) and thermal corrected (red line) potential for  $M_h = 125.09 \text{ GeV}$ ,  $M_t = 173.3 \text{ GeV}$ ,  $\alpha_S = 0.1184$  and  $T = 10^{15} \text{ GeV}$*

notice that no EW minimum is present due to our approximation in which we neglected the quadratic terms. Moreover the tree-level and the complete one-loop effective potential mostly overlap, showing the ability of the improvement to take care of the leading loop contributions. The  $T = 0$  absolute instability is reached at  $\phi \sim 10^9 \text{ GeV}$  due to the zero of the quartic coupling fig. 2.3. At  $T \neq 0$  (we choose  $T = 10^{15} \text{ GeV}$  for illustrative purposes) the thermal corrections dominate over the  $T = 0$  case until  $\phi \sim T$ , after which they are exponentially suppressed, as clear by the form of the thermal integrals (2.19, 2.20).

With the effective potential in our hands the computation of the tunnelling amplitude proceeds similarly

to the  $T = 0$  case with the main deviation represented by the bounce equation. As typical of the finite temperature case, the configuration space of (2.1) undergoes a dimensional reduction to  $\mathcal{O}(3)$  [14, 15, 16]

$$\frac{d^2\phi}{dr^2} + \frac{2}{r} \frac{d\phi}{dr} = \frac{dV_{\text{eff}}(\phi, T)}{d\phi}, \quad \lim_{r \rightarrow \infty} \phi(r) = 0, \quad \left. \frac{d\phi}{dr} \right|_{r=0} = 0, \quad (2.26)$$

with now  $r \equiv |\vec{r}|$ . The corresponding euclidean action for the  $O(3)$  spherically symmetric solution is

$$S_3[\phi(r)] = 4\pi \int_0^\infty dr r^2 \left[ \frac{1}{2} \left( \frac{d\phi}{dr} \right)^2 + V_{\text{eff}}(\phi, T) \right]. \quad (2.27)$$

As we learned from the  $T = 0$  case the full knowledge of the bounce requires to solve (2.26) by means of shooting methods. Differently from that case though, at finite temperature a greater care is required to control and improve the efficiency of the numerical algorithm. With this goal we rescale the field as  $\phi(r) = M_\phi \times \varphi(r)$ , with  $M_\phi = 10 \times T$ , and the three-dimensional distance according to  $x = r \times M_R$ , with  $M_R \equiv \sqrt{V_{\text{MAX}}}/\phi_{\text{MAX}}$ . Note that throughout our analysis we will always find the relation  $\phi_B(0)/T \sim 10$ , corresponding to the value of the field configuration at which the bubble of true vacuum is nucleated. If we consider the leading-order case (at most one-loop effective potential plus main thermal corrections and one-loop RG improvement) we can now have a general survey of the bounces at zero and finite temperature (fig. 2.5).

With the bounce we may compute the vacuum decay rate per unit volume at fixed temperature  $T$  [14, 15, 16]

$$\Gamma(T) \simeq T^4 \left\{ \frac{S_3[\phi_B(r)]}{2\pi T} \right\}^{3/2} e^{-S_3[\phi_B(r)]/T}, \quad (2.28)$$

where  $E_B \equiv S_3[\phi_B(r)]$  represents the energy of a bubble of critical size. A crucial quantity is also the differential decay probability of nucleating a bubble at a given temperature  $T$  which is given by [20]

$$\frac{dP}{d \ln T} \simeq \Gamma(T) \frac{M_P}{T^2} \left( \frac{\tau_U T_0}{T} \right)^3, \quad (2.29)$$

with  $T_0 \simeq 2.35 \times 10^{-4}$  eV and  $\tau_U$  the age of the Universe. Notice that this formula is valid only in a radiation-dominated Universe. The total integrated probability is defined as

$$P(T_{\text{cut-off}}) = \int_0^{T_{\text{cut-off}}} \frac{dP(T')}{dT'} dT'. \quad (2.30)$$

$T_{\text{cut-off}}$  is the cut-off temperature obtained imposing the condition  $\phi_B(0) = \Lambda$ , where  $\Lambda$  is the cut-off scale of the SM, for the moment assumed to be  $\Lambda = 10^{19}$  GeV. The cut-off at  $\Lambda = 10^{19}$  GeV corresponds to a maximum cut-off value on the temperature  $T_{\text{cut-off}} \simeq 10^{18}$  GeV, as expected since  $\phi_B(0)/T \sim 10$ . Larger values of  $\phi_B(0) = \Lambda$  would correspond to a Planck-scale dominated tunneling transition. We have almost all the tools to compute the thermal vacuum stability of the SM. The missing piece is our lack of precision. To illustrate the interplay among the leading order  $T = 0$  and  $T \neq 0$  terms in the effective potential we did not exceed the one-loop accuracy. This is a setting that can only give a very rough idea of the phenomena involved and, in particular for the case of the SM, must necessarily be supplied by next-to-leading contributions. This will obviously include definite two and three-loops derived terms in the RG-functions and in the effective potential, along with the coherent matching between the precision of the evolution equations and the initial conditions to be furnished.

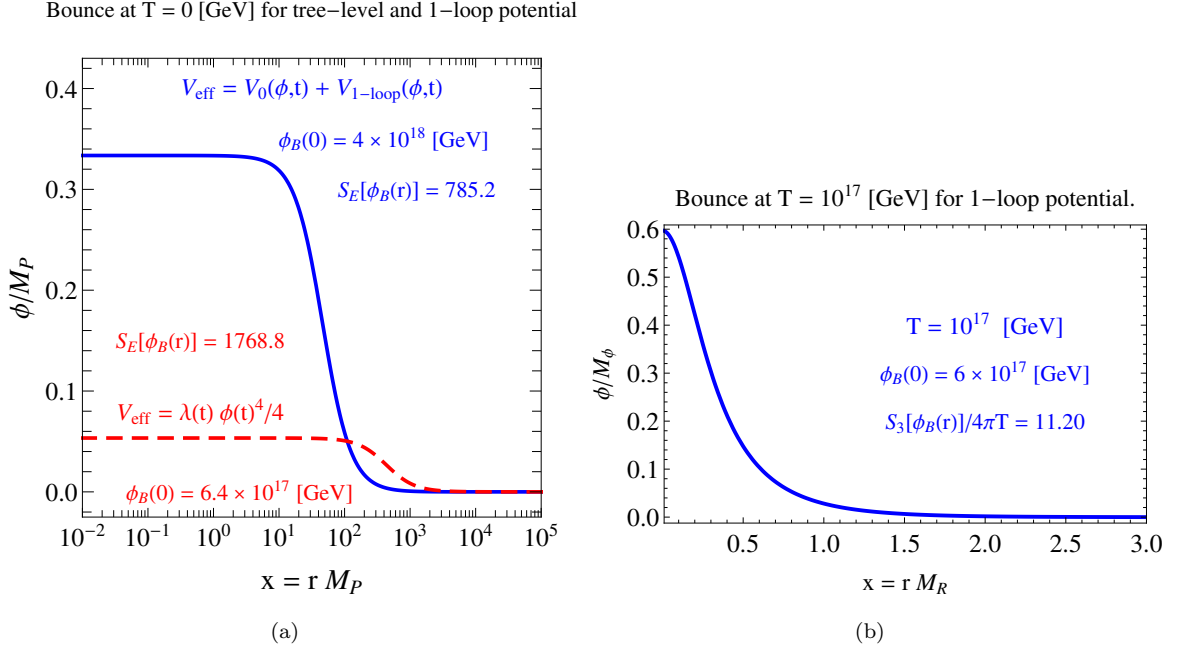


Figure 2.5: Bounce at  $T = 0$  (left panel) and  $T = 10^{17}$  GeV (right panel). At zero temperature we show the bounce solution obtained considering a simple tree-level, RG-improved potential (dashed red line) and the one-loop expression (solid blue line). The field  $\phi$  and the four-dimensional euclidean distance  $r$  are rescaled using the Planck mass  $M_P = 1.22 \times 10^{19}$  GeV. At finite temperature we rescale the field as  $\phi(r) = M_\phi \times \varphi(r)$ , with  $M_\phi = 10 \times T$ . We rescale the three-dimensional distance according to  $x = r \times M_R$ , with  $M_R \equiv \sqrt{V_{\text{MAX}}}/\phi_{\text{MAX}}$ . This prescription greatly improves the efficiency of the numerical shooting method used to solve eq. (2.26). The values of the input SM parameters are the best fit  $M_h = 125.09$  GeV,  $M_t = 173.3$  GeV and  $\alpha_S = 0.1184$ .

### 2.3 The Matching Conditions in the SM

The mismatch of the accuracy between the RG equations and their initial conditions is a point of primary importance and has to be dealt with to secure the consistency of the computations. To gently get close to the SM case, and for future applications in beyond the SM analysis in the next chapters, we begin considering the simpler case where the increase in precision is obtained computing the RGE at two-loop order in  $\overline{MS}$ . These equations must be supplemented with suitable one-loop boundary conditions defined in the same scheme. These consist of  $\overline{MS}$  renormalized couplings and masses evaluated at a given energy scale which correspond to the starting scale of the RG running.

In general, the initial conditions can be unknown free parameters introduced by the specific model which is under investigation, and are directly associated to some measured observables. In order to determine the latter, the  $\overline{MS}$  parameters at the starting scale must be related to these physical observables. This task can be accomplished in two different ways: 1) one can adopt the  $\overline{MS}$  renormalization from the very beginning and obtain the needed  $\overline{MS}$  parameters directly from a set of measured observables or 2) use

a scheme, as the on-shell (OS) one largely used in the electroweak theory, in which the renormalized parameters are expressed in terms of the physical quantities, the pole masses and the Fermi constant, and then translate the on-shell parameters to the corresponding  $\overline{MS}$  expressions through appropriate matching conditions. We follow the second strategy which is quite common in the literature on the perturbative corrections in the SM.

The matching conditions are easily extracted from the obvious relation

$$\alpha_0 = \alpha_{OS} + \delta\alpha_{OS} = \alpha_{\overline{MS}}(\mu) + \delta\alpha_{\overline{MS}}, \quad (2.31)$$

where  $\alpha_0$ ,  $\alpha_{OS}$  and  $\alpha_{\overline{MS}}$  denote, respectively, the bare, the on-shell and the  $\overline{MS}$  expressions of a generic parameter  $\alpha$ . From eq. (2.31) one can extract a  $\overline{MS}$  parameter in terms of its on-shell version obtaining, at one-loop order,

$$\alpha_{\overline{MS}} = \alpha_{OS} + \delta\alpha_{OS} - \delta\alpha_{\overline{MS}} = \alpha_{OS} + \delta\alpha_{OS}|_{finite} \quad (2.32)$$

where the last expression is simply a consequence of the definition of the  $\overline{MS}$  renormalization scheme, in which the counterterms only subtract the UV singular parts. It is clear from eq. (2.32) that the matching conditions between the OS and the  $\overline{MS}$  schemes are defined from the finite part of the OS counterterm. Notice that, at tree level, the  $\overline{MS}$  parameters coincide with their OS version.

Considering the SM case 2.1, the parameters which enter into the RG study are the quartic coupling  $\lambda$ , the top quark Yukawa  $Y_t$  and the gauge coupling constants  $g$ ,  $g_2$  and  $g_3$ . These are computed in terms of the pole masses of the Higgs  $M_h$ , of the top  $M_t$ , of the weak gauge bosons  $M_Z$  and  $M_W$ , and of the Fermi constant  $G_F$ . All these quantities are then translated in the  $\overline{MS}$  scheme using eq. (2.32). Notice that for the  $SU(3)$  strong coupling constant  $g_3$  there is no need to introduce matching conditions because it is directly extracted in the  $\overline{MS}$  renormalization framework as  $\alpha_3(M_Z)$ .

One of the most important SM parameters needed in the determination of the initial conditions of the RG is the Fermi constant  $G_F$ . Using its definition in the effective Fermi theory

$$\frac{G_F}{\sqrt{2}} = \frac{g_0^2}{8M_{W,0}^2}(1 + \Delta r_0) = \frac{1}{2v_0^2}(1 + \Delta r_0), \quad (2.33)$$

we obtain the counterterm of the vev  $v$  in the on-shell scheme  $\delta v_{OS}^2 = \Delta r_0/(\sqrt{2}G_F)$ . We recall that  $G_F$  is extracted from the muon lifetime, computed in the Fermi theory augmented by QED corrections. As a consequence, the computation of the  $\Delta r_0$  electroweak corrections to the  $\mu$  decay requires the subtraction of the pure QED contributions. At one-loop order  $\Delta r_0$  can be decomposed as

$$\Delta r_0 = V - \frac{\Pi_{WW}}{M_W^2} + \frac{\sqrt{2}}{G_F}B + E, \quad (2.34)$$

where  $V$  and  $B$  denote vertex and box corrections,  $\Pi_{WW}$  is the  $W$  boson self-energy evaluated at zero momentum and  $E$  corresponds to the wave-functions contributions. All of them are computed at zero external momenta and are affected by SM corrections (as possible new-physics effects when considering beyond the SM theories). Notice also that we have chosen a renormalization prescription in which the tadpoles are included in the perturbative expansion. This property has the advantage to provide a gauge-independent definition of the mass counterterms and of  $\Delta r_0$ . Nevertheless, the dimensionless parameters

appearing in the Lagrangian, which are the interesting ones for our analysis, are not affected by this choice and the results are independent of the tadpole corrections. The counterterms of the top Yukawa and of the  $SU(2)$  gauge couplings, needed in the matching procedure, are obtained exploiting the relations

$$M_t = Y_{t\text{OS}} \frac{v_{\text{OS}}}{\sqrt{2}}, \quad M_W^2 = g_{2\text{OS}}^2 \frac{v_{\text{OS}}^2}{4}, \quad (2.35)$$

which lead to

$$\delta Y_{t\text{OS}} = Y_{t\text{OS}} \left( \frac{\delta M_t}{M_t} - \frac{\delta v_{\text{OS}}}{v_{\text{OS}}} \right), \quad \delta g_{2\text{OS}} = g_{2\text{OS}} \left( \frac{\delta M_W^2}{2M_W^2} - \frac{\delta v_{\text{OS}}}{v_{\text{OS}}} \right). \quad (2.36)$$

For the Abelian gauge coupling  $g$  the counterterm is slightly more involved being rooted to

$$M_Z \simeq \frac{v}{2} \sqrt{g_2^2 + g^2}, \quad (2.37)$$

which concerns the on-shell values of  $M_Z$  and  $M_W$ :

$$\delta g_{\text{OS}} = g_{\text{OS}} \left( \frac{1}{2} \frac{\delta M_Z^2 - \delta M_W^2}{M_Z^2 - M_W^2} - \frac{\delta v_{\text{OS}}}{v_{\text{OS}}} \right). \quad (2.38)$$

In the previous equation  $\delta v_{\text{OS}}$  is obtained from  $\Delta r_0$  as explained above, while the top, the  $W$  and the  $Z$  boson mass counterterms in the on-shell renormalization scheme are computed from the corresponding self-energies

$$\delta M_t = \text{Re} \Sigma_t(\not{p} = M_t), \quad \delta M_W^2 = \text{Re} \Pi_{WW}(p^2 = M_W^2), \quad \delta M_Z^2 = \text{Re} \Pi_{ZZ}(p^2 = M_Z^2). \quad (2.39)$$

It should now be clear how to proceed when we make a further step in the accuracy including, as mandatory for precision SM studies, three loop RG equations. The details of the corresponding two-loop matching condition are the subject of [26] and, together with the two-loop order effective potential [109] with leading thermal corrections [17, 18, 19], will form the up-to-date highest precision approach to address the investigation of the SM high-energy behavior.

Name	Value	Description
$M_W$	80.384 GeV	$W$ boson pole mass
$M_Z$	91.1876 GeV	$Z$ boson pole mass
$M_h$	125.09 GeV	Higgs boson pole mass
$M_t$	173.34 GeV	Top quark pole mass
$v \equiv (\sqrt{2}G_\mu)^{-1/2}$	246.21971 GeV	Higgs vev from the $\mu$ decay
$\alpha_3(M_Z)$	0.1184	$\overline{\text{MS}}$ QCD structure constant (5 flavors)

Table 2.1: *Physical observables used to extract the SM parameters in the  $\overline{\text{MS}}$  scheme through the matching procedure. For the Higgs mass we used the latest result [24], for all the other parameters we refer to [26].*

## 2.4 Finite temperature Effective Potential of SM beyond leading order

With the help of the matching conditions we can now successfully include the two-loop corrections and up to three-loop RG equations (see [26] and reference therein) for the improvement. Our effective potential has now the following form

$$V_{\text{eff}}(\phi, T) = V_0(\phi) + V_{1\text{-loop}}(\phi) + V_{2\text{-loop}}(\phi) + V_{1\text{-loop}}(\phi, T) + V_{\text{ring}}(\phi, T) , \quad (2.40)$$

and will be the new basis to increase in precision the previous survey on the quantum and thermal corrections.

With 2.40 we can now update fig. 2.4. The effect of moving from one to three-loop RG equations in the

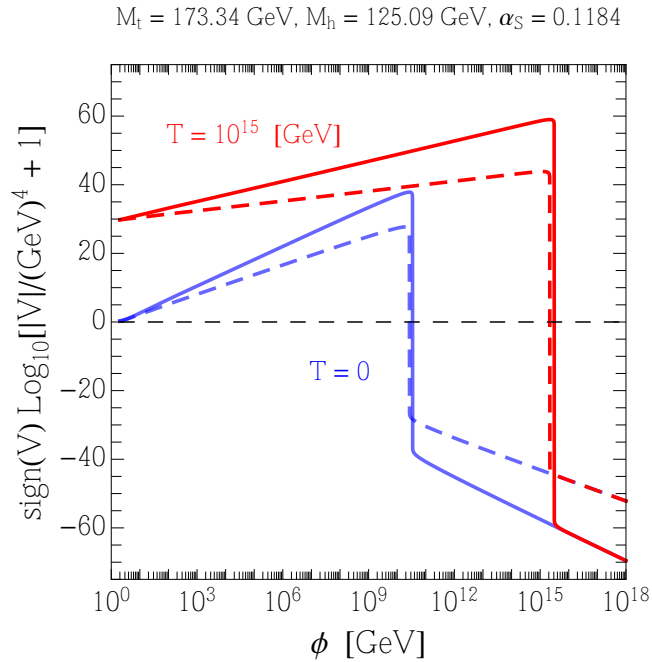


Figure 2.6: *Effective potential and first derivative at zero and finite temperature as a function of the Higgs field. Blue line:  $T = 0$ . Red line: finite temperature  $T = 10^{15} \text{ GeV}$ . Solid line: effective potential. Dashed line: first derivative. The values of the input SM parameters are shown in the plot label.*

improvement, more than the explicit two-loop terms in the potential, has the visible impact (fig. 2.6) in shifting the  $T = 0$  instability field configuration to the higher values of  $\phi \sim 10^{11} \text{ GeV}$ . In agreement with the fig. 2.4 the thermal corrections dominate the effective potential until  $\phi \sim T$ , when the exponential suppression comes in action. The shape of the effective potential at finite temperature can be better visualized in fig. 2.7 where we show the effective potential, normalized with respect to its maximum value, as a function of the Higgs field rescaled according to the ratio  $\phi/T$ . The effective potential changes sign at about  $\phi \simeq 3T$  to then sink towards the true vacuum of the theory. Notice that the latter turns

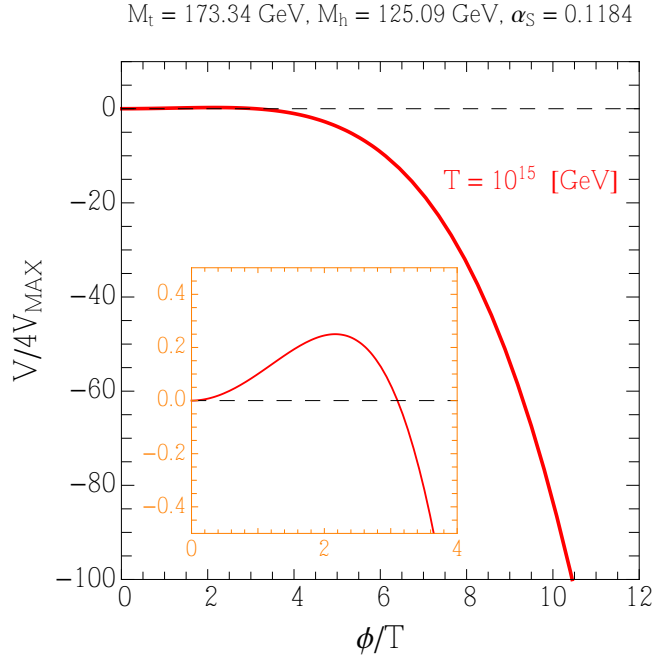


Figure 2.7: *SM effective potential (normalized with respect to four times its maximum value) at  $T = 10^{15}$  GeV. The field  $\phi$  scales as  $\phi/T$ . The values of the input SM parameters are shown in the plot label. In the insert, we zoom in the region close to the maximum (axis labels as for the outer plot).*

out to lie at extremely large field value,  $\phi \approx 10^{30}$  GeV [39]. However, this is not a problem as soon as one assumes the SM to be valid up to the Planck scale: what really matters in terms of tunneling probability, at finite temperature as well as at  $T = 0$ , is the turning point of the bounce solution rather than the precise location of the true vacuum. The former, as we shall clarify in the next section, never exceeds in our analysis Planck-scale values.

## 2.5 Bounce solution and thermal tunneling

We can now continue from where we left, at the end of section 2.2.2, and compute the new bounce for the effective potential 2.40 solving eq. 2.26 by shooting method. The results are depicted in the right panel of fig. 2.8 where we show the SM bounce solution at finite temperature for  $T = 10^{17}$  GeV. Both left and right panel represent a more accurate version of our previous effort of fig. 2.5. In the left panel of fig. 2.9 we show the euclidean action of the bounce solution  $\phi_B(r)$  as a function of the temperature for the best-fit values of  $M_h$ ,  $M_t$ , and  $\alpha_s$ . In the right panel of fig. 2.9 instead, the differential decay probability of nucleating a bubble (2.29) is shown as a function of the temperature.

In the insert plot in the right panel of fig. 2.9 the values of  $\phi_B(0)$  at different temperatures are shown. We may now come to the main results.

Integrating the differential probability using eq. (2.30), we find  $P(T_{\text{cut-off}}) = 5.22 \times 10^{-49} \ll 1$ . Consequently, we conclude that the electroweak vacuum of the SM for the present central values of  $M_h$ ,  $M_t$ , and

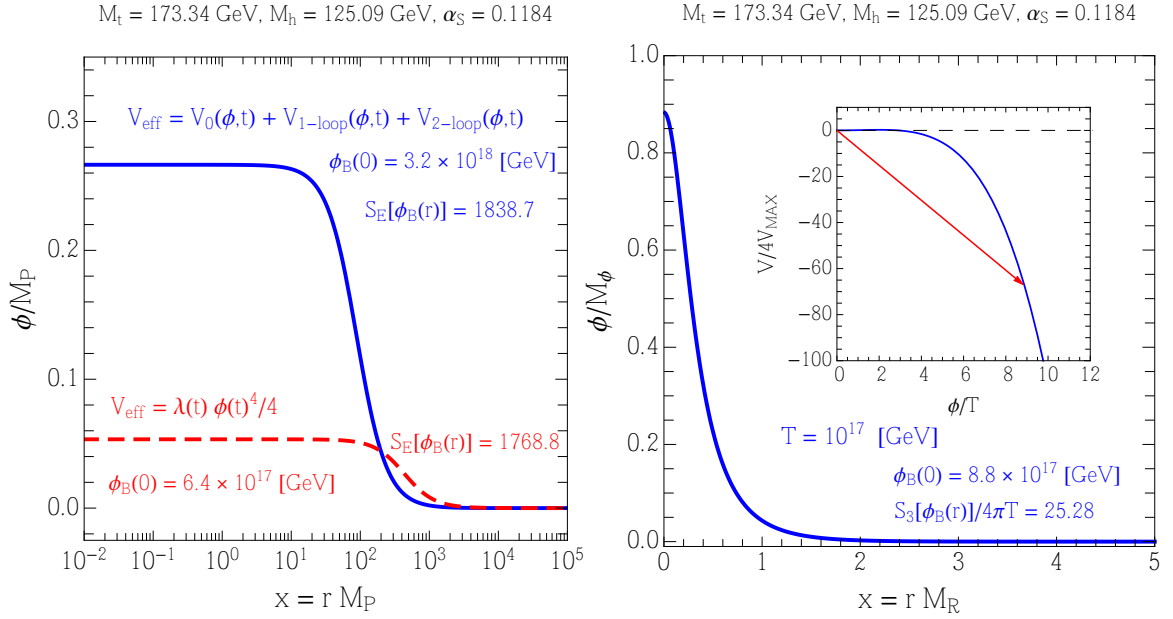


Figure 2.8: *Bounce at  $T = 0$  (left panel) and  $T = 10^{17}$  GeV (right panel). At zero temperature we show the bounce solution obtained considering a simple tree-level, RG-improved potential (dashed red line) and the full two-loop expression (solid blue line). This plot should be compared with fig. 2.5 (see the corresponding caption for the details on the numerical computation). The tip of the arrow corresponds to  $\phi_B(0) = 8.8 \times 10^{17}$  GeV. The values of the input SM parameters are shown in the plot label.*

$\alpha_s$  is unstable but sufficiently long-lived if compared to the age of the Universe, even including thermal corrections with the highest cut-off scale  $\Lambda = 10^{19}$  GeV.

The total probability computed turns out to be much larger than the corresponding one at  $T = 0$ ,  $\sim 10^{-500}$  [39]. So, still allowing for an electroweak vacuum in the metastable phase, we can appreciate the role of the thermal corrections in greatly enhancing the tunneling probability. The thermal corrections affect the computation so deeply that an excursion in the allowed experimental range for  $M_h$ ,  $M_t$ , and  $\alpha_s$  would lead to much more stringent instability bounds if compared to the one at  $T = 0$ . We will carry a more comprehensive analysis in the context of the phase diagram of the SM in section 2.6, for the moment, let us now try to change only the value of  $M_t$ . In fig. 2.10 we show how the total probability of thermal tunneling changes as a function of  $M_t$  for three different values of the Higgs mass,  $M_h = 124.0, 125.09, 127.0$  GeV, with  $\alpha_s = 0.1184$ . The total probability increases going towards larger values of  $M_t$ , and smaller values of  $M_h$ . For illustrative purposes, we show the region corresponding to the best-fit, 1- and 3- $\sigma$  confidence regions of  $M_t$  according to  $M_t = 173.34 \pm 0.8$  GeV. For  $M_h = 125.09$  GeV, we find that the total probability of thermal tunneling equals one for values of  $M_t$  extremely close to the 1- $\sigma$  confidence region. This is a remarkable result, given that at  $T = 0$  the instability bound is reached only for  $M_t \gtrsim 178$  GeV. Motivated by this result, we turn attention to the full phase diagram of the SM.

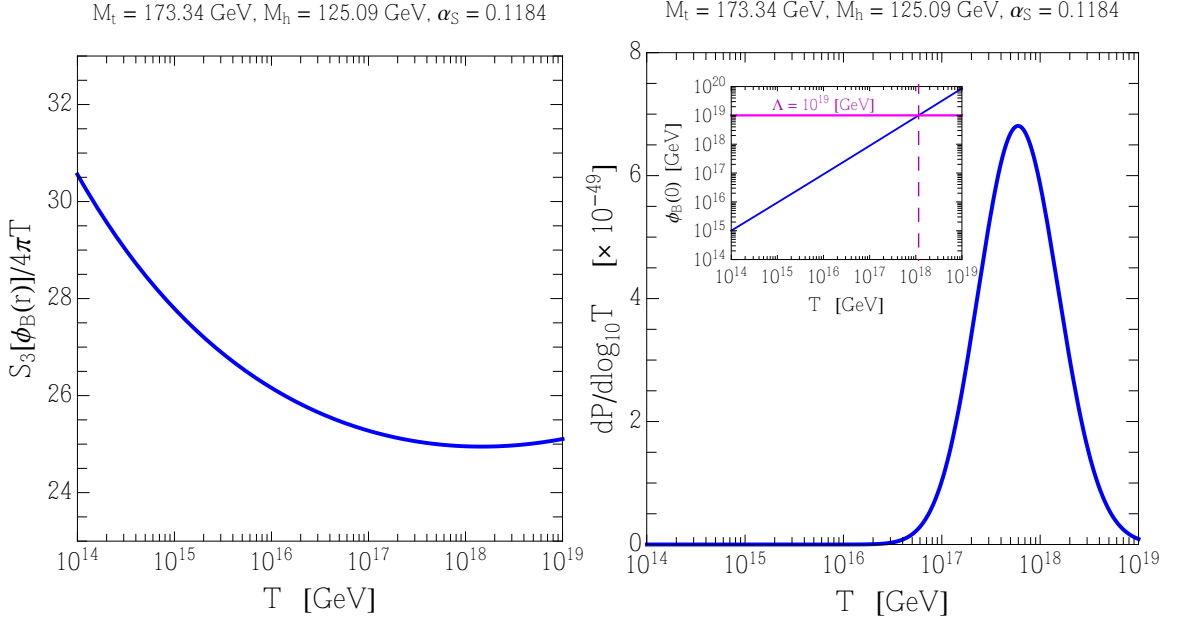


Figure 2.9: *Left panel.* Euclidean action of the bounce solution  $\phi_B(r)$  as a function of the temperature. *Right panel.* Plot of the differential probability  $dP/d\log_{10} T$  as a function of the temperature. In the insert, we show the value of  $\phi_B(0)$  as a function of the temperature. For a given cut-off scale (for instance,  $\Lambda = 10^{19} \text{ GeV}$ , solid horizontal magenta line) the integration of  $dP/d\log_{10} T$  must be cut-offed at the temperature satisfying the condition  $\phi_B(0) \sim \Lambda$  (in this example  $T_{\text{cut-off}} \sim 10^{18} \text{ GeV}$ , vertical dashed magenta line). The values of the input SM parameters are shown in the plot label.

## 2.6 The phase diagram of the Standard Model at finite temperature

The phase diagram of the SM is divided in three regions describing absolute stability, metastability, and instability of the electroweak vacuum depending on the values of the SM parameters. Among them, the top mass, the Higgs mass, and the strong coupling at weak scale play a dominate role. At finite temperature, we add a fourth region in order to discriminate between instability at  $T = 0$  and thermal instability. All in all, the four regions are defined as follows.

- The absolute stability region (green) verifies the condition  $\lambda_{\text{eff}}(\phi) \geq 0$  all the way up to the Planck scale.<sup>2</sup> The effective potential does not develop a second, deeper minimum, and the electroweak vacuum is stable.
- The instability region at finite temperature (red) verifies the condition  $P \geq 1$ , where the thermal tunneling probability is given in eq. (2.30).

<sup>2</sup> $\lambda_{\text{eff}}$  is the effective quartic coupling accounting for one- and two-loop corrections which is extracted from the RG-improved effective potential.

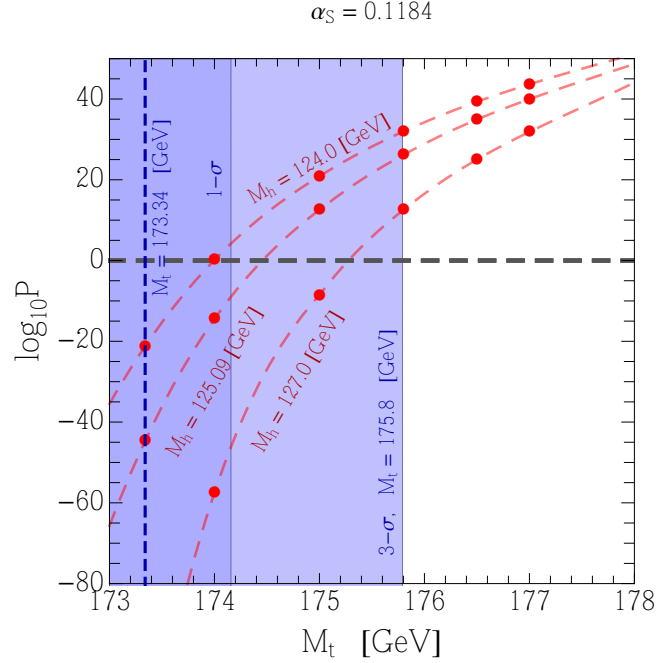


Figure 2.10: Plot of the  $\log_{10}$  of the total probability as a function of the top mass for three different values of the Higgs mass,  $M_h = 124.0, 125.09, 127.0$  GeV. For illustrative purposes, the vertical blue lines mark the best-fit, 1- and 3- $\sigma$  values according to  $M_t = 173.34 \pm 0.8$  GeV.

- At  $T = 0$ , the instability region (marked by the dashed red line) corresponds to a zero-temperature tunneling probability

$$p = \max_R \frac{V_U}{R^4} \exp \left[ -\frac{8\pi^2}{3|\lambda(\mu)|} \right] > 1, \quad (2.41)$$

where  $\tau_U$  is the age of the Universe and  $V_U \sim \tau_U^4$ .

- In the metastability region (yellow)  $\lambda_{\text{eff}}(\phi)$  does become negative below the Planck scale, and the effective potential develops a second minimum deeper than the electroweak one. However, the decay probability verifies  $P < 1$ .

### 2.6.1 Instability bound at finite temperature

In fig. 2.11 we show the phase diagram of the SM in terms of the Higgs and top mass. The gray ellipses refer to the 1-, 2-, and 3- $\sigma$  confidence regions obtained considering  $M_t = 173.3 \pm 0.8$  GeV and  $M_h = 125.09 \pm 0.24$  GeV. At  $T = 0$ , the instability bound correctly reproduces the known result [26] according to which, for instance, values  $M_t \gtrsim 178$  GeV are excluded if  $M_h \simeq 125$  GeV.

At finite temperature, the scenario undergoes a drastic change. As expected, the instability bound is pushed towards lower values of  $M_t$ . Values of  $M_t \gtrsim 174.5$  GeV, for instance, are excluded if  $M_h \simeq 125$  GeV. Including the uncertainties on the strong coupling at the weak scale (dot-dashed lines in fig. 2.11) the bound becomes even more stringent, and values  $M_t \gtrsim 173.6$  GeV are excluded if  $M_h \simeq 125$  GeV and  $\alpha_s = 0.1163$ .

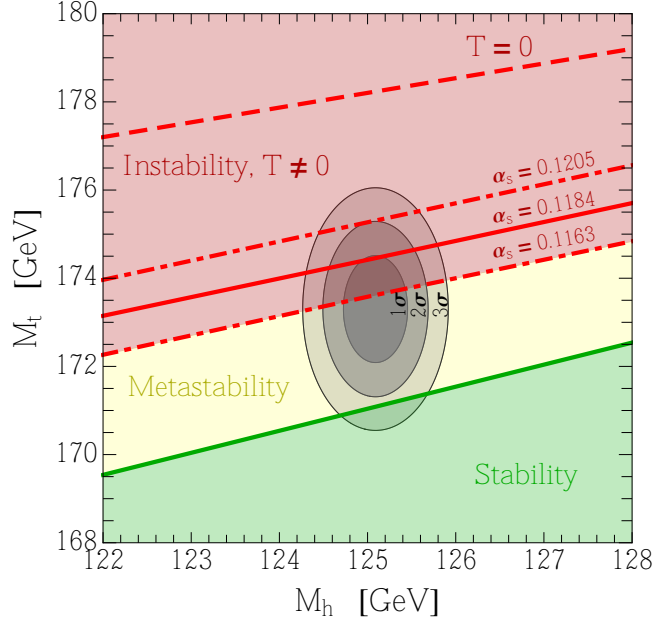


Figure 2.11: *SM phase diagram at finite temperature and cut-off scale  $\Lambda = 10^{19}$  GeV. Solid (dashed) red line: instability bound with (without) thermal corrections. We also show the 1-, 2-, and 3- $\sigma$  ellipses corresponding to  $M_t = 173.3 \pm 0.8$  GeV and  $M_h = 125.09 \pm 0.24$  GeV (assuming a two-dimensional gaussian distribution without correlations).*

At finite temperature, and assuming the highest cut-off scale  $\Lambda = 10^{19}$  GeV, the instability bound excludes, taking into account the present experimental uncertainties on  $\alpha_s$ , almost one half of the allowed experimental range for  $(M_h, M_t)$ . In terms of  $M_t$  we extract the following bound

$$\boxed{\begin{aligned} \frac{M_t}{\text{GeV}} &< 174.459 + 0.4285 \times \left( \frac{M_h}{\text{GeV}} - 125.09 \right) \\ &+ 0.283 \times \left( \frac{\alpha_s - 0.1184}{0.0007} \right) \end{aligned}} \quad (2.42)$$

In fig. 2.12 we show the phase diagram of the SM in terms of the top mass and the strong coupling at the weak scale, keeping  $M_h$  fixed at  $M_h = 125.09$  GeV. As before, the ellipses mark the 1-, 2- and 3- $\sigma$  confidence regions with  $M_t$  as in fig. 2.11 and  $\alpha_s = 0.1184 \pm 0.0007$ . For illustrative purposes, we also show (dashed ellipses) the effect of a 1 GeV shift in the determination of the top pole mass. Such shift symbolically represents the systematic error involved in the naive combination of ATLAS, CMS and TeVatron results used in this thesis work,  $M_t = 173.34 \pm 0.8$  GeV. Moreover, one should always keep in mind that the experimentally measured top mass is not the pole mass entering in the computation of the instability bound but the outcome of a complicated reconstruction of top quark decays (often dubbed the Monte Carlo mass). This fact amounts to a further source of uncertainty. As well known, and emphasized in this plot, the measurement of the top quark pole mass plays a crucial role in the determination of the actual position of the SM in the phase diagram [27]. With the inclusion of thermal corrections, the situation becomes even more severe if compared with the  $T = 0$  case, since now a small shift of the

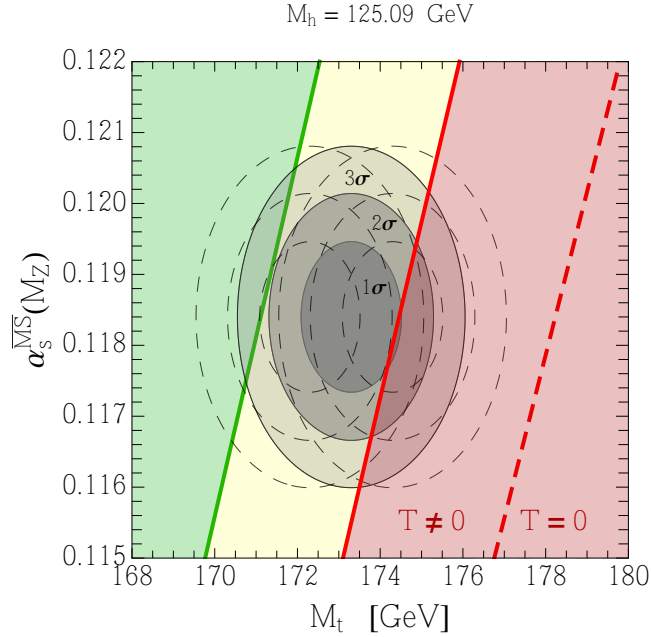


Figure 2.12: *Same as in fig. 2.11 but in the plane  $(M_t, \alpha_s)$ . We also show the effect of a 1 GeV shift in the determination of the top pole mass (dashed ellipses). The Higgs mass is fixed at  $M_h = 125.09$  GeV.*

measured values can drastically change the phase of the electroweak vacuum in both directions, towards the stability as well as the instability region.

### 2.6.2 Instability bound and dependence from cosmology

Thermal corrections are computed assuming the Higgs field in equilibrium with a thermal bath at temperature  $T$ . The occurrence of this condition strongly depends on the thermal history of the Universe. During inflation [28] all the energy is stored in the inflaton field, which slowly rolls down towards the minimum of its effective potential. Once reached, inflation ends, and the inflaton begins to oscillate near the minimum. SM particles are created because of their interactions with the inflaton field: the kinetic energy of the oscillating inflaton is gradually transferred into the ultra-relativistic SM particles produced in the final state of its decay. Eventually, SM particles reach a state of thermal equilibrium at the temperature  $T_{\text{RH}}$ , dubbed reheating temperature [29]. Thenceforth, the temperature scales according to  $T \propto a^{-1}$ , as in the ordinary radiation-dominated phase (as customary,  $a$  is the Friedmann-Robertson-Walker scale factor). Strictly speaking, the applicability of our computation is limited to  $T < T_{\text{RH}}$ . In order to further investigate this important point, we have analyzed two possible scenarios.

#### Instantaneous reheating

In this case the decay probability is given by eq. (2.30), with  $T_{\text{cut-off}} = T_{\text{RH}}$ . In fig. 2.13 we show how the instability bound changes for different values of  $T_{\text{RH}}$ . As clear from the right panel of fig. 2.9, the largest contribution to the total probability comes from the high-temperature region, and a decrease in

the cut-off quickly weakens the instability bound. We show the impact of different reheating temperatures in fig. 2.13. At  $T_{\text{RH}} \simeq 10^{12}$  GeV the instability bound is pushed towards the border of the 3- $\sigma$  band on

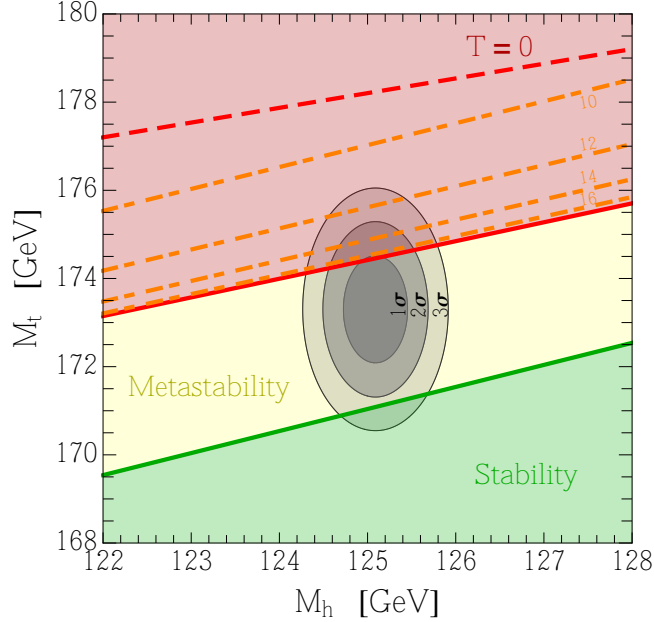


Figure 2.13: *Dependence of the instability bound on the reheating temperature  $T_{\text{RH}}$ , assuming instantaneous reheating. The orange dot-dashed lines correspond to different values  $T_{\text{RH}} = 10^x$  GeV, with—from top to bottom— $x = 10, 12, 14, 16$ .*

( $M_h, M_t$ ). For smaller values of the reheating temperature, e.g.  $T_{\text{RH}} = 10^{10}$  GeV, the SM reenters in the metastability region. The bounds in fig. 2.11 are well described by the following parametric formula

$$\frac{M_t}{\text{GeV}} < 0.283 \times \left( \frac{\alpha_s - 0.1184}{0.0007} \right) + c_1 \times \frac{M_h}{\text{GeV}} + c_2 \times \log_{10} \frac{T_{\text{RH}}}{\text{GeV}} + \frac{c_3}{c_4 \times \log_{10} \frac{T_{\text{RH}}}{\text{GeV}} + c_5} \quad (2.43)$$

with  $c_1 = 0.4612$ ,  $c_2 = 1.907$ ,  $c_3 = -1.2 \times 10^3$ ,  $c_4 = -0.323$ ,  $c_5 = -8.738$ . In concrete, taking  $M_h = 125.09$  GeV,  $\alpha_s = 0.1163$  (close to the 3- $\sigma$  lower bound), and  $T_{\text{RH}} = 10^{16}$  GeV we find  $M_t < 173.65$  GeV.

Before proceeding, let us pause for a moment to comment about the current experimental limits on the reheating temperature. Despite its relevance in our understanding of the early Universe, very little is known about the actual value of the reheating temperature. An obvious lower bound can be obtained requiring a successful Big Bang Nucleosynthesis, and it turns out to be  $T_{\text{RH}} \gtrsim 10$  MeV [30]. As far as the upper bound is concerned, it is possible—assuming instantaneous reheating—to relate the reheating temperature to the energy scale of the inflationary potential [31]; since the latter can be constrained using the limit on the tensor-to-scalar ratio of the amplitudes produced during inflation, it is possible to extract a bound on  $T_{\text{RH}}$ . All in all, one finds  $T_{\text{RH}} \lesssim 10^{16}$  GeV [31]. High values of reheating temperature—as large as the ones considered in fig. 2.13—are therefore experimentally allowed. Moreover, the hypothesis

of instantaneous reheating is a crude, yet not unrealistic, approximation. More likely, reheating is a dynamical process. In the next section we will elaborate this point and its consequences in more detail.

### Including the dynamics of reheating

Reheating is not an instantaneous process. On the contrary, the radiation-dominated phase at  $T < T_{\text{RH}}$  follows a stage of matter domination during which the energy density of the Universe is dominated by the oscillations of the inflaton field [32, 33]. Temperature scales according to  $T \propto a^{-3/8}$  [32, 33]; in other words, during the oscillating phase the Universe cools down more slowly—if compared with the scaling  $T \propto a^{-1}$  of the radiation-dominated phase—because of the heating effect of the inflaton decay. As shown in [32, 33] the maximum value of the temperature is

$$T_{\text{MAX}} = \left(\frac{3}{8}\right)^{2/5} \left(\frac{5}{\pi^3}\right)^{1/8} \frac{g_*^{1/8}(T_{\text{RH}})}{g_*^{1/4}(T_{\text{MAX}})} (M_{\text{P}} H_f T_{\text{RH}}^2)^{1/4}, \quad (2.44)$$

where  $g_*(T)$  is the effective number of degrees of freedom, and  $H_f$  is the Hubble parameter at the end of inflation. The situation is schematically summarized in fig. 2.14. In the region  $T_{\text{RH}} \leq T \leq T_{\text{MAX}}$  we

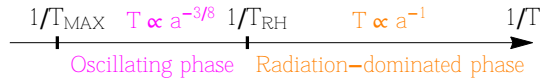


Figure 2.14: *Schematic representation of the thermal evolution of the Universe after inflation. At the end of the reheating process ( $T < T_{\text{RH}}$ ) the temperature scales according to  $T \propto a^{-1}$ , as in the ordinary radiation-dominated phase. During the oscillating phase of the inflaton, before reheating is completed,  $T \propto a^{-3/8}$ .*

can not compute the decay probability using eq. (2.29), since it relies on the assumption of a radiation-dominated Universe. Using the scaling  $T \propto a^{-3/8}$ , in the region  $T_{\text{RH}} \leq T \leq T_{\text{MAX}}$  the differential decay probability becomes [20]

$$\frac{dP}{d \ln T} \simeq \Gamma(T) \frac{M_{\text{P}}}{T^2} \left(\frac{\tau_{\text{U}} T_0}{T_{\text{RH}}}\right)^3 \left(\frac{T_{\text{RH}}}{T}\right)^{10}. \quad (2.45)$$

All in all, the total integrated probability is given by

$$P(T_{\text{RH}}, H_f) = \int_0^{T_{\text{RH}}} \left. \frac{dP(T')}{dT'} \right|_{\text{eq. (2.29)}} dT' + \int_{T_{\text{RH}}}^{T_{\text{MAX}}} \left. \frac{dP(T')}{dT'} \right|_{\text{eq. (2.45)}} dT', \quad (2.46)$$

and it depends on the reheating temperature and the value of the Hubble parameter at the end of inflation via eq. (2.44). Notice that, for a given  $T_{\text{RH}}$ , the Hubble parameter is characterized by the lower bound  $H_f^{\text{min}} = [4\pi^3 g_*(T_{\text{RH}})/45]^{1/2} (T_{\text{RH}}^2/M_{\text{P}})$ ; this bound follows from the limit in which the inflaton energy density equals the energy density of a thermal bath with temperature  $T_{\text{RH}}$ . In fig. 2.15 we show how the instability bound changes for different values of  $T_{\text{RH}}$  including the dynamics of reheating.

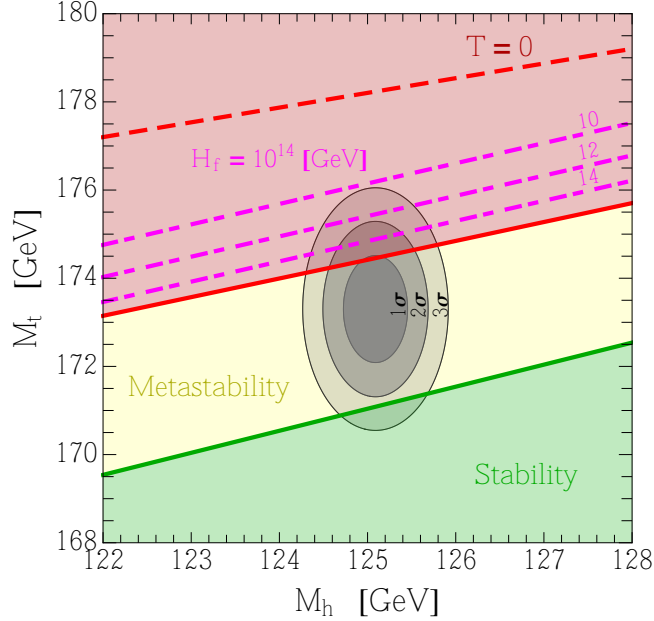


Figure 2.15: *Dependence of the instability bound on the reheating temperature  $T_{\text{RH}}$ , including the dynamics of reheating. The magenta dot-dashed lines correspond to different values  $T_{\text{RH}} = 10^x$  GeV, with—from top to bottom— $x = 10, 12, 14$ . We take  $H_f = 10^{14}$  GeV and  $g_*(T) = 106.75$ .*

For definiteness, we take  $H_f = 10^{14}$  GeV. As expected, comparing the same values of the reheating temperature analyzed in fig. 2.13, the instability bound becomes more stringent including the dynamics of reheating. As a benchmark example, the value  $T_{\text{RH}} = 10^{10}$  GeV—outside the experimental ellipses in fig. 2.13—approaches again the edge of the 3- $\sigma$  region if the oscillating phase is included. In order to better investigate the role of the interplay between the reheating temperature and the Hubble parameter at the end of inflation, in fig. 2.16 we recast the instability bound in the plane  $(H_f, T_{\text{RH}})$  for different values of the top mass. For each value of  $M_t$ , the values of  $T_{\text{RH}}$  above the corresponding red curve are excluded. We notice that the instability bound, for a fixed value of  $M_t$ , becomes stronger increasing the value of  $H_f$ ; this is expected, since the larger  $H_f$  the higher  $T_{\text{MAX}}$ . However, we also notice that the  $H_f$  dependence is very mild (after all  $H_f$  enters only as  $H_f^{1/4}$  in  $T_{\text{MAX}}$ ). As for the rest, fig. 2.16 retraces what already foreseen in fig. 2.15. Stringent bounds on the top mass—close to the present experimentally measured central value—can be reached only for very high (yet reasonable) reheating temperatures. For reheating temperatures  $T_{\text{RH}} \simeq 10^{10}$ - $10^{11}$  GeV, the bound on the top mass is  $M_t \gtrsim 176$  GeV, at the border of the experimental 3- $\sigma$  confidence interval.

Let us now conclude this section summarizing in a nutshell our results. Thermal corrections are relevant for the computation of the instability region in the SM phase diagram, and they can put a very stringent bound on  $M_t$  close to the present measured central value if also the uncertainties on  $\alpha_s$  are included. However, they crucially depend on the temperature of the early Universe. As already noticed in [20, 21], therefore, the fate of the SM and its cosmological history are inextricably linked.

A crucial question now seems to be: what was the highest temperature ever recorded in the early

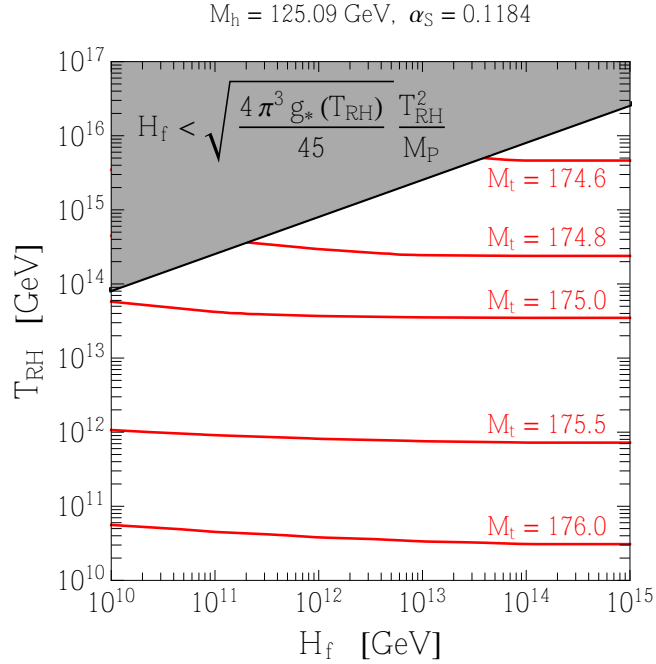


Figure 2.16: *Instability bound in the plane  $(H_f, T_{RH})$ , for different values of the top mass. We include the dynamics of reheating, and we keep fixed  $M_h = 125.09 \text{ GeV}$  and  $\alpha_s = 0.1184$ . The gray region is excluded by the condition  $H_f < H_f^{\min}$ . For each  $M_t$ , the region above the corresponding red curve is excluded.*

Universe after inflation ended? On a general ground, one could be inclined to think that it must have been very high. Let us provide one example in the context of thermal leptogenesis and neutrino mass generation via type-I seesaw [20]. On the one hand, in order for baryogenesis to proceed via leptogenesis the mass scale  $M$  of the sterile neutrinos must be of the order of  $10^9 \text{ GeV}$  or larger [34, 35]; on the other one, in order to produce thermally the heavy neutrino states a reheating temperature of the Universe after inflation of  $T_{RH} > M$  is required. This simple argument seems to point towards a value of the order of  $T_{RH} \gtrsim 10^{10} \text{ GeV}$ , a temperature high enough to generate large thermal corrections, as shown in fig. 2.15.

Moreover in [21] a large reheating temperature after inflation (from  $T_{RH} \simeq 10^7 \text{ GeV}$  up to  $T_{RH} \simeq 10^{17} \text{ GeV}$ , the actual value depending on the instability scale of the Higgs potential and the value of the Hubble constant during inflation) seems to be suggested by inflation itself, since it may tame dangerous quantum fluctuations of the Higgs field.

## 2.7 Comments and conclusions

We revisited and updated the computation of the thermal corrections to the stability of the electroweak vacuum in the SM. We followed the approach of [16], based on *i)* the computation of the effective potential at finite temperature, and *ii)* the exact numerical solution of the bounce equation. We performed a full computation including the most updated expressions for effective potential,  $\beta$  functions and matching

conditions, covering an empty space in the SM research. This effort has led to the corresponding SM phase diagram fig. 2.11 (referred to the parameters  $M_h$  and  $M_t$ ) and fig. 2.12 (referred to the parameters  $M_t$  and  $\alpha_s$ ), a fundamental tool to investigate the SM and its criticality prospect, Thermal corrections turned out to be very important, and they strengthen the constraining power of the instability bound on the SM parameters if compared with the case at  $T = 0$ . Our results show that the instability bound at finite temperature excludes values of the top mass  $M_t \gtrsim 173.6$  GeV, if  $M_h \simeq 125$  GeV, and including the uncertainties on the strong coupling constant at the weak scale. Parametrically, our bound is given by eq. (2.42). Thermal corrections crucially depend on the reheating temperature, hence on the cosmological history of the early Universe after inflation ended. From this perspective, we studied the case corresponding to a limit scenario in which  $T_{\text{RH}} \simeq 10^{18}$  GeV. In order to explore the temperature dependence, we investigated two possible situations. 1) We considered the reheating after inflation as an instantaneous process. According to this simplified assumption, the Universe experienced a sharp transition from the inflationary epoch to the radiation-dominated phase. This led to the results shown in fig. 2.13. The instability bound at finite temperature, now cut-offed at  $T_{\text{cut-off}} = T_{\text{RH}}$ , weakens. However, for  $T_{\text{RH}} \simeq 10^{11}$  GeV the instability bound still lies at the edge of the  $3\text{-}\sigma$  confidence region for the experimentally measured values of  $M_h$  and  $M_t$ . For larger values of  $T_{\text{RH}}$ , the SM enters in the instability region. Parametrically, our bound as a function of  $T_{\text{RH}}$  is given by eq. (2.43). 2) We included in our analysis the dynamics of reheating. The instability bound becomes stronger if compared with the case of instantaneous reheating since it includes the oscillating phase of the inflaton field in the interval  $T_{\text{RH}} \leq T \leq T_{\text{MAX}}$ , where  $T_{\text{MAX}}$  is given by eq. (2.44) and depends on the value of the Hubble parameter at the end of inflation. Our results are shown in fig. 2.15. We find that if  $T_{\text{RH}} \gtrsim 10^{10}$  GeV the SM starts to fall in the instability region of the phase diagram.

To conclude, the metastability region of the SM phase diagram considerably shrinks if thermal corrections to the decay of the electroweak vacuum are included. On the quantitative level, the impact of these corrections depends on the cosmological history of the early Universe, as shown in [20, 21]. From a more qualitative perspective, unveiling the true nature of near-criticality becomes an even more urgent question being the *big desert* hypothesis still not contradicted by the more recent LHC quest.

## Chapter 3

# Vacuum stability in low-scale seesaw models

### 3.1 Introduction

The investigation of chapter 2 was inherently conservative, involving the SM and nothing else. No new degrees of freedom have entered at any energy up to Planck scale, an assumption which has clarified the possibility to successfully extrapolate the SM up to such high-energy. We have seen that the SM is an unstable theory but that can hold phenomenologically, given the small probability of a tunnelling process within cosmic time scale. Also we appreciated how fragile such feature is and how small change in the parameters can drive the SM beyond such safe scenario. This argument poses a natural question about how new physics beyond the SM can modify the (meta)stability of the EW vacuum. To address this question we have to specify which kind of new physics we are referring to and, undeniably, the most compelling one is provided by the observation of non-zero neutrino masses and related oscillations. This is a clear evidence that our conservative approach of chapter 2) has to be overcome and the SM must be supplied with a mechanism responsible for the generation of neutrino masses [42]. This by no means automatically implies that the SM fate will be affected. For instance, a very economical choice to provide neutrino masses would be the so-called type-I seesaw mechanism [43, 44, 45, 46], which asks for an enlarged SM with three heavy right-handed neutrinos with a Majorana mass  $M_R$  breaking lepton number, coupled to the SM Higgs doublet  $H$  and leptonic doublets via a Yukawa coupling  $Y_\nu$ . Although this framework seems to have all the ingredients to bring an exciting change to the quartic coupling evolution of the SM Higgs (fermion degrees lead, in general, to instability), unless we embed this mechanism in a more complex scenario, the large scales involved will totally suppress the influence of the new degrees of freedom in the RG evolution. The main problem is that to have a sizable effect, the Yukawa coupling  $Y_\nu$  must be of order one. Also to accommodate a  $m_\nu \simeq 0.1$  eV for the light neutrino mass scale we would find a Majorana mass scale  $M_R \sim \mathcal{O}(10^{15})$  GeV. This means that the right-handed neutrinos actively participate to the running of  $\lambda$  only for values of the RG scale larger than  $M_R$ . So there is not enough time, in terms of RG evolution, to relevantly alter the SM picture. If instead we

would like to lower the mass scale  $M_R$ , then in order to reproduce the correct order of magnitude for the mass scale of light neutrinos, we would be forced to consider  $Y_\nu \sim \mathcal{O}(10^{-5})$ . A value which is obviously too small to modify the running of  $\lambda$ .

The necessity to overcome such phenomenological boredom led to the introduction of extended seesaw models with both TeV-scale right-handed neutrinos and sizable Yukawa couplings [47, 48, 49, 50, 51, 52]. The key feature of these models is that lepton number is now softly broken via the introduction of extra singlet fermions in addition to the usual right-handed neutrinos. The mass  $M_R$  can be brought down to the EW scale without neither causing troubles with low-energy neutrino phenomenology nor lowering the Yukawa coupling  $Y_\nu$ . As a byproduct of this construction, a very rich low-energy phenomenology emerges. Potentially interesting signals include, for instance, lepton flavor violating radiative decays, deviations from EW precision observables, and production at colliders of heavy Majorana fermions. Equally notable, these class of low-scale seesaw models have large sections of the parameter space capable to alter the metastability of the EW vacuum with interesting consequences for the extrapolation of the model at higher scale.

### 3.2 The inverse seesaw model

In the inverse seesaw (ISS) model the SM field content is extended to incorporate  $n_R$  right-handed neutrinos  $N_R^i$  and  $n_S$  singlet fermionic fields  $S^i$ . The corresponding Lagrangian is given by

$$\mathcal{L}_{\text{ISS}} = i\overline{N_R}\gamma^\mu(\partial_\mu N_R) + i\overline{S}\gamma^\mu(\partial_\mu S) - \left[ \overline{N_R}Y_\nu\tilde{H}^\dagger L + \overline{N_R}M_R S + \frac{1}{2}\overline{S^C}\mu_S S + h.c. \right], \quad (3.1)$$

where  $L \equiv (L^e, L^\mu, L^\tau)^T$  represents the left-handed lepton doublets with the usual contents  $L^{l=e,\mu,\tau} = (\nu_{lL}, l_L)^T$  while  $H$  is the Higgs field, with  $\tilde{H} \equiv i\sigma_2 H^*$ .  $Y_\nu$  is the  $n_R \times 3$  Yukawa matrix mediating the interactions between the SM leptons and the right-handed neutrinos while  $M_R$  and  $\mu_S$  are, respectively,  $n_R \times n_S$  and  $n_S \times n_S$  mass matrices. Both right-handed neutrinos and singlet fermions have lepton number  $\mathbb{L} = 1$ ; consequently, the mass term  $\overline{S^C}\mu_S S$  violates lepton number for two units.

Introducing the left-handed basis  $N_L \equiv (\nu_L, N_R^C, S)^T$  we have, after EW symmetry breaking, the following mass matrix

$$\mathcal{M} = \begin{pmatrix} 0 & m_D^T & 0 \\ m_D & 0 & M_R \\ 0 & M_R^T & \mu_S \end{pmatrix}, \quad (3.2)$$

with  $m_D \equiv vY_\nu/\sqrt{2}$ .

The mass matrix in eq. (3.2) can be diagonalized by means of the following unitary transformation

$$U^T \mathcal{M} U = \mathcal{M}_\Delta \Rightarrow U^\dagger (\mathcal{M}^\dagger \mathcal{M}) U = \mathcal{M}_\Delta^2, \quad N'_L = U^\dagger N_L, \quad (3.3)$$

where  $\mathcal{M}_\Delta$  is the diagonal matrix referred to the mass eigenstates  $N'_L$ . The first three eigenstates correspond to the standard light active neutrinos while the remaining  $n_R + n_S$  states are additional heavy sterile neutrinos.

Following the standard seesaw calculation and assuming the hierarchy  $M_R \gg m_D \gg \mu_S$ , it is possible to extract the effective light neutrino mass matrix

$$m_\nu \approx m_D^T (M_R^T)^{-1} \mu_S M_R^{-1} m_D . \quad (3.4)$$

In the following we consider the case  $n_R = n_S = 3$ . Moreover, without loss of generality, we take  $M_R$  to be real and diagonal. We also work in a basis in which the mass matrix of charged SM leptons is diagonal. Within this framework, in the  $\mu_S \rightarrow 0$  limit the three light neutrinos are massless while the six heavy neutrinos can be recast into three pairs of Majorana particles with three (double degenerate) masses  $M_{Ri}$ ,  $i = 1, 2, 3$ . On a general ground, from eq. (3.4) it follows that the order of magnitude of the light neutrino mass is  $m_\nu \sim \mathcal{O}(\mu_S \times m_D^2/M_R^2)$ . Assuming  $\mu_S \sim \mathcal{O}(1)$  keV, the model can accommodate sub-eV light neutrino masses with  $Y_\nu \sim \mathcal{O}(1)$  couplings and  $M_R \sim \mathcal{O}(1 - 10)$  TeV seesaw scale. These order of magnitude estimates lie at the hearth of the ISS scenario. Small values of  $\mu_S$  are expected by virtue of the 't Hooft naturalness criterion [54], since the limit  $\mu_S \rightarrow 0$  increases the symmetry of the theory. Interestingly, the keV scale nicely fits the typical mass scale characterizing warm dark matter; in the ISS models with  $n_R \neq n_S$  the spectrum – in addition to light and heavy neutrinos – also contains intermediate states with keV mass that are valuable warm dark matter candidates [55]. The estimates  $Y_\nu \sim \mathcal{O}(1)$  and  $M_R \sim \mathcal{O}(1 - 10)$  TeV represent the most relevant phenomenological properties of the ISS model since they allow for sizable (and, in principle, measurable) mixing effects between light active and heavy sterile neutrinos. This issue is particularly striking if compared with the typical high-scale characterizing the minimal type-I seesaw [43, 44, 45, 46] – that is  $M_R \sim \mathcal{O}(10^{15})$  GeV for order one Yukawa couplings – in which mixing effects, typically of order  $\mathcal{O}(m_D^2/M_R^2)$ , are negligible. As we will see in section 3.3, the occurrence of both the peculiar conditions  $Y_\nu \sim \mathcal{O}(1)$  and  $M_R \sim \mathcal{O}(1 - 10)$  TeV is of fundamental importance to determine the stability of the EW vacuum in the context of the ISS model. We will employ, as done in many phenomenological applications, the generalized Casas-Ibarra parametrization [56]

$$Y_\nu = \frac{\sqrt{2}}{v} V^* \sqrt{\hat{M}} R \sqrt{\hat{m}_\nu} U_{\text{PMNS}}^\dagger , \quad (3.5)$$

where  $\sqrt{\hat{m}_\nu}$  is the diagonal matrix defined by the square roots of the eigenvalues corresponding to the three light neutrinos,  $m_{\nu i}$  with  $i = 1, 2, 3$  hereafter, and  $\sqrt{\hat{M}}$  is the diagonal matrix containing the square roots of the eigenvalues of  $M \equiv M_R \mu_S^{-1} M_R^T$  whose diagonalization is defined by means of the transformation  $V^T M V = \hat{M}$ .  $R$  is an arbitrary  $3 \times 3$  complex orthogonal matrix parametrized by three complex angles which encodes the remaining degrees of freedom. Finally,  $U_{\text{PMNS}}$  corresponds to the unitary Pontecorvo-Maki-Nakagawa-Sakata (PMNS) leptonic mixing matrix. Assuming the standard picture with three neutrino flavors the matrix  $U_{\text{PMNS}}$  can be parametrized as follows

$$U_{\text{PMNS}} = \begin{pmatrix} c_{12}c_{13} & s_{12}c_{13} & s_{13}e^{-i\delta_{\text{CP}}} \\ -s_{12}c_{23} - c_{12}s_{13}s_{23}e^{i\delta_{\text{CP}}} & c_{12}c_{23} - s_{12}s_{13}s_{23}e^{i\delta_{\text{CP}}} & c_{13}s_{23} \\ s_{12}s_{23} - c_{12}s_{13}c_{23}e^{i\delta_{\text{CP}}} & -s_{12}s_{23} - s_{12}s_{13}c_{23}e^{i\delta_{\text{CP}}} & c_{13}c_{23} \end{pmatrix} , \quad (3.6)$$

where  $c_{ij} \equiv \cos \theta_{ij}$  and  $s_{ij} \equiv \sin \theta_{ij}$ . In addition to the Dirac CP violation phase  $\delta_{\text{CP}}$  there are also two Majorana CP violation phases (not shown in eq. (3.6)). The latter are physical only if light neutrinos are Majorana particles, otherwise they can be always rotated away from the Lagrangian in the mass basis.

In the following we omit the three phases of the PMNS matrix, since the Majorana phases are completely unknown and there are only preliminary hints about a non-zero Dirac phase.

### 3.2.1 Bounds from low-energy neutrino data

To be as close as possible to neutrino phenomenology we take into account a global analysis of neutrino oscillation data, based on the latest results of the Daya Bay [57], RENO [58, 59], T2K [60, 61] and MINOS [62, 63] experiments, which allowed to determine the oscillation parameters  $\Delta m_{21}^2$ ,  $|\Delta m_{31}^2|$  ( $|\Delta m_{32}^2|$ , depending on the ordering),  $\theta_{12}$ ,  $\theta_{23}$ ,  $\theta_{13}$  with unprecedented high precision. In this thesis, we use the latest results of the  $\mathcal{N}$ fit group [64]. As customary, we define  $\Delta m_{ij}^2 \equiv m_{\nu i}^2 - m_{\nu j}^2$ , and we adopt the convention that results for the mass squared differences are reported with respect to the one with the largest absolute value.

#### ◦ Neutrino mass squared differences

3- $\sigma$  C.L. ranges on the mass squared differences

$$\Delta m_{21}^2/10^{-5}\text{eV}^2 = (7.02 \rightarrow 8.09) , \quad \begin{cases} \Delta m_{31}^2/10^{-3}\text{eV}^2 = (2.317 \rightarrow 2.607) & \text{NO} \\ \Delta m_{32}^2/10^{-3}\text{eV}^2 = (-2.590 \rightarrow -2.307) & \text{IO} \end{cases} \quad (3.7)$$

where the first (second) possibility refers to the assumption of normal (inverted) ordering.

#### ◦ Leptonic mixing matrix

3- $\sigma$  C.L. ranges on the magnitude of the elements of the leptonic mixing matrix in eq. (3.6)

$$\sin^2 \theta_{12} = (0.270 \rightarrow 0.344) , \quad (3.8)$$

$$\sin^2 \theta_{23} = \begin{cases} (0.382 \rightarrow 0.643) \\ (0.389 \rightarrow 0.644) \end{cases} , \quad \sin^2 \theta_{13} = \begin{cases} (0.0186 \rightarrow 0.0250) & \text{NO} \\ (0.0188 \rightarrow 0.0251) & \text{IO} \end{cases} \quad (3.9)$$

#### ◦ Unitarity

In the basis where the charged lepton mass matrix is diagonal, the leptonic mixing matrix in the ISS model is given by the rectangular  $3 \times 9$  sub-matrix corresponding to the first three rows of the matrix  $U$  defined in eq. (3.3), with the  $3 \times 3$  block corresponding to the (non-unitary)  $\tilde{U}_{\text{PMNS}}$ . Bounds on the non-unitarity of the matrix  $\tilde{U}_{\text{PMNS}}$  were derived in [65, 66, 67] using an effective field theory approach. These bounds can be recast as follows<sup>1</sup>

$$\epsilon_{\alpha\beta} \equiv \left| \sum_{i=4}^9 U_{\alpha i} U_{\beta i}^* \right| = \left| \delta_{\alpha\beta} - (\tilde{U}_{\text{PMNS}} \tilde{U}_{\text{PMNS}}^\dagger)_{\alpha\beta} \right| , \quad (3.10)$$

$$\left| \tilde{U}_{\text{PMNS}} \tilde{U}_{\text{PMNS}}^\dagger \right| = \begin{pmatrix} (0.9979 \rightarrow 0.9998) & < 10^{-5} & < 0.0021 \\ < 10^{-5} & (0.9996 \rightarrow 1.0) & < 0.0008 \\ < 0.0021 & < 0.0008 & (0.9947 \rightarrow 1.0) \end{pmatrix} .$$

<sup>1</sup>Strictly speaking, the bounds in eq. (3.10) are valid only if the masses of the sterile neutrinos lie above the EW scale (where they can be safely integrated out). This is always the case in our numerical analysis (see section 3.2.2).

◦ **Additional constraints**

The absolute values of neutrino masses  $m_{\nu i}$  are unknown. Cosmology sets the most stringent upper bounds using data from the Cosmic Microwave Background (CMB) radiation, supernovae and galaxy clustering. Assuming the validity of the  $\Lambda$ CDM model [68], the Planck collaboration placed the upper bound  $\sum_i m_{\nu i} < 0.66$  eV at 95% C.L. [68]; this bound becomes even more stringent adding data on the Baryon Acoustic Oscillation,  $\sum_i m_{\nu i} < 0.23$  eV at 95% C.L. [68]. In our analysis we scan over the interval  $10^{-4}$  eV  $\leq m_{\nu 1} \leq 10^{-1}$  eV for the mass of the lightest neutrino.

### 3.2.2 Relevant parameter space and setup for the numerical analysis

#### Target observables

The presence of sterile neutrino states affects the SM charge current interaction via the mixing matrix in eq. (3.3). Going from gauge to mass eigenstates we have

$$\mathcal{L}_{\text{CC}} = -\frac{g_2}{\sqrt{2}} \sum_{l=e,\mu,\tau} \bar{l}_L \gamma^\mu W_\mu^- \nu_{lL} + h.c. = -\frac{g_2}{\sqrt{2}} \sum_{l=e,\mu,\tau} \sum_{i=1}^9 \bar{l}_L \gamma^\mu W_\mu^- U_{li} N_L^i + h.c. , \quad (3.11)$$

where  $g_2$  is the weak coupling constant. By means of these interactions, and depending on their masses and mixings with light active neutrinos, the presence of new sterile states can relevantly affect numerous observables, like for instance leptonic and semi-leptonic decays (with a special focus on flavor violating processes) [69, 70, 71, 72, 73, 74, 75, 76, 77, 78], invisible  $Z$  boson decay width [79], Higgs boson decays [80, 81, 82, 83], direct production in meson decay [84].

In order to investigate the stability of the EW vacuum in a region of the parameter space of particular interest for present and future experimental prospects, we focus on the lepton flavor violating process  $\mu \rightarrow e\gamma$  and the neutrino-less double beta decay ( $0\nu 2\beta$  hereafter).

As far as the radiative  $\mu \rightarrow e\gamma$  decay is concerned, the rate induced by the presence of sterile neutrinos is given by [85, 86]

$$\text{Br}(\mu \rightarrow e\gamma) = \frac{3\alpha}{32\pi} \left| \sum_{i=1}^9 U_{\mu i}^* U_{ei} \mathcal{G} \left( \frac{m_{\nu i}^2}{M_W^2} \right) \right|^2 , \quad (3.12)$$

where  $\alpha$  is the electromagnetic fine structure constant and  $M_W$  the  $W$  mass. The loop function is given by  $\mathcal{G}(x) \equiv (10 - 43x + 78x^2 - 49x^3 + 4x^4 + 18x^3 \ln x) / [3(-1+x)^4]$ . The present experimental upper bound, reported by the MEG collaboration, is  $\text{Br}(\mu \rightarrow e\gamma) < 5.7 \times 10^{-13}$  at 90% C.L. [87].

The amplitude of the  $0\nu 2\beta$  process is proportional to the so-called effective neutrino mass,  $m_{\text{eff}}^{\nu_e}$ . Current experiments (among others, GERDA [88], EXO-200 [89, 90], and KamLAND-ZEN [91]), put an upper limit in the range  $|m_{\text{eff}}^{\nu_e}| \lesssim 140 - 700$  MeV. In the presence of sterile state the effective neutrino mass is given by [92]

$$\begin{aligned} m_{\text{eff}}^{\nu_e} &\simeq \sum_{i=1}^9 U_{ei}^2 p^2 \frac{m_{\nu i}}{p^2 - m_{\nu i}^2} \simeq \sum_{i=1}^3 U_{ei}^2 m_{\nu i} + p^2 \left( U_{e4}^2 \frac{m_{\nu 4}}{p^2 - m_{\nu 4}^2} + U_{e5}^2 \frac{m_{\nu 5}}{p^2 - m_{\nu 5}^2} \right. \\ &+ \left. U_{e6}^2 \frac{m_{\nu 6}}{p^2 - m_{\nu 6}^2} + U_{e7}^2 \frac{m_{\nu 7}}{p^2 - m_{\nu 7}^2} + U_{e8}^2 \frac{m_{\nu 8}}{p^2 - m_{\nu 8}^2} + U_{e9}^2 \frac{m_{\nu 9}}{p^2 - m_{\nu 9}^2} \right) , \end{aligned} \quad (3.13)$$

where  $p^2 \simeq -(125 \text{ MeV})^2$  is the momentum of the virtual neutrino. Notice that, since we are considering the regime  $m_{\nu_{i=4,\dots,9}}^2 \gg p^2$ , heavy neutrinos decouple in eq. (3.13) and the dominant contribution to  $m_{\text{eff}}^{\nu_e}$  comes from the light active neutrinos.

### Strategy and first numerical results

We now perform a scan over the parameter space of the model. Our procedure goes as follows. First, we randomly generate *i*) the light neutrino masses  $m_{\nu_{i=1,2,3}}$  and the leptonic mixing angles  $\theta_{12}, \theta_{23}, \theta_{13}$  according to the corresponding  $1-\sigma$  intervals allowed by the analysis of present experimental data, *ii*) the entries of the matrices  $M_R$  and  $\mu_S$  in the intervals  $10^2 \text{ GeV} \leq M_{Ri} \leq 10^2 \text{ TeV}$ ,  $10^{-1} \text{ keV} \leq (\mu_S)_{ij} \leq 10^2 \text{ keV}$  and *iii*) the complex angles defining the arbitrary matrix  $R$  in the interval  $[0, 2\pi]$ . Second, we reconstruct the full Yukawa matrix  $Y_\nu$  using the generalized Casas-Ibarra parametrization in eq. (3.5). Finally, plugging back  $M_R$ ,  $\mu_S$  and  $Y_\nu$  into eq. (3.2), we diagonalize the mass matrix  $\mathcal{M}$  in order to find the full  $9 \times 9$  mixing matrix  $U$ . The phases of the mixing matrix are fixed using eq. (3.3), by means of the condition  $m_{\nu_i} \geq 0$  for all  $i$ . As a consistency test, for each point of the scan we check that the mass matrix  $\mathcal{M}$ , randomly generated as discussed above, correctly reproduces after diagonalization light neutrino masses and mixing angles in agreement with the bounds presented. Equipped by these results we can easily compute the branching ratio  $\text{Br}(\mu \rightarrow e\gamma)$  in eq. (3.12) and the effective neutrino mass in eq. (3.13). We show our results in fig. 3.1 for the normal ordering and in fig. 3.2 for the inverted ordering. In the upper (lower) panels of both figures we show the branching ratio  $\text{Br}(\mu \rightarrow e\gamma)$  (the effective neutrino mass  $m_{\text{eff}}^{\nu_e}$ ) as a function of the lightest heavy neutrino mass  $m_{\nu_4}$  (plot on the left) and the trace of the Yukawa couplings  $\text{Tr}(Y_\nu^\dagger Y_\nu)$  (plot on the right). Few comments are in order.

1. Normal and inverted ordering produce very similar distributions considering the radiative decay  $\text{Br}(\mu \rightarrow e\gamma)$ . This is caused by the well-known fact that the contribution of light active neutrinos is strongly suppressed by the extremely small value of light neutrino masses. In the ISS model a non-zero contribution to  $\text{Br}(\mu \rightarrow e\gamma)$  is entirely generated by the additional heavy neutrinos, and controlled by the mixings  $U_{\mu i}, U_{ei} \sim m_D/M_R$  (see eq. (3.23) in section 3.3.2). We notice that in our scan we can obtain a signal close to the present experimental bound even considering  $m_{\nu_4}$  as large as 10 TeV and  $\text{Tr}(Y_\nu^\dagger Y_\nu)$  as small as  $10^{-3}$ . For completeness we show in the left panel of fig. 3.3 the result of our numerical scan in the plane  $[\text{Tr}(Y_\nu^\dagger Y_\nu), m_{\nu_4}]$ . We mark in dark cyan points with  $\text{Br}(\mu \rightarrow e\gamma) \geq 10^{-13}$ . Points with large Yukawa couplings (e.g.  $\text{Tr}(Y_\nu^\dagger Y_\nu) \gtrsim 0.5$ ) and sizable  $\mu \rightarrow e\gamma$  rate are generated in the whole interval of analyzed masses for the right-handed neutrinos.
2. Normal and inverted ordering produce completely different distributions considering the effective neutrino mass  $m_{\text{eff}}^{\nu_e}$ . In this case the contributions of additional heavy neutrinos decouple since their masses are much larger than the typical momentum scale  $p^2 \simeq -(125 \text{ MeV})^2$ . Therefore, in our numerical scan the ISS model resembles the typical scenario with only three light active neutrinos. The situation is well represented by the right panel of fig. 3.3 where we show the effective neutrino mass for the normal and inverted ordering as a function of minimal neutrino mass. The normal ordering is suppressed since the largest neutrino mass is multiplied by the small value of  $s_{13}$ . However, in both cases the effective neutrino mass is close to the future sensitivity of the EXO-200

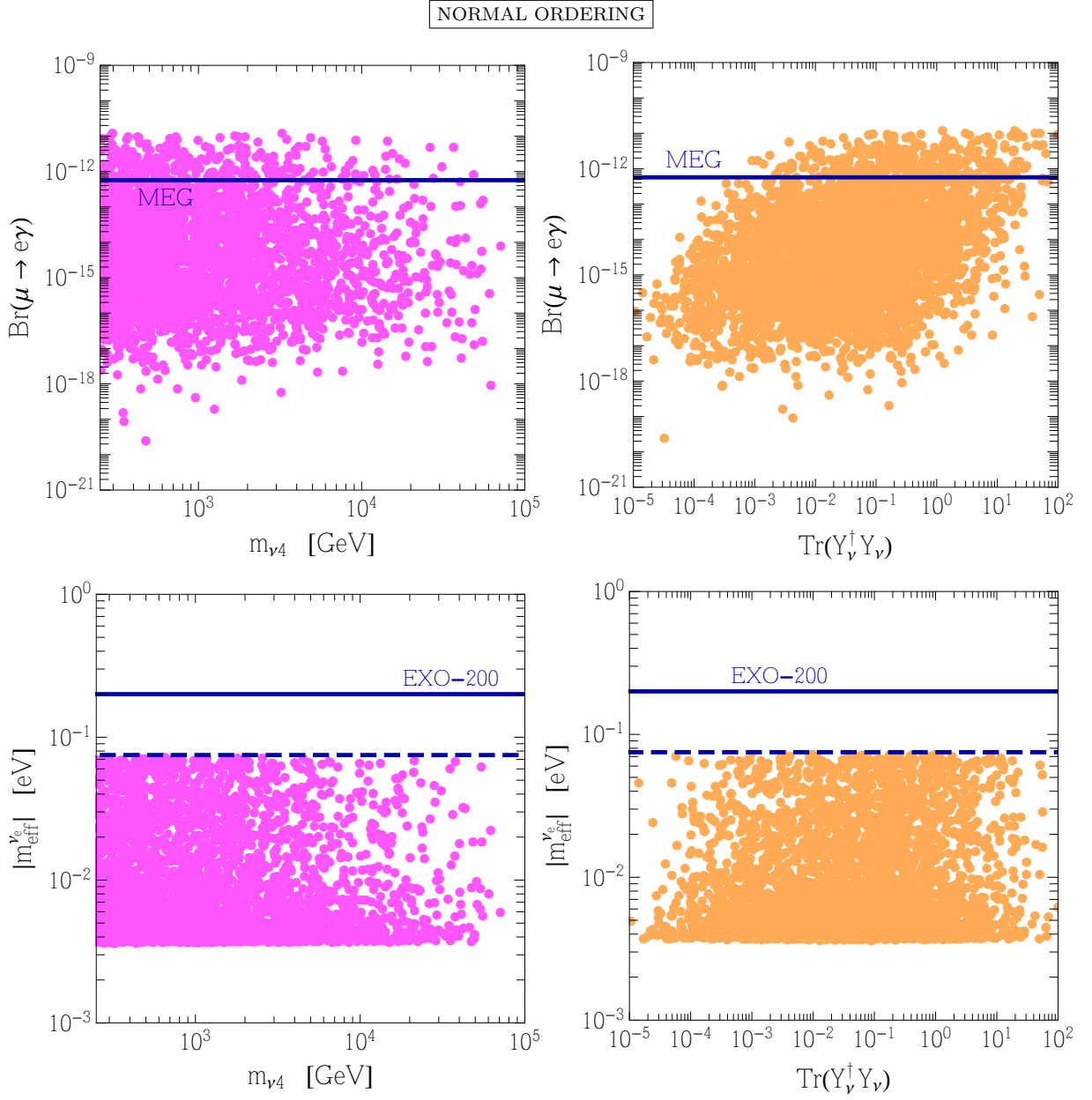


Figure 3.1: Upper panel. Branching ratio for the decay process  $\mu \rightarrow e\gamma$  as a function of the mass of the lightest sterile neutrino (left panel) and the trace of the Yukawa couplings  $\text{Tr}(Y_\nu^\dagger Y_\nu)$  (right panel). The blue horizontal line represents the upper bound set by the MEG collaboration [87]. Lower panel. Effective neutrino mass as a function of the mass of the lightest sterile neutrino (left panel) and the trace of the Yukawa couplings  $\text{Tr}(Y_\nu^\dagger Y_\nu)$  (right panel). The blue solid (dashed) line represents the upper bound (future sensitivity) of the EXO-200 experiment [90]. All points comply with the bounds discussed in section 3.2.1.

experiment.

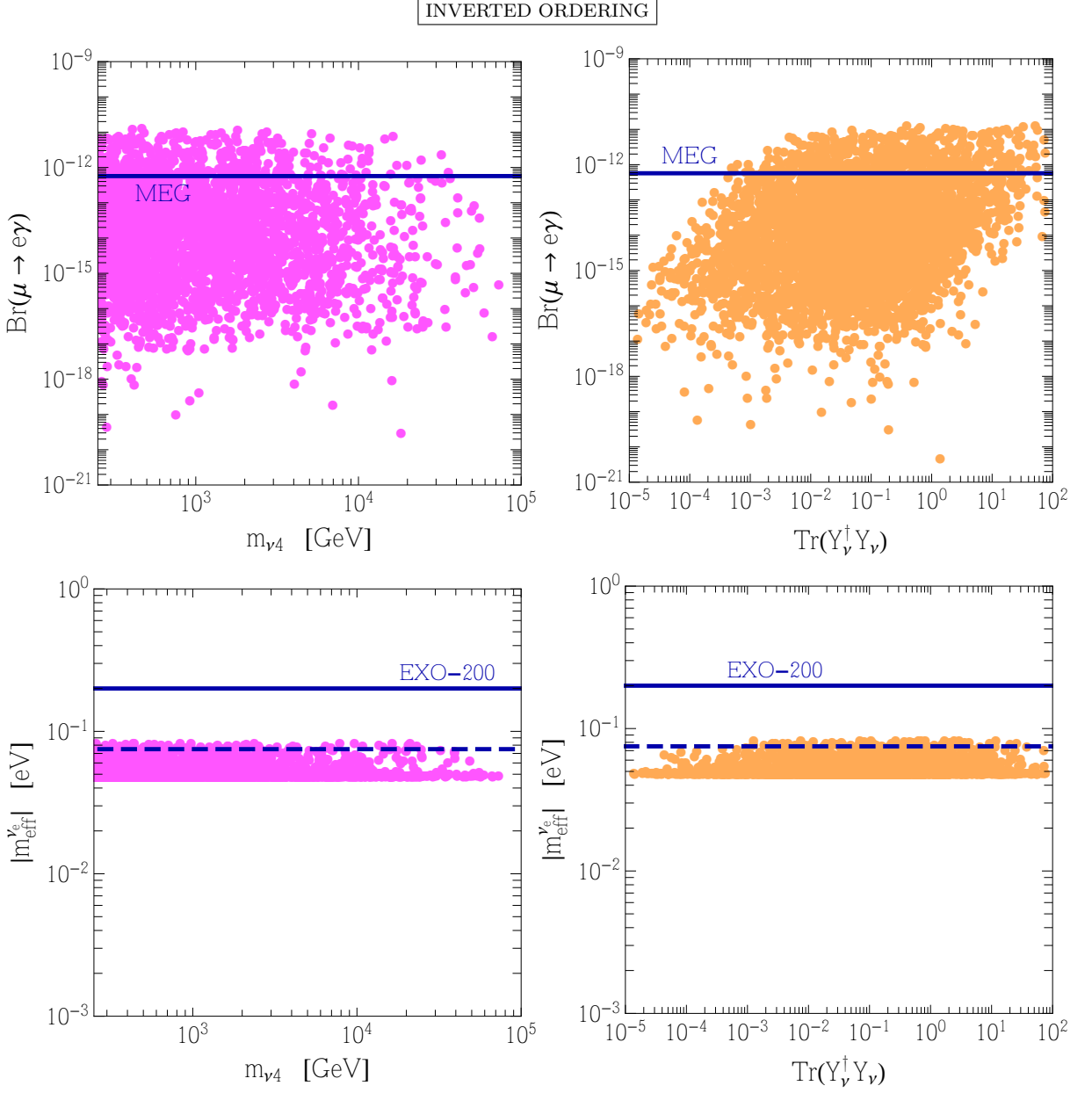


Figure 3.2: Same as in fig. 3.1, but considering the inverted ordering.

### Additional remarks

Let us close this section summarizing further predictions and constraints on the inverse seesaw scenario.

*Collider searches at the LHC.* At the LHC right-handed neutrinos with a mass not far above or below the Higgs mass and with a sizable Yukawa coupling  $Y_\nu \gtrsim \mathcal{O}(10^{-2})$  affect the Higgs decay  $h \rightarrow \bar{l}l\nu\bar{\nu}$  (see [80] for a recent analysis). Present bounds hold in the range  $60 \leq M_R \leq 200$  GeV with  $10^{-2} \leq Y_\nu \leq 2$ .<sup>2</sup>

<sup>2</sup>These bound were obtained in [80] considering a simplified setup with only one light flavor of heavy neutrinos. Consequently, here  $Y_\nu$  indicates the corresponding Yukawa coupling to the Higgs doublet.

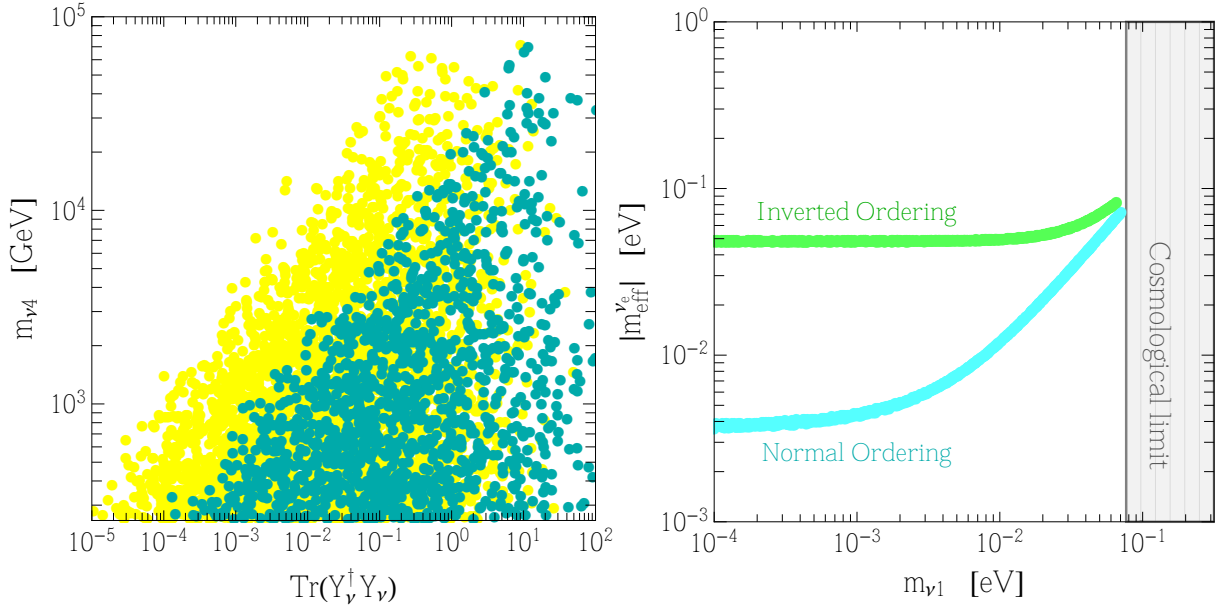


Figure 3.3: *Left panel.* Distribution of our numerical scan in the plane  $[\text{Tr}(Y_\nu^\dagger Y_\nu), m_{\nu 4}]$  considering the normal ordering (the inverted ordering gives an analogue result). All points comply with the bounds discussed in section 3.2.1. Points with  $\text{Br}(\mu \rightarrow e\gamma) \geq 10^{-13}$  are marked in dark cyan. On the qualitative level, the plot shows that Yukawas  $\text{Tr}(Y_\nu^\dagger Y_\nu) \gtrsim 0.5$  arise in the whole range of analyzed masses for the right-handed neutrinos. *Right panel.* Effective neutrino mass as a function of the lightest neutrino mass considering both normal and inverted ordering. Our scan correctly reproduces, as expected if the heavy neutrinos decouple if compared with the typical virtual momentum  $p^2 \simeq -(125 \text{ MeV})^2$ , the well-known result characterizing the presence of only three light active neutrinos.

Furthermore, the CMS collaboration placed upper limits on the active-sterile neutrino mixings in the same mass range for  $M_R$  considering direct production of heavy neutrinos [93, 94].<sup>3</sup> These values of masses and couplings may have an impact on the stability of the EW vacuum, thus providing an additional motivation for the analysis that we shall perform in the next section.

*Fit of LEP data via oblique parameters.* The fit of LEP data still provides today an important constraint on beyond the SM physics. The presence of additional sterile neutrinos modifies the oblique radiative corrections [96, 97, 98, 99, 100, 101, 102, 103]. In [79] it was shown that right-handed neutrino masses of the order  $M_{Ri} \sim \mathcal{O}(10)$  TeV, together with violation of unitarity of the order  $\epsilon_{\alpha\beta} \sim 10^{-3} \div 10^{-6}$ , can improve the fit of LEP data with respect to the SM.

*Leptogenesis.* In the inverse seesaw scenario the decay of (nearly degenerate) heavy Majorana neutrinos can realize the so-called resonant leptogenesis [104]. Remarkably, resonant leptogenesis can be realized with heavy Majorana neutrinos as light as 1 TeV [105] (in contrast with the usual thermal leptogenesis, realized in the type-I seesaw, in which  $M_R \gtrsim 10^9$  GeV [106]).

<sup>3</sup>See [95] for prospects at future lepton colliders.

*Naturalness.* On a general ground, whenever a threshold with particles of mass  $M$  coupled to the Higgs with strength  $\xi$  is present, quantum corrections generate a contribution  $\delta m_H^2 \approx \xi^2 M^2 / 16\pi^2$  to the renormalized Higgs boson mass. If  $\delta m_H^2 \gg v^2$ , an unnatural cancellation between  $\delta m_H^2$  and the bare Higgs mass is required in order to reproduce the observed value of the Higgs boson mass. The condition  $\delta m_H^2 \lesssim v^2$  can be used as a criterion to construct natural model of new physics [107, 108]. In the context of inverse seesaw models, the scale  $M$  is the mass of right-handed heavy neutrinos  $M_R$ , and the coupling  $\xi$  is the Yukawa coupling  $Y_\nu$ . TeV-scale values of  $M_R$  and  $\mathcal{O}(1)$  Yukawa couplings satisfy the naturalness condition.

To sum up, the presence of heavy neutrinos with a mass not far above the EW scale and a sizable Yukawa coupling with the Higgs boson has extremely rich phenomenological consequences. Motivated by such results, we are now in the position to tackle the second part of the analysis in which we aim to investigate the impact of heavy neutrinos on the stability of the EW vacuum.

### 3.3 Stability of the electroweak vacuum and low-scale seesaw

The key ingredients for the study of the stability of the EW potential have been presented in chapter 2 and will now be adapted to our investigation. The instability scale  $\Lambda$  is identified with the Higgs field value for which the potential becomes smaller than its value at the EW minimum. If such scale does not exist we will declare the vacuum as *absolute stable*, otherwise the Higgs vacuum is not the global minimum, and the tunnelling may occur. The decay probability is computed from the bounce solution (see chapter 2 for details) and the comparison with the universe age defines the condition for a *metastable* vacuum. This can be translated into a lower bound on the Higgs effective quartic coupling  $\lambda_{\text{eff}}$ , reaching negative values, that at leading order reads as

$$|\lambda_{\text{eff}}(\mu)| > \frac{8\pi^2}{3} \frac{1}{\log(\tau\mu)}, \quad (3.14)$$

(where, as always,  $\tau$  is the age of the Universe  $\tau = 4.35 \times 10^{17}$  sec and  $\mu$  is the renormalization scale of the RG running). The metastable position in the phase space diagram [26] and fig. 2.11 can then be drastically affected by the inclusion of extra fermionic degrees of freedom, as right-handed neutrinos in seesaw extensions, driving the model to an unstable phase. Therefore, by requiring the metastability of the EW vacuum, together with the perturbativity of the gauge, scalar and Yukawa couplings up to the Planck mass, we are able to constrain the parameter space. In the following sections we will highlight the theoretical tools needed in our stability analysis, with some inevitable redundancies with chapter 2, stressing the peculiar adjustments needed to be done in order to adapt that SM oriented analysis to the requirements of this model.

#### 3.3.1 The Higgs effective quartic coupling

From a preliminary analysis one can show that also in this case we can use the high-energy approximation

$$V_{\text{eff}}(\phi, t) \approx \frac{\lambda_{\text{eff}}(\phi, t)}{4} \phi^4, \quad (3.15)$$

due to the fact that the vacuum instability appears at a scale much bigger than the EW minimum. The effective quartic coupling  $\lambda_{\text{eff}}$  is extracted from the RG-improved effective potential at two-loop order in the SM [109] and at one-loop for the right-handed neutrino corrections, computed in the  $\overline{\text{MS}}$  renormalization scheme and in the Landau gauge. The effective quartic coupling at one-loop order in the SM [110] is

$$\lambda_{\text{eff}}(\phi, t) \approx e^{4\Gamma(t)} \left\{ \lambda(t) + \frac{1}{16\pi^2} \sum_{p=W, Z, h, \chi, t} N_p \kappa_p^2(t) \left[ \ln \frac{\kappa_p(t) e^{2\Gamma(t)} \phi^2}{\mu(t)^2} - C_p \right] \right\}, \quad (3.16)$$

where the  $p$ -coefficients are summarized in table 3.1 and  $\Gamma(t)$  is defined as

$$\Gamma(t) = \int_0^t dt' \gamma(t'), \quad (3.17)$$

with  $\gamma$  the anomalous dimension of the Higgs field.

	$t$	$W^\pm$	$Z$	$h$	$\chi^\pm$	$\chi^0$
$N_p$	-12	6	3	1	2	1
$C_p$	3/2	5/6	5/6	3/2	3/2	3/2
$\kappa_p$	$y_t^2/2$	$g_2^2/4$	$(g_2^2 + g_Y^2)/4$	$3\lambda$	$\lambda$	$\lambda$

Table 3.1: SM  $p$ -coefficients entering in eq. (3.16).

As expected (see chapter 1) the contribution of the heavy neutrinos to the RG-improved effective potential has the form

$$\Delta V_{\text{eff}}^\nu(\phi, t) = -\frac{1}{32\pi^2} \sum_{i=1,2,3} \theta_{\nu i}(t) 2\mathcal{M}_{\nu i}^4(\phi, t) \left[ \ln \frac{\mathcal{M}_{\nu i}^2(\phi, t)}{\mu(t)^2} - \frac{3}{2} \right], \quad (3.18)$$

where  $\mathcal{M}_{\nu i}(\phi, t)$  are the three (double degenerate) non-zero eigenvalues of the  $9 \times 9$  mass matrix

$$\mathcal{M}_\phi(t) = \begin{pmatrix} 0 & Y_\nu(t)^T \phi(t)/\sqrt{2} & 0 \\ Y_\nu(t) \phi(t)/\sqrt{2} & 0 & \hat{M}_{Ri} \\ 0 & \hat{M}_{Ri} & 0 \end{pmatrix}, \quad (3.19)$$

with  $\hat{M}_{Ri} \equiv \text{diag}(M_{R1}, M_{R2}, M_{R3})$  and  $\phi(t) = e^{\Gamma(t)} \phi$ , meanwhile  $\theta_{\nu i}(t) = \theta(t - \ln M_{Ri}/\mu_0)$  take in account the threshold scale [111]. Compared with eq. (3.2), we are considering the  $\mu_S \rightarrow 0$  limit in which the three light neutrinos are massless.

The factor of two in eq. (3.18) comes from the fact that each non-zero eigenvalue is double degenerate.

As we know the RG running parameter  $t$  must be chosen in such a way that the convergence of perturbation theory – otherwise spoiled by the presence of large logs – is improved. With no surprise we follow the prescription  $\mu(t) = \phi$ .

The contribution of heavy neutrinos to the effective potential produces two distinctive effects on the RG-evolution of the effective quartic coupling in eq. (3.16) which ask for the introduction of thresholds in the spirit of section 1.4.1.

- Above each threshold  $M_{Ri}$  and at high values of renormalization scale  $\mu(t) \gg M_{Ri}$  it contributes explicitly to  $\lambda_{\text{eff}}$  introducing the correction

$$\lambda_{\text{eff}}^{\nu i}(\phi, t) = -\frac{1}{16\pi^2} 4\kappa_{\nu i}^4(t) \left[ \ln \frac{\kappa_{\nu i}^2(t) e^{2\Gamma(t)} \phi^2}{\mu(t)^2} - \frac{3}{2} \right], \quad (3.20)$$

where  $\kappa_{\nu i}(t)$  is the coefficient of the  $\phi$ -dependent part of  $\mathcal{M}_{\nu i}(\phi, t)$ .

- Below each threshold  $M_{Ri}$  the corresponding heavy neutrinos are integrated out. The matching produces the threshold correction to the effective potential

$$\Delta V_{\text{th}}^{\nu i}(\phi, t) = -\frac{1}{32\pi^2} 2\mathcal{M}_{\nu i}^4(\phi, t) \left[ \ln \frac{\mathcal{M}_{\nu i}^2(\phi, t)}{M_{Ri}^2} - \frac{3}{2} \right], \quad (3.21)$$

which translates into a threshold correction  $\Delta\lambda_{\text{th}}^{\nu i}$  to the Higgs quartic coupling at the  $M_{Ri}$  mass scale which can be extracted from the  $\phi^4$  term of eq. 3.21 and it is explicitly given by

$$\Delta\lambda_{\text{th}}^{\nu i}(t) = \frac{1}{6} \left. \frac{d\Delta V_{\text{th}}^{\nu i}(\phi, t)}{d\phi} \right|_{\phi=0}. \quad (3.22)$$

### 3.3.2 The Matching Conditions in the SM plus low-scale seesaw

The RG equations employed in this thesis are computed in the  $\overline{\text{MS}}$  renormalization scheme and must be equipped with suitable initial conditions for the running parameters evaluated in the same scheme. The main features of the procedure have been illustrated in section 2.3 and here we pause to extend those results in light of the introduction of new degrees of freedom. The details of the strategy to match at the highest precision the SM sector can be found in [26] where the SM two-loop (NNLO) corrections to the matching conditions have been discussed. In particular, in [26] a complete two-loop analysis has been performed in the EW sector and the N3LO (three-loop) pure QCD effect has been included in the matching of the top Yukawa coupling and the strong coupling constant. The running of the latter from  $M_Z$  to  $M_t$ , which is the starting scale of our stability analysis, has been performed including the QCD four-loop  $\beta$  function. In low-scale seesaw extensions, the right-handed neutrino corrections to the matching conditions can be important and must be taken into account. In our analysis we have considered all the SM results given in [26], supplemented by new physics contributions computed at one-loop order from the Lagrangian in eq. (3.1). In particular, the additional neutrinos introduce corrections to the masses of the gauge bosons  $M_Z$ ,  $M_W$ , the Higgs  $M_h$ , the quark top  $M_t$  and to the muon decay, from which the Fermi constant  $G_\mu$  is extracted. These corrections depend on the masses of the heavy neutrinos, their interactions with the SM fields mediated by the Yukawa couplings  $Y_\nu$  (obtained from the parametrization in eq. (3.5)), and the full  $9 \times 9$  mixing matrix  $U$ . Due to the mass hierarchy  $M_R \gg m_D$ , and to the smallness of the light neutrino masses – which can be safely neglected in the computation of the matching conditions at the EW scale – the mixing matrix  $U$  can be expanded in the ratio  $m_D/M_R$ , with  $\mu_S \rightarrow 0$ , as

$$U = \begin{pmatrix} 1 & \frac{1}{\sqrt{2}} m_D^\dagger M_R^{-1} & \frac{i}{\sqrt{2}} m_D^\dagger M_R^{-1} \\ 0 & \frac{1}{\sqrt{2}} & -\frac{i}{\sqrt{2}} \\ -M_R^{-1} m_D & \frac{1}{\sqrt{2}} & \frac{i}{\sqrt{2}} \end{pmatrix} + \mathcal{O}\left(\frac{m_D^2}{M_R^2}\right). \quad (3.23)$$

Notice that the PMNS block has been set to the unit matrix, consistently with the approximation  $m_{\nu i} \simeq 0$ .

Moreover, we have verified the Appelquist-Carazzone theorem in the new physics sector. In particular, we have checked the decoupling of right-handed neutrino contributions from the matching conditions in the limit of large Majorana masses. This has to be expected since these masses are not generated by spontaneous symmetry breaking of the Higgs field.

Concerning the matching conditions of the Yukawa matrix  $Y_\nu$ , computing perturbative corrections to the matching conditions at the EW scale will not considerably improve the precision on the determination of  $Y_\nu$  in the  $\overline{\text{MS}}$  scheme (since in any case  $Y_\nu$  turns out to be related to unknown parameters by means of eq. (3.5)). Therefore, for the sake of simplicity, we decided to match the  $\overline{\text{MS}}$  Yukawa matrix  $Y_\nu$  to its OS version at the tree-level, namely  $Y_\nu(M_t) \simeq Y_\nu$ .

### 3.3.3 The renormalization group equations

All the dimensionless couplings  $(\lambda, y_t, g_i, Y_\nu)$  are evolved from the top-mass scale,  $M_t$ , up to the Planck scale using the three-loop (NNLO) RG equations for the SM parameters and the two-loop (NLO)  $\beta$  functions for the Yukawa matrix  $Y_\nu$ . Here  $g_i$  stands for the three gauge coupling constants and we have retained only the top-quark contribution in the SM Yukawa sector. The system of coupled RG equations is then given by

$$\frac{d\lambda(t)}{dt} = \beta_\lambda(\lambda, y_t, g_i, Y_\nu), \quad (3.24)$$

$$\frac{dy_t(t)}{dt} = \beta_{y_t}(\lambda, y_t, g_i, Y_\nu), \quad (3.25)$$

$$\frac{dg_i(t)}{dt} = \beta_{g_i}(\lambda, y_t, g_i, Y_\nu), \quad (3.26)$$

$$\frac{dY_\nu(t)}{dt} = \beta_{Y_\nu}(\lambda, y_t, g_i, Y_\nu), \quad (3.27)$$

where the  $\beta$  functions are computed in perturbation theory in the  $\overline{\text{MS}}$  renormalization scheme. Due to their lengthy expressions, we present only the one-loop corrections to the r.h.s. of eqs. (3.24–3.27), namely

$$\begin{aligned} \beta_\lambda &= \kappa \left[ 24\lambda^2 + \lambda \left( 12y_t^2 + 4\text{Tr}(Y_\nu^\dagger Y_\nu) - \frac{9}{5}g_1^2 - 9g_2^2 \right) - 6y_t^4 - 2\text{Tr}(Y_\nu^\dagger Y_\nu)^2 \right. \\ &\quad \left. + \frac{27}{200}g_1^4 + \frac{9}{8}g_2^4 + \frac{9}{20}g_1^2 g_2^2 \right], \end{aligned} \quad (3.28)$$

$$\beta_{y_t} = \kappa \left[ -\frac{17}{20}g_1^2 - \frac{9}{4}g_2^2 - 8g_3^2 + \frac{3}{2}y_t^2 + \text{Tr}(Y_\nu^\dagger Y_\nu) \right] y_t, \quad (3.29)$$

$$\beta_{g_1} = \kappa \frac{41}{10}g_1^3, \quad \beta_{g_2} = -\kappa \frac{19}{6}g_2^3, \quad \beta_{g_3} = -\kappa 7g_3^3, \quad (3.30)$$

$$\beta_{Y_\nu} = \kappa \left[ \left( -\frac{9}{20}g_1^2 - \frac{9}{4}g_2^2 + 3y_t^2 + \text{Tr}(Y_\nu^\dagger Y_\nu) \right) Y_\nu + \frac{3}{2}Y_\nu Y_\nu^\dagger Y_\nu \right], \quad (3.31)$$

where  $\kappa = 1/(16\pi^2)$  and the Abelian gauge coupling is given in the GUT normalization  $g_1 = \sqrt{5/3}g$ . Notice that the RG equations given above are defined for a renormalization scale  $\mu$  bigger than any particle mass of the model. For lower scales, heavy degrees of freedom are integrated out and the corresponding coupling must be removed by hand from the  $\beta$  functions. Indeed, in the  $\overline{\text{MS}}$  renormalization scheme the decoupling

of heavy degrees of freedom is not automatic and has to be explicitly implemented at the different particle thresholds.

As far as the vacuum stability is concerned, the right-handed neutrinos behave like the top-quark and drive  $\lambda$  to negative values faster than the SM case. This is clear from eq. (3.28). On the other hand, their impact on the top Yukawa coupling – see eq. (3.29) – is to increase  $y_t$  all along the RG evolution. Actually, this is another source of vacuum destabilization with respect to the SM picture, because a bigger value of  $y_t$  has a bigger decreasing effect on the Higgs quartic coupling. Nevertheless, the overall behavior of the top-quark Yukawa coupling is dictated by the large and negative QCD corrections which lead to a decreasing  $y_t$ . These features can be easily deduced from fig. 3.4, left panel, where the running of the SM couplings is depicted. Here solid lines represent the evolution in the seesaw extended scenario, while dashed curves correspond to the pure SM.

Contrary to the top Yukawa case, the QCD contributions are obviously absent – at least in the leading one-loop approximation – from the evolution of  $Y_\nu$ , and the  $\text{Tr}(Y_\nu^\dagger Y_\nu)$  term, which affects  $\beta_\lambda$  e  $\beta_{y_t}$ , is always increasing. This feature, shown in the right panel of fig. 3.4, has a negative impact both on the vacuum stability and on the perturbativity of  $Y_\nu$  which can be violated, if  $|Y_{\nu ij}| > \sqrt{4\pi}$ , during the RG evolution for sufficiently big values of the Yukawa coupling at the EW scale. In the same figure the decoupling of the heavy right-handed neutrinos below their mass thresholds is also manifest. Indeed, for  $\mu \ll M_{Ri}$ , the  $N_{Ri}^i$  neutrino is integrated out and does not contribute to the RG running: the corresponding row in the Yukawa matrix  $Y_\nu$  is frozen, and enters in the  $\beta$  functions only above the threshold scale  $M_{Ri}$  as shown in eq. (3.32) where we mark with a generic  $\times$  non-zero entries for the Yukawa matrix  $Y_\nu$ .

$$\begin{array}{ccccccc}
 & \text{SM} & & \text{EFT}_1 & & \text{EFT}_2 & & \text{Full theory} \\
 \hline
 Y_\nu = & \begin{pmatrix} 0 & 0 & 0 \\ 0 & 0 & 0 \\ 0 & 0 & 0 \end{pmatrix} & \longrightarrow & \begin{pmatrix} \times & \times & \times \\ 0 & 0 & 0 \\ 0 & 0 & 0 \end{pmatrix} & \longrightarrow & \begin{pmatrix} \times & \times & \times \\ \times & \times & \times \\ 0 & 0 & 0 \end{pmatrix} & \longrightarrow & \begin{pmatrix} \times & \times & \times \\ \times & \times & \times \\ \times & \times & \times \end{pmatrix} \\
 & & & M_{R1} & & M_{R2} & & M_{R3} \\
 & & & \text{threshold} & & \text{threshold} & & \text{threshold}
 \end{array} \tag{3.32}$$

Finally, we show in fig. 3.5 the evolution of the effective quartic coupling  $\lambda_{\text{eff}}$  in two different scenarios. In the left panel the inverse seesaw is realized with  $\text{Tr}(Y_\nu^\dagger Y_\nu) \simeq 0.36$ , while in the right panel the Yukawa matrix is such that  $\text{Tr}(Y_\nu^\dagger Y_\nu) \simeq 0.6$ . In the latter case the effects of  $Y_\nu$ , which affects the RG running above the threshold scales, are quite large and  $\lambda_{\text{eff}}$  is driven outside the metastability region below the Planck scale.

### 3.4 Comments and conclusions

To summarize the results let briefly remind our main strategy. The Yukawa matrices generated following the prescription outlined in section 3.2.2 enter as initial conditions, together with all the other SM external parameters, in the solution of the RGEs in eqs. (3.24–3.27). From the effective potential, improved by the running couplings previously computed, we extract the Higgs effective quartic coupling  $\lambda_{\text{eff}}$  in eq. (3.16).

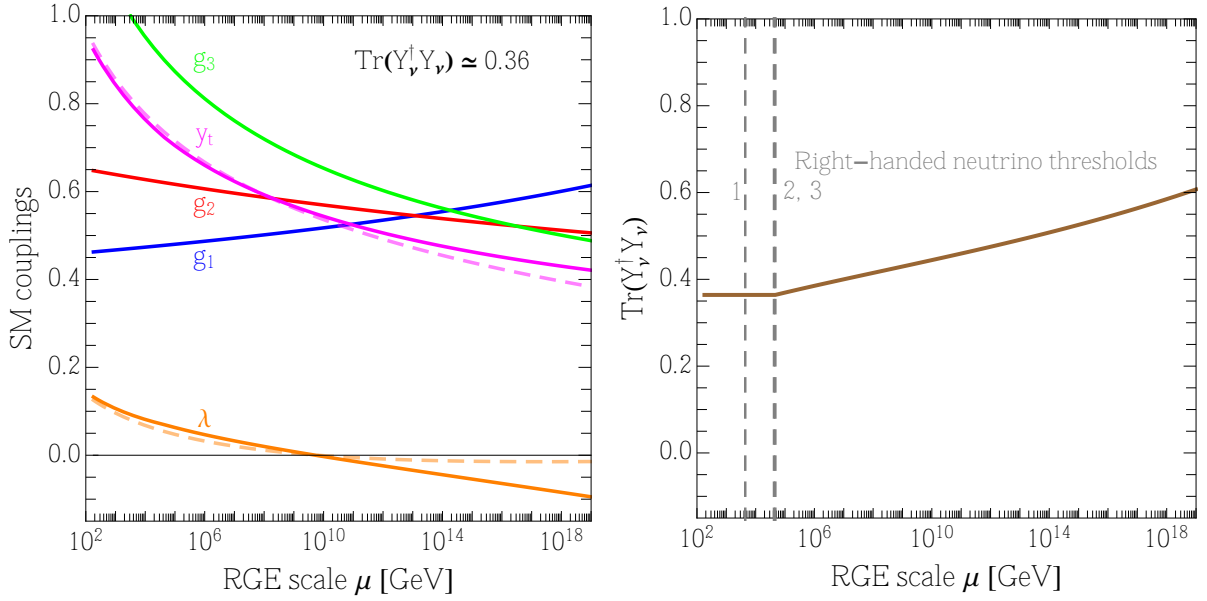


Figure 3.4: *Left panel.* RG evolution of the SM couplings. Solid lines take into account the effects of right-handed neutrinos in the inverse seesaw model with  $\text{Tr}(Y_\nu^\dagger Y_\nu) \simeq 0.36$  at the EW scale. Dashed lines represent the running of couplings in the SM. *Right panel.* Evolution of  $\text{Tr}(Y_\nu^\dagger Y_\nu)$ . The heavy right-handed neutrino thresholds are explicitly shown.

Finally, we use eq. (3.14) to check whether the analyzed points violate the metastability bound on the EW vacuum.

We show our results in fig. 3.6 for the normal ordering and in fig. 3.7 for the inverted ordering. In order to make contact with phenomenology, in both cases we present the impact of the metastability bound with respect to the observables targeted in section 3.2.2, namely the branching ratio  $\text{Br}(\mu \rightarrow e\gamma)$  (left panel) and the effective neutrino mass (right panel). The red points are excluded by the metastability bound: the EW vacuum would decay too fast in the true vacuum of the EW potential.

Our numerical analysis clearly indicates that points with Yukawa couplings such that  $\text{Tr}(Y_\nu^\dagger Y_\nu) \gtrsim 0.4$  are excluded. This bound does not depend on the assumed hierarchy, since light neutrino masses are irrelevant. Most importantly, the excluded points lie in a region of the parameter space that is close to the present bounds and future experimental sensitivities for both the analyzed observables. Moreover, as clear from the left panel of fig. 3.3, the metastability bound applies in the whole range of analyzed masses for the right-handed neutrinos. This is an interesting piece of information since, for instance, searches for heavy neutrinos with  $m_{\nu 4} \sim \mathcal{O}(100)$  GeV and sizable Yukawa couplings are currently ongoing at the LHC (see section 3.2.2).

Generalization of this computation to the case of the double and linear seesaw mechanism are presented in the appendix A.

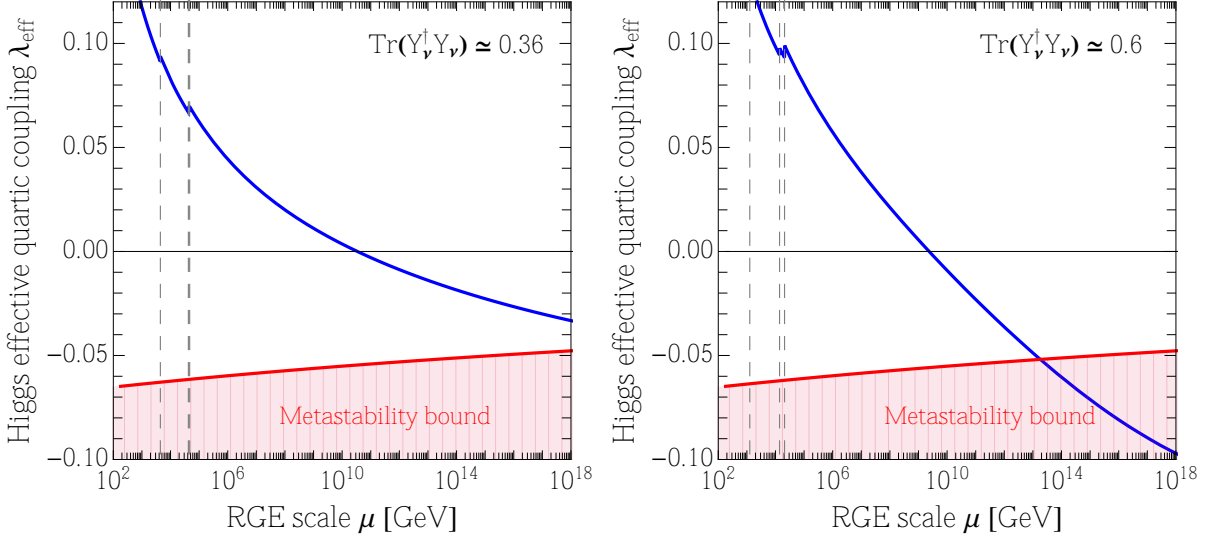


Figure 3.5: *RG evolution of the effective Higgs quartic coupling in the inverse seesaw model in two different setup:  $\text{Tr}(Y_\nu^\dagger Y_\nu) \simeq 0.36$  (left panel) and  $\text{Tr}(Y_\nu^\dagger Y_\nu) \simeq 0.6$  (right panel). In the latter case the Yukawa couplings have a sizable impact on  $\lambda_{\text{eff}}$  and the metastability bound is violated below the Planck scale.*

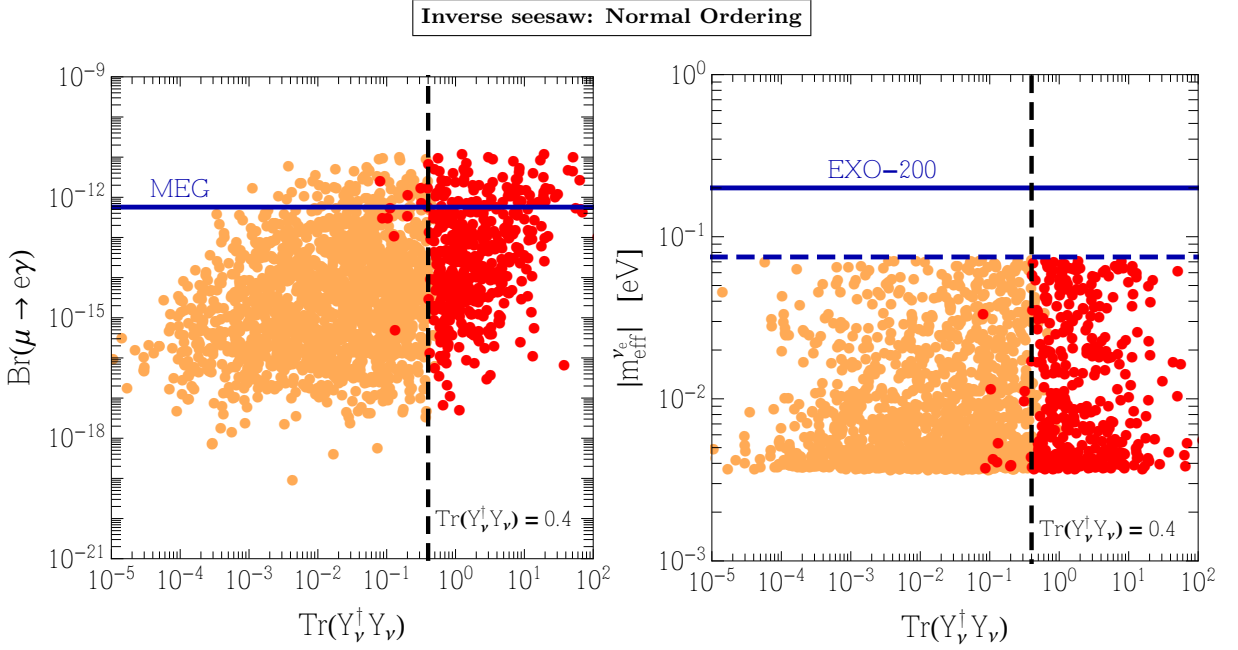


Figure 3.6: *Impact of the vacuum stability analysis on the branching ratio  $\text{Br}(\mu \rightarrow e\gamma)$  (left panel) and the effective neutrino mass (right panel) in the ISS model. All points comply with the bounds discussed in section 3.2.1. Red points violate the metastability bound discussed in section 3.3.*

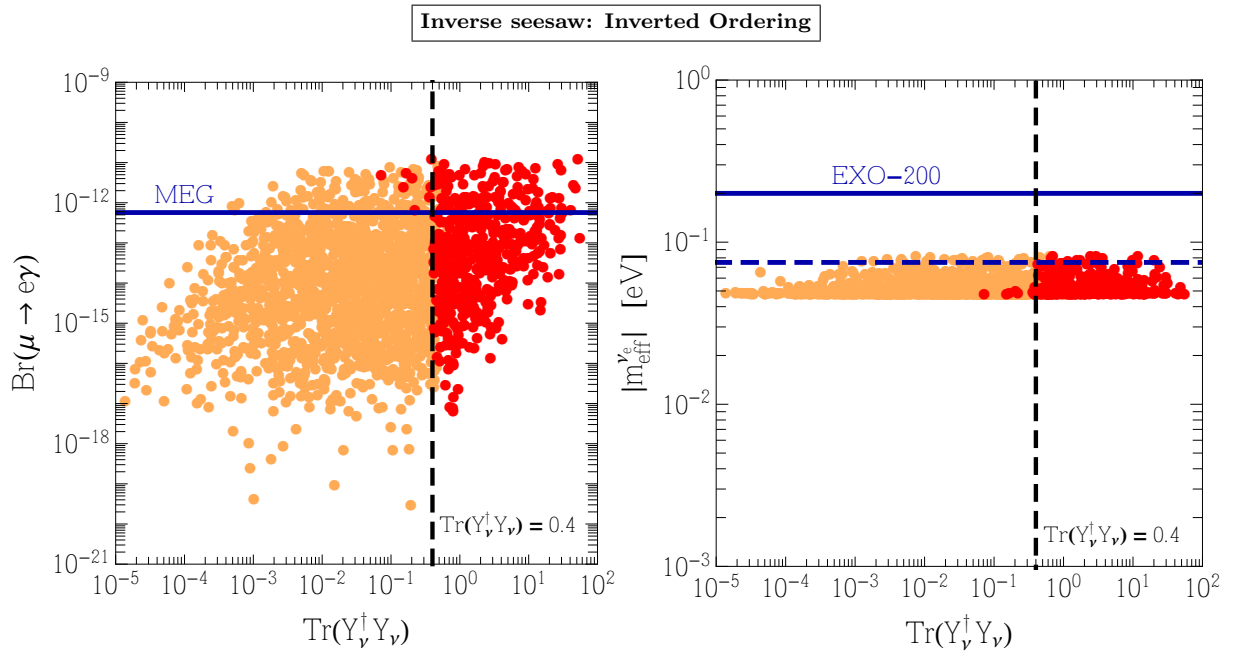


Figure 3.7: Same as in fig. 3.6, but considering the inverted ordering.



## Chapter 4

# Non-anomalous $U(1)'$ models, from LHC to GUT scale.

### 4.1 Introduction

In chapter 3 the most economical and natural setting to account for neutrino masses and oscillation has been avoided being defined as untestable<sup>1</sup> and not capable to affect the SM RG-evolution. It is now time to rescue the type-I seesaw [43, 44, 45, 46] from this depressing position promoting its role in a slightly more complex scenario, where the minimal content of right-handed (RH) neutrinos goes along a likewise minimal gauge extension. In such a case the new fermion, scalar and gauge content all together participate in giving testable and measurable effects which can, in principle, be uniquely linked to the model.

In this chapter we will investigate a minimal renormalizable Abelian extension of the SM. Minimal because of the contained matter content that will be necessary to ensure the consistency of the theory. In practice, to satisfy the cancellation of the gauge and gravitational anomalies, the fermion spectrum asks naturally for RH neutrino, one for each generation (we assume universality between the flavour families), which has  $B - L = -1$  (Baryon minus Lepton number) charge and is singlet under the SM gauge group. Concerning the scalar sector, in addition to the SM-like Higgs doublet  $H$ , a complex scalar field  $\chi$  is needed to achieve the spontaneous breaking of the extra Abelian symmetry. The new scalar field can be chosen to be SM singlet with charge  $B - L = 2$  and its vacuum expectation value  $x$ , which we choose in the TeV range, provides the mass to the  $Z'$  gauge boson and to the RH neutrinos. The latter acquire a Majorana mass through the Yukawa interactions and thus the type-I seesaw mechanism comes naturally in our framework.

---

<sup>1</sup>At least under the lens of the tools involved in this thesis.

## 4.2 The model

### 4.2.1 Charge assignment in minimal Abelian extension

The gauge extension that we are considering has the same content of the SM augmented by a single extra  $U(1)'$  factor, i.e.  $SU(3) \times SU(2) \times U(1)_Y \times U(1)'$ . It is extremely fascinating that the renormalizability requirement, in the guise of anomaly cancellation, can strongly shape and constrain the extra-SM content. To appreciate the consequences of this, apparently formal, request, we start assigning generic charges  $z_Q, z_L$  for the left-handed (LH) quark and lepton doublets  $Q_L^i, L^i$ , and the charges  $z_u, z_d, z_e$  for the right-handed (RH)  $u_R^i, d_R^i$  and  $e_R^i$  quarks and leptons. The charges of the RH neutrinos  $\nu_{R,k}$  are denoted as  $z_k$  and, for the sake of generality, we will not fix the number  $n$  of them.

Notice that we will omit the indices from the definition of the charges since the conditions for anomaly cancellation will be universal, the same for each fermion generation. Finally, the charges of the two scalars  $H$  and  $\chi$  are denoted as  $z_H$  and  $z_\chi$  respectively.

We have the following cancellation conditions for the non-Abelian  $SU(2)$  and  $SU(3)$  anomalies

$$\begin{aligned} U(1)'SU(2)SU(2) : & \quad 3z_Q + z_L = 0, \\ U(1)'SU(3)SU(3) : & \quad 2z_Q - z_u - z_d = 0, \end{aligned} \quad (4.1)$$

which fix  $z_L = -3z_Q$  and  $z_d = 2z_Q - z_u$  in terms of  $z_Q$  and  $z_u$ . Two other conditions are

$$\begin{aligned} U(1)'U(1)_Y U(1)_Y : & \quad z_Q - 8z_u - 2z_d + 3z_L - 6z_e = 0, \\ U(1)'U(1)'U(1)_Y : & \quad z_Q^2 - 2z_u^2 + z_d^2 - z_L^2 + z_e^2 = 0, \end{aligned} \quad (4.2)$$

for the mixed  $U(1)$  anomalies. From the first of the two requirements in eq. (4.2) one can immediately extract the relation  $z_e = -2z_Q - z_u$ , while the second condition of the same equation is automatically satisfied using the solutions found from eq. (4.1). We have summarized in Tab.4.1 the spectrum of the theory that we will be using in our phenomenological study.

The constraints on the charges  $z_k$  of the SM singlet fermions are obtained from the conditions of cancellation of the  $U(1)'$  cubic anomalies, together with those from the gravitational anomaly. The latter involve the  $U(1)'$  current and two gravitons  $G$  (two insertions of the stress-energy tensor of the SM). In the general case with  $n$  singlet fermions one has, respectively

$$U(1)'U(1)'U(1)' : \quad \sum_{k=1}^n z_k^3 = 3[6z_Q^3 - 3z_u^3 - 3z_d^3 + 2z_L^3 - z_e^3] = 3(z_u - 4z_Q)^3, \quad (4.3)$$

for the cubic anomaly and

$$U(1)'GG : \quad \sum_{k=1}^n z_k = 3[6z_Q - 3z_u - 3z_d + 2z_L - z_e] = 3(z_u - 4z_Q), \quad (4.4)$$

for the gravitational anomaly, where we have used the constraints extracted from Eqs. (4.1) and (4.2).

Finally, combining together the two conditions in eq. (4.4), one obtains the cubic relation

$$\left( \sum_{k=1}^n z_k \right)^3 = 9 \sum_{k=1}^n z_k^3. \quad (4.5)$$

	$SU(3)_c$	$SU(2)_w$	$U(1)_Y$	$U(1)'$
$Q_L$	3	2	1/6	$z_Q$
$u_R$	3	1	2/3	$z_u$
$d_R$	3	1	-1/3	$2z_Q - z_u$
$L$	1	2	-1/2	$-3z_Q$
$e_R$	1	1	-1	$-2z_Q - z_u$
$H$	1	2	1/2	$z_H$
$\nu_{R,k}$	1	1	0	$z_k$
$\chi$	1	1	0	$z_\chi$

Table 4.1: Charge assignment of fermions and scalars in the  $U(1)'$  SM extension.

For instance, the constraints in eq. (4.4) imply, for  $n = 0$  and  $n = 1$ , the condition  $z_u = 4z_Q$ , which brings either to the trivial solution or to a solution which is  $Y$ -sequential. In this latter case the  $U(1)'$  charge assignment is proportional to that of  $U(1)_Y$ . In the  $n = 2$  case one obtains, instead,  $z_1 = -z_2$ . We see how for  $n < 3$  the only charge assignments are trivial, a copy of the hypercharge or a setting with the charges of the two fermions compensating each other.

A more interesting solution, which we will use in this thesis, is found for  $n = 3$ . In this case each of the  $\nu_{R,k}$  is assigned to a separate generation. For example, the choice  $z_1 = z_2 = z_3 \equiv z_\nu$  allows to find the simple solution  $z_\nu = z_u - 4z_Q$ . The cancellation of the gravitational anomalies, can be imposed, in general, at inter-generational level. In the present analysis we will stick, however, to the completely symmetric (family independent) assignment of the RH neutrinos charges  $z_1 = z_2 = z_3$ , which allow to reduce the corresponding parameter space. With this choice, the  $U(1)'GG$  constraint from the gravitational anomaly reduces to a single equation for just one charge. On the other hand, the cancellation of the analogue gravitational anomalies in the SM, obtained from the  $U(1)_YGG$  sector, is a natural consequence of the hypercharge assignments of the same model, and does not generate any additional constraint.

As we have shown above, the solutions of the anomaly cancellation conditions are defined in terms of the two free  $U(1)'$  charges,  $z_Q$  and  $z_u$ , of the LH quark doublet  $Q_L$  and of the RH up quark  $u_R$ . This is the main information of this section and we restate it again in a more clear way: the charge assignments of the new matter content under the additional Abelian group are, in the case of a neutrino per generation, all spanned by just two arbitrary number. Notice also that those numbers can be traded for any other more convenient choice of independent charges. With this in mind we see how the generators of the  $U(1)'$  gauge group can be re-expressed, in general, as a linear combination of the SM hypercharge,  $Y$ , and the  $B - L$  quantum number,  $Y_{B-L}$ . Indeed, we have

$$z = \alpha_Y Y + \alpha_{B-L} Y_{B-L}. \quad (4.6)$$

In eq. (4.6) the coefficients  $\alpha_Y$  and  $\alpha_{B-L}$  are functions of the two independent charges and are explicitly given by  $\alpha_Y = 2z_u - 2z_Q$  and  $\alpha_{B-L} = 4z_Q - z_u$ . In the  $B - L$  case, we set  $\alpha_Y = 0$  (i.e.  $z_u = z_Q$ ).

The charges of the two scalars can be fixed from the requirement of gauge invariance of the Yukawa

interactions. From the Yukawa coupling of the electron  $\bar{L}H e_R$  we have

$$(3z_Q) + z_H + (-2z_Q - z_u) = 0, \quad (4.7)$$

which gives  $z_H = z_u - z_Q$ , implying that the ordinary Higgs field is singlet respect to  $B-L$ . Concerning the charge of the scalar field  $\chi$ , the Majorana mass term  $\chi \overline{\nu_R^c} \nu_R$ , in the case of family independent (symmetric) charge assignment  $z_\nu = z_u - 4z_Q$ , we get the condition  $z_\chi = -2z_\nu$ . For a  $B-L$  charge assignment we obtain  $z_\chi = 2$ ,  $z_u = z_Q = 1/3$ .

## 4.2.2 Kinetic Mixing

The inclusion of multiple Abelian factors has dramatic and exciting consequences which are a unique trait of this class of models. We have seen one: the ability to span the ensemble of anomaly free  $U(1)'$  extensions with just two parameters. Strongly connected with this property is the kinetic mixing between the Abelian groups, apparently<sup>2</sup> introducing a new coupling  $\tilde{g}$  to the arena. To stress such connection we will address in this section the formal technicalities to be used in the multiple  $U(1)$  framework.

Working in full generality, we consider a theory with two  $U(1)$  gauge symmetries ( $U(1)_1 \times U(1)_2$ ) and a single fermion  $\psi$  which couples to the two gauge fields  $A_\mu^1$  and  $A_\mu^2$  by the currents

$$j_k^\mu = q_k \bar{\psi} \gamma^\mu \psi \quad (4.8)$$

with charges  $q_k$ . It is a well known fact that for Abelian groups the single field-strength tensor  $F_{\mu\nu}^{A^k} = \partial_\mu A_\nu^k - \partial_\nu A_\mu^k$  are invariants, and not just covariants. Therefore we can write the kinetic term in the gauge-invariant Lagrangian as

$$\mathcal{L}_{12} = -\frac{1}{4} F_{\mu\nu}^{A^1} F^{A^1 \mu\nu} - \frac{1}{4} F_{\mu\nu}^{A^2} F^{A^2 \mu\nu} - \frac{\kappa}{2} F_{\mu\nu}^{A^1} F^{A^2 \mu\nu}. \quad (4.9)$$

The corresponding interaction Lagrangian is given by

$$\mathcal{L}_{int} = g_1 (j_1^\mu A_\mu^1) + g_2 (j_2^\mu A_\mu^2) \quad (4.10)$$

where we have denoted with  $g_1$  and  $g_2$  the couplings of the two Abelian symmetries. The mixing term  $\kappa$  in the kinetic Lagrangian can be eliminated performing a rotation by an angle  $\phi = \pi/4$  of the two gauge fields  $A_\mu^k$ , followed by a rescaling. The rotation is given by

$$\begin{pmatrix} A_\mu^1 \\ A_\mu^2 \end{pmatrix} = \begin{pmatrix} \cos \phi & -\sin \phi \\ \sin \phi & \cos \phi \end{pmatrix} \begin{pmatrix} \bar{B}_\mu^1 \\ \bar{B}_\mu^2 \end{pmatrix} \quad (4.11)$$

which brings eq. (4.9) into the form

$$\mathcal{L}_{12} = -\frac{1-\kappa}{4} F_{\mu\nu}^{\bar{B}^1} F^{\bar{B}^1 \mu\nu} - \frac{1+\kappa}{4} F_{\mu\nu}^{\bar{B}^2} F^{\bar{B}^2 \mu\nu} \quad (4.12)$$

in terms of a kinetically diagonal basis  $\bar{B}_\mu^i$  ( $i = 1, 2$ ). The rescaling involves the matrix relation

$$\begin{pmatrix} \bar{B}_\mu^1 \\ \bar{B}_\mu^2 \end{pmatrix} = \begin{pmatrix} \frac{1}{\sqrt{1-\kappa}} & 0 \\ 0 & \frac{1}{\sqrt{1+\kappa}} \end{pmatrix} \begin{pmatrix} B_\mu^1 \\ B_\mu^2 \end{pmatrix} \quad (4.13)$$

<sup>2</sup>“Apparently” in respect to the two other parameters  $\alpha_Y$  and  $\alpha_{B-L}$ .

expressed by a new orthogonal basis  $(B^1, B^2)$ . The total transformation whence takes the form

$$\begin{pmatrix} A_\mu^1 \\ A_\mu^2 \end{pmatrix} = \mathcal{R}_\kappa \begin{pmatrix} B_\mu^1 \\ B_\mu^2 \end{pmatrix} \quad (4.14)$$

with

$$\mathcal{R}_\kappa = \frac{1}{\sqrt{2}} \begin{pmatrix} \frac{1}{\sqrt{1-\kappa}} & -\frac{1}{\sqrt{1+\kappa}} \\ \frac{1}{\sqrt{1-\kappa}} & \frac{1}{\sqrt{1+\kappa}} \end{pmatrix} \quad (4.15)$$

and allows to re-express eq. (4.9) in the standard form as

$$\mathcal{L}_{12} = -\frac{1}{4} F_{\mu\nu}^{B^1} F^{B^1 \mu\nu} - \frac{1}{4} F_{\mu\nu}^{B^2} F^{B^2 \mu\nu}. \quad (4.16)$$

Notice that  $\mathcal{R}_\kappa$  is a matrix of  $Gl(2, R)$ . After these fields redefinitions, the two gauge currents  $j_1$  and  $j_2$  will mix with the two gauge fields  $B^1$  and  $B^2$ .

Having eliminated the kinetic mixing with eq. (4.14), the interaction term in the Lagrangian is parametrized by the covariant derivative

$$\mathcal{D}^\mu = \partial^\mu + iQ^T G \mathcal{B}^\mu, \quad \mathcal{B}_\mu \equiv \begin{pmatrix} B_\mu^1 \\ B_\mu^2 \end{pmatrix} \quad (4.17)$$

where  $Q^T = (q_1, q_2)$  is the charge array and  $G$  is a matrix product of the original coupling  $(g_1, g_2)$  with the orthogonal matrix  $\mathcal{R}_\kappa$

$$G = \begin{pmatrix} g_1 & 0 \\ 0 & g_2 \end{pmatrix} \mathcal{R}_\kappa \equiv \begin{pmatrix} g_{11} & g_{12} \\ g_{21} & g_{22} \end{pmatrix}. \quad (4.18)$$

It is convenient to introduce the rotation matrix

$$O_R = \begin{pmatrix} \cos \theta & -\sin \theta \\ \sin \theta & \cos \theta \end{pmatrix} = \frac{1}{\sqrt{g_{22}^2 + g_{21}^2}} \begin{pmatrix} g_{22} & g_{21} \\ -g_{21} & g_{22} \end{pmatrix}, \quad (4.19)$$

and parametrize the coupling matrix  $G$  in terms of three independent couplings  $(g, g'_1, \tilde{g})$ , directly related to the original couplings  $g_1, g_2$  and to the mixing parameter  $\kappa$ . With the inclusion of this extra rotation, the coupling matrix  $G$  can be set in a triangular form

$$\tilde{G} = G O_R^T = \begin{pmatrix} g & \tilde{g} \\ 0 & g'_1 \end{pmatrix}, \quad (4.20)$$

where the off-diagonal coupling  $\tilde{g}$  parametrizes the mixing between the  $U(1)$  Abelian symmetries.

After the triangularization of the Abelian coupling matrix, the complete gauge-covariant derivative is given by

$$\mathcal{D}^\mu = \partial^\mu + iQ^T \tilde{G} O_R \mathcal{B}^\mu. \quad (4.21)$$

The new linear combinations of the gauge fields

$$\begin{pmatrix} B_\mu \\ B'_\mu \end{pmatrix} = O_R \begin{pmatrix} B_\mu^1 \\ B_\mu^2 \end{pmatrix} \quad (4.22)$$

provides the diagonal basis for the kinetic terms of the Lagrangian. This approach is directly applicable to an original gauge symmetry  $SU(3) \times SU(2) \times U(1)_Y \times U(1)_z$ , assuming the existence of a kinetic mixing between the two  $U(1)$ 's of the form given by eq. (4.9). If we denote with  $Y$  and  $z$  the corresponding charges ( $q_1 = Y, q_2 = z$ ), the covariant derivative is taken to be of the non diagonal form

$$\mathcal{D}_\mu = \partial_\mu + ig_3 T^a G_\mu^a + ig_2 t^a W_\mu^a + igY B_\mu + i(\tilde{g}Y + g'_1 z) B'_\mu \quad (4.23)$$

where  $g$  and  $g'_1$  are the coupling constants associated with  $U(1)_Y$  and  $U(1)'$  respectively. Now we notice an interesting connection. From eq. (4.23), and the previous analysis, the covariant derivative appeared as

$$\mathcal{D}_\mu = \partial_\mu + igY B_\mu + i(\tilde{g}Y + g'_1 z) B'_\mu + \dots \quad (4.24)$$

From section 4.2.1 we know that, in all generality, our extra generator can be put in the form (4.6). So by a redefinition of the couplings we can always rewrite our covariant (Abelian) derivative as involving only the generators of the SM hypercharge and  $B - L$ :

$$\mathcal{D}_\mu = \partial_\mu + igY B_\mu + i(\tilde{g}Y + g'_1 Y_{B-L}) B'_\mu + \dots, \quad (4.25)$$

where  $B_\mu$  and  $B'_\mu$  are now the gauge fields of the  $U(1)_Y$  and  $U(1)_{B-L}$  gauge groups, respectively, while  $g_1$ ,  $Y$  and  $g'_1$ ,  $Y_{B-L}$  become the corresponding couplings and charges. The mixing between the two Abelian groups, described by  $\tilde{g}$ , can therefore account, together with the overall strength  $g'$ , with all the charge assignments previously spanned by  $\alpha_Y$  and  $\alpha_{B-L}$ . For instance the effective coupling and charge, here introduced as  $g_E Y_E \equiv \tilde{g}Y + g'_1 Y_{B-L}$ , can recover specific benchmark models as the pure  $B - L$  model, obtained enforcing  $\tilde{g} = 0$  ( $Y_E = Y_{B-L}$ ), or the Sequential SM (SSM), by requiring  $g'_1 = 0$  ( $Y_E = Y$ ). The  $U(1)_R$  extension, instead, is realized by the condition  $\tilde{g} = -2g'_1$  while the  $U(1)_\chi$  arising from  $SO(10)$  unification is described by  $\tilde{g} = -4/5g'_1$ .

Therefore, a continuous variation of the mixing coupling  $\tilde{g}$  allows to span over the entire class of anomaly-free Abelian extensions of the SM with three RH neutrinos and no loss of generality is present in choosing the  $U(1)_{B-L}$  gauge group to parametrize this class of minimal  $Z'$ .

### 4.2.3 Scalar sector and spontaneous symmetry breaking

Moving to the scalar sector we must accommodate for the new complex SM-singlet degree of freedom  $\chi$ . The potential is given by

$$V(H, \chi) = m_1^2 H^\dagger H + m_2^2 \chi^\dagger \chi + \lambda_1 (H^\dagger H)^2 + \lambda_2 (\chi^\dagger \chi)^2 + \lambda_3 (H^\dagger H) (\chi^\dagger \chi), \quad (4.26)$$

which is the most general renormalizable scalar potential of a  $SU(2)$  doublet  $H$  and a complex scalar  $\chi$ . To address the stability issues we must ensure that the potential is bounded from below, a requirement which is achieved by the following conditions

$$\lambda_1 > 0, \quad \lambda_2 > 0, \quad 4\lambda_1\lambda_2 - \lambda_3^2 > 0, \quad (4.27)$$

obtained by requiring the corresponding Hessian matrix to be definite positive at large field values. After spontaneous EWSB, the mass eigenstates  $H_{1,2}$  of the two scalars are defined by the orthogonal transformation

$$\begin{pmatrix} H_1 \\ H_2 \end{pmatrix} = \begin{pmatrix} \cos \alpha & -\sin \alpha \\ \sin \alpha & \cos \alpha \end{pmatrix} \begin{pmatrix} H \\ \chi \end{pmatrix}, \quad (4.28)$$

where the scalar mixing angle  $\alpha$  is given by

$$\tan 2\alpha = \frac{\lambda_3 v x}{\lambda_1 v^2 - \lambda_2 x^2} \quad (4.29)$$

and the masses of the physical scalars are

$$m_{H_{1,2}}^2 = \lambda_1 v^2 + \lambda_2 x^2 \mp \sqrt{(\lambda_1 v^2 - \lambda_2 x^2)^2 + (\lambda_3 v x)^2}, \quad (4.30)$$

with  $m_{H_2} > m_{H_1}$  and  $H_1$  identified with the 125.09 GeV Higgs boson.

Eqs. (4.29)–(4.30) can easily be inverted as

$$\begin{aligned} \lambda_1 &= \frac{m_{H_1}^2}{4v^2} (1 + \cos 2\alpha) + \frac{m_{H_2}^2}{4v^2} (1 - \cos 2\alpha), \\ \lambda_2 &= \frac{m_{H_1}^2}{4x^2} (1 - \cos 2\alpha) + \frac{m_{H_2}^2}{4x^2} (1 + \cos 2\alpha), \\ \lambda_3 &= \sin 2\alpha \left( \frac{m_{H_2}^2 - m_{H_1}^2}{2vx} \right), \end{aligned} \quad (4.31)$$

relations which can be used to define the initial conditions on the quartic couplings through the physical masses  $m_{H_{1,2}}$ , the VEVs  $v, x$  and the mixing angle  $\alpha$ . Notice that the light (heavy) Higgs boson couples to SM particles proportionally to  $\cos \alpha$  ( $\sin \alpha$ ), while the interaction with the  $Z'$  and heavy neutrinos is provided by the complementary angle  $\sin \alpha$  ( $\cos \alpha$ ).

When the two scalars acquire non-vanishing VEVs, the neutral component of the gauge sector becomes massive and with mass eigenstates determined by two mixing angles: the usual Weinberg angle  $\theta_w$  and a new mixing angle  $\theta'$ , for which

$$\tan 2\theta' = \frac{2\tilde{g}\sqrt{g_1^2 + g_2^2}}{\tilde{g}^2 + (4g_1'x/v)^2 - g_1^2 - g_2^2}, \quad (4.32)$$

with values in the interval  $-\pi/4 \leq \theta' \leq \pi/4$ . In contrast, the charged gauge bosons are unaffected by the presence of the extra Abelian factor and their masses remain as in the SM.

The mixing angle is completely defined in terms of the mass of the  $Z'$ , through the VEV  $x$  of the singlet scalar, and of its gauge couplings. In general it is always non-vanishing unless  $\tilde{g} = 0$  which corresponds to the pure  $B - L$  model. The EW Precision Tests (EWPTs) have considerably constrained the mixing angle to small values, namely,  $|\theta'| \lesssim 10^{-3}$  [141, 115], in which case

$$\theta' \simeq \tilde{g} \frac{M_Z v/2}{M_{Z'}^2 - M_Z^2}. \quad (4.33)$$

This relation can be satisfied provided either  $\tilde{g} \ll 1$  or  $M_Z/M_{Z'} \ll 1$ , the latter condition allowing a generous range of values for  $\tilde{g}$ .

Finally, the Yukawa Lagrangian is

$$\mathcal{L}_Y = \mathcal{L}_Y^{SM} - Y_\nu^{ij} \bar{L}^i \tilde{H} \nu_R^j - Y_N^{ij} \overline{(\nu_R^i)^c} \nu_R^j \chi + h.c. \quad (4.34)$$

where  $\mathcal{L}_Y^{SM}$  is the SM contribution. Notice that a Majorana mass term for the RH neutrinos,  $M = \sqrt{2}xY_N$ , is dynamically generated by the VEV  $x$  of the complex scalar  $\chi$  and, therefore, the type-I seesaw mechanism is automatically implemented through spontaneous symmetry breaking. The light physical neutrinos emerge as a combination of the left-handed SM neutrinos and a highly damped sterile RH component, while the heavier ones are mostly RH. The damping term in such combinations is proportional to the ratio of the Dirac and Majorana masses.

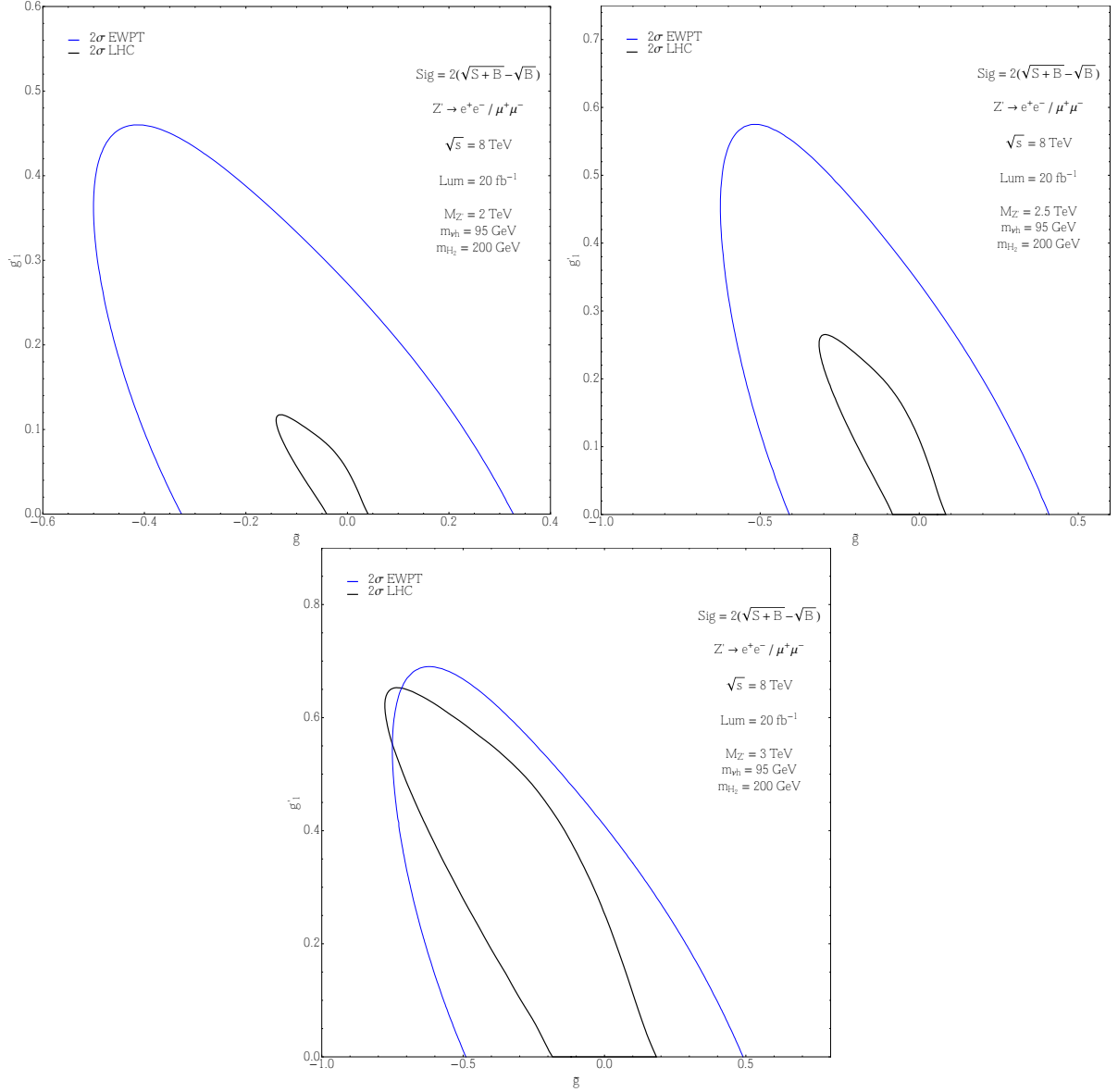
### 4.3 Constraints from EWPTs and LHC searches

The  $(\tilde{g}, g'_1)$  parameter space, in terms of which we are building our analysis, is subjected to well established bounds coming from EWPTs extracted from LEP2 data. These bounds can be recast into constraints for a well-defined set of higher-dimensional operators [141] which describe the effects of new physics. For the Abelian extension under study, these operators have been computed in [115] in terms of the  $Z'$  mass and gauge couplings  $\tilde{g}, g'_1$  neglecting, however, the impact of the heavy neutrinos and of the extended scalar sector. To these constraints we added the one drawn from the more recent data of the first Run of LHC at 8 TeV and  $\mathcal{L} = 20 \text{ fb}^{-1}$ , based on a signal-to-background analysis for the di-lepton (electrons and muons) channel<sup>3</sup>. Next-to-Next-to-Leading-Order (NNLO) Quantum Chromo-Dynamics (QCD) effects are taken into account through a  $k$ -factor correction. We show in fig. 4.1 the exclusion limit at 95% Confidence Level (CL) from both EWPTs and DY studies for three values of the  $M_{Z'}$ , namely  $M_{Z'} = 2, 2.5$  and 3 TeV. For the masses of the  $Z'$  under our investigation, the LHC studies represent a strong improvement with respect to the EW related ones, with the only comparable case being the one with  $M_{Z'} = 3$  TeV. Consequently, we will employ all such tight bounds in the following sections.

The sequential ( $g'_1 = 0$ ) and pure  $B - L$  ( $\tilde{g} = 0$ ) models are strongly constrained while the leptophobic direction in which the  $Z'$  coupling to leptons is minimal ( $g'_1/\tilde{g} \simeq -3/4$ ) obviously represents the least bounded charge assignment. Moreover, we have explicitly verified that the bounds from the DY analysis are not considerably modified by the values of the heavy neutrino mass and the parameters of the extra scalar sector, such dependence entering only in the total width of the  $Z'$  boson.

The extra scalar sector is strongly constrained by Higgs searches at LEP, Tevatron and LHC experiments. The present exclusion limits are enforced using `HiggsBounds` [142, 143, 144, 145, 146] and the agreement of the model with the signal strength measurements of the discovered 125.09 GeV Higgs scalar is taken into account via `HiggsSignals` [147]. The results in the  $(m_{H_2}, \alpha)$  plane are reported in fig. 4.2. The most sensitive exclusion channels are depicted with different colours depending on the  $H_2$  mass (fig. 4.2(a)). The most effective exclusion search, covering almost all the  $m_{H_2}$  mass interval from 150 GeV to 450 GeV, is of a Higgs boson decaying into a pair of  $W$  and  $Z$  bosons [148] (blue region). In particular, the fully leptonic and semileptonic decay channels have been considered for  $H \rightarrow W^+W^-$  while for  $H \rightarrow ZZ$  the final states containing four charged leptons, two charged leptons and two quarks or two

<sup>3</sup>We are grateful to Juri Fiaschi for this analysis.

Figure 4.1: EWPTs vs bounds from a significance analysis at the LHC for different  $Z'$  masses.

neutrinos have been studied. Finally, in fig. 4.2(b), we show a  $\chi^2$  compatibility fit with the Higgs signal measurements in the  $(m_{H_1}, \alpha)$  plane. We have chosen a fixed reference value for the  $H_2$  mass, namely  $m_{H_2} = 200$  GeV, and for the heavy neutrino mass,  $m_{\nu_h} = 95$  GeV, so that only SM-like decay channels are open for the lightest scalar  $H_1$ . The requirement of a compatibility at  $2\sigma$  results anyway into a weaker bound with respect to the exclusion limits that we have taken into account in all the following analyses.

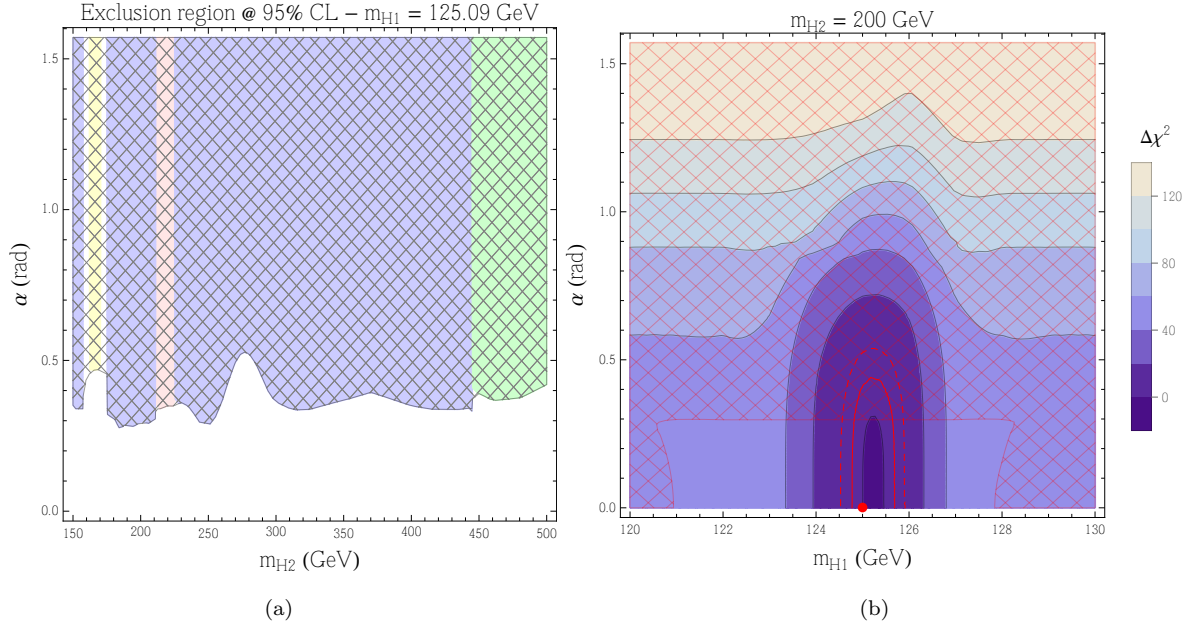


Figure 4.2: (a) Excluded region by LEP+Tevatron+LHC in the  $(m_{H_2}, \alpha)$  plane for fixed  $m_{H_1} = 125.09$  GeV,  $m_{\nu_h} = 95$  GeV and  $M_{Z'} = 2$  TeV obtained using HiggsBounds. The most sensitive exclusion channels are the four leptonic decay of two  $Z$  bosons [149] (red region), the full leptonic decay of two  $W^\pm$  bosons [150] (yellow region), the heavy Higgs decays into two  $Z$ s or  $W^\pm$  s [148] (blue region) and a combined search in five decay modes:  $\gamma\gamma$ ,  $ZZ$ ,  $W^+W^-$ ,  $\tau\tau$  and  $bb$  [151] (green region). (b) Fit results using HiggsSignals with  $m_{H_2} = 200$  GeV. The colours indicate levels of  $\Delta\chi^2$  from the best fit point,  $\chi^2/ndf = 97.5/89$  (red point corresponding to the SM Higgs:  $m_{H_1} = 125.09$  GeV,  $\alpha = 0$ ). Solid (dashed) red line corresponds to  $1\sigma$  ( $2\sigma$ ) contours. The hatched region is excluded at 95% CL.

## 4.4 The RG analysis

After the investigation of the SM in chapter 2, and of its extension by low-scale seesaw mechanisms in chapter 3, we continue the exploitation of RG methods in studying their constraining ability over the parameter space of our anomaly-free  $U(1)'$  model. In particular we will require perturbativity of the couplings and stability of the vacuum. Moving from our experience in building the stability analysis with increasing accuracy [134, 137], we will use two-loop RG equations and matching condition at one-loop level. As shown in [137] the step from one to two-loop order is required to avoid spurious instabilities which disappear at a two-level analysis.

### 4.4.1 RG equations and the Abelian mixing

Before delving in the complex scenario of the matching conditions let's pause for a moment to discuss one of the more interesting feature of these models, which is particularly visible in our approach. From the previous sections we have learned how anomaly freedom and Abelian invariance force us to consider the non canonical form of the covariant derivative (4.25) with the mixing establishing, via the ratio  $\tilde{g}/g'_1$ ,

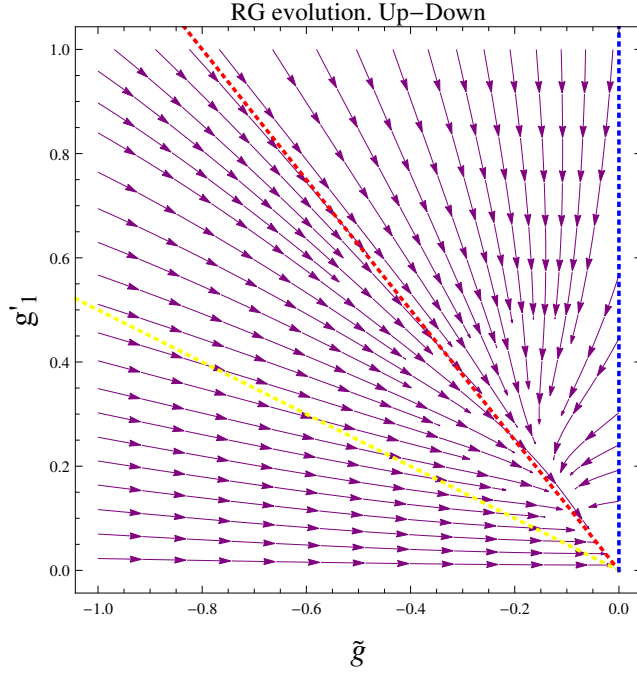


Figure 4.3: *Opposite of the vector field  $(\beta_{\tilde{g}}, \beta_{g'_1})$  in the space  $(\tilde{g}, g'_1)$  with the direction of  $U(1)_{B-L}$  (blue dotted line),  $U(1)_\chi$  (red dotted line) and  $U(1)_R$  (yellow dotted line) charge assignments. The sign of the  $\beta$  functions has been reversed to appreciate the evolution from high to low energies. Notice the direction of  $U(1)_\chi$  which is stable under RG [113].*

the charge assignment of the particles in respect to the  $Z'$  (actually the corresponding gauge eigenstate). It is natural to ask if such ratio, that is the charge assignment, is a constant of the RG evolution. The answer to this question is rooted to the renormalization of theories with multiple Abelian factors, and we refer to [113] for the proof about the mandatory use of the mixing to absorb radiative corrections. More prosaically we inspect the one-loop  $\beta$  functions of the mixing and of the  $g'_1$  (see Appendix B-C for the complete one and two-loop order)

$$\begin{aligned}\beta_{g'_1}^{(1)} &= 12g_1'^3 + \frac{32}{3}g_1'^2\tilde{g} + \frac{41}{6}g_1'\tilde{g}^2, \\ \beta_{\tilde{g}}^{(1)} &= \frac{41\tilde{g}^3}{6} + \frac{32}{3}g_1'^2g'_1 + \frac{41}{3}g_1'^2\tilde{g} + \frac{32}{3}g_1'\tilde{g}^2 + 12g_1'^2\tilde{g}\end{aligned}\quad (4.35)$$

where clearly appears how impossible is to keep  $\tilde{g}/g'_1$  stable under radiative corrections <sup>4</sup>.

Stated differently: measurements of a given charge assignment at LHC scale need the support of the RG analysis to draw conclusions about the corresponding charge assignment at higher energy scales, maybe directly linked to some GUT embedding (fig. 4.3).

<sup>4</sup>With one important exception, see caption in fig. 4.3

#### 4.4.2 The Matching Conditions in the $SM \times U(1)'$

To apply the method of section 2.3 to our model we must recognize the modifications which are introduced in the one-loop structure of the theory by fields not belonging to the SM spectrum. We will adopt a mixed renormalization procedure in which the known SM parameters are renormalized in the on-shell scheme, while the  $\overline{MS}$  is used for the additional couplings and masses introduced by the extended gauge and neutrino sectors and for the vacuum expectation value  $x$  of the extra scalar. On the other hand, for the sake of simplicity, all the remaining parameters in the scalar sector, containing both the Higgs-like quartic coupling and the two new quartic interactions, are renormalized in the on-shell scheme. Such a mixed scheme is not unusual in QFTs as it is already employed, for instance, in the SM, and in particular for the computation of the strong corrections to electroweak observables.

As shown in [114], one of the interesting features of this hybrid renormalization scheme, besides its simplicity, is that the Appelquist-Carrazzone decoupling theorem is explicit manifest. Indeed, the SM limit of measurable quantities is straightforwardly obtained for  $x \rightarrow \infty$ , with  $x$  defined in the  $\overline{MS}$  scheme. This has been the main motivation for our renormalization setup. The SM-like parameters which enter into this RG study are linked to the pole masses and to the Fermi constant in the way illustrated in section 2.3. The unknown dimensionless parameters introduced by the  $U(1)'$  extension, with the only exception of those in the scalar potential, are directly employed in the  $\overline{MS}$  scheme from the very beginning (or, equivalently, are matched to their counterparts at tree level). These are the Abelian gauge coupling constants,  $g'_1$  and  $\tilde{g}$ , and the Yukawa of the right-handed neutrinos  $Y_N$ . Instead, the quartic couplings  $\lambda_2$  and  $\lambda_3$  are matched at one-loop from the on-shell physical mass of the heavy scalar  $m_{h_2}$  and from the the mixing angle  $\alpha$ .

The matching of the Fermi constant  $G_F$  to get the counterterm of the SM Higgs vev  $v$  involves the process of  $\mu$  decay which is generically affected by new physics. This can be appreciated in Fig.4.4 where we show some of the dominant one-loop perturbative contributions clearly not present in the SM. Corrections proportional to the neutrino mixing angle  $\alpha_i$ , as the ones depicted in Fig.4.5, can instead be safely neglected due to the smallness of the ratio between the Dirac and the Majorana masses. The counterterms of the Abelian gauge coupling  $g$  deserves also a special attention because its defining relation gets modified in the  $U(1)'$  extension with respect to the SM case. Nevertheless such departure from the SM is parametrized by the mixing angle  $\theta'$  allowing us to use the same form already met for the strict SM case (2.38)

$$\delta g_{OS} = g_{OS} \left( \frac{1}{2} \frac{\delta M_Z^2 - \delta M_W^2}{M_Z^2 - M_W^2} - \frac{\delta v_{OS}}{v_{OS}} \right).$$

The remaining Abelian coupling,  $g'$  and  $\tilde{g}$ , could be related, in principle, to the pole mass of the  $Z'$  and to the OS expression of the mixing angle  $\theta'$ , but, belonging these two free parameters to the  $U(1)'$  extension, we choose to work directly with their  $\overline{MS}$  expression.

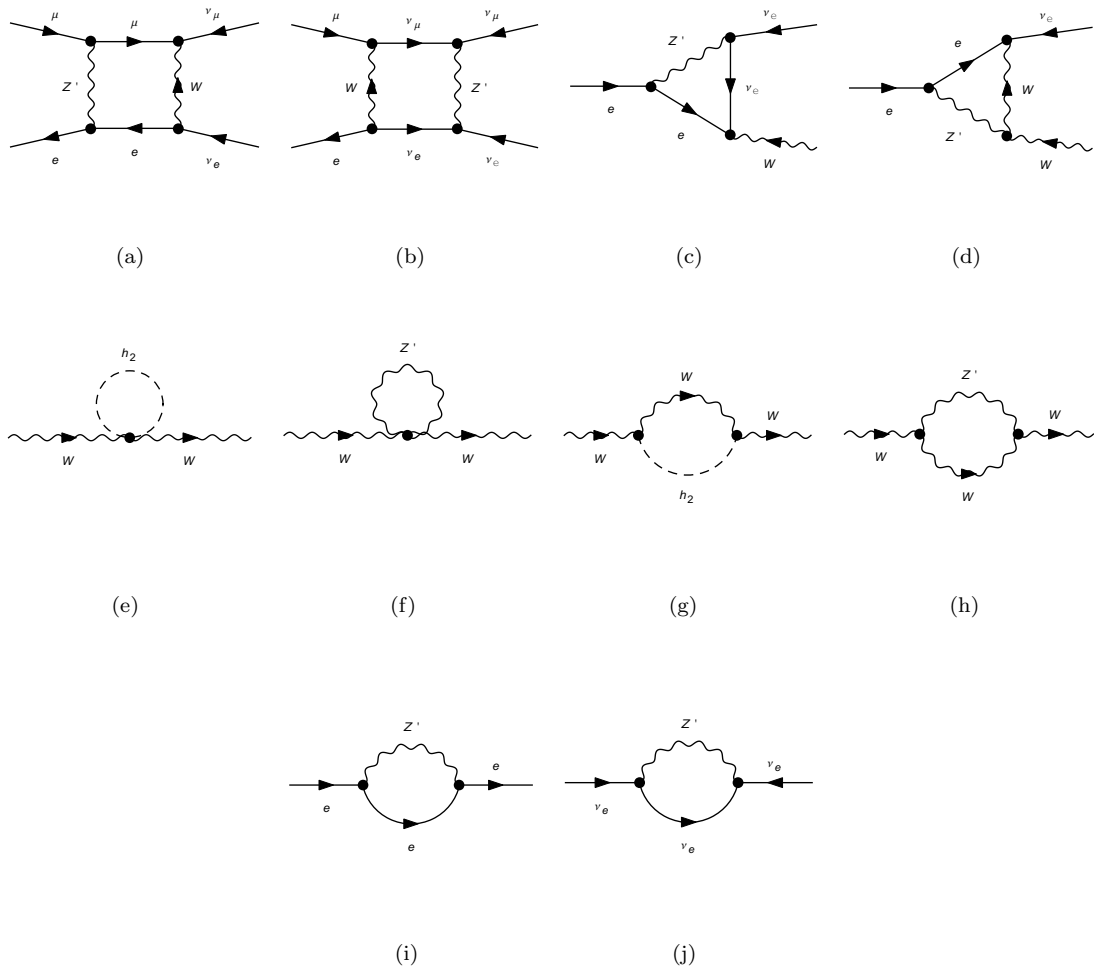


Figure 4.4: Some of the new-physics diagrams appearing in the one-loop perturbative expansion of the  $\mu$  decay. These define the radiative corrections to  $G_F$  of Eq. (2.34). In particular, the diagrams in Figs.(a),(b) enter in the computation of  $B$ , those in Figs.(c),(d) define  $V$ , Figs.(e)-(h) enter in the calculation of the  $W$  self-energy and Figs.(i)-(j) in the external leg corrections  $E$ .

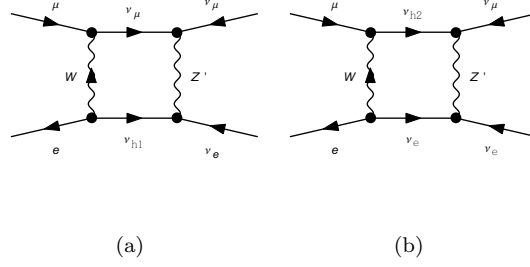


Figure 4.5: Some of the one-loop box diagrams defining the  $\mu$  decay proportional to the neutrino mixing angle.

The major differences in the matching relations, with respect to the SM case, are found in the scalar sector due to the presence of new quartic interactions. Using the defining equations in eq. (4.31) we obtain

$$\begin{aligned}
\delta\lambda_{1\text{OS}} &= \frac{m_{H_1}^2}{4v_{\text{OS}}^2} (1 + \cos 2\alpha_{\text{OS}}) \left( \frac{\delta m_{H_1}^2}{m_{H_1}^2} - 2\frac{\delta v_{\text{OS}}}{v_{\text{OS}}} - 2\delta\alpha_{\text{OS}} \tan \alpha_{\text{OS}} \right) \\
&+ \frac{m_{H_2}^2}{4v_{\text{OS}}^2} (1 - \cos 2\alpha_{\text{OS}}) \left( \frac{\delta m_{H_2}^2}{m_{H_2}^2} - 2\frac{\delta v_{\text{OS}}}{v_{\text{OS}}} + 2\delta\alpha_{\text{OS}} \cot \alpha_{\text{OS}} \right), \\
\delta\lambda_{2\text{OS}} &= \frac{m_{H_1}^2}{4v_{\text{OS}}^2} (1 - \cos 2\alpha_{\text{OS}}) \left( \frac{\delta m_{H_1}^2}{m_{H_1}^2} + 2\delta\alpha_{\text{OS}} \cot \alpha_{\text{OS}} \right) \\
&+ \frac{m_{H_2}^2}{4v_{\text{OS}}^2} (1 + \cos 2\alpha_{\text{OS}}) \left( \frac{\delta m_{H_2}^2}{m_{H_2}^2} - 2\delta\alpha_{\text{OS}} \tan \alpha_{\text{OS}} \right), \\
\delta\lambda_{3\text{OS}} &= \lambda_{3\text{OS}} \left( \frac{\delta m_{H_2}^2 - \delta m_{H_1}^2}{m_{H_2}^2 - m_{H_1}^2} - \frac{\delta v_{\text{OS}}}{v_{\text{OS}}} + 2\delta\alpha_{\text{OS}} \cot 2\alpha_{\text{OS}} \right), \tag{4.36}
\end{aligned}$$

where

$$\delta m_{H_i}^2 = \text{Re} \Pi_{H_i H_i}(p^2 = m_{H_i}^2), \quad \delta\alpha_{\text{OS}} = \frac{\text{Re} \Pi_{H_1 H_2}(p^2 = m_{H_1}^2)}{m_{H_1}^2 - m_{H_2}^2}. \tag{4.37}$$

Notice that, in the last of the previous equations, the mixed scalar self-energy  $\Pi_{H_1 H_2}$  has been evaluated at  $p^2 = m_{H_1}^2$ . This choice enforces the absence of mixing between the two tree-level mass eigenstates  $H_1, H_2$  also at one-loop level and at a particular scale, given by  $m_{H_1}$ .

#### 4.4.3 The stability analysis

After have paid our painful tribute to the matching conditions we can now proceed to the extrapolation of the model. We identify the regions in which the class of the Abelian extensions under study possesses a stable vacuum (described by the conditions given in eq. (4.27)) and is characterized by a weakly coupled regime (couplings are required to be less than  $\sqrt{4\pi}^5$ ) along the RG evolution, up to some given scales

<sup>5</sup>The parameters upon which the perturbative expansion is performed are usually in the form of  $\sqrt{\alpha} = g/\sqrt{4\pi}$  rather than  $g$ .

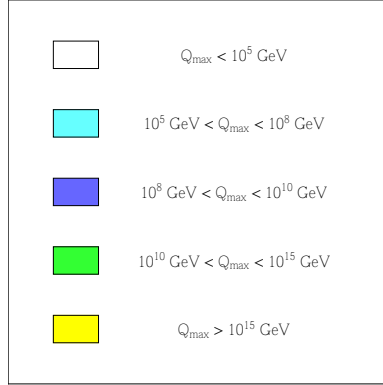


Figure 4.6: Legend of the different regions defined by the maximum scale  $Q_{\max}$  up to which the model is stable and perturbative.

which will be specified below. These regions are defined in the space of the new parameters, evaluated at the EW scale, introduced by these minimal Abelian extensions. We will focus, in particular, on the impact of the Abelian gauge couplings  $\tilde{g}$ ,  $g'_1$ , of the scalar mixing angle  $\alpha$  and of the masses of the heavy Higgs  $H_2$  and  $Z'$  boson.

For ease of reference, the legend of the stability and perturbativity regions, according to the maximum scale  $Q_{\max}$  up to which the vacuum is stable and the model remains perturbative, is depicted in fig. 4.6. In the cyan region the new parameters of these Abelian extensions are such that the stability and/or the perturbativity is lost at a scale  $Q_{\max}$  lower than the instability scale of the SM (see chapter 2, fig. 2.6 in particular). A  $Z'$  model with gauge couplings lying in this region of the parameter space worsen the high-energy behaviour of the SM and clearly calls, with more urgency, for an embedding into a complex scenario, such as GUT unification, already appearing below the  $10^8$  GeV. In the blue region the  $U(1)'$  extensions behave, from the stability point of view, as the SM, whose instability scale  $\Lambda_{\text{SM}} \sim 10^{8-10}$  GeV. In contrast, the green and yellow regions delineate portions of the parameter space in which this class of models is more stable than the SM, up to the GUT scale and above, thus identifying them as compelling extensions of the EW theory. In fig. 4.7 we show the regions of stability and perturbativity, up to some given scale  $Q_{\max}$ , as a function of the two Abelian couplings  $\tilde{g}$ ,  $g'_1$  and for different values of the scalar mixing angle  $\alpha$ . These results have been obtained for  $M_{Z'} = 2$  TeV and  $m_{\nu_h} = 95$  GeV which corresponds to a Yukawa coupling  $Y_N$  of order  $10^{-2}$ . This value is too small to affect the RG evolution of the quartic scalar couplings, therefore the destabilizing effect of new fermionic degrees of freedom is completely suppressed. Indeed, a  $Y_N \gtrsim 0.3$  is, at least, required to appreciate the impact of the heavy RH neutrinos in the running of the scalar sector [137]. This roughly corresponds to  $m_{\nu_h} \simeq 0.2 (M_{Z'}/g'_1)$  for  $M_{Z'} \gg M_Z$ .

The constraints coming from di-lepton searches at the LHC with  $\sqrt{s} = 8$  TeV and  $M_{Z'} = 2$  TeV strongly restrict the allowed parameter space in the  $(\tilde{g}, g'_1)$  plane completely leaving out the cyan regions and therefore only selecting the configurations in which the model is at least as stable as the SM. The dashed lines correspond to three particular and very common  $U(1)'$  extensions which can be described, in our conventions, by straight lines in the  $(\tilde{g}, g'_1)$  plane. These are, in anti-clockwise direction, the pure

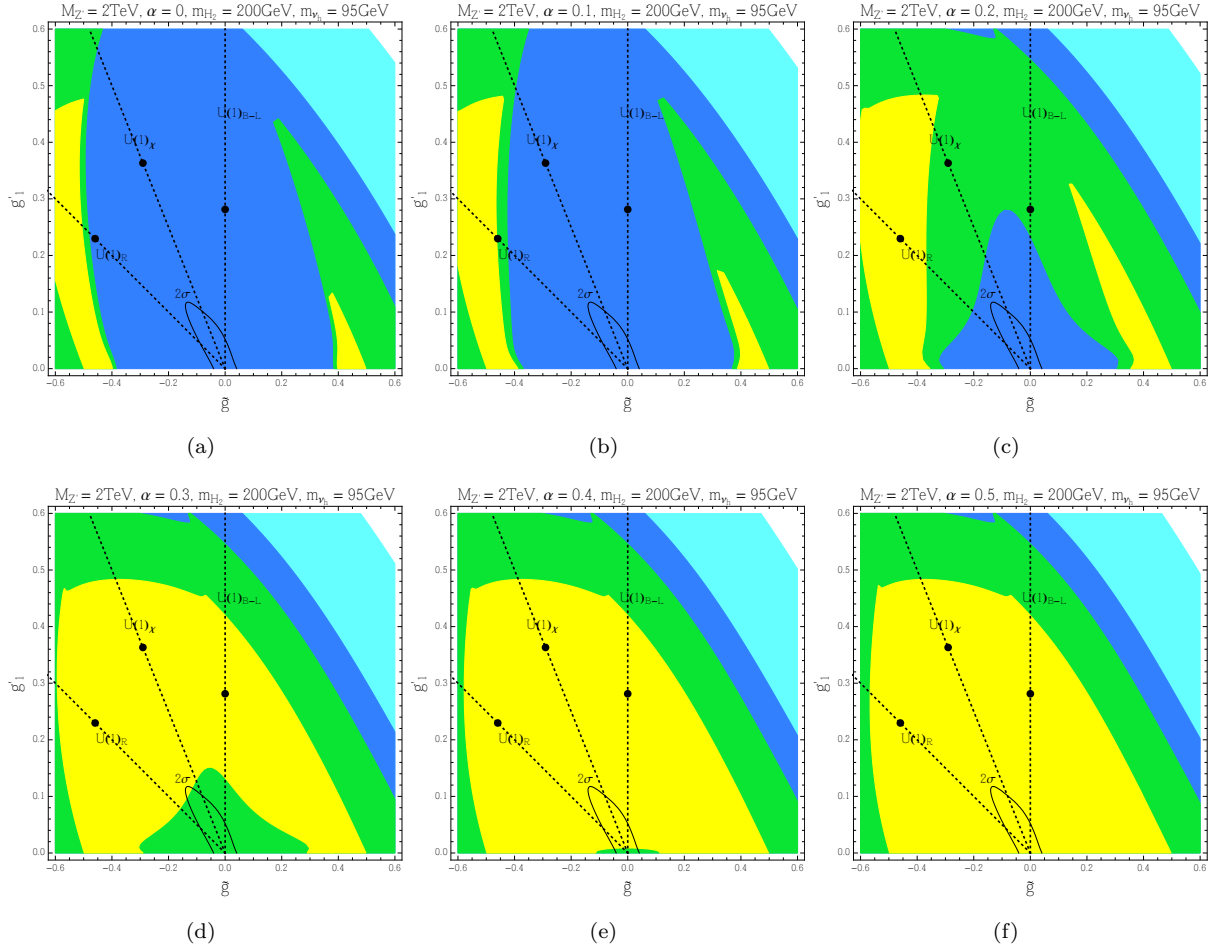
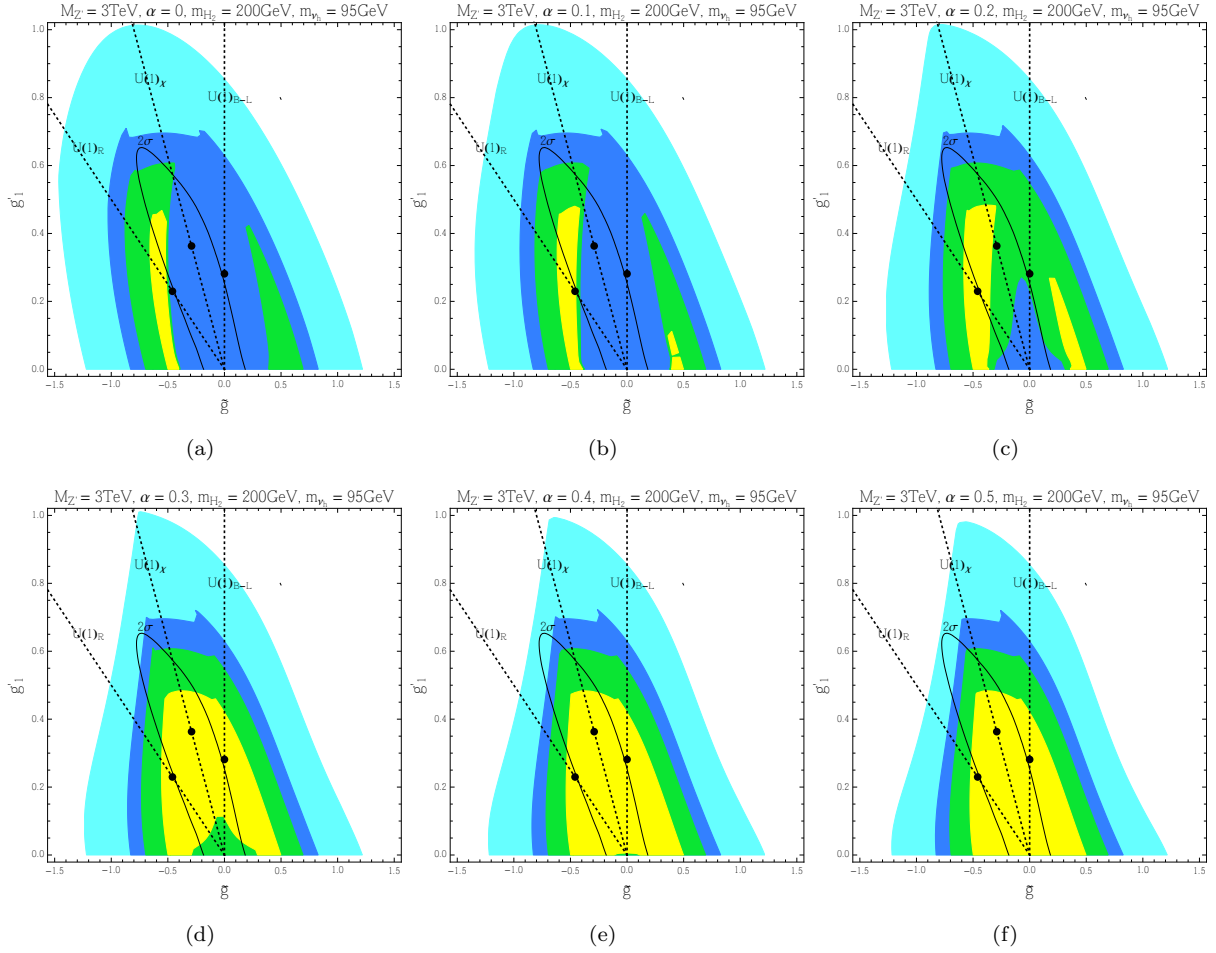


Figure 4.7: Stability and perturbativity regions in the  $(\tilde{g}, \tilde{g}'_1)$  plane for different values of the scalar mixing angle  $\alpha$ . The coloured regions are defined according to  $Q_{\max}$ , the maximum value of the stability and perturbativity scale reached by the model. The corresponding legend is depicted in fig. 4.6.

Figure 4.8: Same as fig. 4.7 with  $M_{Z'} = 3 \text{ TeV}$ .

$U(1)_{B-L}$ , the  $U(1)_X$  and the  $U(1)_R$  extensions, while the sequential SM lies on the  $\tilde{g}$  axis. The black dots represent the benchmark models usually addressed in the literature in which the Abelian gauge couplings are fixed to specific values. Notice also that these reference points, although allowed by EWPTs, are excluded by LHC data if  $M_{Z'} = 2 \text{ TeV}$ .

As one can easily notice from fig. 4.7, the effect of the mixing angle  $\alpha$  of the two scalars is crucial for identifying the regions in which the vacuum is stable. Indeed, scalar degrees of freedom, contrary to the fermionic ones, usually drive the instability scale towards higher values improving the stability of the potential. In the  $\alpha = 0$  case (which corresponds to  $\lambda_3 = 0$ ), the extra scalar sector is decoupled from the SM Higgs doublet and the RG evolution of the  $U(1)'$  extension shares the same behaviour of the SM if the new Abelian gauge couplings are sufficiently small. If  $\alpha$  moves away from zero, the two scalar sectors begin to communicate and the stability effect of the complex scalar  $\chi$  becomes quickly significant, preventing the decay of the vacuum up to the GUT scale and above.

In fig. 4.8 we show the same study for  $M_{Z'} = 3 \text{ TeV}$ . The regions defined by the RG analysis are unchanged with respect to the  $M_{Z'} = 2 \text{ TeV}$  case but the LHC bounds become looser. This allows

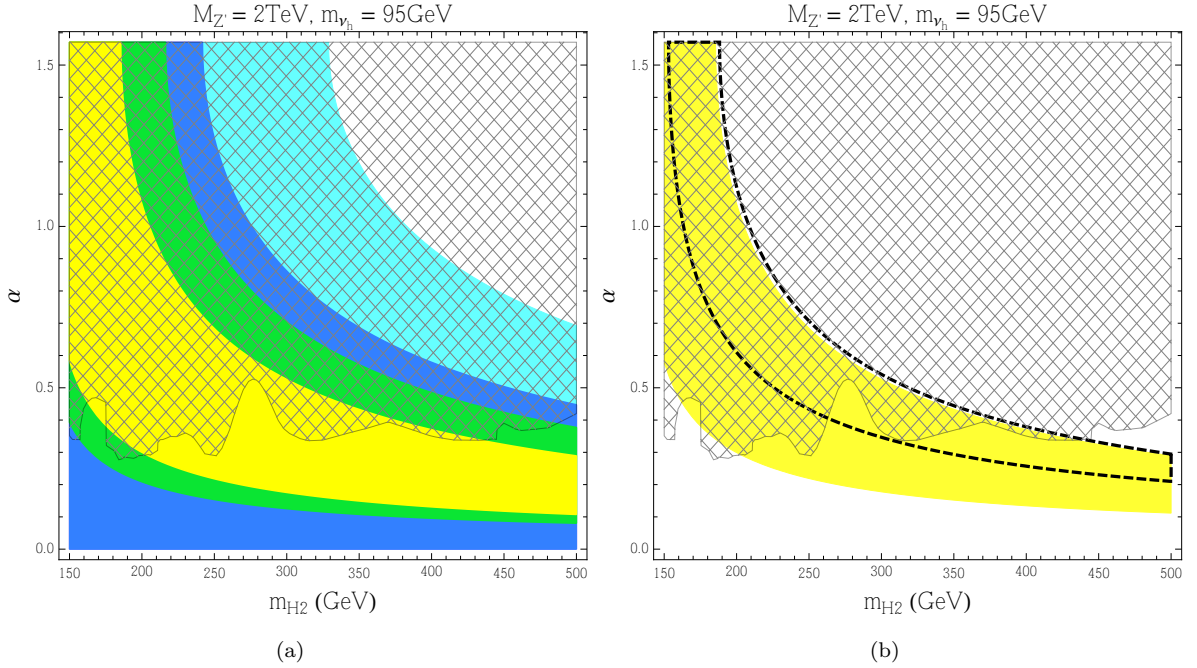


Figure 4.9: (a) Stability and perturbativity regions in the  $(m_{H_2}, \alpha)$  plane according to the colour legend described in fig. 4.6. (b) Comparison between NLO (yellow region) and LO (region delimited by dashed line) results for the requirements of stability and perturbativity up to the GUT scale. The hatched area is excluded by the `HiggsBounds` analysis.

to explore bigger values of the Abelian gauge couplings which can even fall in a region in which the perturbativity is spoiled (cyan), although only for a small slice of the parameter space. For these values, a bigger  $\alpha$  is ineffective to increase  $Q_{\max}$  because the poor behaviour of the model is due to the loss of perturbativity in the Abelian sector and not to the instability of the vacuum. For heavier  $Z'$ s, the constraints from di-lepton searches at the LHC are overtaken by EWPTs which still enclose this Abelian extension in a configuration almost as stable as the SM, provided  $m_{\nu_h} \lesssim M_{Z'}$ .

A similar study is carried out in the  $(m_{H_2}, \alpha)$  plane in order to emphasize the impact of the extended scalar sector. The results are presented in fig. 4.9(a) where the hatched area has been excluded by LHC data using the `HiggsBounds` tool. The  $U(1)'$  Abelian gauge couplings used for this particular analysis are  $\tilde{g} = -0.13$  and  $g'_1 = 0.11$ , which have been chosen on the  $2\sigma$  contour line. We have explicitly verified that different values on the same curve do not lead to any qualitative change. Interestingly, the cyan region, in which the RG behaviour of these models worsens with respect to the SM case, is completely disallowed for  $m_{H_2} \lesssim 500$  GeV. Notice also that, for  $m_{H_2} \lesssim 250$  GeV, both stability and perturbativity are satisfied, up to the GUT scale and above, mainly for a highly-mixed scalar sector while, for heavier  $H_2$ , the mixing angle is bounded from above and the same regions extend horizontally. These regions will eventually shrink at bigger values of the heavy Higgs mass due to a loss of perturbativity of the  $\lambda_2$  quartic coupling.

To highlight the impact of a NLO analysis we show in fig. 4.9(b) the region of stability and perturbativity

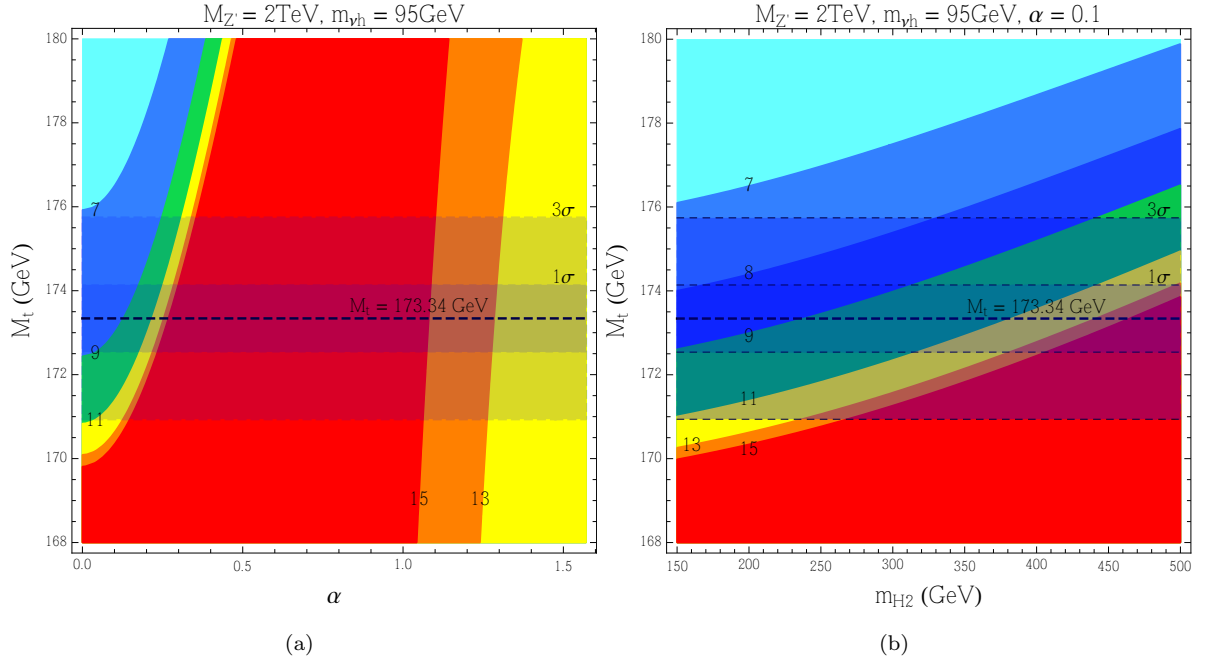


Figure 4.10: Stability and perturbativity regions in the (a)  $(\alpha, M_t)$  and (b)  $(m_{H_2}, M_t)$  spaces. The regions are enclosed by  $Q_{\text{max}} = 10^x\text{ GeV}$  with  $x = 7, 8, 9, 11, 13, 15$ .

up to the GUT scale at NLO (yellow region) in comparison to a LO only (region enclosed in the dashed curve) study in which only one-loop  $\beta$  functions and tree-level matching conditions are employed. It is evident that, in a NLO analysis, the parameter space providing a well-behaved theory up to high energies broadens towards smaller values of the scalar mixing angle  $\alpha$ , which are, quite interestingly, in the region allowed by Higgs searches at the LHC.

In fig. 4.10 we show regions of stability and perturbativity as a function of the top pole mass  $M_t$  and of  $\alpha$  (fig. 4.10(a) with  $m_{H_2} = 200\text{ GeV}$ ) or  $m_{H_2}$  (fig. 4.10(b) with  $\alpha = 0.1$ ). The bold numbers  $x$  on the boundaries of the different coloured regions represent the maximum scale of stability and perturbativity  $Q_{\text{max}} = 10^x\text{ GeV}$ . The dashed line corresponds to the central value of the top mass  $M_t = 173.34 \pm 0.76\text{ GeV}$  [152] which is an average from the combined analysis of ATLAS, CMS, CDF and D0, extracted through Monte Carlo (MC) modeling of production and decay of the top quark in hadronic collisions. Due to its origin, the measurement leads to the so-called MC mass which does represent neither the pole mass nor the  $\overline{\text{MS}}$  mass. Usually, one assumes that the MC mass is sufficiently close to the pole mass with differences estimated of the order of 1 GeV [153, 154, 155] and then extracts its  $\overline{\text{MS}}$  value using matching conditions at the EW scale. The corresponding Yukawa coupling  $Y_t$  is then determined and fed to the RG equations. Unfortunately, this procedure is plagued by many sources of uncertainty and therefore it would be much better, due to its critical role [139, 26, 140, 38, 27], if the MC event generators were defined directly in terms of the  $\overline{\text{MS}}$  Yukawa parameter. The analysis presented in fig. 4.10 show us the critical impact of the top mass, investigated in a window of 1 and 3  $\sigma$  according to [152], and how it is affected by the parameters of the enlarged scalar potential. As one naively expects, the mixing angle

$\alpha$  weakens the destabilizing effect of the top (fig. 4.10(a)) and eventually completely overcomes it for  $\alpha \gtrsim 0.4$ . The restoration of the vacuum stability, for a fixed value of the top mass, also appears as one increases the mass  $m_{H_2}$  of the heavy Higgs (fig. 4.10(b)). Contrary to  $\alpha$ , the effect of  $m_{H_2}$  is softened and, in the range  $150 \text{ GeV} \leq m_{H_2} \leq 500 \text{ GeV}$  with  $\alpha = 0.1$ , only shifts the instability induced by the top quark to higher values of its mass.

## 4.5 LHC Phenomenology

A prime reason for our selection of the parameter space to be investigated has been to put the model at the verge of the more up-to-date LHC quest. Therefore is no surprise that we can encounter a rich prospect of collider visibility. In this section we will explore the possible experimental signatures that characterize the class of  $Z'$  models encompassed by our general analysis.

### 4.5.1 $Z'$ production and decay

In fig. 4.11 the different branching ratios of a  $Z'$  decaying in fermions are displayed for the values of  $M_{Z'} = 2, 2.5$  and  $3 \text{ TeV}$  and for different  $\tilde{g}$  (dashed regions are excluded according to fig. 4.1). The partial decay width of the  $Z'$  decaying into leptons and quarks is

$$\Gamma(Z' \rightarrow f\bar{f}) = \frac{M_{Z'}}{12\pi} C_f \sqrt{1 - \frac{4m_f^2}{M_{Z'}^2}} \left[ \frac{C_{f,L}^2 + C_{f,R}^2}{2} \left(1 - \frac{m_f^2}{M_{Z'}^2}\right) + 3C_{f,L} C_{f,R} \frac{m_f^2}{M_{Z'}^2} \right], \quad (4.38)$$

where  $C_f$  is the colour factor while  $C_{f,L/R}$  are the left/right-handed couplings of the fermion  $f$  to the  $Z'$  boson. These are given by

$$C_{f,L} = -e \frac{s'}{s_W c_W} (T_f^3 - s_W^2 Q_f) + \bar{g}_{f,L} c', \quad C_{f,R} = e \frac{s_W s'}{c_W} Q_f + \bar{g}_{f,R} c', \quad (4.39)$$

where we have used the short-hand notation  $s_W \equiv \sin \theta_W$ ,  $c_W \equiv \cos \theta_W$ ,  $s' \equiv \sin \theta'$  and  $c' \equiv \cos \theta'$ , with  $T_f^3$  being the third component of the weak isospin,  $Q_f$  the electric charge in unit of  $e$  and  $\bar{g}_{f,L/R} = \tilde{g} Y_{f,L/R} + g'_1 z_{f,L/R}$ . The hypercharge  $Y_{f,L/R}$  is normalized as  $Y_f = Q_f - T_f^3$  while  $z_f$  is the  $U(1)'$  charge which we have identified with the  $B-L$  quantum number. The decay width of the  $Z'$  into heavy neutrinos is

$$\Gamma(Z' \rightarrow \nu_h \nu_h) = \frac{M_{Z'}}{24\pi} (z_{\nu_R} g'_1 c')^2 \left(1 - \frac{4m_{\nu_h}^2}{M_{Z'}^2}\right) \sqrt{1 - \frac{4m_{\nu_h}^2}{M_{Z'}^2}}. \quad (4.40)$$

It is clear how the favourite channel for the pure  $B-L$  is in two charged leptons [117]. This decay mode provides nearly 40% of the width, the remainder being almost equally shared by the decays into light quarks, heavy and light neutrinos (note that we considered the branching for charged leptons, light and heavy neutrino states summed over generations). When we turn our attention to the gauge mixing, the decay mode hierarchy is drastically changed. In the limit of a sequential  $Z'$ , which is recovered for  $g'_1 = 0$ , a preference for light quark decays reaches the highest value of 60% for the Branching Ratio (BR). The leptonic decay mode is sub-dominant in this range but starts becoming sizeable with increasing  $g'_1$ . This is to be expected given the restoration of the pure  $B-L$  case in the limit of large  $g'_1$  (equivalent to

$\tilde{g} \rightarrow 0$ ). The BR in heavy neutrinos shows a variability with  $g'_1$ . Moving from zero in the sequential limit it reaches the highest contribution at  $\sim 30\%$  of the BR in the pure  $B-L$  case. Indeed, the partial width  $Z' \rightarrow \nu_h \nu_h$  is independent of  $\tilde{g}$  and it is solely controlled by the Abelian coupling  $g'_1$ .

The possibility to explore different  $Z'$  model configurations is enabled by gauge mixing, which opens new decay channels into SM bosons, which are absent in the pure  $B-L$ , namely,  $Z' \rightarrow W^+W^-$ ,  $ZH_1$  and  $ZH_2$ . The corresponding partial decay widths are given by

$$\begin{aligned}\Gamma(Z' \rightarrow W^+W^-) &= \frac{1}{48\pi} \frac{e^2 c_W^2}{s_W^2} s'^2 M_{Z'} \sqrt{1 - \frac{4M_W^2}{M_{Z'}^2} \left[ \frac{1}{4} \frac{M_{Z'}^4}{M_W^4} + 4 \frac{M_{Z'}^2}{M_W^2} - 17 - 12 \frac{M_W^2}{M_{Z'}^2} \right]}, \\ \Gamma(Z' \rightarrow ZH_1) &= \frac{1}{96\pi M_{Z'}^2} \left[ c_\alpha v(c'g_Z - s'\bar{g})(c'\bar{g} + s'g_Z) + 4s_\alpha x z_\chi^2 g_1'^2 s' c' \right]^2 p_Z \left( \frac{E_Z^2}{M_Z^2} + 2 \right), \\ \Gamma(Z' \rightarrow ZH_2) &= \frac{1}{96\pi M_{Z'}^2} \left[ s_\alpha v(c'g_Z - s'\bar{g})(c'\bar{g} + s'g_Z) - 4c_\alpha x z_\chi^2 g_1'^2 s' c' \right]^2 p_Z \left( \frac{E_Z^2}{M_Z^2} + 2 \right),\end{aligned}\tag{4.41}$$

where  $p_Z$  and  $E_Z$  are the momentum and the energy of the  $Z$  boson in the  $Z'$  rest frame. Moreover, in the previous equations, we have defined  $s_\alpha \equiv \sin \alpha$ ,  $c_\alpha \equiv \cos \alpha$ ,  $g_Z = e/(s_W c_W)$ ,  $\bar{g} = \tilde{g} + 2g'_1 z_H$  where  $z_H$  and  $z_\chi$  are, respectively, the  $U(1)'$  charges of the SM  $SU(2)$  doublet and singlet scalar which, in our case, are  $z_H = 0$  and  $z_\chi = 2$ .

The interplay between the mixing in the Abelian and scalar sectors is visible in the corresponding BRs as given in fig. 4.12. The decays into charged gauge bosons and  $ZH_1$  represent the main patterns regardless of the value of the scalar mixing angle in the range  $0 \leq \alpha \leq 0.2$  ( $\alpha = 0.2$  is a very conservative choice, larger values are possible depending on the  $H_2$  mass, see fig. 4.2) with kinematics accounting for the main differences. The non-zero scalar mixing also clears the way for a  $ZH_2$  channel but with a highly dumped BR not exceeding the 0.1% value. To understand these features, it is instructive to study the partial widths in eq. (4.41) in the  $M_{Z'} \gg M_Z, M_W, M_{H_{1,2}}$  regime taking into account the smallness of the gauge mixing angle  $\theta'$  through eq. (4.33). In this limit we obtain

$$\Gamma(Z' \rightarrow W^+W^-) = \frac{1}{c_\alpha^2} \Gamma(Z' \rightarrow ZH_1) = \frac{1}{s_\alpha^2} \Gamma(Z' \rightarrow ZH_2) = \frac{1}{192\pi} \frac{e^2 s'^2}{s_W^2 c_W^2} \frac{M_{Z'}^5}{M_Z^4},\tag{4.42}$$

which clearly describes the behaviour depicted in fig. 4.12. We concentrate now on the on-shell production of a  $Z'$  gauge boson through DY mode to accommodate the discovery/exclusion opportunities of our model in LHC Run 2. The computation has been performed using **CalcHep** [156] and the corresponding  $U(1)'$  model file implementation [121, 123] on the High Energy Physics Model Data-Base (HEPMDB) [157]. From this perspective, we present in fig. 4.13 the corresponding cross section at 13 TeV as a function of  $g'_1$  and for different values of  $\tilde{g}$  and  $Z'$  mass. We consider the bounds coming from the previous significance analysis from DY at LHC Run 1 and highlight the excluded  $g'_1$  with dotted lines. The  $Z'$  of the pure  $B-L$  model, which is strongly constrained in terms of  $g'_1$ , is characterized by a cross section up to  $\sigma = 5$  fb for  $M_{Z'} = 2$  TeV and up to  $\sigma = 10$  fb for  $M_{Z'} = 3$  TeV. Increasing  $\tilde{g}$  may increase the  $Z'$  coupling to quarks and also allow higher values of  $g'_1$  and consequently more sizeable cross sections but without exceeding the  $\sigma = 100$  fb, a value approached at  $M_{Z'} = 3$  TeV and  $\tilde{g} = -0.6$ .

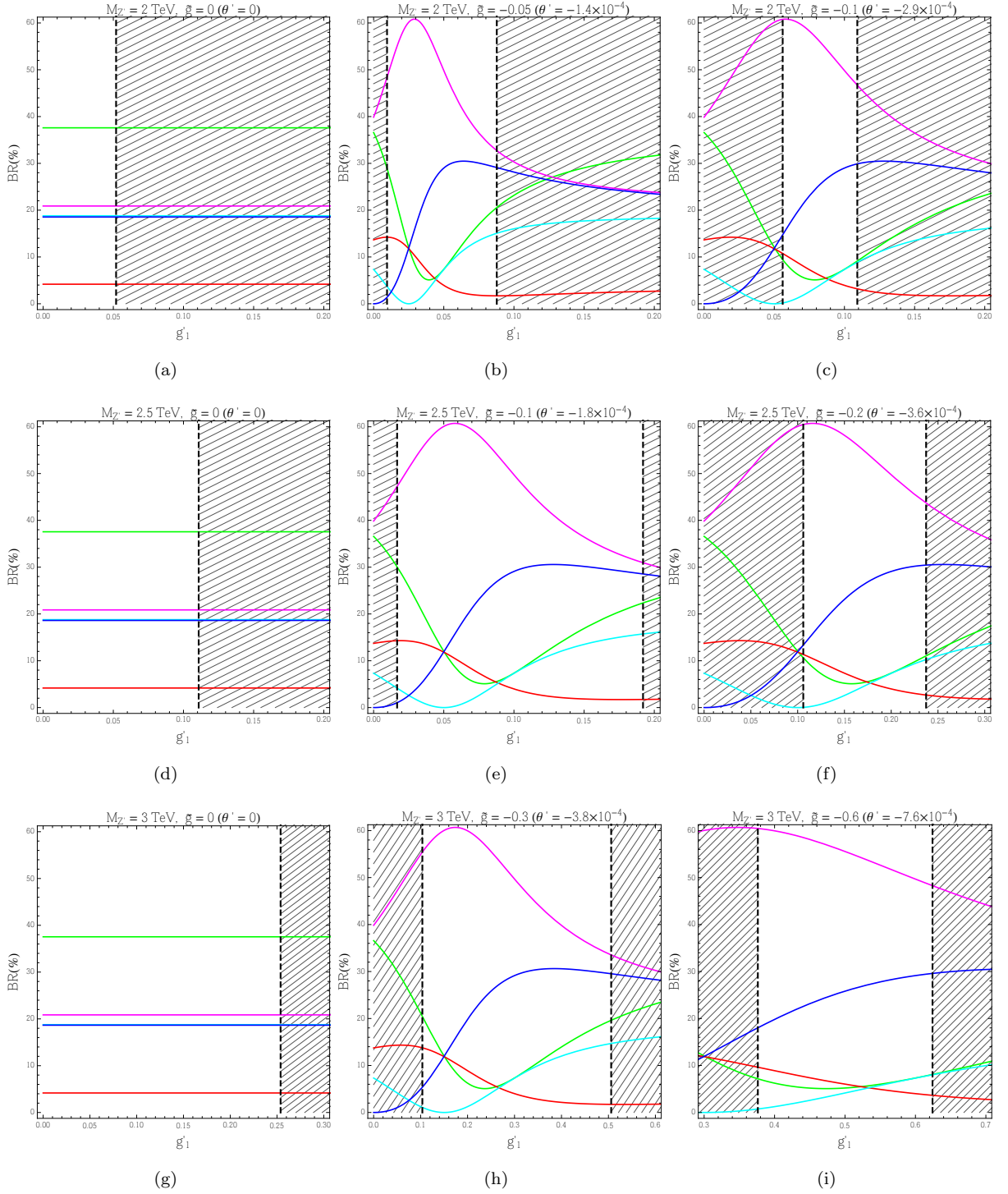


Figure 4.11:  $Z'$  BRs into fermionic final states as a function of  $g'_1$  for several values of  $\tilde{g}$  and for  $M_{Z'} = 2, 2.5, 3$  TeV. The  $\tilde{g} = 0$  case corresponds to the pure  $B - L$ . Dashed regions are excluded by LHC Run 1 data at 95% CL. The green, cyan, purple, red and blue lines correspond to the  $Z'$  decay into two charged leptons, light neutrinos, light quarks, top quarks and heavy neutrinos, respectively.

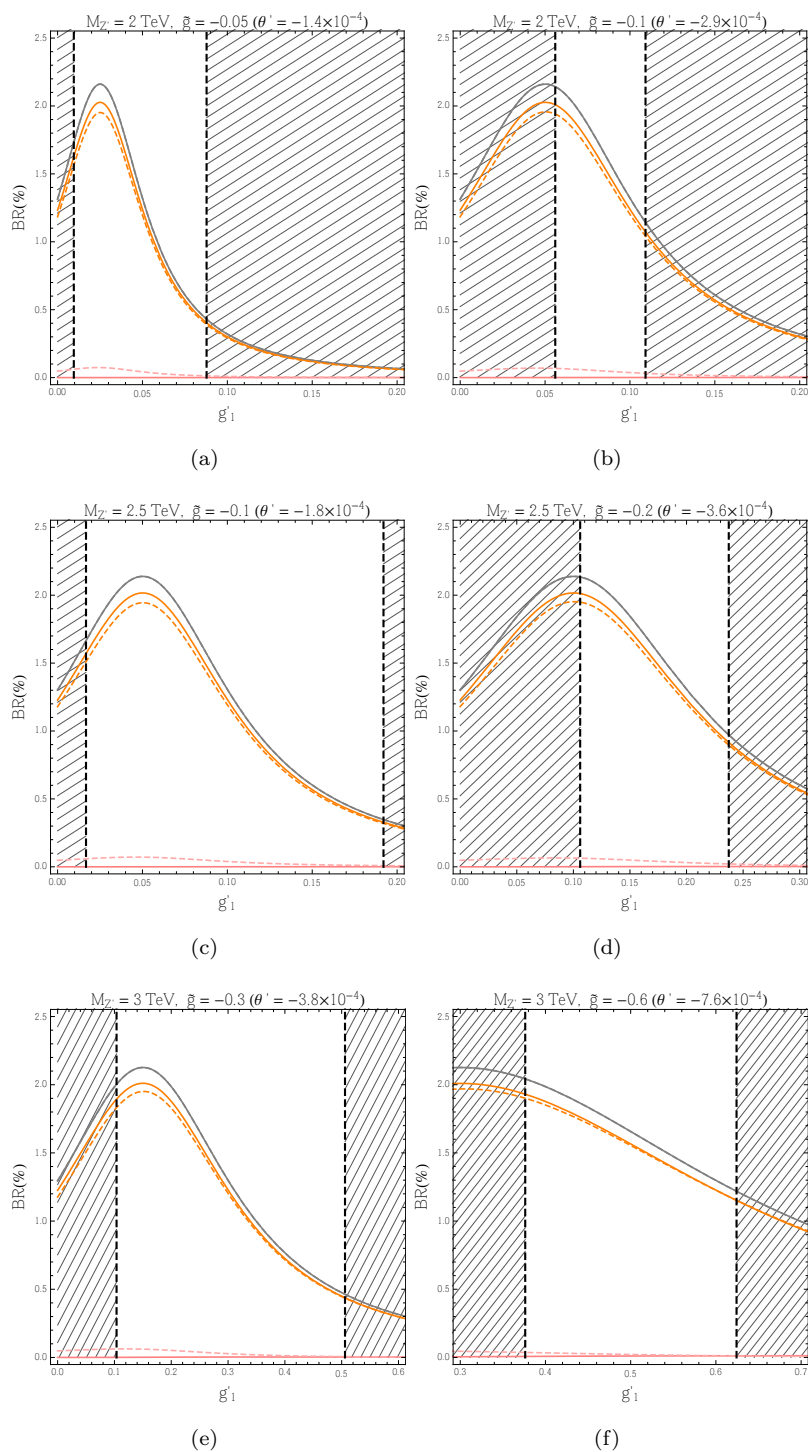


Figure 4.12:  $Z'$  BRs into  $WW$  (gray),  $ZH_1$  (orange) and  $ZH_2$  (pink) as a function of  $g_1$  for several values of  $\tilde{g}$  and for  $M_{Z'} = 2, 2.5, 3 \text{ TeV}$ . In the pure  $B-L$  case these decay channels are absent. Solid (dashed) lines correspond to  $\alpha = 0$  ( $\alpha = 0.2$ ). Dashed regions are excluded by LHC Run 1 at 95% CL

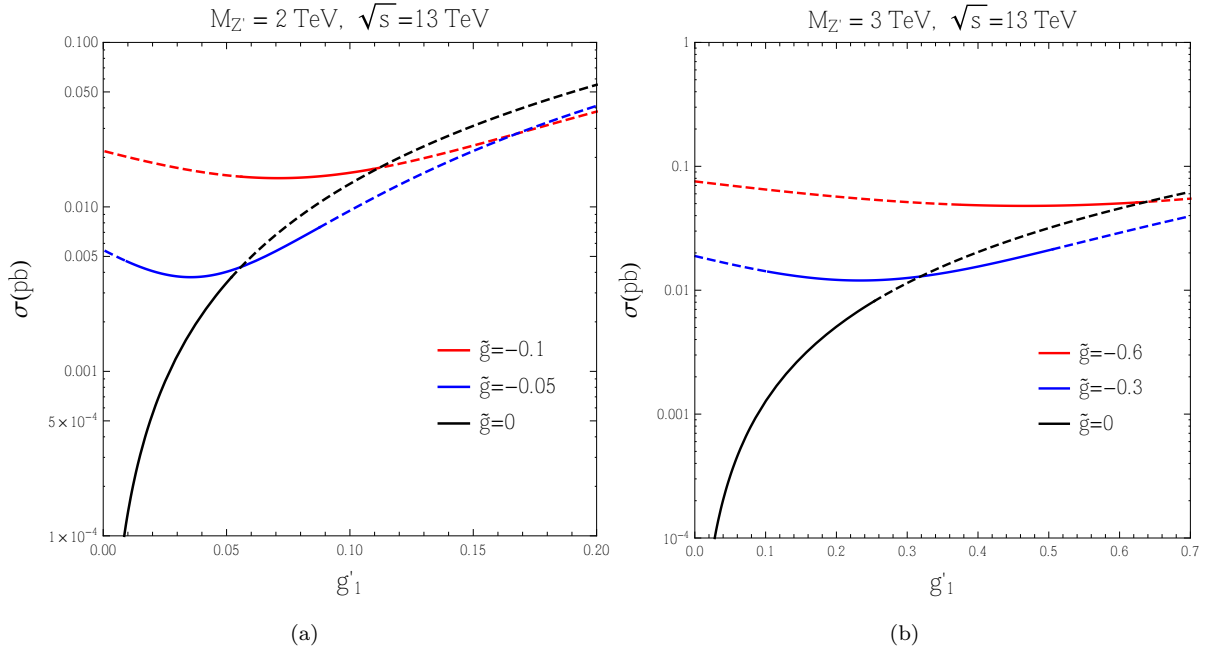


Figure 4.13:  $Z'$  hadro-production cross sections at the LHC as a function of  $g'_1$  for different values of  $\tilde{g}$ . The dotted parts of the lines refer to values of  $g'_1$  excluded by LHC Run 1.

### Hallmark LHC signatures from a $U(1)'$ $Z'$

The production of heavy neutrinos from  $Z'$  decay is a smoking-gun signal of the particular minimal class of models considered, where an extended fermion sector is required to cure the anomalies of the new gauge boson. The successive decays of the heavy neutrino may result in distinctive multi-lepton signatures which have been under recent investigation (see, for instance, [158] for the 2-lepton, [117] for the 3-lepton and [159, 160] for the 4-lepton channel). We explore here the role played, in this process, by the new Abelian couplings and different assignments of  $Z'$  and  $\nu_h$  masses computing the cross section for the production of heavy neutrinos from a decaying  $Z'$ . The results are plotted in fig. 4.14 with contour plots computed for a Centre-of-Mass (CM) energy of 13 TeV.

### 4.5.2 Higgs production and decay

In this section we address the collider perspectives for a scalar signal of  $B-L$  origin at the LHC. In our setup the parameter space defining the new scalar sector consists of the mass of the physical heavy scalar  $m_{H_2}$  and the related scalar mixing angle  $\alpha$ . The mixing angle plays, as expected, a central role scaling all the interactions with SM-like particles by  $\cos(\alpha)$  ( $\sin(\alpha)$ ) when involving a  $H_1$  ( $H_2$ ) and with the complementary angle when involving particles in the peculiar spectrum of the  $U(1)'$  model (as  $Z'$  and heavy neutrinos). Also, the case with  $m_{H_2} > 2m_{H_1}$  offers the chance to investigate new decay channels with multi-scalars, an important hallmark of the mechanism responsible for our extended spontaneous EWSB. Here, we build on the results presented in [120] for a pure  $B-L$  scenario taking into account the

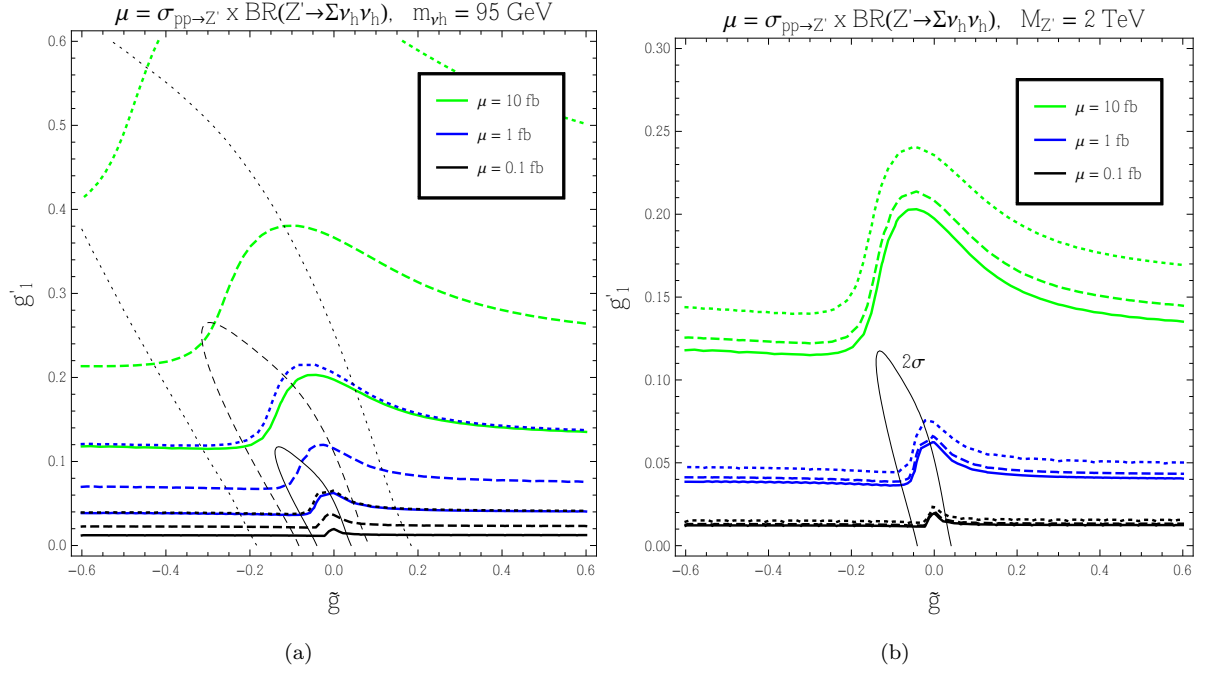


Figure 4.14: Contour plots of the cross section times BR for the process  $pp \rightarrow Z' \rightarrow \nu_h \nu_h$  at the LHC with  $\sqrt{s} = 13$  TeV in the  $(\tilde{g}, g_1)$  plane. (a) Solid, dashed and dotted lines refer to  $M_{Z'} = 2, 2.5, 3$  TeV, respectively, for  $m_{\nu_h} = 95$  GeV. (b) Solid, dashed and dotted lines refer to  $m_{\nu_h} = 95, 300, 500$  GeV, respectively, for  $M_{Z'} = 2$  TeV.

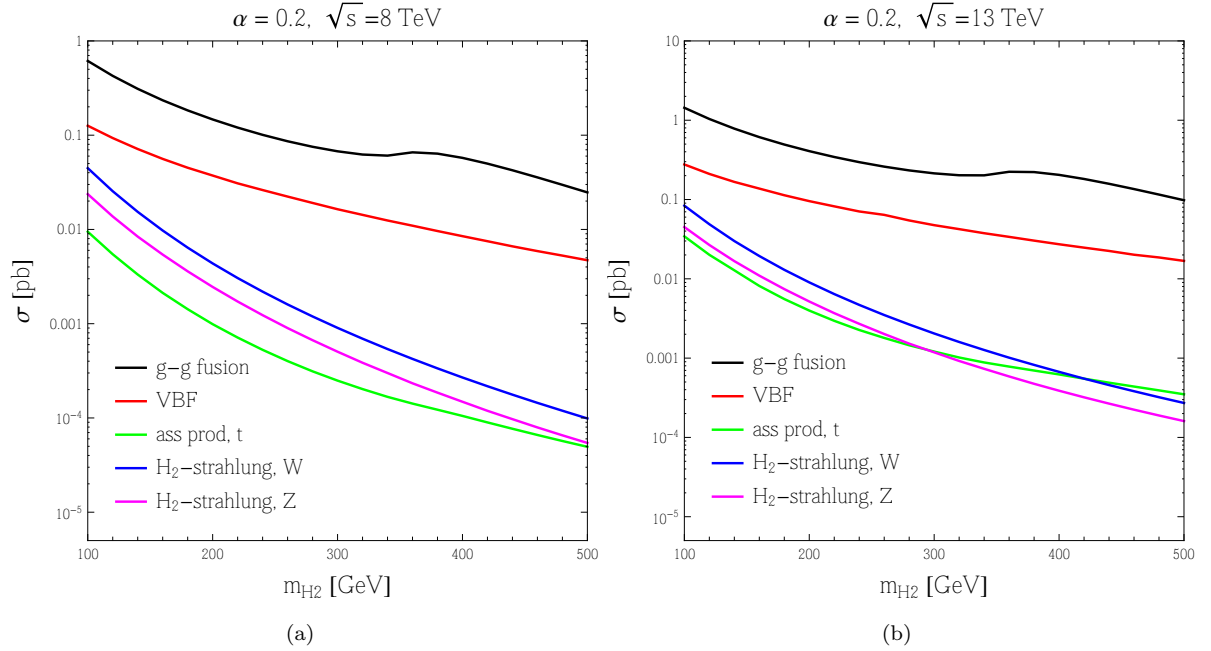


Figure 4.15: Heavy-Higgs production cross sections at the LHC for  $\sqrt{s} = 8$  TeV (a) and  $\sqrt{s} = 13$  TeV (b) CM energy as a function of the  $H_2$  mass for  $\alpha = 0.2$ .

new exclusion data from Higgs searches and the impact of the gauge mixing coupling  $\tilde{g}$ .

### Standard production mechanisms

The most important set of mechanisms exploited to reveal the SM-like 125.09 GeV Higgs boson at LHC involve gluon-gluon fusion, vector-boson fusion,  $t\bar{t}$  associated production and Higgs-strahlung. The cross sections for these standard production channels of the light scalar  $H_1$ , which we assume to coincide with the 125.09 GeV Higgs boson, can be simply obtained from the SM results by a rescaling with a  $\cos^2 \alpha$  factor. Here, instead, we present in fig. 4.15 the cross sections related to such processes for the case of the heavy scalar Higgs ( $H_2$ ) production as function of its mass and with the benchmark value of the mixing angle  $\alpha = 0.2$  for  $\sqrt{s} = 8$  and  $\sqrt{s} = 13$  TeV as CM energy at the LHC. The hierarchy of the cross sections is the same as for the SM Higgs case, the  $H_2$  couplings to SM particles being rescaled by a factor of  $\sin \alpha$ .

### Non-standard production mechanisms

The connection of the extended scalar sector with the remaining particles allows for new mechanisms for heavy Higgs production. Among these, the associated production with the  $Z'$  boson is of great importance, opening a window towards the  $U(1)'$ -specific spectrum. In fig. 4.16 we plot the variation of the cross section for the process  $q\bar{q} \rightarrow Z'^* \rightarrow Z' H_{1,2}$  with respect to the scalar mixing angle. A fixed value of the heavy scalar mass has been taken and different benchmarks of  $Z'$  mass and couplings have been

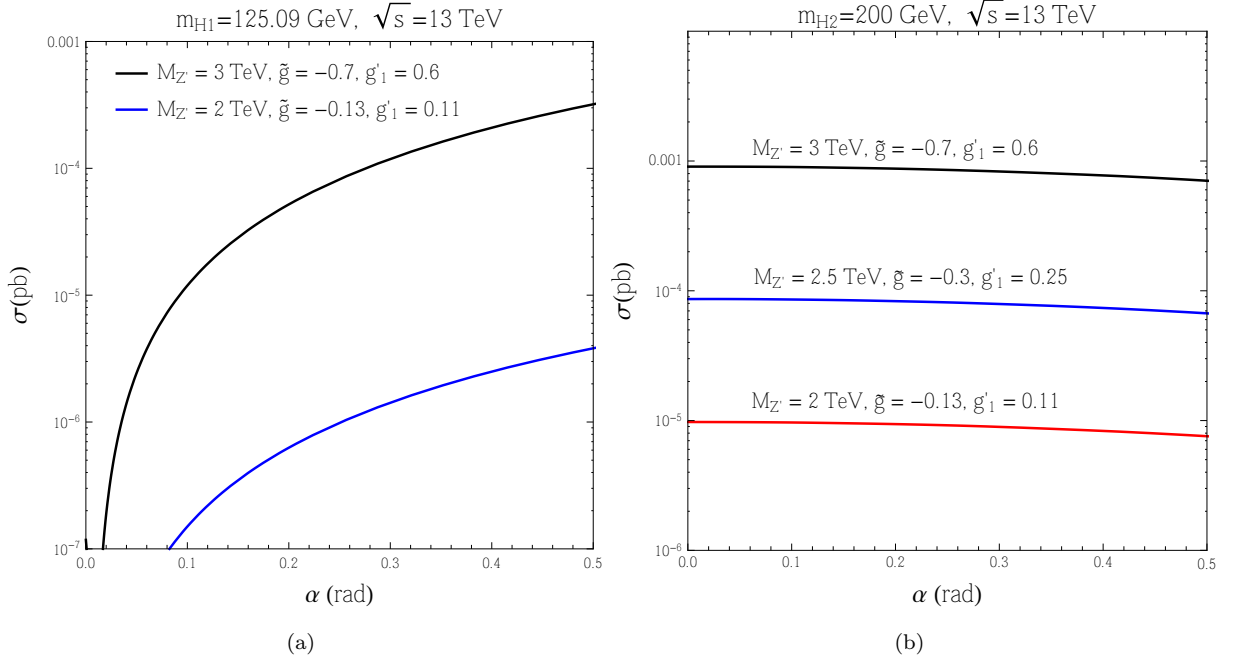


Figure 4.16: Cross sections for associated production of the light (a) and heavy (b) Higgs boson with the  $Z'$  as a function of the scalar mixing angle  $\alpha$  in the  $0 \leq \alpha \leq 0.5$  range for different values of  $M_{Z'}$  and gauge couplings.

considered. Notice that, due to the  $Z - Z'$  mixing, the same final state can be obtained with a  $Z$  exchanged in the  $s$ -channel. (We have verified that this contribution and its interference with the  $Z'$  diagram are non-negligible). The influence of the gauge sector in this production mechanism is translated in the enhancing effect from the Abelian gauge couplings and leads to a maximum value of  $\sigma = 1$  fb. Despite the small cross section, this is the only accessible production channel for  $H_2$  when  $\alpha = 0$ . The ensuing couplings have been chosen appropriately within the 95% CL area of fig. 4.1 and compensate for the dumping effect in the cross section due to the increasing  $Z'$  mass.

### BRs and widths of the Higgs bosons

We now move to the investigation of the various decay modes of  $H_2$  in two particle final states and the role played by the related unknown parameter space. We begin by studying the variation of the branchings of  $H_2$  for a change of its mass in the range 150–500 GeV. Two benchmark points have been considered with two assignments of the scalar mixing angle, consistent with the bounds extracted from Higgs searches, and a common value for the heavy neutrino and  $Z'$  masses, as for the Abelian gauge couplings set at  $g'_1 = 0.11$  and  $\tilde{g} = -0.13$ . The resulting BRs are shown in fig. 4.17. With respect to the SM case, new decay channels are accessible, namely, the  $H_2 \rightarrow H_1 H_1$  and  $H_2 \rightarrow \nu_h \nu_h$ , the former almost ubiquitous in many extensions of the scalar sector, the latter being a hallmark of  $U(1)'$  scenarios. For both values of the mixing considered,  $\alpha = 0.1$  and  $0.28$ , the main channel is represented by the decay into charged gauge

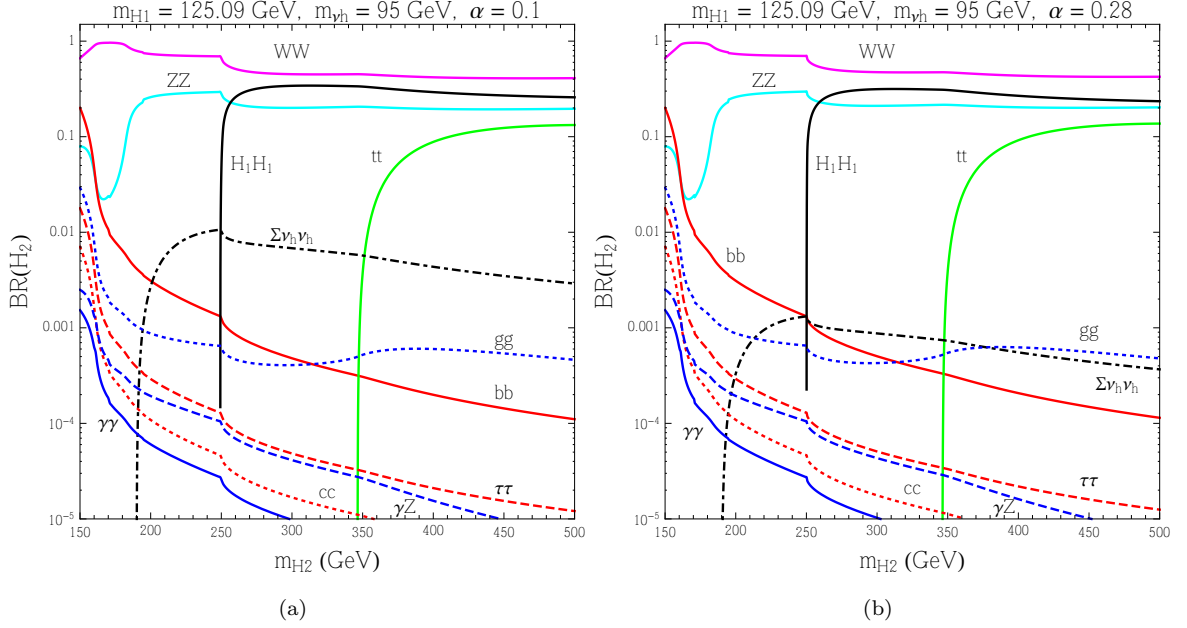


Figure 4.17: BRs of  $H_2$  for (a)  $\alpha = 0.1$  and (b)  $\alpha = 0.28$ . The other parameters are chosen as follow:  $m_{H_1} = 125.09$  GeV,  $m_{\nu_h} = 95$  GeV,  $M_{Z'} = 2$  TeV,  $g'_1 = 0.11$  and  $\tilde{g} = -0.13$ .

boson, a predominance which is weakly challenged only by the decay in two  $Z$ s and, when overcomes the threshold at  $m_{H_2} = 250$  GeV, by the one in two light scalars. Indeed, the hierarchy of the different decay modes in SM final states is the same as that of the SM Higgs, the partial decay widths being rescaled by a factor of  $\sin^2 \alpha$ . The scalar mixing enters critically in the BRs into heavy neutrinos. When the corresponding kinematical region is allowed, it is evident that a heavy Higgs  $H_2$  mainly projecting onto the SM scalar singlet (for smaller values of  $\alpha$ ) has, in our model, a stronger interaction with the heavy neutrinos, and, at the same time, a weaker coupling to SM particles. The corresponding BR endures a one order of magnitude suppression when  $\alpha$  is raised to 0.28. In fig. 4.18 we show the  $H_2$  BRs as a function of the scalar mixing angle for two values of its mass in order to explore different kinematical regions. Indeed, moving from the  $m_{H_2} = 200$  GeV to the  $m_{H_2} = 500$  GeV case, the decays in a top quark pair and in two  $H_1$  become accessible. As mentioned before, the role of  $\alpha$ , for the interaction structure of our model, is clarified by the interplay between the decay in heavy neutrino and the other modes. In both cases shown in fig. 4.18 the increase in  $\alpha$  causes the dropping of the heavy neutrino decay mode and a growth of the SM-like decay channels. Notice also that the  $H_2 \rightarrow H_1 H_1$  mode does not have a trivial dependence on  $\alpha$ .

In fig. 4.19 the dependence on  $\alpha$  and  $m_{H_2}$  of the heavy Higgs total width is illustrated. In fig. 4.19(a) the heavy scalar masses were allowed to span in the range  $150 \text{ GeV} \leq m_{H_2} \leq 500 \text{ GeV}$  while three different assignments  $\alpha = 0, 0.1, 0.28$  have been considered. The case with zero mixing singles out in showing a recognizable threshold due to the heavy neutrino decay being the only allowed channel. The values of the width rapidly grow when such threshold is exceeded reaching the MeV order. Further, with the

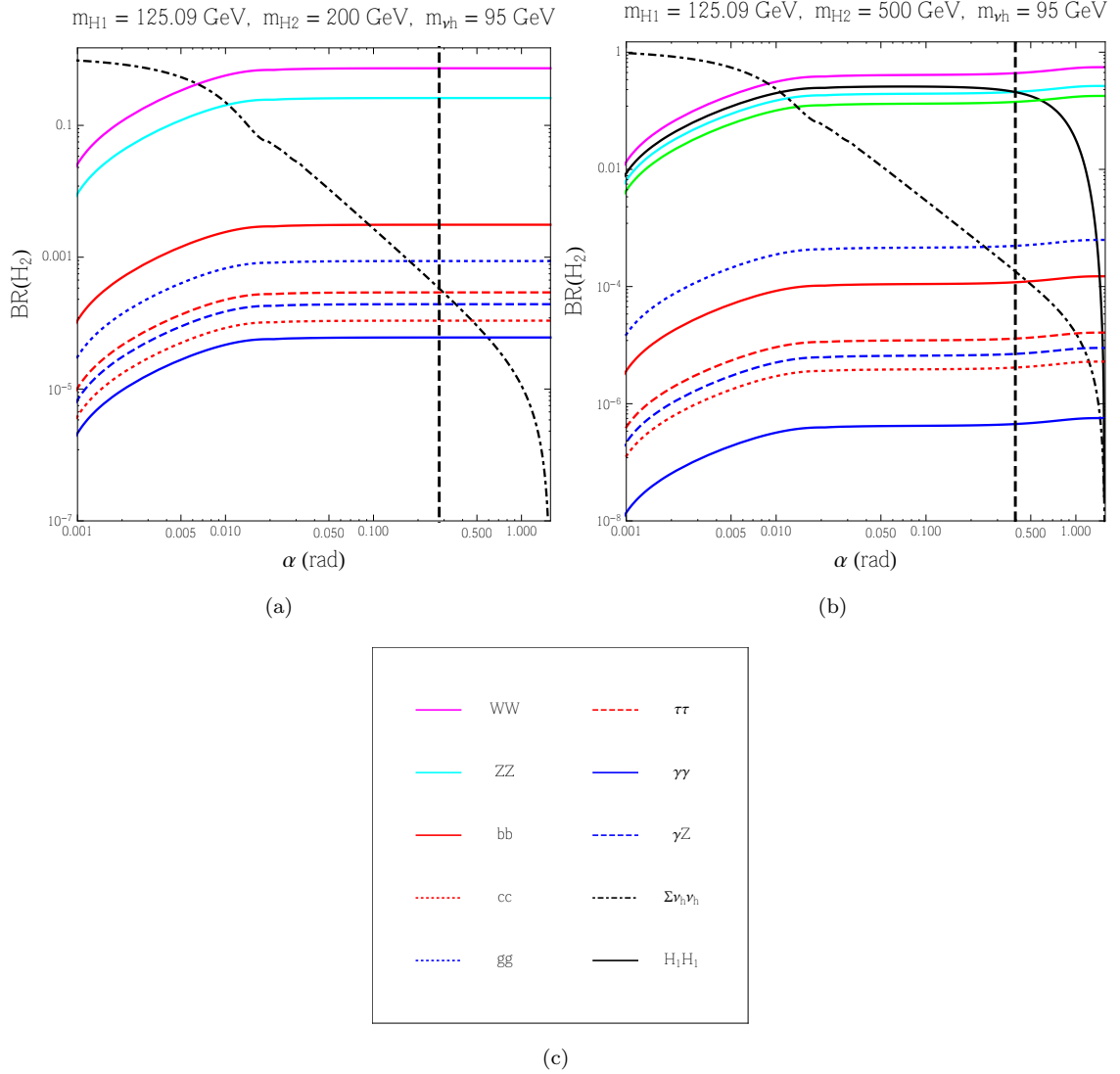


Figure 4.18: BRs of  $H_2$  for (a)  $m_{H_2} = 200 \text{ GeV}$  and (b)  $m_{H_2} = 500 \text{ GeV}$ . The other parameters are chosen as follow:  $m_{H_1} = 125.09 \text{ GeV}$ ,  $m_{\nu_h} = 95 \text{ GeV}$ ,  $M_{Z'}$  = 2 TeV,  $g'_1 = 0.11$  and  $\tilde{g} = -0.13$ . The corresponding legend is depicted in (c). The regions on the right of the vertical dashed lines are excluded by HiggsBounds.

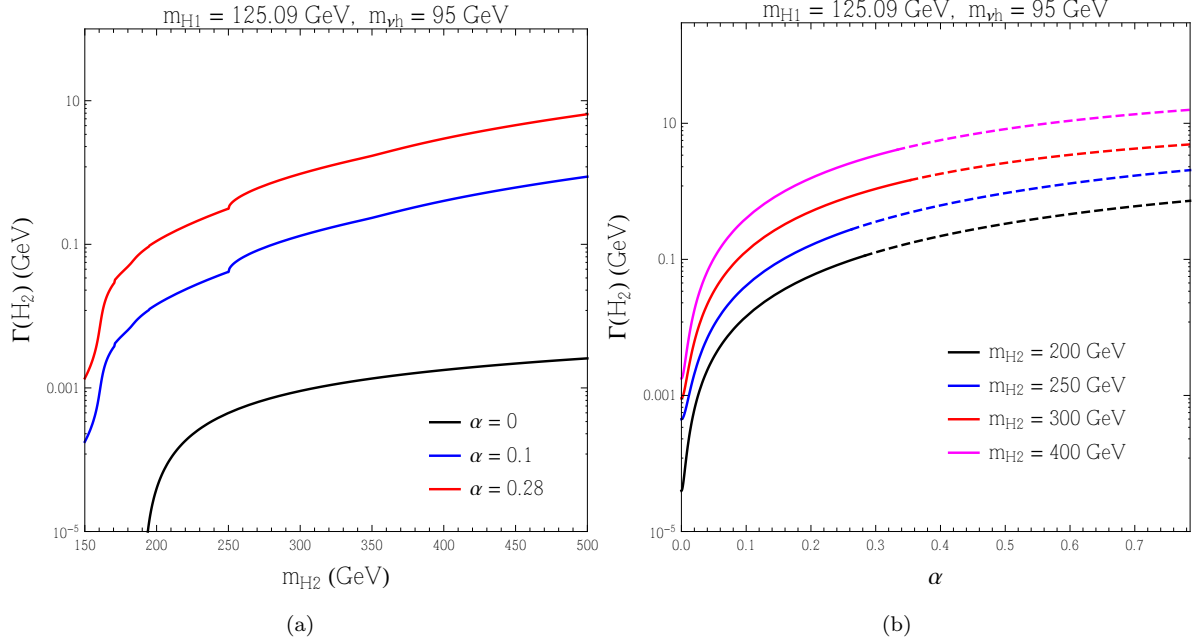


Figure 4.19: The  $H_2$  total decay width as a function of  $m_{H_2}$  for different values of  $\alpha$  (a) and as a function of  $\alpha$  for different values of  $m_{H_2}$  (b). The other parameters are chosen as follow:  $m_{H_1} = 125.09$  GeV,  $m_{\nu_h} = 95$  GeV,  $M_{Z'}$  = 2 TeV,  $g'_1 = 0.11$  and  $\tilde{g} = -0.13$ . In fig. (b) the dashed parts of the curves are excluded by the HiggsBounds analysis.

increase of the scalar mixing the width experiences another sizeable growth due to the now open SM decay channels. Also for such cases the channel  $H_2 \rightarrow H_1 H_1$  is available resulting in a mild threshold in the width plot. We can appreciate how the non-zero mixing causes a large increment in the width allowing values of order GeV to be reached for high  $m_{H_2}$  values. The critical role of the scalar mixing angle is more visible in fig. 4.19(b) where we considered the variation of the width respect to  $\alpha$  in the range  $0 \leq \alpha \leq 0.8$ . For the given choices of  $m_{H_2}$ , the constraints coming from Higgs searches at the LHC have been taken into account excluding a large sector (dashed lines) of the values of  $\alpha$  in the plot.

Let us now turn to the decay patterns of the SM-like Higgs state,  $H_1$ . When  $m_{H_1} > 2m_{\nu_h}$  a new interesting channel become accessible to it,  $H_1 \rightarrow \nu_h \nu_h$  (into heavy neutrinos), otherwise it behaves as the SM Higgs boson, with the same BRs and a total width rescaled by a factor of  $\cos^2 \alpha$ . We show in fig. 4.20(a) the light Higgs decay mode into a pair of heavy neutrinos for  $m_{\nu_h} = 50$  GeV and for three different benchmark points. For comparison we also show the BRs of some decay channel of the SM Higgs boson. Quite interestingly the neutrino BR spans from 0.1% to 1% becoming comparable to, or even exceeding, the  $\gamma\gamma$  mode of the SM Higgs. The behaviour of the depicted curves can be understood by scrutinizing the structure of the  $H_1 \nu_h \nu_h$  vertex. This is proportional to  $\sin \alpha(m_{\nu_h}/x) \sim \sin \alpha g'_1(m_{\nu_h}/M_{Z'})$  and therefore, for fixed  $m_{\nu_h}$ , can be increased by growing the ratio  $g'_1/M_{Z'}$ . Taking into account the LHC limits on the Abelian gauge couplings discussed in section 4.3, which are obviously more constraining for lower  $Z'$  masses, we find a bigger ratio for  $M_{Z'} = 3$  TeV, in which case  $g'_1$  is allowed to vary up to 0.6.

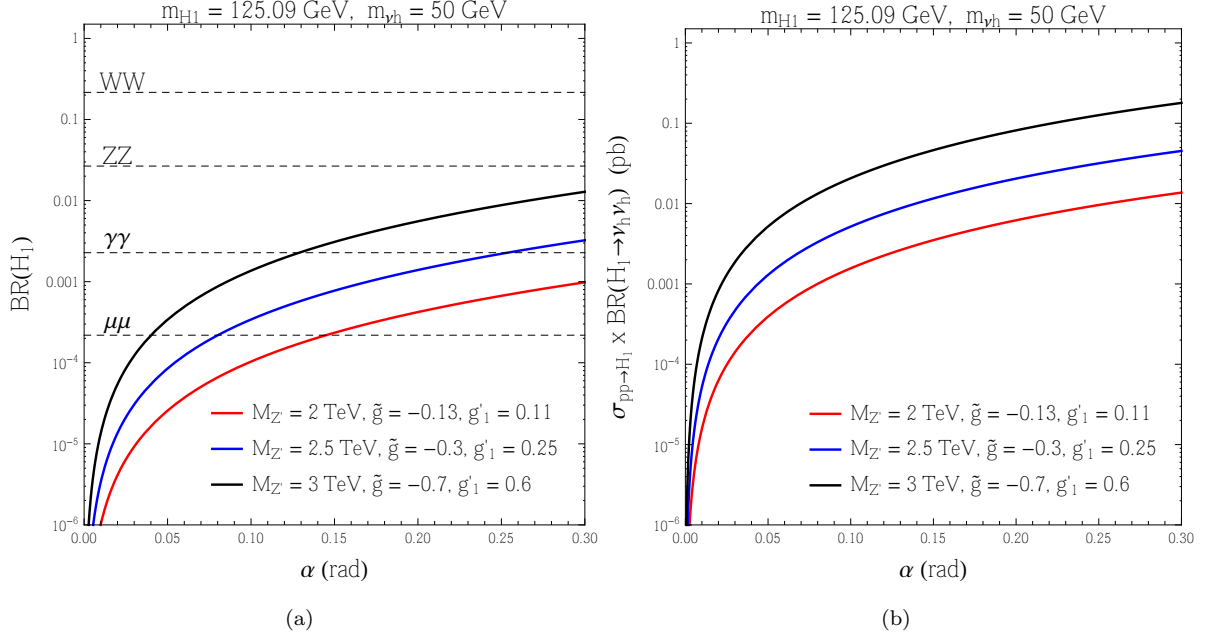


Figure 4.20: (a) Branching ratio of the  $H_1 \rightarrow \nu_h \nu_h$  mode. For reference some of the SM Higgs branching ratios are shown with dashed lines. (b) Cross section times BR for the process  $pp \rightarrow H_1 \rightarrow \nu_h \nu_h$  at the LHC with  $\sqrt{s} = 13$  TeV. Only the gluon fusion channel has been considered. In both plots we have chosen  $m_{\nu_h} = 50$  GeV and different assignments of  $M_{Z'}$  and the gauge couplings.

For completeness, we depict in fig. 4.20(b) the  $\sigma \times BR$  values for the process  $pp \rightarrow H_1 \rightarrow \nu_h \nu_h$  at the LHC with 13 TeV CM energy, which can reach 100 fb. Notice that the  $H_1$  production cross section scales with a factor of  $\cos^2 \alpha$  with respect to the SM case, which is reproduced by a vanishing scalar mixing angle. In such case  $\sigma(gg \rightarrow H_1) = 44.08$  pb [161] which has been used to normalize our cross section.

### Hallmark LHC signatures from $U(1)'$ Higgs states

The production cross sections and decay BRs of  $H_2$  can be combined with the recent limits, coming from LHC search on the extended Higgs sector, to probe realistic discovery opportunities. Our phenomenological scenario calls for a  $\sqrt{s} = 13$  TeV CM energy and an integrated luminosity of  $100 \text{ fb}^{-1}$ , as expected to be collected at LHC. From what has been illustrated in the previous analysis, the heavy scalar decay can reveal its presence and that of the remaining beyond-SM spectrum through peculiar decay channels. Such distinctive signatures involve heavy neutrinos and light scalars. Considering production from gluon-gluon fusion we project in the  $(m_{H_2}, \alpha)$  plane, fig. 4.21(a), the contour of equal value for the cross section times BR of the process  $pp \rightarrow H_2 \rightarrow \nu_h \nu_h$ . We kept the heavy neutrinos at a common degenerate mass of 95 GeV, summing the final state over generations, and considered the benchmark point in the extended gauge sector with  $M_{Z'} = 2$  TeV,  $\tilde{g} = -0.13$  and  $g'_1 = 0.11$ . The values of  $\sigma = 0.1, 0.2$  fb and  $0.5$  fb illustrate the magnitude involved and the number of neutrino events that can be expected. We crossed the results with the stability/perturbativity implications of a given choice of the parameter space. We

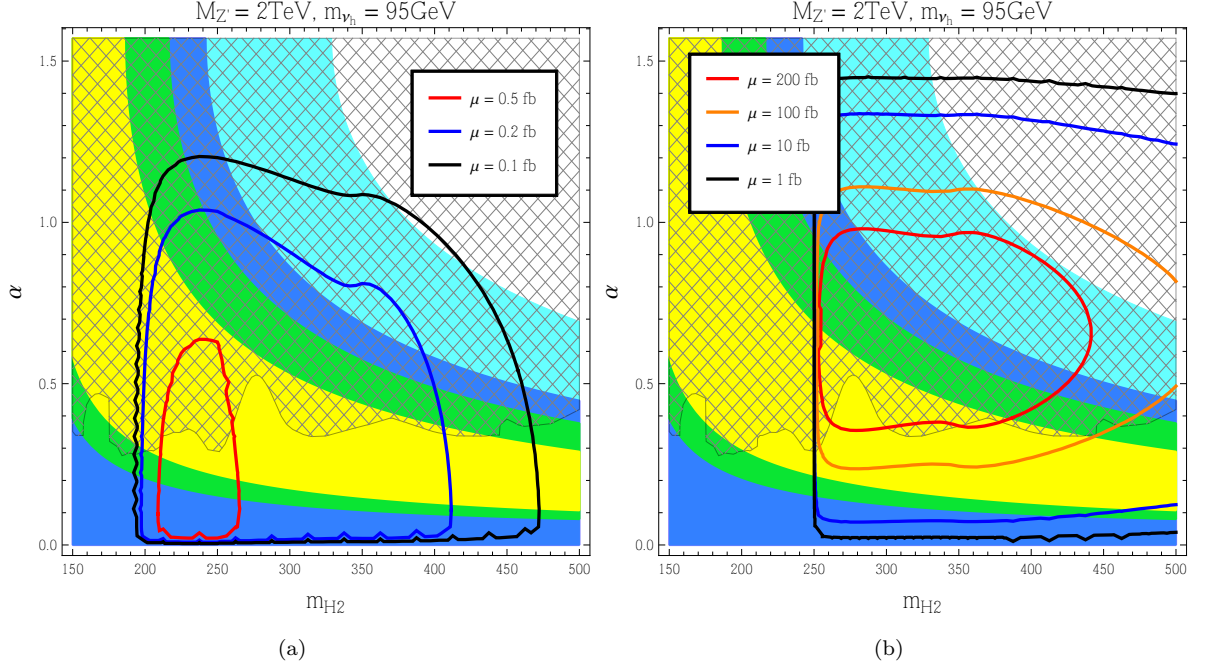


Figure 4.21: Contour plots of the cross section times BR for the processes  $pp \rightarrow H_2 \rightarrow \nu_h \nu_h$  (a) and  $pp \rightarrow H_2 \rightarrow H_1 H_1$  (b) at the LHC with  $\sqrt{s} = 13$  TeV in the  $(m_{H_2}, \alpha)$  plane. Only the gluon fusion channel has been considered. The parameters have been chosen as follows:  $M_{Z'} = 2$  TeV,  $\tilde{g} = -0.13$  and  $g'_1 = 0.11$ .

notice how the request to exceed 50 events selects a restricted area of the heavy scalar mass, roughly  $200 \text{ GeV} \leq m_{H_2} \leq 250 \text{ GeV}$ , with values of the scalar mixing not excluded (hatched area) by LHC data. The same area covers a region with a scale of stability/perturbativity breaking greater than the SM case. A more generous response is obtained when the gluon-gluon cross section is multiplied for the branching of  $H_2 \rightarrow H_1 H_1$ . In fig. 4.21(b) are drawn, for the latter process and the same setting of masses and gauge parameters of the previous figure, the contours with  $\sigma = 0.1, 1, 100$  and  $200$  fb. Above the threshold  $m_{H_2} = 250$  GeV, the scalar mixing angle can critically raise the value of  $\sigma$  leading potentially to  $\sim 100$  events. The LHC limits severely intervene to exclude large value of  $\alpha$  with the resulting effect of an upper bound of  $\sim 200$  events in the space investigated.

The  $H_2$  decay in light scalars or heavy neutrinos states represents a peculiar feature of our minimal class of  $Z'$  models, nevertheless a search aimed to a heavy scalar discovery would favor different channels. From the previous analysis of the BRs (see figs. 4.17-4.18),  $H_2$  decays in  $WW$ ,  $ZZ$  and  $t\bar{t}$  are the main candidates as search channels. Consequently, we proceed by testing the gluon-gluon induced cross section of such channels against the LHC exclusion limits in fig. 4.22. The corresponding contours of equal value for the cross section of  $pp \rightarrow H_2 \rightarrow WW$  and  $pp \rightarrow H_2 \rightarrow ZZ$  are illustrated in figs. 4.22a-b. The two cases share the absence of a threshold in the interval of  $m_{H_2}$  considered and a cross section increasing with the scalar mixing. At the highest values of mixing allowed the  $WW$  decay is more capable to get close to 1

pb while the  $ZZ$  decay has a weaker growth as can be read off from the path of the line  $\sigma = 0.2$  pb. The process  $pp \rightarrow H_2 \rightarrow t\bar{t}$  completes our survey. The threshold is sufficiently high to concern only a small section of the  $(m_{H_2}, \alpha)$  plane. The values of the cross section times BR depicted are for  $\sigma = 10, 25, 50$  fb.

## 4.6 Comments and conclusions

We have shown how production and decay patterns peculiar to a class of  $U(1)'$  models involving the entirety of their additional particle spectrum, i.e., heavy neutrinos, a second Higgs state and a  $Z'$ , at times interplaying with each other in experimental signatures accessible at the second stage of the LHC, can be linked to the high scale behaviour of such scenarios. This has been made possible by combining the description of their low and high-energy dynamics through an advanced RG analysis which specifically used as boundary conditions only those potentially accessible by experiment at present and in the near future. The role of the running kinetic mixing, and, in a way, of the charge assignment of  $U(1)'$  revealed how RG methods will be crucial, in case of discovery, to properly read the hints of a unified structure at higher energy. Our survey has also touched a more general aspect that may affect other different attempts of SM extension. In particular the analysis pursued in fig. 4.10 has clarified how the critical and unnatural role of *pure* SM parameters may be relaxed when considering an embedding in a simple and minimal extension by a scalar singlet.

We look forward to extend a similar effort to the case of anomalous  $U(1)$  charge assignments linked to an E6 GUT. In such case only a single new parameter must be added, to account for an  $U(1)_\psi$  component of the charge. A general survey, with a slight modification of the methods previously developed, can then be pursued.

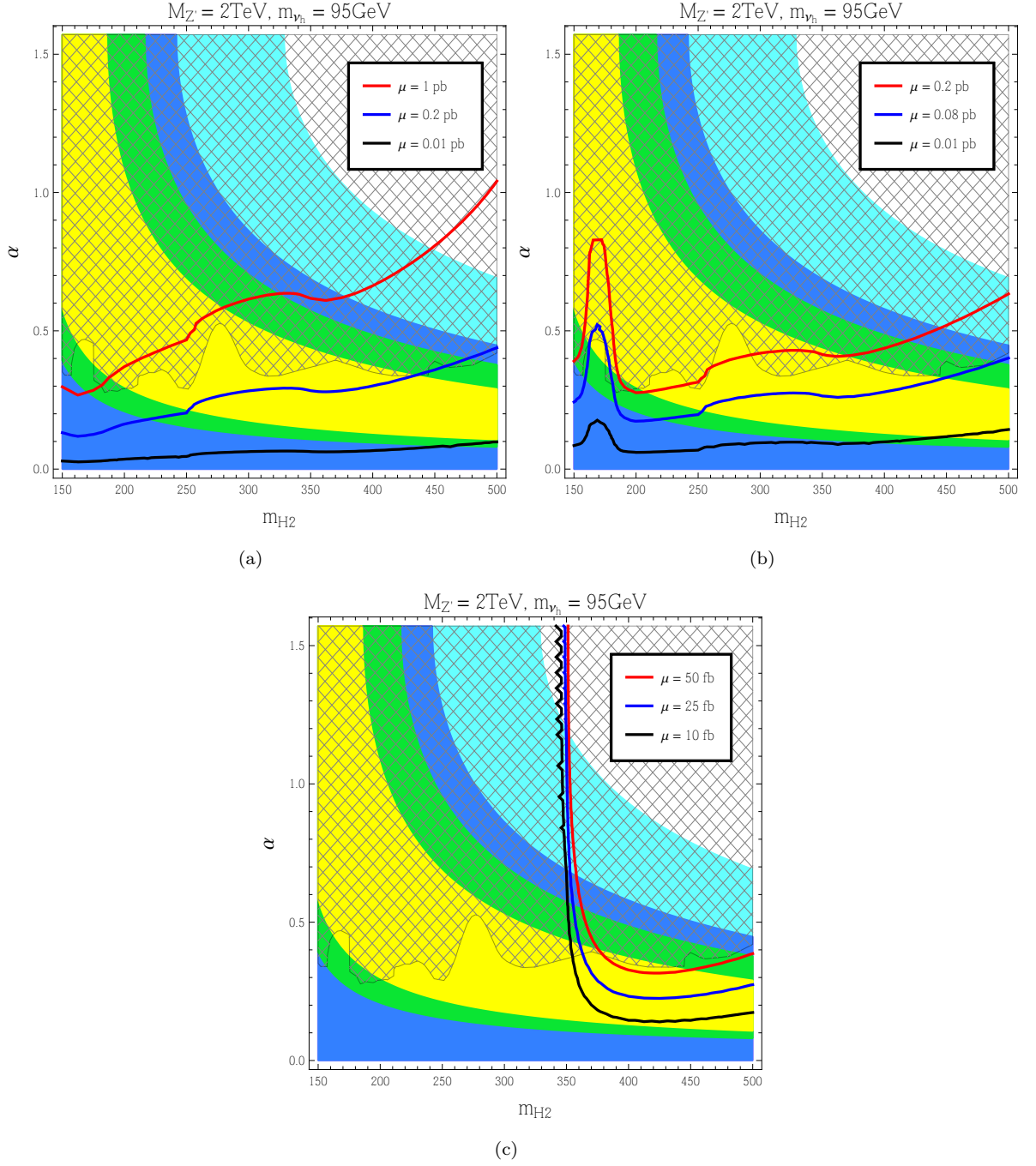


Figure 4.22: Contour plots of the cross section times BR for the processes  $pp \rightarrow H_2 \rightarrow WW$  (a),  $pp \rightarrow H_2 \rightarrow ZZ$  (b) and  $pp \rightarrow H_2 \rightarrow t\bar{t}$  (c) at the LHC with  $\sqrt{s} = 13$  TeV in the  $(m_{H_2}, \alpha)$  plane. Only the gluon fusion channel has been considered. The parameters have been chosen as follows:  $M_{Z'} = 2$  TeV,  $\tilde{g} = -0.13$  and  $g'_1 = 0.11$ .

## Chapter 5

# Final remarks

The dark energy and matter content of the Universe, the matter-antimatter asymmetry, the unnatural distribution of its dimensionless parameters. All these puzzles form some of the clear indications that the SM cannot be the end of the story and that some unknown modification has to take place way before the inclusion of gravity at Planck scale. Obviously no one expects all the answers to come from a sequence of collider with a center of mass energy in exponential growth every decade. More likely, unless a technological revolution will take place, the direct collider research will only be restricted to bite the lowest levels in the energy span that link the Fermi to the Planck scale. New strategies must be invoked to address the exploration of more fundamental, high-energy structures that will always live out of the reach of our direct detection.

Cosmological measurements are certainly of big help in providing a picture of the time, where GUT-like (and upper) energies were exciting the particle content of the “ultimate” theory. Radiative corrections, on their side, also supply a twofold opportunity for our quest. As usually explored, they affect low-energy observables by loop contributions, often clear and measurable, storing the information of high-energy degrees of freedom that are virtually exchanged. This ability of radiative corrections to link different scales, manifests itself also when considering the running of renormalized parameters. The dreamed scenario being the one where an ensemble of disconnected low-energy inputs appear as related, or better unified, when extrapolated at higher energies.

*The subject of this thesis* is the interplay between the phenomenological and the more formal aspects of the RG extrapolation. We suggest the partial conclusions 2.7, 3.4 and 4.6 for a more detailed survey of our results, but we stress here how the general and common flavour along all the chapters is that a coherent application of the RG, when supported with the choice of boundary conditions of experimental value, gives a unique instrument to study the place of a successfully low-energy parametrization into a bigger picture. This scientific attitude, that enjoy a close bound between the experimental characterization and the formal development, has also been our personal achievement that has emerged in our PhD years of research and that will form a solid basis for our, hopefully, future quests.



# Appendix A

## Linear and double seesaw

In full generality, we introduce a Majorana mass term for the right-handed neutrinos and a Yukawa coupling for the fermionic singlets

$$\begin{aligned} \mathcal{L} = & i\overline{N_R}\gamma^\mu(\partial_\mu N_R) + i\overline{S}\gamma^\mu(\partial_\mu S) \\ & - \left[ \overline{N_R}Y_\nu\tilde{H}^\dagger L + \overline{S^C}Y_S\tilde{H}^\dagger L + \overline{N_R}M_R S + \frac{1}{2}\overline{N_R^C}M_N N_R + \frac{1}{2}\overline{S^C}\mu_S S + h.c. \right]. \end{aligned} \quad (\text{A.1})$$

In the left-handed basis  $N_L \equiv (\nu_L, N_R^C, S)^T$  we have, after EW symmetry breaking, the following mass matrix

$$\mathcal{M} = \begin{pmatrix} 0 & m_D^T & m_S^T \\ m_D & M_N & M_R \\ m_S & M_R^T & \mu_S \end{pmatrix}, \quad (\text{A.2})$$

with  $m_D \equiv vY_\nu/\sqrt{2}$  and  $m_S \equiv vY_S/\sqrt{2}$ .

- The linear seesaw [112] corresponds to  $\mu_S = 0$ ,  $M_N = 0$

$$\mathcal{M}_{\text{LSS}} = \begin{pmatrix} 0 & m_D^T & m_S^T \\ m_D & 0 & M_R \\ m_S & M_R^T & 0 \end{pmatrix}. \quad (\text{A.3})$$

In this case the only source of lepton number violation comes from  $m_S$ . Following the standard seesaw approximation we find

$$m_\nu \approx m_D^T (M_R^T)^{-1} m_S + m_S^T M_R^{-1} m_D. \quad (\text{A.4})$$

Generalizing the Casas-Ibarra parametrization [56], we obtain [53]

$$Y_\nu = \frac{\sqrt{2}}{v} M_R (m_S^T)^{-1} U_{\text{PMNS}}^* \sqrt{\hat{m}_\nu} A \sqrt{\hat{m}_\nu} U_{\text{PMNS}}^\dagger, \quad (\text{A.5})$$

where  $A$  is a  $3 \times 3$  matrix satisfying the equation  $A + A^T = \mathbf{1}$ . Consequently,  $A_{ii} = 1/2$  and  $A_{ij} = -A_{ji}$ .

- The double seesaw corresponds to  $m_S = 0$

$$\mathcal{M}_{\text{DSS}} = \begin{pmatrix} 0 & m_D^T & 0 \\ m_D & M_N & M_R \\ 0 & M_R^T & \mu_S \end{pmatrix}. \quad (\text{A.6})$$

The Majorana mass term  $M_N$ , in addition to  $\mu_S$ , violates lepton number for two units. We assume the hierarchy  $M_N \gg M_R \gg m_D \gg \mu_S$ . Integrating out the heavy fields  $N_R$ , we find the effective Lagrangian

$$\begin{aligned} \mathcal{L}_{\text{DSS}}^{\text{eff}} &= \frac{1}{2} \overline{L_i^C} \tilde{H}^* (Y_\nu^T M_N^{-1} Y_\nu)_{ij} \tilde{H}^\dagger L_j + \frac{1}{2} \overline{S_i^C} (M_R^T M_N^{-1} Y_\nu)_{ij} \tilde{H}^\dagger L_j \\ &+ \frac{1}{2} \overline{L_i^C} \tilde{H}^* (Y_\nu^T M_N^{-1} M_R)_{ij} S_j + \frac{1}{2} \overline{S_i^C} (M_R^T M_N^{-1} M_R)_{ij} S_j - \frac{1}{2} \overline{S^C} \mu_S S + h.c. . \end{aligned} \quad (\text{A.7})$$

In the left-handed basis  $N_L = (\nu_L, S)^T$  eq. (A.7) corresponds, after EW symmetry breaking, to the mass matrix

$$\mathcal{M}_{\text{DSS}}^{\text{eff}} = \begin{pmatrix} -m_D^T M_N^{-1} m_D & -m_D^T M_N^{-1} M_R \\ -M_R^T M_N^{-1} m_D & \mu_S - M_R^T M_N^{-1} M_R \end{pmatrix}. \quad (\text{A.8})$$

After block-diagonalization we find

$$V^T \mathcal{M}_{\text{DSS}}^{\text{eff}} V = \begin{pmatrix} m_\nu & 0 \\ 0 & M_{\text{heavy}} \end{pmatrix}, \quad (\text{A.9})$$

where

$$m_\nu = -m_D^T M_N^{-1} m_D - (m_D^T M_N^{-1} M_R) (\mu_S - M_R^T M_N^{-1} M_R)^{-1} (M_R^T M_N^{-1} m_D), \quad (\text{A.10})$$

$$M_{\text{heavy}} = \mu_S - M_R^T M_N^{-1} M_R. \quad (\text{A.11})$$

From eq. (A.10) it follows that  $m_\nu \rightarrow 0$  if  $\mu_S \rightarrow 0$  since the type-I contribution  $m_D^T M_N^{-1} m_D$  cancels out between the two remaining terms. Considering a perturbative expansion in  $\mu_S$ , we find

$$m_\nu \approx m_D^T (M_R^T)^{-1} \mu_S M_R^{-1} m_D. \quad (\text{A.12})$$

As a result, the Casas-Ibarra parametrization is analogue to eq. (3.5). The unitary mixing matrix  $V$  in eq. (A.9) has the general structure

$$V = \begin{pmatrix} \sqrt{\mathbf{1} - BB^\dagger} & B \\ -B^\dagger & \sqrt{\mathbf{1} - B^\dagger B} \end{pmatrix}, \quad (\text{A.13})$$

and, at the lowest order, we find  $B^* = m_D^T (M_R^T)^{-1}$ . For the sake of simplicity, we focus on the case with  $n_R = n_S = 3$ , and we assume  $M_R = \text{diag}(M_{Ri})$ , and  $M_N = \text{diag}(M_{Ni})$  with  $i = 1, 2, 3$ . In this case the heavy block in eq. (A.9) simplifies to  $M_R^T M_N^{-1} M_R = \text{diag}(M_{Ri}^2/M_{Ni})$ . In eq. (A.7) the interactions between the lepton doublets  $L_i$  and the three singlet fermions  $S_i$  are mediated by an effective Yukawa matrix  $\tilde{Y}_\nu \equiv M_R^T M_N^{-1} Y_\nu$ . The previous assumption implies  $(\tilde{Y}_\nu)_{ij} = M_{Ri} (Y_\nu)_{ij} / M_{Ni}$ .

## A.1 Linear seesaw: results

For definiteness, we focus on the case with  $n_R = n_S = 3$ . Considering the low-energy neutrino data, we follow the same strategy outlined in section 3.2.2. We make use of the Casas-Ibarra parametrization in eq. (A.5) to numerically reconstruct the Yukawa matrix  $Y_\nu$ , and we randomly scan over the intervals  $10^2 \text{ GeV} \leq M_{Ri} \leq 10^2 \text{ TeV}$ ,  $10^{-2} \text{ keV} \leq (m_S)_{ij} \leq 10^2 \text{ keV}$ , and  $10^{-1} \leq A_{ij} \leq 10^2$ . As done for the inverse seesaw, we discard points unable to comply with the bounds discussed in section 3.2.1. As far as the stability of the EW vacuum is concerned, in the  $m_S \rightarrow 0$  limit the mass matrix  $\mathcal{M}_{\text{LSS}}$  in eq. (A.3) reduces to the same structure already studied in the inverse seesaw case (see eq. (3.2)). Consequently, in the definition of the Higgs effective quartic coupling we employ the same RG equations, matching conditions and effective potential used in the inverse seesaw analysis. We show the final result of our analysis in fig. A.1 considering a normal ordering of light neutrino masses.

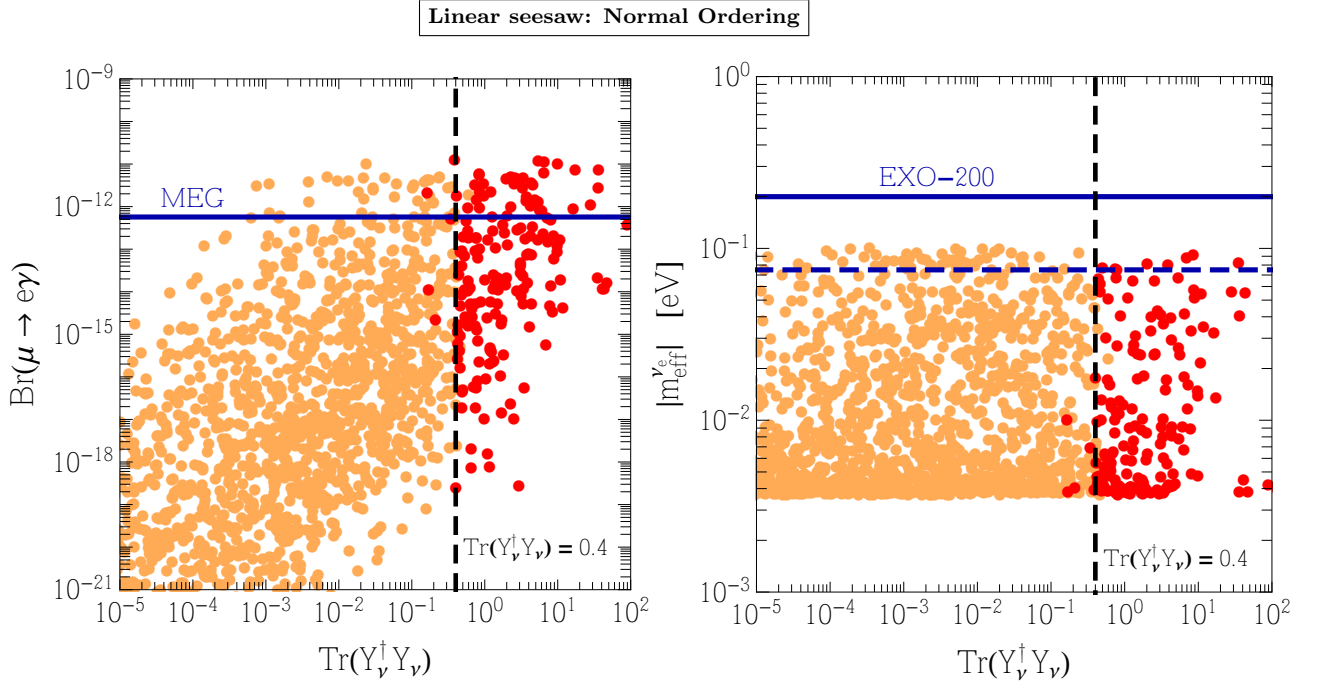


Figure A.1: *The same as in fig. 3.6 but considering the linear seesaw.*

As expected, we find the same quantitative conclusion if compared with the inverse seesaw case. Yukawa couplings such that  $\text{Tr}(Y_\nu^\dagger Y_\nu) \gtrsim 0.4$  are excluded by the metastability bound. Remarkably, considering both the lepton flavor violating process  $\mu \rightarrow e\gamma$  and the  $0\nu 2\beta$ , these points lie in a region of the parameter space close to present or future sensitivities.

## A.2 Double seesaw: results

We follow the same approach already exploited for the inverse and linear seesaw models. However, in the double seesaw case there are few remarkable differences. We use the Casas-Ibarra parametrization

in eq. (3.5) to sample the Yukawa matrix  $Y_\nu$ , and we randomly scan over the intervals  $10 \text{ TeV} \leq M_{Ri} \leq 10^3 \text{ TeV}$ ,  $10^9 \text{ GeV} \leq M_{Ni} \leq 10^{11} \text{ GeV}$ , and  $10 \text{ keV} \leq (\mu_S)_{ij} \leq 10^4 \text{ keV}$ . Few comments are in order. First, notice that this choice of parameters – optimized in order to obtain  $\mathcal{O}(1)$  Yukawa couplings – respects the hierarchy  $M_N \gg M_R \gg m_D \gg \mu_S$  assumed above (see discussion below eq. (A.6)). Second, we expect the following order of magnitude estimates: for the mixing parameter in eq. (A.13),  $B \sim \mathcal{O}(10^{-3})$ ; for the mass of the heavy neutrinos in eq. (A.11),  $M_{\text{heavy}} \sim \mathcal{O}(1) \text{ GeV}$ ; for the effective Yukawa coupling in eq. (A.7),  $\tilde{Y}_\nu \sim 10^{-5} Y_\nu$ . Armed with these numbers, we can outline as follows. At large renormalization scale values,  $\mu \gg M_{Ni}$ , the model is described by the full Lagrangian in eq. (A.1) (with  $Y_S = 0$ ). In terms of the RG running, the only relevant parameter is the Yukawa matrix  $Y_\nu$  describing the interactions between the Higgs doublet, the lepton doublets and the three right-handed heavy neutrinos. At this stage, the situation is formally equivalent to the familiar type-I seesaw.<sup>1</sup> There is, however, one remarkable difference. In the type-I seesaw right-handed neutrino masses  $M_{Ni} \sim \mathcal{O}(10^9) \text{ GeV}$  require, in order to reproduce low-energy neutrino phenomenology, small Yukawa couplings (typically  $Y_\nu \sim 10^{-5}$ ). As a consequence, the impact of the interactions  $\overline{N}_R Y_\nu \tilde{H}^\dagger L + h.c.$  on the running of the Higgs quartic couplings is negligible. In the double seesaw case, on the contrary, we are allowed to consider  $\mathcal{O}(1)$  Yukawa couplings since the mass of light neutrinos is set by  $\mu_S$  (see eq. (A.12)). Below the thresholds  $M_{Ni}$  the heavy right-handed neutrinos are integrated out, and eventually the model is described by the effective Lagrangian in eq. (A.7). Given our choice of parameters, in this region the running is approximately equivalent to the pure SM since for the effective Yukawa interactions  $\overline{L}^C \tilde{H}^* \tilde{Y}_\nu S$  we expect  $\tilde{Y}_\nu \sim 10^{-5} Y_\nu$ .

We summarize our results in fig. A.2. In the left panel, we show the running of the effective Higgs quartic coupling for a specific realization of the double seesaw model with  $\text{Tr}(Y_\nu^\dagger Y_\nu) \simeq 0.62$ . Above the thresholds  $M_{Ni}$  the Yukawa couplings  $Y_\nu$  largely affect the running of  $\lambda_{\text{eff}}$  eventually violating the metastability bound before the Planck scale. In the right panel we show the result of our numerical scan focusing on the effective neutrino mass relevant for the  $0\nu 2\beta$ . The most striking difference with respect to the inverse and linear seesaw models (see, respectively, figs. 3.6, A.1) is that the presence of additional neutrinos with mass  $M_{\text{heavy}} \sim \mathcal{O}(1) \text{ GeV}$  gives a sizable contribution to  $m_{\text{eff}}^{\nu e}$ . As a result, numerous points in our numerical analysis are close to (or even exceed) the present experimental bound. We find that Yukawa couplings such that  $\text{Tr}(Y_\nu^\dagger Y_\nu) \gtrsim 0.6$  are excluded by the metastability bound.

---

<sup>1</sup>In concrete, the contribution of each heavy right-handed neutrino to the effective quartic coupling is given by eq. (3.20) (divided by two, since now there is no double degeneracy) while for the  $\beta$  functions we exploit the same two-loop expression already discussed in section 3.3.3 (see eq. (3.31) for the one-loop approximation).

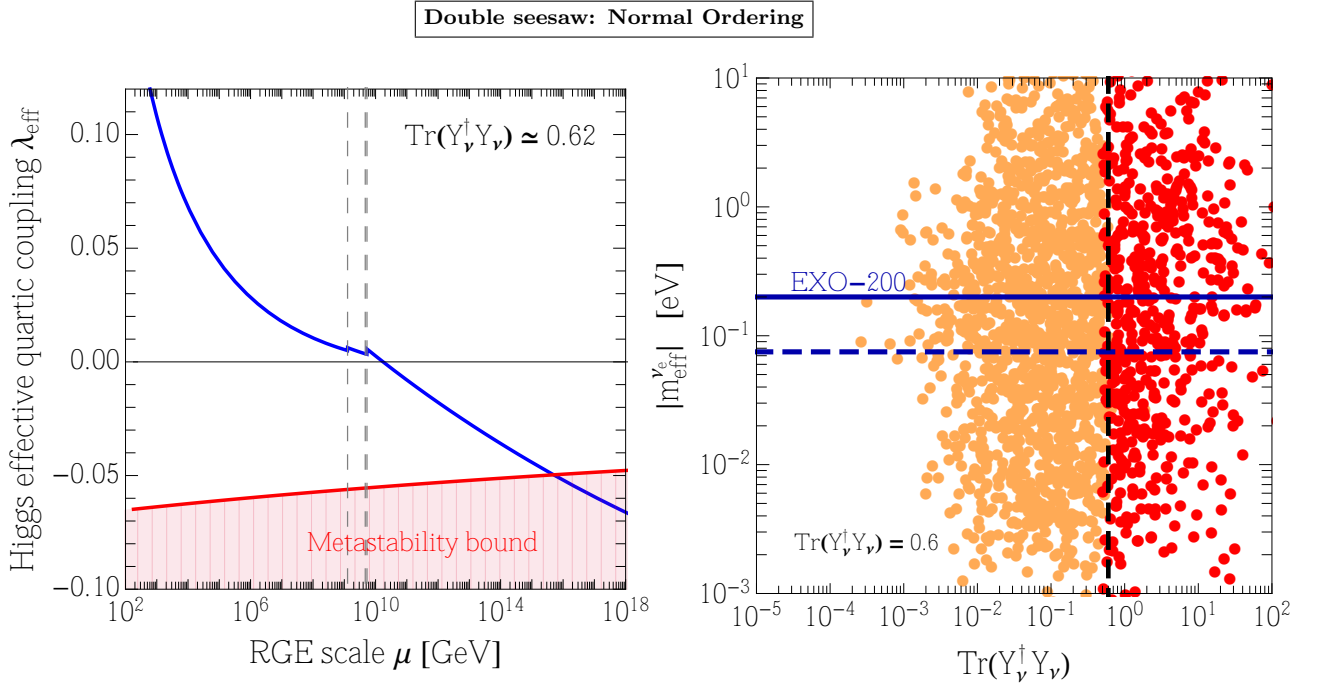


Figure A.2: *Left panel.* Running of the effective Higgs quartic coupling in the double seesaw model. *Right-handed neutrinos* with mass  $M_{N_i} \sim \mathcal{O}(10^9)$  GeV (vertical dashed lines) notably affect the RG evolution thanks to  $\mathcal{O}(1)$  Yukawa couplings. In the analyzed case, Yukawa couplings such that  $\text{Tr}(Y_\nu^\dagger Y_\nu) \approx 0.62$  exceed the metastability bound below the Planck scale. *Right panel.* Effective neutrino mass as a function of the trace of the Yukawa couplings,  $\text{Tr}(Y_\nu^\dagger Y_\nu)$ .



## Appendix B

# One-loop $\beta$ functions for non-anomalous $U(1)'$ model with generic charge assignment

We give in this appendix the one-loop  $\beta$  functions employed in chapter 4 with complete freedom in the choice of the  $U(1)'$  charge, given in term of  $z_Q$ , charge of the quark doublet, and  $z_u$ , charge of the RH quark up ([162, 163]).

### $\beta$ functions of gauge coupling constants

$$\beta_g^{(1)} = \frac{41g^3}{6} \quad \beta_{g_2'}^{(1)} = -\frac{19g_2'^3}{6} \quad \beta_{g_3'}^{(1)} = -7g_3'^3 \quad (\text{B.1})$$

$$\beta_{g_1'}^{(1)} = g_1'^2 \left( \frac{46\tilde{g}z_Q}{3} + \frac{50\tilde{g}z_u}{3} \right) + \frac{41g_1'\tilde{g}^2}{6} + g_1'^3 (-44z_Qz_u + 134z_Q^2 + 18z_u^2) \quad (\text{B.2})$$

$$\begin{aligned} \beta_{\tilde{g}}^{(1)} &= \tilde{g} \left( \frac{41g^2}{3} - 44g_1'^2 z_Q z_u + 134g_1'^2 z_Q^2 + 18g_1'^2 z_u^2 \right) + \tilde{g}^2 \left( \frac{46g_1'z_Q}{3} + \frac{50g_1'z_u}{3} \right) \\ &+ \frac{41\tilde{g}^3}{6} + \frac{46}{3}g^2 g_1' z_Q + \frac{50}{3}g^2 g_1' z_u \end{aligned} \quad (\text{B.3})$$

### $\beta$ functions of Yukawa interactions

$$\begin{aligned} \beta_{Y_t}^{(1)} &= Y_t \left( -g_1'\tilde{g}z_Q - 4g_1'\tilde{g}z_u - \frac{17\tilde{g}^2}{12} - \frac{17g^2}{12} - \frac{9g_2'^2}{4} - 8g_3'^2 - 3g_1'^2 z_Q^2 - 3g_1'^2 z_u^2 \right) + \frac{9Y_t^3}{2} \\ \beta_{Y_N}^{(1)} &= Y_N \left( 48g_1'^2 z_Q z_u - 96g_1'^2 z_Q^2 - 6g_1'^2 z_u^2 \right) + 10Y_N^3 \end{aligned} \quad (\text{B.4})$$

**$\beta$  functions of quartic scalar interactions**

$$\begin{aligned}
\beta_{\lambda_1}^{(1)} &= \lambda_1 \left( 12g'_1 \tilde{g} z_Q - 12g'_1 \tilde{g} z_u - 3\tilde{g}^2 - 3g^2 - 9g_2^2 + 24g_1'^2 z_Q z_u - 12g_1'^2 z_Q^2 - 12g_1'^2 z_u^2 + 12Y_t^2 \right) \\
&\quad - 3g^2 g'_1 \tilde{g} z_Q + 3g^2 g'_1 \tilde{g} z_u + \frac{3}{4} g^2 \tilde{g}^2 - 36g_1'^3 \tilde{g} z_Q z_u^2 + 36g_1'^3 \tilde{g} z_Q^2 z_u - 12g_1'^3 \tilde{g} z_Q^3 + 12g_1'^3 \tilde{g} z_u^3 \\
&\quad - 18g_1'^2 \tilde{g}^2 z_Q z_u + 9g_1'^2 \tilde{g}^2 z_Q^2 + 9g_1'^2 \tilde{g}^2 z_u^2 - 3g_1' \tilde{g}^3 z_Q - 3g_2^2 g_1' \tilde{g} z_Q + 3g_1' \tilde{g}^3 z_u + 3g_2^2 g_1' \tilde{g} z_u \\
&\quad + \frac{3\tilde{g}^4}{8} + \frac{3}{4} g_2^2 \tilde{g}^2 + \frac{3g^4}{8} - 6g^2 g_1'^2 z_Q z_u + 3g^2 g_1'^2 z_Q^2 + 3g^2 g_1'^2 z_u^2 + \frac{3}{4} g_2^2 g^2 - 6g_2^2 g_1'^2 z_Q z_u \\
&\quad + 3g_2^2 g_1'^2 z_Q^2 + 3g_2^2 g_1'^2 z_u^2 + \frac{9g_2^4}{8} - 24g_1'^4 z_Q z_u^3 + 36g_1'^4 z_Q^2 z_u^2 - 24g_1'^4 z_Q^3 z_u + 6g_1'^4 z_Q^4 \\
&\quad + 6g_1'^4 z_u^4 + 24\lambda_1^2 + \lambda_3^2 - 6Y_t^4
\end{aligned} \tag{B.5}$$

$$\begin{aligned}
\beta_{\lambda_2}^{(1)} &= -1536g_1'^4 z_Q z_u^3 + 9216g_1'^4 z_Q^2 z_u^2 - 24576g_1'^4 z_Q^3 z_u + 24576g_1'^4 z_Q^4 + 96g_1'^4 z_u^4 \\
&\quad + \lambda_2 \left( 384g_1'^2 z_Q z_u - 768g_1'^2 z_Q^2 - 48g_1'^2 z_u^2 + 24Y_N^2 \right) + 20\lambda_2^2 + 2\lambda_3^2 - 48Y_N^4
\end{aligned} \tag{B.6}$$

$$\begin{aligned}
\beta_{\lambda_3}^{(1)} &= \lambda_3 \left( 6g_1' \tilde{g} z_Q - 6g_1' \tilde{g} z_u - \frac{3\tilde{g}^2}{2} - \frac{3g^2}{2} - \frac{9g_2^2}{2} + 204g_1'^2 z_Q z_u - 390g_1'^2 z_Q^2 - 30g_1'^2 z_u^2 \right. \\
&\quad \left. + 12\lambda_1 + 8\lambda_2 + 12Y_N^2 + 6Y_t^2 \right) - 432g_1'^3 \tilde{g} z_Q z_u^2 + 1152g_1'^3 \tilde{g} z_Q^2 z_u - 768g_1'^3 \tilde{g} z_Q^3 + 48g_1'^3 \tilde{g} z_u^3 \\
&\quad - 96g_1'^2 \tilde{g}^2 z_Q z_u + 192g_1'^2 \tilde{g}^2 z_Q^2 + 12g_1'^2 \tilde{g}^2 z_u^2 - 480g_1'^4 z_Q z_u^3 + 1584g_1'^4 z_Q^2 z_u^2 \\
&\quad - 1920g_1'^4 z_Q^3 z_u + 768g_1'^4 z_Q^4 + 48g_1'^4 z_u^4 + 4\lambda_3^2
\end{aligned} \tag{B.7}$$

## Appendix C

# Two-loop $\beta$ functions for non-anomalous $U(1)'$ model

We give in this appendix the complete set of the two-loop  $\beta$  functions employed in chapter 4 ([162, 163]). The choice for  $z_Q$  and  $z_u$  is the one corresponding to  $B-L$  assignment.

### $\beta$ functions of gauge coupling constants

$$\beta_{g_2}^{(2)} = g_2^3 \left( 4g_1' \tilde{g} + \frac{3\tilde{g}^2}{2} + \frac{3g^2}{2} + 12g_3^2 + 4g_1'^2 - \frac{3Y_t^2}{2} \right) + \frac{35g_2^5}{6} \quad (\text{C.1})$$

$$\beta_{g_3}^{(2)} = g_3^3 \left( \frac{4g_1' \tilde{g}}{3} + \frac{11\tilde{g}^2}{6} + \frac{11g^2}{6} + \frac{9g_2^2}{2} + \frac{4g_1'^2}{3} - 2Y_t^2 \right) - 26g_3^5 \quad (\text{C.2})$$

$$\beta_g^{(2)} = g^3 \left( \frac{164g_1' \tilde{g}}{9} + \frac{199\tilde{g}^2}{18} + \frac{9g_2^2}{2} + \frac{44g_3^2}{3} + \frac{92g_1'^2}{9} - \frac{17Y_t^2}{3} \right) + \frac{199g^5}{18} \quad (\text{C.3})$$

$$\begin{aligned} \beta_{\tilde{g}}^{(2)} &= \tilde{g}^2 \left( \frac{656g^2 g_1'}{9} + 12g_2^2 g_1' + \frac{32g_3^2 g_1'}{3} + \frac{448g_1'^3}{9} - \frac{10g_1' Y_t^2}{3} \right) \\ &+ \tilde{g}^3 \left( \frac{199g^2}{6} + \frac{9g_2^2}{2} + \frac{44g_3^2}{3} + \frac{184g_1'^2}{3} - \frac{17Y_t^2}{6} \right) \\ &+ \tilde{g} \left( \frac{199g^4}{9} + \frac{644g^2 g_1'^2}{9} - \frac{17}{3} g^2 Y_t^2 + 9g_2^2 g^2 + \frac{88}{3} g_3^2 g^2 + 12g_2^2 g_1'^2 \right) \\ &+ \frac{32}{3} g_3^2 g_1'^2 + \frac{800g_1'^4}{9} - 12g_1'^2 Y_t^2 - \frac{4}{3} g_1'^2 Y_t^2 \\ &+ \frac{328g_1' \tilde{g}^4}{9} + \frac{199\tilde{g}^5}{18} + \frac{164g^4 g_1'}{9} + \frac{224g^2 g_1'^3}{9} \\ &- \frac{10}{3} g^2 g_1' Y_t^2 + 12g^2 g_2^2 g_1' + \frac{32}{3} g^2 g_3^2 g_1' \end{aligned} \quad (\text{C.4})$$

$$\begin{aligned}
\beta_{g_1'}^{(2)} &= g_1'^3 \left( \frac{184\tilde{g}^2}{3} + \frac{92g^2}{9} + 12g_2^2 + \frac{32g_3^2}{3} - 12Y_N^2 - \frac{4Y_t^2}{3} \right) \\
&+ g_1'^2 \left( \frac{164g^2\tilde{g}}{9} - \frac{10}{3}\tilde{g}Y_t^2 + \frac{328\tilde{g}^3}{9} + 12g_2^2\tilde{g} + \frac{32}{3}g_3^2\tilde{g} \right) \\
&+ g_1' \left( \frac{199}{18}g^2\tilde{g}^2 - \frac{17}{6}\tilde{g}^2Y_t^2 + \frac{199\tilde{g}^4}{18} + \frac{9}{2}g_2^2\tilde{g}^2 + \frac{44}{3}g_3^2\tilde{g}^2 \right) \\
&+ \frac{448g_1'^4\tilde{g}}{9} + \frac{800g_1'^5}{9}
\end{aligned} \tag{C.5}$$

### $\beta$ functions of Yukawa interactions

$$\begin{aligned}
\beta_{Y_t}^{(2)} &= Y_t^3 \left( \frac{25g_1'\tilde{g}}{4} + \frac{131\tilde{g}^2}{16} + \frac{131g^2}{16} + \frac{225g_2^2}{16} + 36g_3^2 + 3g_1'^2 - 12\lambda_1 \right) \\
&+ Y_t \left( \frac{502}{27}g^2g_1'\tilde{g} + \frac{1187}{108}g^2\tilde{g}^2 + \frac{665g_1'^3\tilde{g}}{27} + \frac{1085}{36}g_1'^2\tilde{g}^2 + \frac{502g_1'\tilde{g}^3}{27} \right. \\
&+ \frac{9}{4}g_2^2g_1'\tilde{g} - \frac{20}{9}g_3^2g_1'\tilde{g} + \frac{1187\tilde{g}^4}{216} - \frac{3}{4}g_2^2\tilde{g}^2 + \frac{19}{9}g_3^2\tilde{g}^2 + \frac{1187g^4}{216} \\
&+ \frac{91g^2g_1'^2}{12} - \frac{3}{4}g_2^2g^2 + \frac{19}{9}g_3^2g^2 + \frac{3}{4}g_2^2g_1'^2 - \frac{8}{9}g_3^2g_1'^2 - \frac{23g_2^4}{4} \\
&\left. - 108g_3^4 + 9g_2^2g_3^2 + \frac{203g_1'^4}{27} + 6\lambda_1^2 + \frac{\lambda_3^2}{2} \right) - 12Y_t^5
\end{aligned} \tag{C.6}$$

$$\begin{aligned}
\beta_{Y_N}^{(2)} &= Y_N \left( -\frac{32g_1'^3\tilde{g}}{3} - \frac{35}{6}g_1'^2\tilde{g}^2 - 127g_1'^4 + 4\lambda_2^2 + \lambda_3^2 \right) \\
&+ (206g_1'^2 - 32\lambda_2)Y_N^3 - 44Y_N^5
\end{aligned} \tag{C.7}$$

### $\beta$ functions of quartic scalar interactions

$$\begin{aligned}
\beta_{\lambda_1}^{(2)} &= -\frac{32}{3}g^4g_1'\tilde{g} - \frac{379}{16}g^4\tilde{g}^2 - 13g^2g_1'^2\tilde{g}^2 - 10g^2g_1'\tilde{g}Y_t^2 - \frac{64}{3}g^2g_1'\tilde{g}^3 \\
&- \frac{32}{3}g_2^2g^2g_1'\tilde{g} + \lambda_1^2(36\tilde{g}^2 + 36g^2 + 108g_2^2 - 144Y_t^2) \\
&- \frac{19}{2}g^2\tilde{g}^2Y_t^2 - \frac{379}{16}g^2\tilde{g}^4 - \frac{559}{24}g_2^2g^2\tilde{g}^2 + \lambda_1 \left( \frac{80}{3}g^2g_1'\tilde{g} + \frac{629}{12}g^2\tilde{g}^2 \right. \\
&+ 34g_1'^2\tilde{g}^2 + \frac{50}{3}g_1'\tilde{g}Y_t^2 + \frac{80g_1'\tilde{g}^3}{3} + \frac{85}{6}\tilde{g}^2Y_t^2 + \frac{629\tilde{g}^4}{24} + \frac{39}{4}g_2^2\tilde{g}^2 \\
&+ \frac{629g^4}{24} + \frac{85}{6}g^2Y_t^2 + \frac{39}{4}g_2^2g^2 + \frac{45}{2}g_2^2Y_t^2 + 80g_3^2Y_t^2 - \frac{73g_2^4}{8} \\
&\left. + \frac{20}{3}g_1'^2Y_t^2 - 10\lambda_3^2 - 3Y_t^4 \right) + 20g_1'^2\lambda_3\tilde{g}^2 - 4g_1'^2\tilde{g}^2Y_t^2 - 13g_1'^2\tilde{g}^4 \\
&- 13g_2^2g_1'^2\tilde{g}^2 - \frac{20}{3}g_1'\tilde{g}Y_t^4 - 10g_1'\tilde{g}^3Y_t^2 + 6g_2^2g_1'\tilde{g}Y_t^2 - \frac{32g_1'\tilde{g}^5}{3}
\end{aligned}$$

$$\begin{aligned}
& -\frac{32}{3}g_2^2g_1'\tilde{g}^3 - \frac{8}{3}\tilde{g}^2Y_t^4 - \frac{19}{4}\tilde{g}^4Y_t^2 + \frac{21}{2}g_2^2\tilde{g}^2Y_t^2 - \frac{379\tilde{g}^6}{48} - \frac{289}{48}g_2^4\tilde{g}^2 \\
& -\frac{559}{48}g_2^2\tilde{g}^4 - \frac{379g^6}{48} - \frac{19}{4}g^4Y_t^2 - \frac{559}{48}g_2^2g^4 - \frac{8}{3}g^2Y_t^4 + \frac{21}{2}g_2^2g^2Y_t^2 \\
& -\frac{289}{48}g_2^4g^2 - 32g_3^2Y_t^4 - \frac{9}{4}g_2^4Y_t^2 + \frac{305g_2^6}{16} + 32g_1'^2\lambda_3^2 - \frac{8}{3}g_1'^2Y_t^4 \\
& -312\lambda_1^3 - 4\lambda_3^3 - 12\lambda_3^2Y_N^2 + 30Y_t^6
\end{aligned} \tag{C.8}$$

$$\begin{aligned}
\beta_{\lambda_2}^{(2)} &= -\frac{8192g_1'^5\tilde{g}}{3} - \frac{5344}{3}g_1'^4\tilde{g}^2 + 40g_1'^2\lambda_3\tilde{g}^2 + \\
& \lambda_2 \left( \frac{1280g_1'^3\tilde{g}}{3} + \frac{844}{3}g_1'^2\tilde{g}^2 + 2112g_1'^4 + 120g_1'^2Y_N^2 - 20\lambda_3^2 + 48Y_N^4 \right) \\
& + 4\lambda_3^2\tilde{g}^2 + 4g^2\lambda_3^2 + 12g_2^2\lambda_3^2 - 7168g_1'^6 + 768g_1'^4Y_N^2 + \lambda_2^2 \left( 448g_1'^2 - 240Y_N^2 \right) \\
& + 192g_1'^2Y_N^4 - 240\lambda_2^3 - 8\lambda_3^3 + 768Y_N^6 - 12\lambda_3^2Y_t^2
\end{aligned} \tag{C.9}$$

$$\begin{aligned}
\beta_{\lambda_3}^{(2)} &= -\frac{512}{3}g^2g_1'^3\tilde{g} + \lambda_3^2 \left( \tilde{g}^2 + g^2 + 3g_2^2 + 16g_1'^2 - 72\lambda_1 - 48\lambda_2 - 24Y_N^2 - 12Y_t^2 \right) \\
& -\frac{713}{3}g^2g_1'^2\tilde{g}^2 + \lambda_3 \left( \frac{40}{3}g^2g_1'\tilde{g} + \frac{557}{24}g^2\tilde{g}^2 + \frac{640g_1'^3\tilde{g}}{3} + \frac{497}{3}g_1'^2\tilde{g}^2 \right. \\
& + \frac{25}{3}g_1'\tilde{g}Y_t^2 + \frac{40g_1'\tilde{g}^3}{3} + 24\lambda_1\tilde{g}^2 + \frac{85}{12}\tilde{g}^2Y_t^2 + \frac{557\tilde{g}^4}{48} + \frac{15}{8}g_2^2\tilde{g}^2 + \frac{557g^4}{48} \\
& + 24g^2\lambda_1 + \frac{85}{12}g^2Y_t^2 + \frac{15}{8}g_2^2g^2 + 72g_2^2\lambda_1 + \frac{45}{4}g_2^2Y_t^2 + 40g_3^2Y_t^2 - \frac{145g_2^4}{16} \\
& + 672g_1'^4 + 256g_1'^2\lambda_2 + 60g_1'^2Y_N^2 + \frac{10}{3}g_1'^2Y_t^2 - 60\lambda_1^2 - 40\lambda_2^2 - 96\lambda_2Y_N^2 \\
& \left. - 72Y_N^4 - 72\lambda_1Y_t^2 - \frac{27Y_t^4}{2} \right) - 656g_1'^4\tilde{g}^2 - 160g_1'^3\tilde{g}Y_t^2 - \frac{1024}{3}g_1'^3\tilde{g}^3 \\
& + 120g_1'^2\lambda_1\tilde{g}^2 + 80g_1'^2\lambda_2\tilde{g}^2 + 48g_1'^2\tilde{g}^2Y_N^2 - 76g_1'^2\tilde{g}^2Y_t^2 - \frac{713}{3}g_1'^2\tilde{g}^4 \\
& - 45g_2^2g_1'^2\tilde{g}^2 - 64g_1'^4Y_t^2 - 11\lambda_3^3
\end{aligned} \tag{C.10}$$



# Bibliography

- [1] M. Gell-Mann and F. E. Low, Phys. Rev. **95** (1954) 1300.
- [2] S. R. Coleman and E. J. Weinberg, Phys. Rev. D **7** (1973) 1888.
- [3] G. Jona-Lasinio, Nuovo Cim. **34** (1964) 1790.
- [4] N. Cabibbo, L. Maiani, G. Parisi and R. Petronzio, Nucl. Phys. B **158**, 295 (1979).
- [5] L. F. Abbott, Acta Phys. Polon. B **13** (1982) 33.
- [6] R. Jackiw, Phys. Rev. D **9** (1974) 1686.
- [7] M. E. Peskin and D. V. Schroeder, Reading, USA: Addison-Wesley (1995) 842 p
- [8] C. Ford, D. R. T. Jones, P. W. Stephenson and M. B. Einhorn, Nucl. Phys. B **395** (1993) 17 [hep-lat/9210033].
- [9] T. Appelquist and J. Carazzone, Phys. Rev. D **11** (1975) 2856.
- [10] H. Georgi, Ann. Rev. Nucl. Part. Sci. **43** (1993) 209.
- [11] M. Bando, T. Kugo, N. Maekawa and H. Nakano, Prog. Theor. Phys. **90** (1993) 405 [hep-ph/9210229].
- [12] S. R. Coleman, Phys. Rev. D **15** (1977) 2929 Erratum: [Phys. Rev. D **16** (1977) 1248].
- [13] C. G. Callan, Jr. and S. R. Coleman, Phys. Rev. D **16** (1977) 1762.
- [14] G. W. Anderson, Phys. Lett. B **243** (1990) 265.
- [15] P. B. Arnold and S. Vokos, Phys. Rev. D **44** (1991) 3620.
- [16] J. R. Espinosa and M. Quiros, Phys. Lett. B **353** (1995) 257 [hep-ph/9504241].
- [17] M. Quiros, Helv. Phys. Acta **67** (1994) 451.
- [18] J. I. Kapusta and C. Gale, “Finite-temperature field theory: Principles and applications.”
- [19] D. J. Gross, R. D. Pisarski and L. G. Yaffe, Rev. Mod. Phys. **53** (1981) 43.
- [20] J. R. Espinosa, G. F. Giudice and A. Riotto, JCAP **0805**, 002 (2008) [arXiv:0710.2484].

- [21] J. R. Espinosa, G. F. Giudice, E. Morgante, A. Riotto, L. Senatore, A. Strumia and N. Tetradis, [arXiv:1505.04825].
- [22] G. Aad *et al.* [ATLAS Collaboration], Phys. Lett. B **716**, 1 (2012) [arXiv:1207.7214].
- [23] S. Chatrchyan *et al.* [CMS Collaboration], Phys. Lett. B **716**, 30 (2012) [arXiv:1207.7235].
- [24] G. Aad *et al.* [ATLAS and CMS Collaborations], Phys. Rev. Lett. **114**, 191803 (2015) [arXiv:1503.07589].
- [25] G. Degrassi, S. Di Vita, J. Elias-Miro, J. R. Espinosa, G. F. Giudice, G. Isidori and A. Strumia, JHEP **1208** (2012) 098 [arXiv:1205.6497].
- [26] D. Buttazzo, G. Degrassi, P. P. Giardino, G. F. Giudice, F. Sala, A. Salvio and A. Strumia, JHEP **1312** (2013) 089 [arXiv:1307.3536].
- [27] F. Bezrukov and M. Shaposhnikov, J. Exp. Theor. Phys. **120**, 335 (2015) [Zh. Eksp. Teor. Fiz. **147**, 389 (2015)] [arXiv:1411.1923].
- [28] For a review, see: A. D. Linde, Contemp. Concepts Phys. **5**, 1 (1990) [hep-th/0503203].
- [29] R. Allahverdi, R. Brandenberger, F. Y. Cyr-Racine and A. Mazumdar, Ann. Rev. Nucl. Part. Sci. **60** (2010) 27 [arXiv:1001.2600].
- [30] L. F. Abbott and S. Y. Pi, Singapore, Singapore: World Scientific (1986) 697 p
- [31] P. A. R. Ade *et al.* [Planck Collaboration], [arXiv:1502.02114].
- [32] R. J. Scherrer and M. S. Turner, Phys. Rev. D **31** (1985) 681.
- [33] G. F. Giudice, E. W. Kolb and A. Riotto, Phys. Rev. D **64** (2001) 023508 [hep-ph/0005123].
- [34] G. F. Giudice, A. Notari, M. Raidal, A. Riotto and A. Strumia, Nucl. Phys. B **685** (2004) 89 [hep-ph/0310123].
- [35] S. Davidson, E. Nardi and Y. Nir, Phys. Rept. **466**, 105 (2008) [arXiv:0802.2962].
- [36] L. Delle Rose, C. Marzo and A. Urbano, JHEP **1605** (2016) 050 [arXiv:1507.06912].
- [37] G. Isidori, G. Ridolfi and A. Strumia, Nucl. Phys. B **609** (2001) 387 [hep-ph/0104016].
- [38] S. Alekhin, A. Djouadi and S. Moch, Phys. Lett. B **716**, 214 (2012) [arXiv:1207.0980].
- [39] V. Branchina, E. Messina and M. Sher, Phys. Rev. D **91**, 013003 (2015) [arXiv:1408.5302].
- [40] B. M. Kastening, Phys. Lett. B **283** (1992) 287.
- [41] M. Bando, T. Kugo, N. Maekawa and H. Nakano, Phys. Lett. B **301** (1993) 83 [hep-ph/9210228].
- [42] S. Weinberg, Phys. Rev. D **22**, 1694 (1980).

- [43] P. Minkowski, Phys. Lett. **B67**, 421 (1977).
- [44] M. Gell-Mann, P. Ramond and R. Slansky, (1979), Print-80-0576 (CERN).
- [45] T. Yanagida, (KEK lectures, 1979), ed. Sawada and Sugamoto (KEK, 1979).
- [46] R. N. Mohapatra and G. Senjanovic, Phys. Rev. Lett. **44**, 91 (1980).
- [47] R. N. Mohapatra and J. W. F. Valle, Phys. Rev. D **34**, 1642 (1986).
- [48] M. C. Gonzalez-Garcia and J. W. F. Valle, Phys. Lett. B **216**, 360 (1989).
- [49] A. Pilaftsis, Z. Phys. C **55**, 275 (1992) [[hep-ph/9901206](#)].
- [50] R. N. Mohapatra, S. Antusch, K. S. Babu, G. Barenboim, M. C. Chen, A. de Gouvea, P. de Holanda and B. Dutta *et al.*, Rept. Prog. Phys. **70**, 1757 (2007) [[hep-ph/0510213](#)].
- [51] A. de Gouvea, J. Jenkins and N. Vasudevan, Phys. Rev. D **75**, 013003 (2007) [[hep-ph/0608147](#)].
- [52] J. Kersten and A. Y. Smirnov, Phys. Rev. D **76**, 073005 (2007) [[arXiv:0705.3221](#)].
- [53] D. V. Forero, S. Morisi, M. Tortola and J. W. F. Valle, JHEP **1109**, 142 (2011) [[arXiv:1107.6009](#)].
- [54] G. 't Hooft, *Recent Developments in Gauge Theories* in Proc. 1979 Cargèse Summer Institute (ed. G. 't Hooft e al., Plenum Press, NY 1980).
- [55] A. Abada, G. Arcadi and M. Lucente, JCAP10(2014)001 [[arXiv:1406.6556](#)].
- [56] J. A. Casas and A. Ibarra, Nucl. Phys. B **618**, 171 (2001) [[hep-ph/0103065](#)].
- [57] F. P. An *et al.* [Daya Bay Collaboration], Phys. Rev. Lett. **112**, 061801 (2014) [[arXiv:1310.6732](#)].
- [58] J. K. Ahn *et al.* [RENO Collaboration], Phys. Rev. Lett. **108**, 191802 (2012) [[arXiv:1204.0626](#)].
- [59] S.-H. Seo, talk at NEUTRINO 2014, *XXVI International Conference on Neutrino Physics and Astrophysics*, June 2-7, 2014, Boston (U.S.A.) [SLIDES].
- [60] K. Abe *et al.* [T2K Collaboration], Phys. Rev. Lett. **111**, no. 21, 211803 (2013) [[arXiv:1308.0465](#)].
- [61] K. Abe *et al.* [T2K Collaboration], Phys. Rev. Lett. **112**, 061802 (2014) [[arXiv:1311.4750](#)].
- [62] P. Adamson *et al.* [MINOS Collaboration], Phys. Rev. Lett. **110**, no. 25, 251801 (2013) [[arXiv:1304.6335](#)].
- [63] P. Adamson *et al.* [MINOS Collaboration], Phys. Rev. Lett. **110**, no. 17, 171801 (2013) [[arXiv:1301.4581](#)].
- [64] M. C. Gonzalez-Garcia, M. Maltoni and T. Schwetz, JHEP **1411**, 052 (2014) [[arXiv:1409.5439](#)]. See also the  $\mathcal{L}$ fit website.
- [65] S. Antusch, J. P. Baumann and E. Fernandez-Martinez, Nucl. Phys. B **810**, 369 (2009) [[arXiv:0807.1003](#)].

- [66] S. Antusch and O. Fischer, JHEP **1410**, 94 (2014) [[arXiv:1407.6607](#)].
- [67] L. Basso, O. Fischer and J. J. van der Bij, Europhys. Lett. **105**, no. 1, 11001 (2014) [[arXiv:1310.2057](#)].
- [68] P. A. R. Ade *et al.* [Planck Collaboration], Astron. Astrophys. **571**, A16 (2014) [[arXiv:1303.5076](#)].
- [69] R. E. Shrock, Phys. Lett. B **96**, 159 (1980).
- [70] R. E. Shrock, Phys. Rev. D **24**, 1232 (1981).
- [71] A. Ilakovac and A. Pilaftsis, Nucl. Phys. B **437**, 491 (1995) [[hep-ph/9403398](#)].
- [72] F. Deppisch and J. W. F. Valle, Phys. Rev. D **72**, 036001 (2005) [[hep-ph/0406040](#)].
- [73] A. Abada, D. Das, A. M. Teixeira, A. Vicente and C. Weiland, JHEP **1302**, 048 (2013) [[arXiv:1211.3052](#)].
- [74] A. Abada, A. M. Teixeira, A. Vicente and C. Weiland, JHEP **1402**, 091 (2014) [[arXiv:1311.2830](#)].
- [75] D. N. Dinh, A. Ibarra, E. Molinaro and S. T. Petcov, JHEP **1208** (2012) 125 [JHEP **1309** (2013) 023] [[arXiv:1205.4671](#)].
- [76] A. Ibarra, E. Molinaro and S. T. Petcov, Phys. Rev. D **84**, 013005 (2011) [[arXiv:1103.6217](#)].
- [77] A. Ibarra, E. Molinaro and S. T. Petcov, JHEP **1009**, 108 (2010) [[arXiv:1007.2378](#)].
- [78] P. Humbert, M. Lindner and J. Smirnov, JHEP **1506**, 035 (2015) [[arXiv:1503.03066](#)].
- [79] E. Akhmedov, A. Kartavtsev, M. Lindner, L. Michaels and J. Smirnov, JHEP **1305**, 081 (2013) [[arXiv:1302.1872](#)].
- [80] P. S. Bhupal Dev, R. Franceschini and R. N. Mohapatra, Phys. Rev. D **86**, 093010 (2012) [[arXiv:1207.2756](#)].
- [81] A. Das and N. Okada, Phys. Rev. D **88**, 113001 (2013) [[arXiv:1207.3734](#)].
- [82] C. G. Cely, A. Ibarra, E. Molinaro and S. T. Petcov, Phys. Lett. B **718**, 957 (2013) [[arXiv:1208.3654](#)].
- [83] P. Bandyopadhyay, E. J. Chun, H. Okada and J. C. Park, JHEP **1301**, 079 (2013) [[arXiv:1209.4803](#)].
- [84] A. Kusenko, Phys. Rept. **481**, 1 (2009) [[arXiv:0906.2968](#)].
- [85] S. T. Petcov, Sov. J. Nucl. Phys. **25**, 340 (1977) [Yad. Fiz. **25**, 641 (1977)] [Sov. J. Nucl. Phys. **25**, 698 (1977)] [Yad. Fiz. **25**, 1336 (1977)].
- [86] S. M. Bilenky, S. T. Petcov and B. Pontecorvo, Phys. Lett. B **67**, 309 (1977).
- [87] J. Adam *et al.* [MEG Collaboration], Phys. Rev. Lett. **110**, 201801 (2013) [[arXiv:1303.0754](#)].

- [88] M. Agostini *et al.* [GERDA Collaboration], Phys. Rev. Lett. **111**, no. 12, 122503 (2013) [[arXiv:1307.4720](#)].
- [89] M. Auger *et al.* [EXO Collaboration], Phys. Rev. Lett. **109**, 032505 (2012) [[arXiv:1205.5608](#)].
- [90] J. B. Albert *et al.* [EXO-200 Collaboration], Nature **510**, 229 (2014) [[arXiv:1402.6956](#)].
- [91] A. Gando *et al.* [KamLAND-Zen Collaboration], Phys. Rev. Lett. **110**, no. 6, 062502 (2013) [[arXiv:1211.3863](#)].
- [92] M. Blennow, E. Fernandez-Martinez, J. Lopez-Pavon and J. Menendez, JHEP **1007**, 096 (2010) [[arXiv:1005.3240](#)].
- [93] S. Chatrchyan *et al.* [CMS Collaboration], Phys. Lett. B **717**, 109 (2012) [[arXiv:1207.6079](#)].
- [94] For a phenomenological review, see: A. Atre, T. Han, S. Pascoli and B. Zhang, JHEP **0905**, 030 (2009) [[arXiv:0901.3589](#)].
- [95] S. Antusch and O. Fischer, JHEP **1505**, 053 (2015) [[arXiv:1502.05915](#)].
- [96] M. E. Peskin and T. Takeuchi, Phys. Rev. Lett. **65**, 964 (1990);
- [97] M. Golden and L. Randall, Nucl. Phys. B **361**, 3 (1991);
- [98] B. Holdom and J. Terning, Phys. Lett. B **247**, 88 (1990).;
- [99] M. E. Peskin and T. Takeuchi, Phys. Rev. D **46**, 381 (1992);
- [100] G. Altarelli and R. Barbieri, Phys. Lett. B **253**, 161 (1991);
- [101] G. Altarelli, R. Barbieri and S. Jadach, Nucl. Phys. B **369**, 3 (1992) [Erratum-ibid. B **376**, 444 (1992)].
- [102] R. Barbieri, A. Pomarol and R. Rattazzi, Phys. Lett. B **591**, 141 (2004) [[hep-ph/0310285](#)];
- [103] R. Barbieri, A. Pomarol, R. Rattazzi and A. Strumia, Nucl. Phys. B **703**, 127 (2004) [[hep-ph/0405040](#)].
- [104] A. Pilaftsis and T. E. J. Underwood, Nucl. Phys. B **692**, 303 (2004) [[hep-ph/0309342](#)].
- [105] P. H. Gu and U. Sarkar, Phys. Lett. B **694**, 226 (2010) [[arXiv:1007.2323](#)].
- [106] S. Davidson, E. Nardi and Y. Nir, Phys. Rept. **466**, 105 (2008) [[arXiv:0802.2962](#)];
- [107] M. Farina, D. Pappadopulo and A. Strumia, JHEP **1308**, 022 (2013) [[arXiv:1303.7244](#)].
- [108] M. Fabbrichesi and A. Urbano, [[arXiv:1504.05403](#)].
- [109] C. Ford, I. Jack and D. R. T. Jones, Nucl. Phys. B **387**, 373 (1992) [Nucl. Phys. B **504**, 551 (1997)] [[hep-ph/0111190](#)].

- [110] See, for instance: J. A. Casas, J. R. Espinosa and M. Quiros, *Phys. Lett. B* **342**, 171 (1995) [[hep-ph/9409458](#)].
- [111] See, for instance: M. Quiros, [hep-ph/9901312](#).
- [112] M. Malinsky, J. C. Romao and J. W. F. Valle, *Phys. Rev. Lett.* **95**, 161801 (2005) [[hep-ph/0506296](#)].
- [113] F. del Aguila, M. Masip and M. Perez-Victoria, *Nucl. Phys. B* **456** (1995) 531 [[hep-ph/9507455](#)].
- [114] P. H. Chankowski, S. Pokorski, and J. Wagner, *Z-prime and the Appelquist-Carrazzone decoupling*, *Eur.Phys.J.* **C47** (2006) 187–205, [[hep-ph/0601097](#)].
- [115] E. Salvioni, G. Villadoro, and F. Zwirner, *Minimal Z-prime models: Present bounds and early LHC reach*, *JHEP* **11** (2009) 068, [[arXiv:0909.1320](#)].
- [116] S. Khalil and A. Masiero, *Radiative B-L symmetry breaking in supersymmetric models*, *Phys.Lett.* **B665** (2008) 374–377, [[arXiv:0710.3525](#)].
- [117] L. Basso, A. Belyaev, S. Moretti, and C. H. Shepherd-Themistocleous, *Phenomenology of the minimal B-L extension of the Standard model: Z' and neutrinos*, *Phys. Rev.* **D80** (2009) 055030, [[arXiv:0812.4313](#)].
- [118] L. Basso, S. Moretti, and G. M. Pruna, *Constraining the  $g'_1$  coupling in the minimal B – L Model*, *J.Phys.* **G39** (2012) 025004, [[arXiv:1009.4164](#)].
- [119] L. Basso, A. Belyaev, S. Moretti, G. M. Pruna, and C. H. Shepherd-Themistocleous, *Z' discovery potential at the LHC in the minimal B – L extension of the Standard Model*, *Eur. Phys. J.* **C71** (2011) 1613, [[arXiv:1002.3586](#)].
- [120] L. Basso, S. Moretti, and G. M. Pruna, *Phenomenology of the minimal B – L extension of the Standard Model: the Higgs sector*, *Phys.Rev.* **D83** (2011) 055014, [[arXiv:1011.2612](#)].
- [121] L. Basso, S. Moretti, and G. M. Pruna, *A Renormalisation Group Equation Study of the Scalar Sector of the Minimal B-L Extension of the Standard Model*, *Phys.Rev.* **D82** (2010) 055018, [[arXiv:1004.3039](#)].
- [122] E. Accomando, A. Belyaev, L. Fedeli, S. F. King, and C. Shepherd-Themistocleous, *Z' physics with early LHC data*, *Phys. Rev.* **D83** (2011) 075012, [[arXiv:1010.6058](#)].
- [123] L. Basso, S. Moretti, and G. M. Pruna, *Theoretical constraints on the couplings of non-exotic minimal Z' bosons*, *JHEP* **08** (2011) 122, [[arXiv:1106.4762](#)].
- [124] L. Basso, K. Mimasu, and S. Moretti, *Z' signals in polarised top-antitop final states*, *JHEP* **09** (2012) 024, [[arXiv:1203.2542](#)].
- [125] L. Basso, K. Mimasu, and S. Moretti, *Non-exotic Z' signals in  $\ell^+\ell^-$ ,  $b\bar{b}$  and  $t\bar{t}$  final states at the LHC*, *JHEP* **11** (2012) 060, [[arXiv:1208.0019](#)].

- [126] E. Accomando, D. Becciolini, A. Belyaev, S. Moretti, and C. Shepherd-Themistocleous, *Z' at the LHC: Interference and Finite Width Effects in Drell-Yan*, *JHEP* **10** (2013) 153, [[arXiv:1304.6700](#)].
- [127] E. Accomando, A. Belyaev, J. Fiaschi, K. Mimasu, S. Moretti, and C. Shepherd-Themistocleous, *Forward-backward asymmetry as a discovery tool for Z' bosons at the LHC*, *JHEP* **01** (2016) 127, [[arXiv:1503.02672](#)].
- [128] E. Accomando, A. Belyaev, J. Fiaschi, K. Mimasu, S. Moretti, and C. Shepherd-Themistocleous, *A<sub>FB</sub> as a discovery tool for Z' bosons at the LHC*, [arXiv:1504.03168](#).
- [129] N. Okada and S. Okada, *Z'\_{BL} portal dark matter and LHC Run-2 results*, *Phys. Rev.* **D93** (2016), no. 7 075003, [[arXiv:1601.07526](#)].
- [130] Z. Kang, P. Ko, and J. Li, *New Avenues to Heavy Right-handed Neutrinos with Pair Production at Hadronic Colliders*, *Phys. Rev.* **D93** (2016), no. 7 075037, [[arXiv:1512.08373](#)].
- [131] L. Basso, *Minimal Z' models and the 125 GeV Higgs boson*, *Phys. Lett.* **B725** (2013) 322–326, [[arXiv:1303.1084](#)].
- [132] A. Datta, A. Elsayed, S. Khalil, and A. Moursy, *Higgs vacuum stability in the B – L extended standard model*, *Phys.Rev.* **D88** (2013), no. 5 053011, [[arXiv:1308.0816](#)].
- [133] J. Chakraborty, P. Konar, and T. Mondal, *Constraining a class of B-L extended models from vacuum stability and perturbativity*, *Phys. Rev.* **D89** (2014), no. 5 056014, [[arXiv:1308.1291](#)].
- [134] C. Coriano, L. Delle Rose, and C. Marzo, *Vacuum Stability in U(1)-Prime Extensions of the Standard Model with TeV Scale Right Handed Neutrinos*, *Phys. Lett.* **B738** (2014) 13–19, [[arXiv:1407.8539](#)].
- [135] S. Oda, N. Okada, and D.-s. Takahashi, *Classically conformal U(1)? extended standard model and Higgs vacuum stability*, *Phys. Rev.* **D92** (2015), no. 1 015026, [[arXiv:1504.06291](#)].
- [136] A. Das, N. Okada, and N. Papapietro, *Electroweak vacuum stability in classically conformal B-L extension of the Standard Model*, [arXiv:1509.01466](#).
- [137] C. Coriano, L. Delle Rose, and C. Marzo, *Constraints on abelian extensions of the Standard Model from two-loop vacuum stability and U(1)<sub>B-L</sub>*, *JHEP* **02** (2016) 135, [[arXiv:1510.02379](#)].
- [138] A. Das, S. Oda, N. Okada, and D.-s. Takahashi, *Classically conformal U(1)' extended standard model, electroweak vacuum stability, and LHC Run-2 bounds*, [arXiv:1605.01157](#).
- [139] F. Bezrukov, M. Y. Kalmykov, B. A. Kniehl, and M. Shaposhnikov, *Higgs Boson Mass and New Physics*, *JHEP* **1210** (2012) 140, [[arXiv:1205.2893](#)].
- [140] I. Masina, *Higgs boson and top quark masses as tests of electroweak vacuum stability*, *Phys.Rev.* **D87** (2013), no. 5 053001, [[arXiv:1209.0393](#)].

- [141] G. Cacciapaglia, C. Csaki, G. Marandella, and A. Strumia, *The Minimal Set of Electroweak Precision Parameters*, *Phys.Rev.* **D74** (2006) 033011, [[hep-ph/0604111](#)].
- [142] P. Bechtle, O. Brein, S. Heinemeyer, G. Weiglein, and K. E. Williams, *HiggsBounds: Confronting Arbitrary Higgs Sectors with Exclusion Bounds from LEP and the Tevatron*, *Comput. Phys. Commun.* **181** (2010) 138–167, [[arXiv:0811.4169](#)].
- [143] P. Bechtle, O. Brein, S. Heinemeyer, G. Weiglein, and K. E. Williams, *HiggsBounds 2.0.0: Confronting Neutral and Charged Higgs Sector Predictions with Exclusion Bounds from LEP and the Tevatron*, *Comput. Phys. Commun.* **182** (2011) 2605–2631, [[arXiv:1102.1898](#)].
- [144] P. Bechtle *et. al.*, *Recent Developments in HiggsBounds and a Preview of HiggsSignals*, *PoS CHARGED2012* (2012) 024, [[arXiv:1301.2345](#)].
- [145] P. Bechtle *et. al.*, *HiggsBounds-4: Improved Tests of Extended Higgs Sectors against Exclusion Bounds from LEP, the Tevatron and the LHC*, *Eur. Phys. J.* **C74** (2014) 2693, [[arXiv:1311.0055](#)].
- [146] P. Bechtle, S. Heinemeyer, O. Stal, T. Stefaniak, and G. Weiglein, *Applying Exclusion Likelihoods from LHC Searches to Extended Higgs Sectors*, [arXiv:1507.06706](#).
- [147] P. Bechtle, S. Heinemeyer, O. Stl, T. Stefaniak, and G. Weiglein, *HiggsSignals: Confronting arbitrary Higgs sectors with measurements at the Tevatron and the LHC*, *Eur. Phys. J.* **C74** (2014), no. 2 2711, [[arXiv:1305.1933](#)].
- [148] **CMS** Collaboration, V. Khachatryan *et. al.*, *Search for a Higgs Boson in the Mass Range from 145 to 1000 GeV Decaying to a Pair of W or Z Bosons*, *JHEP* **10** (2015) 144, [[arXiv:1504.00936](#)].
- [149] **CMS** Collaboration, *Properties of the Higgs-like boson in the decay  $H$  to  $ZZ$  to  $4l$  in  $pp$  collisions at  $\sqrt{s} = 7$  and  $8$  TeV*, **CMS-PAS-HIG-13-002**.
- [150] **CMS** Collaboration, *Update on the search for the standard model Higgs boson in  $pp$  collisions at the LHC decaying to  $W + W$  in the fully leptonic final state*, **CMS-PAS-HIG-13-003**.
- [151] **CMS** Collaboration, *Combination of standard model Higgs boson searches and measurements of the properties of the new boson with a mass near 125 GeV*, **CMS-PAS-HIG-12-045**.
- [152] **ATLAS, CDF, CMS, D0** Collaboration, *First combination of Tevatron and LHC measurements of the top-quark mass*, [arXiv:1403.4427](#).
- [153] A. Buckley *et. al.*, *General-purpose event generators for LHC physics*, *Phys. Rept.* **504** (2011) 145–233, [[arXiv:1101.2599](#)].
- [154] A. Juste, S. Mantry, A. Mitov, A. Penin, P. Skands, E. Varnes, M. Vos, and S. Wimpenny, *Determination of the top quark mass circa 2013: methods, subtleties, perspectives*, *Eur. Phys. J.* **C74** (2014) 3119, [[arXiv:1310.0799](#)].
- [155] S. Frixione and A. Mitov, *Determination of the top quark mass from leptonic observables*, *JHEP* **09** (2014) 012, [[arXiv:1407.2763](#)].

- [156] A. Belyaev, N. D. Christensen, and A. Pukhov, *CalcHEP 3.4 for collider physics within and beyond the Standard Model*, *Comput. Phys. Commun.* **184** (2013) 1729–1769, [[arXiv:1207.6082](#)].
- [157] M. Bondarenko, A. Belyaev, L. Basso, E. Boos, V. Bunichev, *et. al.*, *High Energy Physics Model Database : Towards decoding of the underlying theory (within Les Houches 2011: Physics at TeV Colliders New Physics Working Group Report)*, [arXiv:1203.1488](#).
- [158] W. Emam and S. Khalil, *Higgs and Z-prime phenomenology in B-L extension of the standard model at LHC*, *Eur. Phys. J.* **C52** (2007) 625–633, [[arXiv:0704.1395](#)].
- [159] K. Huitu, S. Khalil, H. Okada, and S. K. Rai, *Signatures for right-handed neutrinos at the Large Hadron Collider*, *Phys. Rev. Lett.* **101** (2008) 181802, [[arXiv:0803.2799](#)].
- [160] S. Khalil and S. Moretti, *The B – L Supersymmetric Standard Model with Inverse Seesaw at the Large Hadron Collider*, [arXiv:1503.08162](#).
- [161] LHC Higgs Cross Section Working Group,  
<https://twiki.cern.ch/twiki/bin/view/LHCPhysics/CERNYellowReportPageAt13TeV>.
- [162] M. x. Luo, H. w. Wang and Y. Xiao, *Phys. Rev. D* **67** (2003) 065019 [[hep-ph/0211440](#)].
- [163] R. M. Fonseca, M. Malinsky and F. Staub, *Phys. Lett. B* **726** (2013) 882 [[arXiv:1308.1674](#)].